DEPARTMENT OF ELECTRONIC & ELECTRICAL ENGINEERING

University of Strathclyde Engineering

Advanced radar systems and algorithms for space object localization

Author: Sebastián Díaz Riofrío

Student Number: 202091810

Supervisors:

Prof. Carmine Clemente

Prof. Massimiliano Vasile

A thesis submitted in partial fulfilment for the requirement of the degree of Doctorate of Philosophy

September 2025

Abstract

With the increasing number of space objects, there is a growing need to monitor the geospace, the region surrounding the Earth, to prevent collisions, which would generate additional space debris. Radar can be employed for space situational awareness tasks, specifically for space object localization. While most space situational awareness radar systems are ground-based, with some using radio telescopes as receivers, recent advancements in spaceborne radar could offer more cost-effective solutions. In this context, this thesis investigates the design and signal processing solutions for spaceborne and ground-based radars for space situational awareness.

The spaceborne radar operates in a forward scatter configuration, a special bistatic case in which the bistatic angle is approximately 180°. The system is passive, meaning it exploits signals from third-party sources to perform radar tasks. The proposed design considers the radar mounted on a CubeSat orbiting on a low Earth orbit. As the antenna is the most constraining component of a CubeSat, potentially determining its size, a directivity analysis of various antennas is conducted alongside a radar range equation analysis to identify the most suitable option. Furthermore, the received signals are processed to enhance the signal-to-noise ratio through multiple integration across multiple operating frequencies and to enable accurate target localization, with particular attention to reducing the computational cost of motion parameter estimation. To achieve this, the traditional bank-of-correlators matched filter approach proposed in previous studies is replaced by a novel zoom-in matched filter algorithm coupled with

a recurrent neural network classifier.

The ground segment is investigated using a long-baseline distributed radar. In this setup, one transmitter and multiple receivers spread across the Earth are considered. Each transmitter–receiver combination forms a bistatic pair. Multiple receivers are employed to combine bistatic measurements and provide more accurate and reliable target localization. The system is first analysed from the perspective of the radar range equation. A processing strategy based on the multiple-input-multiple-output ambiguity function is then introduced to address the challenge of target localization.

Contents

List of Figures

List of Tables

Acronyms

3D-PAA 3-Dimensional Phased Array Antenna. 71

AF Ambiguity Function. 150

AI Artificial Intelligence. 54, V

AWGN Additive White Gaussian Noise. 31

CNN Convolutional Neural Network. 55

CPF Complex Profile Function. 42

CPI Coherent Processing Interval. 28

EM electromagnetic. 11

FrFT Fractional Fourier Transform. 128

FS Forward Scatter. 5

FSR Forward Scatter Radar. 39

GEO Geostationary Equatorial Orbit. 4

IO Illuminator of Opportunity. 5

ISAR Inverse Synthetic Aperture Radar. 39

LEO Low Earth Orbit. 2

LFM Linear Frequency Modulation. 32

LSTM Long Short Term Memory. 58, V

ME Moving-Ends. 40

MIMO AF Multiple-Input-Multiple-Output Ambiguity Function. 8

NN Neural Network. 54

PAM Phased Array of Monopoles. 71

PBR Passive Bistatic Radar. 5, 38

PRF Pulse Repetition Frequency. 18

PRI Pulse Repetition Interval. 18

RAF Radiation Array Factor. 73

RCS Radar Cross-Section. 5, 16

RF radiofrequency. 11

RFS Reverse Forward Scatter. 47

RHS Radio Holographic Signal. 40

RNN Recurrent Neural Network. 55

RRE Radar Range Equation. 22

SAR Synthetic Aperture Radar. 38

SCR Signal-to-Clutter Ratio. 22

SCR Signal-to-Interference Ratio. 22

SIMO Single-Input-Multiple-Output. 7

SISAR Shadow Inverse Synthetic Aperture Radar. 39

SNR Signal-to-Noise Ratio. 6

SSA Space Situational Awareness. 1

List of Symbols

Global symbols

λ	Wavelength
φ	Independent variable in a function
B_W	Bandwidth of a signal
D	Aperture dimension of the antenna
f	Frequency
f_0	Operating frequency
j	Imaginary unit
k_n	Boltzmann constant
SNR	Signal-to-noise ratio
T_0	Standard temperature
ω_f	Angular frequency
a	Discrete index
b	Discrete index
c_0	Speed of light

k Wave number

t Time variable

Radar symbols

β Bistatic angle

Δf_D Doppler frequency resolution

ΔR Range resolution

Δr_{bs} Bistatic range resolution

ΔT_{max} Maximum delay time associated to the maximum unambiguous range

$\dot{R}$ Range rate

σ Radar cross section

σ_{bs} Bistatic RCS

σ_{min} Minimum RCS for a given minimum SNR

τ Pulse width

τ_Δ Radar delay

A_e Effective area of the antenna

CPI Coherent processing interval

d_t Duty cycle

$EIRP$ Effective isotropic radiated power

F Noise factor

f_D Doppler frequency shift

f_r Resulting received frequency with Doppler frequency shift

f_t Transmitted frequency

$f_{D,max}$ Maximum unambiguous Doppler frequency shift

G_r Gain of the receiving antenna

G_t Gain of the transmitting antenna

G_{LNA} Gain of the low-noise amplifier

G_{sp} Signal processing gain

K_{np} Multiple integration factor

L_a Atmospheric losses

L_r Receiver losses

L_s System losses

L_t Transmit losses

L_{sp} Signal processing losses

n_p Number of pulses to integrate

P_n Power of the thermal noise

P_r Received power

P_t Transmitted power

P_{avg} Average transmitted power

P_{reft} Reflected power

PRF Pulse repetition frequency

PRI Pulse repetition interval

Q_i Power density at a certain distance

Q_P Power intensity

Q_r Power density back at the radar

R_1 Distance from the transmitter to the target

R_2 Distance from the target to the transmitter

r_{bs} Bistatic range

R_{det} Detection range

R_{max} Maximum unambiguous range

R_{min} Minimum range

R_{ua} Unambiguous range

RCS_{bs} Bistatic RCS

SNR_c Signal-to-noise ratio for coherent integration

SNR_{ant} SNR after the antenna

$SNR_{bs;a_{bs},b_{bs}}$ SNR for a bistatic pair when the signal emitted from the transmitter a_{bs} is received by the b_{bs} receiver

SNR_{min} Minimum SNR to ensure detection

SNR_{ms} SNR for multistatic radar

SNR_{nc} Signal-to-noise ratio for non-coherent integration

SNR_{pc} SNR with pulse compression

SNR_u SNR for an unmodulated pulse

T_s System noise temperature

T_d Dwell time

v_r Radial component of the speed of the target

ΔT Time between transmission and the radar signal reception

R Radar range

Signal processing symbols

α_{FrFT} Fractional order of the FrFT

$\delta_D(\cdot)$ Dirac delta function

ϕ_{FrFT} FrFT rotation angle associated to the α_{FrFT} fractional order

$A_{FrFT,0}$ Factor in the FrFT kernel

AF Ambiguity function

$c(t)$ Original baseband transmitted signal

K_f Number of points in a discrete Fourier transform

K_f Number of points in the discrete Fourier Transform

k_f Discrete Fourier transform index

$K_{\alpha_{FrFT}}$ FrFT kernel

m_{FrFT} Integer number in the FrFT kernel

$s_1[n]$ Discrete signal for convolution

$s_2[n]$ Discrete signal for convolution

$S_D[k_f]$ K_f-point discrete Fourier Transform digital signal

$s_D[n]$ Inverse discrete Fourier Transform digital signal

$s_{MF}(t)$ Received baseband signal after the matched filter

$s_{MF}(t)$ Reference signal for the matched filter

$s_{NC}(t)$ Signal after non-coherent processing

$s_R(t)$ Received baseband signal

$X_{\alpha_{FrFT}}$ FrFT of order α_{FrFT} of the discrete signal $x[n]$

$x_{MF}(t)$ Received FS signal for the matched filter

$y_{MF}(t)$ Output of the matched filter

N Number of samples in a discrete time signal

n Discrete index in a discrete time signal

Forward scatter radar symbols

α_{spc} Inclination angle of the circular orbit in the XY plane in the FS configuration

η η function for the forward scatter signal

γ γ function for the forward scatter signal

Γ_p Γ variable for the target for the forward scatter signal

Γ_R Γ variable for the receiver for the forward scatter signal

Γ_T Γ variable for the transmitter for the forward scatter signal

ω_{spc} Angular speed of the space object in the FS configuration

P_{spc} Position of the space object in the FS configuration

Q Q function for the forward scatter signal

R_{spc} Distance from the centre of the Earth to the space object in the FS configuration

(x', y', z') Cartesian coordinates and axis for when the centre of the target is considered as the origin in the FS configuration

$(X, Y, Z)(t)$ Cartesian coordinates over time in the FS configuration

α_1 Angle between y'-axis and the position vector from the transmitter to the target

α_2 Angle between y'-axis and the position vector from the target to the transmitter

α_p Inclination angle of the orbit, or trajectory angle, of the target

α_R Inclination angle of the orbit, or trajectory angle, of the receiver

α_T Inclination angle of the orbit, or trajectory angle, of the transmitter

$\dot{H}(x')$ Reconstructed complex profile function

ϵ_τ Function of the shadow profile of the target

$\sigma_{FS,max}$ Maximum RCS in the forward scatter configuration

σ_{FS} RCS in the forward scatter configuration

θ_{FS} Radius of the forward scatter main lobe

$a_{1,\cdots,m}$ Maxima of the correlation function used in the bank of correlators

A_{FS} Amplitude of the transmitted signal for the Forward scatter scenario

A_{trg} Forward scatter area, the area of the silhouette of the target

E_{FS} Forward scatter signal

$H(x')$ Complex profile function

$h(x')$ Height difference

$m(x')$ Median line of the profile of the target

r_1 Distance from the transmitter to every point of the target

r_2 Distance from every point of the target to the transmitter

r_{c1} Distance from the transmitter the target when t = 0 in the FS configuration

r_{c2} Distance from the target to the receiver when t = 0 in the FS configuration

R_p Distance from the centre of the Earth to the target

R_R Distance from the centre of the Earth to the receiver

r_{trg} Radius of assumed target sphere

R_T Distance from the centre of the Earth to the transmitter

S_{FS} Surface of the target in the forward scatter configuration

t_{obs} Observation, or integration, time in the forward scatter configuration

Ground-based radar symbols

ψ Angle between half the bistatic angle and the trajectory to the target

θ_{Rx} Angle between the normal and the position vector from the receiver to the target

θ_{Tx} Angle between the normal and the position vector from the transmitter to the target

d_{Rx} Distance from the receiver to the target

d_{Tx} Distance from the transmitter to the target

G_c Gravitational constant

h_{earth} Altitude of a space object

$L_{Tx,Rx}$ Distance from the transmitter to the receiver, the baseline

M_{earth} Mass of the Earth

R_{earth} Earth radius

r_{earth} Distance from the centre of the Earth to a space object

v_{esc} Orbital escape speed

Multiple frequency system symbols

$\hat{E}_b$ Averaged forward scatter signal when the first b channels are used

$\hat{H}_a$ The reconstructed CPF for the a-th value of the SNR

$\text{MSE}_{FS,b}$ MSE when the first b channels are averaged

$\mathrm{MSE}_{SNR,a}$ Mean square error for the a-th value of SNR

$E_{FS,1}$ Forward scatter signal for the first channel

$E_{fs,avg}$ Averaged forward scatter signal

$E_{fs,a}$ Forward scatter signal for frequency channel a

N_f Number of frequency channels

n_{CPF} The number of samples from the CPFs

n_{sFS} Number of samples per forward scatter signal

Zoom-in matched filter algorithm symbols

$\bar{\mu}_{\mathbf{abs,err,alt}}$ Absolute mean error for the altitude

$\bar{\mu}_{\mathbf{err,alt}}$ Mean error for the altitude

κ_{i_L} Threshold value for iteration i_L in the zoom-in algorithm

$\sigma_{\mathbf{abs,err,alt}}$ Variance of the random Gaussian variable model for the absolute error of the altitude

$\sigma_{\mathbf{err,alt}}$ Variance of the random Gaussian variable model for the error of the altitude

alt_{rx} Altitude of the receiver in the zoom-in algorithm

alt_{tx} Altitude of the transmitter in the zoom-in algorithm

D_{trg} Diameter of assumed target sphere

i_L Iteration number in the zoom-in algorithm

L Number of iterations in the zoom-in algorithm

M_{alt,i_L} Number of altitude points around the maxima for iteration i_L of the zoom-in algorithm

M_{alt} Number of altitude points in the initial grid of the zoom-in algorithm

M_{ang,i_L} Number of angle points around the maxima for iteration i_L of the zoom-in algorithm

M_{ang} Number of angle of trajectory points in the initial grid of the zoom-in algorithm

N_{sz} Number of points calculated for the profile of the target in the zoom-in algorithm

t_{ite} Time per iteration

Multiple-input-multiple-output ambiguity function symbols

$(p_x, p_y, p_z))$ x, y, z components of the position of the target

$(p_{c,x}, p_{c,y}, p_{c,z})$ x, y, z components the assumed position vector of the target

$(v_x, v_y, v_z))$ x, y, z components of the speed of the target

$(v_{c,x}, v_{c,y}, v_{c,z})$ x, y, z components of the assumed speed vector of the target

$\vec{p}$ Position vector of a target

$\vec{p}_c$ Assumed position vector of the target

$\vec{v}$ Speed vector of a target

$\vec{v}_c$ Assumed speed vector of the target

$AF_{a,b}$ Ambiguity function for bistatic pair of a transmitter and b receiver

$f_{D;a,b}$ Doppler frequency shift resulting from the perceived speed for signal for transmitter a and receiver b

M_{bs} Number of receivers in a bistatic system

N_{bs} Number of transmitters in a bistatic system

$s_{a,b}$ Signal coming from transmitter a and receiver b

Neural network symbols

α_A Step size in the Adam algorithm

$\beta_{A,1}$ Exponential decay rate for the first moment estimates in the Adam algorithm

$\beta_{A,2}$ Exponential decay rate for the second moment estimates in the Adam algorithm

$\Delta_{\Theta_{NN}}$ Gradient with respect to Θ in the recurrent neural network

$\epsilon_{A,1}$ Denominator offset in the Adam algorithm

$\hat{m}_{A,\mathfrak{t}}$ Bias-corrected first moment vector of the Adam algorithm

$\hat{v}_{A,\mathfrak{t}}$ Bias-corrected second moment vector of the Adam algorithm

$\mathfrak{t}$ Time unit in the recurrent neural network

σ_H Hard-sigmoid function

σ_l Logistic function

$\Theta_{NN,0}$ Initial $U_{NN}, V_{NN}, W_{NN}, b_{NN}, c_{NN}$ parameters of the recurrent neural network in the Adam algorithm

Θ_{NN} Variable representing $U_{NN}, V_{NN}, W_{NN}, b_{NN}, c_{NN}$ parameters in the recurrent neural network

a_f Class number in a neural network

b_f Class number in a neural network

$e_{NN,\mathfrak{t}}$ Error vector in the recurrent neural network

$f_{NN,a}(\cdot)$ Activation function

$f_{NN,in}$ Activation function of the input gate in the recurrent neural network

$f_{NN,out}$ Activation function of the output gate in the recurrent neural network

$f_{NN,u_{NN}}$ Squashing function of the unit u_{NN} in the recurrent neural network

$G_{NN,\mathfrak{t}}$ Gradient vector in the recurrent neural network

$g_{NN}(x_{NN})$ Squashed activation function in the recurrent neural network

$h_{NN}(t)$ Hidden state of the recurrent neural network

$h_{NN}(x_{NN})$ Activation function in the recurrent neural network

$m_{A,0}$ Initial first moment vector of the Adam algorithm

$m_{A,t}$ First moment estimate vector of the Adam algorithm

N_{cl} Number of classes in a neural network

$o_{NN}(t)$ Output of the recurrent neural network

Q_{a_f} Softmax function associated with the a_f class

$s_{NN,m_{NN},c_{NN}}$ State of the cell c_{NN} of the memory block m_{NN} in the recurrent neural network

$softmax(\cdot)$ Softmax function

U_{NN} Weight matrix of the recurrent neural network

$v_{A,0}$ Initial second moment vector of the Adam algorithm

$v_{A,t}$ Second moment estimate vector of the Adam algorithm

V_{a_f} Output of a neural network associated with the a_f class

V_{b_f} Output of a neural network associated with the b_f class

V_{NN} Weight matrix of the recurrent neural network

$W_{NN,[u_{NN},u_{NN}]}$ Weight that connects the unit u_{NN} to itself in the recurrent neural network

W_{NN} Weight matrix of the recurrent neural network

$x_{NN}(t)$ Input feature signal for an recurrent neural network

$y_{NN,in}$ Input gate of a LSTM block in the recurrent neural network

$y_{NN,m_{NN},c_{NN}}$ Cell output of the recurrent neural network

$y_{NN,out}$ Output gate of a LSTM block in the recurrent neural network

$y_{NN,u_{NN}}$ Output of the unit u_{NN} of the recurrent neural network

$z_{u_{NN}}$ Weighted input of the unit u_{NN} in the recurrent neural network

b_{NN} Bias term

c_{NN} Bias term

Antenna design symbols

η_a Efficiency of the antenna

$\hat{r}$ Unit position vector pointing to the position of interest

$\vec{r}_a$ Position vector of element a

c_a Complex-valued excitation coefficient of element a

D_{el} Directivity pattern of a single antenna element

d_{pa} Diameter of a parabolic antenna

G_{pa} Gain of a parabolic antenna

N_{el} Number of elements in the array

RAF Radiation array factor

U_a Beam pattern of the array

Other symbols

θ_i Incidence angle

θ_r Reflection angle

$\theta_{sinc,-3\,\mathrm{dB}}$ Half power of the main lobe of the sinc function

A_c Area of a circle

D_a Antenna aperture

$E_{EM,x}$ Electric field in the X axis

$E_{EM,y}$ Electric field in the Y axis

n_{ir} Index of refraction

P_D Probability of detection in a radar system

P_{FA} Probability of false alarm in a radar system

r_c Radius of a circle

v_{mat} Speed of the EM in the material

$E_{EM,0}$ Peak amplitude of the electric field of the EM wave

E_{EM} Electric field of the EM wave

z_{EM} Z axis for the electromagnetic wave

Preface/Acknowledgements

This work was supported by the European Space Agency (ESA), Open Space Innovation Platform (OSIP) idea ID I-2019-00565.

I would like to thank my wife's patience and support through the last part of this journey. I would also like to thank my parents for insisting me to study when I was a kid.

Chapter 1

Introduction

Radar (RAdio Detection And Ranging) is, as the acronym suggests, a system and technology that detects and ranges targets using electromagnetic radio waves. Radio makes reference to the radiofrequencies, the electromagnetic spectrum that covers the frequencies from 30 kHz to 300 GHz [1], although in practice the frequencies can be much higher and still be considered radiofrequencies. Modern radars perform more tasks than just detection and ranging, they also track targets, estimate their speed, and produce images. Therefore, radar systems are used in a wide variety of applications, from defence to air traffic control.

With the birth of radar, numerous questions about its potential applications emerged. After the Second World War, Project Diana was launched to try to bounce electromagnetic waves off the moon. In 1946, the project was successfully completed and the results were published in [2, 3]. This was the first instance in history in which radar was used for outer space. The success of Project Diana opened the possibility of using radar for Space Situational Awareness (SSA).

Optic sensors are also utilized in SSA [4, 5, 6, 7] and astronomy, as they are able to capture detailed images. However, radar sensors offer several significant advantages over optical sensors. Most notably, radar sensors have the capability to operate effectively in all weather conditions, including rain, fog, and cloud cover, which often hinder optical sensors. Additionally, radar systems can function equally well during both day and

night, providing consistent and reliable data irrespective of the time of day. Due to these benefits, radar sensors are frequently employed in SSA, making them a common tool in locating and tracking, monitoring, objects in space.

1.1 Motivation

In recent years the amount of space objects orbiting around the Earth has increased dramatically [8]. The increasing number of space objects orbiting around the Earth, from large satellites to small CubeSats, as seen on Figure 1.1, has created the need for systems that can monitor those space objects. These can be either cooperative, such as the artificial satellites, or uncooperative, such as space debris or small meteorites. It is important to know the location of them to minimize the risk of a space collision. Failure to avoid a collision will lead to operational disruption.

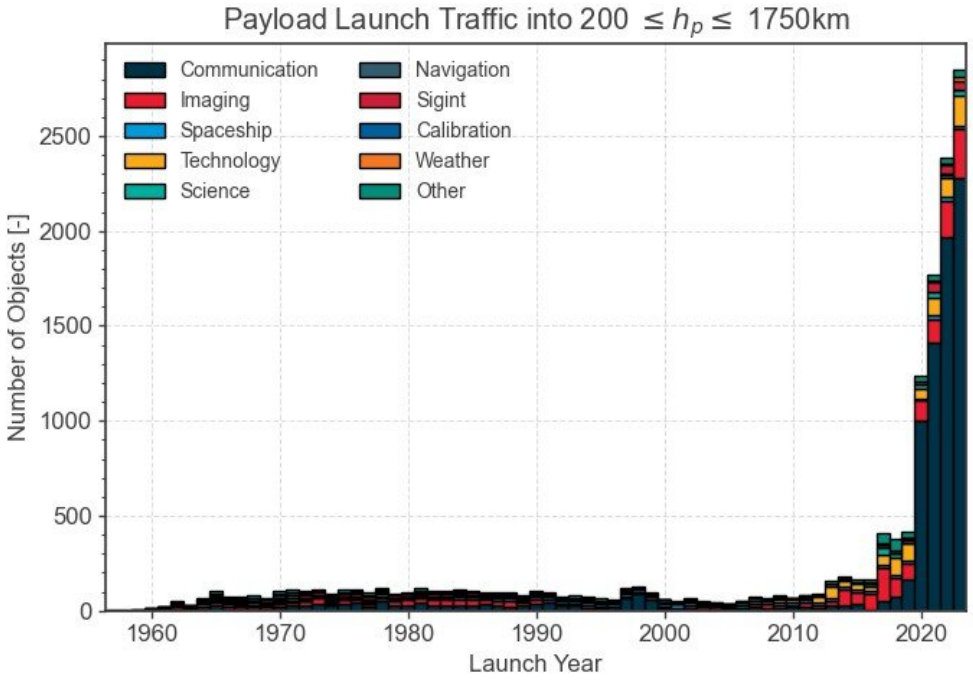

Figure 1.1: Payload launch during recent years for low-Earth orbit orbits, taken from [8]

According to the 2024 space environment report from the European Space Agency (ESA) [8], the number of objects larger than 10 cm in Low Earth Orbit (LEO) is over

34 000, and the number objects larger than 1 cm is over a million. Moreover, as the launching of micro-satellites for commercial and scientific purposes has become more affordable, the LEO space is getting overcrowded. All these facts have led to a higher chance of collision, Figure 1.2. Therefore, the localization of space objects for SSA has become an important topic to research.

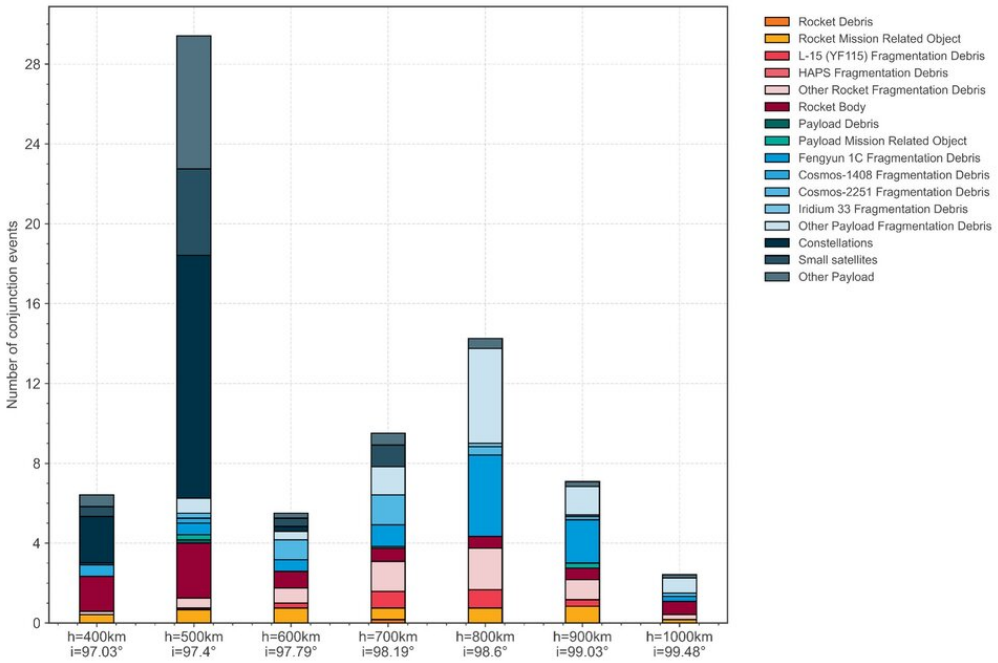

Figure 1.2: Near collision events per altitude, taken from [8]

While there are radio telescopes, antennas, that could be used as part of a radar system for SSA purposes, the majority of them are used for astronomy purposes. Therefore, with the increasing risk of collision between different space objects, SSA-only dedicated system are becoming more prevalent. Such is the case with the ground-based radars that LeoLabs has deployed in Costa Rica [9] and the Azores [10].

Two types of systems could be designed: a spaceborne radar and a ground-based radar. On one hand, the main advantage of using a spaceborne radar for SSA is that the atmospheric difficulties are overcome, as the atmosphere at LEO altitudes is very thin [11] and its effect is minimal. The power capabilities are much lower, however this is compensated by the smaller distance ranges that the radar works with. On the

other hand, the advantages of a ground-based radar would be the ease of maintenance and upgrades, if needed, and, most importantly, the higher power capabilities, which are needed to cover the larger distance ranges that the radar would cover. It should be noted that when talking about very high altitudes, such as Geostationary Equatorial Orbit (GEO), or just geostationary, targets, the advantages of spaceborne radars in relationship to the distance are diminished since the altitude of a GEO target is approximately 35 786 km. Certainly, it would be possible to set a spaceborne radar monitoring GEO satellites, nonetheless, the radar platform would need high power requirements to be able to communicate with the ground station. Because of the physics of the speeds at those altitudes, the radar would only be able to monitor a few GEO satellites, which would render this possible solution rather impractical. Therefore, in these cases, a ground-based radar would be more reasonable. Consequently, a combination of spaceborne and ground-based radars would represent the optimal solution for SSA.

1.2 Research questions and innovations

The aim of the thesis is to develop novel radar concepts, signal processing techniques and algorithms in the context of SSA. Some of the radar concepts that are going to be introduced in the following paragraphs will be more deeply studied in Chapter 2.

The thesis will introduce solutions tailored for the two mentioned categories: ground-based radar and spaceborne radar. The ground-based radar comes from the aforementioned necessity of having a system to monitor the near-Earth space. The spaceborne radar comes from the same need plus the additional demand of having a low-cost solution, as demonstrated in [12]. In this context, the University of Strathclyde has an on-going project, the STRATHcube project [13], which aims to launch a CubeSat carrying the spaceborne radar payload. Please note that a CubeSat [14] is a small satellite of size 1U, 2U, or up to even 12U [15], with $1\text{U} = 10 \times 10 \times 10\,\text{cm}^3$. While the developments of this thesis are not directly linked to STRATHcube, the author engaged with the team to provide input regarding the functioning, potential limitations and requirements for the radar system.

In [12] the spaceborne system was designed to be mounted on a CubeSat. The radar system was Passive Bistatic Radar (PBR) in a Forward Scatter (FS) configuration. The main advantage of the FS configuration is the higher Radar Cross-Section (RCS) compared to a monostatic radar if the frequency is high enough [16]. The CubeSat will be orbiting at an altitude of 500 km, and the Illuminator of Opportunity (IO), will be the OneWeb constellation satellites, which are orbiting at higher altitudes, at 1200 km. The main advantage of using a constellation of satellites is that the large amount of standardized transmitters that increases the possibility of detecting space objects. The spaceborne radar will receive signals from the IOs and process them to obtain the FS signals. These will be stored onboard and later downloaded to a ground station for the extraction of the motion parameters of the possible target.

The aim of the spaceborne radar study is to develop a system that generates a high-quality FS signal and processes them in less time than established methods while maintaining comparable accuracy. The research questions, and solutions to the same, that have been identified are:

- **Which is the optimal antenna type to be mounted on the spaceborne radar?** This will be solved by comparing the different features of the antennas. A radar range equation analysis will be computed per each antenna. The features that are going to be looked at are:
  - Robustness of the mount in the CubeSat platform.
  - Directivity.
  - Steering angle.
  - Receiver complexity for that antenna.

  There have been several studies on possible array processing techniques for FS radar [17, 18], and a few works have investigated the feasibility of antennas suitable for CubeSat deployment in FS radar configurations [19]. However, the literature remains limited in addressing the possible antennas for the radar spaceborne scenario. This study aims to contribute to filling this gap.

- **How to increase the Signal-to-Noise Ratio (SNR) of the FS signal for a better signal quality?** To decrease the possibility of erring when obtaining the motion parameters from the orbital target, the SNR should be high. While the immediate solution could be to increase the transmitted power, it would not possible, as the parameters from the IOs cannot be changed. The other possible solution could be to increase the signal acquisition time, as the received power will also increase, but by increasing the acquisition time, the computational time for extracting the motion parameters of the target will also increase. Therefore, to increase Signal-to-Noise Ratio (SNR) via a multiple integration approach for FS for better signal quality, could be a valid approach.

  A dual-frequency Forward Scatter (FS) system was proposed in [20]. The approach exploits the fact that Doppler signatures of moving targets are correlated across different operating frequencies, whereas clutter is largely uncorrelated. By re-sampling and cross-correlating signals from different frequency channels, the system enhances the processing gain and enables reliable detection of moving targets. However, this solution is presented for a stationary transmitter and receiver case with relatively low frequencies, 64 MHz and 135 MHz. As it going to be seen in Chapter 4, when the operating frequencies are comparatively high in the moving-ends scenario, the FS signals are similar enough to be integrated without needing to pre-process them.

- **How to improve on the bank of correlators approach for the extraction of the motion parameters of the target from the FS signal?** This research question focuses on enhancing the established bank of correlators, or matched filter approach, for motion parameter estimation by reducing computational time.

  Various approaches based on banks of correlators have been proposed in the literature. In [21], the velocity and trajectory angle of the crossing target were extracted. The initial analysis assumed the target crossed the midpoint at a perpendicular angle, which enabled the introduction of quasi-optimal processing. In this approach, only the phase signal, rather than the full FS signal, was replicated

for different velocity values and then correlated with the received FS signal. The method was subsequently evaluated for varying crossing points and trajectory angles. The velocity estimation remained accurate for different trajectory angles and for crossings near the midpoint. Nonetheless, its performance degraded when the crossing occurred close to either the receiver or the transmitter. The quasi-optimal approach was also used in [22], where the speed and distance from the receiver were estimated. The speed was accurately extracted, while the range estimation presented a relatively large error. The authors of [23] assumed the crossing point to be known and estimated the velocity components. More recently, [24] introduced a method for the spaceborne radar case, employing the bank of correlators to estimate the altitude and trajectory angle of a space object orbiting the Earth. However, as noted in [20, 21], the bank of correlators approach is computationally expensive. To mitigate this issue, a zoom-in strategy combined with a machine learning solution is proposed to significantly reduce computation time.

Furthermore, a ground-based radar will also be investigated. The reason being to be able to explore how to extend the capabilities of more classic systems and to explore new configurations and processing methods. The ground station will have a Single-Input-Multiple-Output (SIMO) configuration. To integrate the different sensor readings coherent and non-coherent fusion will be investigated. Two different set of targets are going to be examined: LEO and GEO targets. A particular feature of this system is that the different bistatic pairs will have a very long baseline, sometimes resulting in the transmitter and receiver being in different continents.

Part of research in the ground-based radar will be to asses the feasibility of it. This will be completed by using a radar range equation analysis. The challenge and solution of the ground-based radar is:

- **How to properly process the different bistatic readings?** In [25] a Time Difference of Arrival (TDOA) solution wags introduced for a multistatic radar system, where the transmitter and the receivers were positioned in Italy. Certainly, a similar TDOA solution could be used for the long baseline multistatic case.

Nonetheless, the sensitivity of such method to the errors in the range estimation [26] and the compensation in range needed because of the long baseline, yield this method ineffective.

The processing tool that has been found useful in this situation is the Multiple-Input-Multiple-Output Ambiguity Function (MIMO AF). As it is going to be seen in Chapter 6, the MIMO AF, even if it is more computationally heavy, is also more robust to the errors of the bistatic measurements estimation.

Certainly, it will be necessary to thoroughly assess the performance of these novel developments. This assessment will involve simulating to determine their effectiveness and efficiency. By doing so, any potential issues or areas for improvement could be identified, and their suitability for radar applications in SSA could be validated.

1.3 Thesis outline

The rest of the thesis has been written as follows. In Chapter 2 and Chapter 3 the preliminary knowledge and established techniques are reviewed. First, the radar definitions and concepts are explained. Secondly, some of the techniques and mathematical tools used in the design of the radar system and the processing of radar signals relevant for this thesis are introduced. Finally, the state of the art of the spaceborne and ground-based radar for SSA are described.

Following the establishment of the radar principles and preliminary knowledge, Chapter 4 and Chapter 5 present the developed spaceborne radar framework. Chapter 4 focuses on the antenna study, building on [27], and introduces the multiple integration approach for the FS signals, based on [28]. Chapter 5 describes the signal processing solution for extracting the motion parameters of orbital targets in the FS scenario, part of which was introduced in [29]. In addition, Chapter 6 introduces the long baseline multistatic ground-based radar framework, presented in [30] and applied in [31]. These chapters provide detailed system characterizations, including the parameters employed in the proposed processing pipelines. Finally, Chapter 7 concludes the thesis and discusses future work.

1.4 List of publications of the author

[27] Sebastián Díaz Riofrío, Christos V. Ilioudis, Carmine Clemente, Massimiliano Vasile, and Nobuyuki Kaya. "Space debris search and track forward scatter radar system with different phased array antennas". In: *8th European Conference on Space Debris*. Vol. 1. 2021.

[28] Sebastián Díaz Riofrío, Christos V. Ilioudis, Carmine Clemente, and Massimiliano Vasile. "Multiple Observation Integration Approach for Sisar Imaging Radar Systems with the Purpose of Space Surveillance". In: *2021 21st International Radar Symposium (IRS)*. 2021, pp. 1–9. DOI: 10.23919/IRS51887.2021.9466230.

[29] Sebastián Díaz Riofrío, Christos V. Ilioudis, Carmine Clemente, and Massimiliano Vasile. "Recurrent Neural Network aided Zoom-In Matched Filter algorithm for motion parameter estimation from Forward Scatter signals for Space Situational Awareness". In: *2025 25st International Radar Symposium (IRS)*. 2021.

[30] Sebastián Díaz Riofrío, Simão Da Graça Marto, Christos Ilioudis, Massimiliano Vasile, and Carmine Clemente. "Performance analysis of ground-based long baseline radar distributed systems for space situational awareness". In: *IET Radar, Sonar & Navigation* 18.4 (2024), pp. 586–597. DOI: https://doi.org/10.1049/rsn2.12477. eprint: https://ietresearch.onlinelibrary.wiley.com/doi/pdf/10.1049/rsn2.12477. URL: https://ietresearch.onlinelibrary.wiley.com/doi/abs/10.1049/rsn2.12477.

[31] Simão da Graça Marto, Sebastián Díaz Riofrío, Christos Ilioudis, Carmine Clemente, and Massimiliano Vasile. "Satellite manoeuvre detection with multistatic radar". English. In: *Journal of the Astronautical Sciences* 70.5 (Sept. 2023). ISSN: 0021-9142. DOI: 10.1007/s40295-023-00399-3.

Chapter 2

Radar principles

This chapter introduces the basic radar concepts and methods that have been employed during the research journey of the thesis. Furthermore, some of the existing radar processing methods that have been utilized are explained. These foundational concepts and tools will serve as the basis for the development presented novelties. The concepts that are presented on this Chapter are based on [1, 32].

2.1 Radar overview

Since radar will be employed, it is important to provide an overview of the functioning of such systems, covering both the physical principles and the mathematical aspects.

2.1.1 Concept of radar

A radar is a system that emits electromagnetic (EM) signals in the radiofrequency (RF) spectrum into a medium, typically air, to illuminate a region of interest and detect, measure the distance to, track and/or image objects, between other tasks, based on the reflection of the EM waves. Additionally, RF generally refers to signals within the 3 kHz to 300 GHz frequency spectrum, though in practice, higher frequencies may still be considered RF.

As mentioned, radar systems can measure the distance, also known as range, to the target, the detected object, which could be used for target localization. The range can

be estimated using the time it takes for the signal to travel to the target and return to the receiver. (2.1) shows the mathematical expression of the range, where R is the range, c_0 is the speed of light, and ΔT is the time between the transmission of the signal and its reception.

$$R = \frac{c_0 \cdot \Delta T}{2} \tag{2.1}$$

Since radar employs EM waves, it is common for the system to encounter interference when receiving the echo signal. These interferences can be:

- Internal and external electronic noise.
- Reflections from objects that are not of interest, also known as clutter.
- Unintentional EM waves from other human-made sources, also known as EM interferences (EMI).
- Intentional jamming from electronic countermeasures (ECM). These could be caused by devices that saturate the medium with noise or that create false targets.

2.1.2 The physics of EM waves

EM waves, as its name suggests, are composed by electric and magnetic field waves oscillating at a carrier frequency. The electric field, ($\boldsymbol{E}$), is orthogonal to the magnetic field, ($\boldsymbol{B}$). The direction of propagation is perpendicular to both fields and follows the right-hand rule, where the vector product between the electric and the magnetic field, ($\boldsymbol{E} \times \boldsymbol{B}$), determines the direction of wave propagation. Furthermore, EM waves propagate through space at the speed of light.

The amplitude of the electric field of an EM wave propagating along the z-axis can be mathematically expressed as:

$$E_{EM} = E_{EM,0} \cos\left(kz - \omega_f t + \phi_{EM,0}\right), \tag{2.2}$$

where $E_{EM,0}$ is the peak amplitude, and $\phi_{EM,0}$ is the initial phase. The wave number,

k, a kind of *spatial frequency*, and the angular frequency, ω_f, are related by:

$$\begin{aligned} k &= \frac{2\pi}{\lambda}, \\ \omega_f &= 2\pi f, \end{aligned} \tag{2.3}$$

where λ is the wavelength in meters, and f is the carrier frequency in Hertz.

The relation between the wavelength and frequency is:

$$\lambda \cdot f = c_0. \tag{2.4}$$

$\phi_{EM,0}$, also known as fixed or initial phase, depends on the E_{EM} initial conditions. The concept of the relative phase, $\Delta\phi_{EM}$, is the phase difference between two waves, which:

- $\Delta\phi_{EM} = 0$, then the two waves are *in phase*.
- $\Delta\phi_{EM} \neq 0$, then the two waves are *out of phase*.

If two waves occupy the same location at the same time and have the same frequency, their interference can be constructive or destructive, depending on whether they are in phase or out of phase, respectively. The amplitude of constructive interference is greater than the initial amplitudes of the individual waves, whereas the amplitude of destructive interference is lower than the initial amplitudes of the individual waves.

2.1.3 Intensity

The intensity, Q_P, of a wave is defined as the power per unit area. Mathematically, is expressed as the transmitted power divided by the area of a sphere of radius R:

$$Q_P = \frac{P_t}{4\pi R^2}, \tag{2.5}$$

where P_t is the total transmitted power, and R is the radius, which could also be interpreted as the distance from the source. From this equation, we can observe that intensity decreases proportionally to $1/R^2$, following the inverse square law.

If the wavefront curvature is less than $\lambda/16$ over a given aperture dimension D_a, the wave is considered planar. This condition is satisfied if the distance from the source to the aperture is at least $2D_a^2/\lambda$. This region is known as the far-field or plane-wave approximation.

2.1.4 Polarization

Polarization is the description of the motion and orientation of the propagation of the electric field vector. It is given by the phase offset and amplitudes of $E_{EM,x}$ and $E_{EM,y}$. There are three types of polarization:

- In the case of linear polarization, the electric field vector lies entirely within a single plane, while the associated magnetic field vector is oriented perpendicularly to both the electric field and the direction of wave propagation.
- On circular polarization the electrical field is on two planes, the amplitudes are the same and the phase difference between $E_{EM,x}$ and $E_{EM,y}$ is $\Delta\phi_{EM,0} = \pi/2$.
- On elliptical polarization the amplitudes are different and $\Delta\phi_{EM,0} \neq 0$.

2.1.5 Interaction of EM waves with matter

2.1.5.1 Diffraction

Diffraction is the bending of EM waves as they propagate through an aperture or around the edge of an object. If:

- The antenna aperture, D_a, is much larger than the wavelength, λ, diffraction effects are minimal.
- The antenna aperture, D_a, is much smaller than the wavelength, λ, diffraction effects become significant.

The angular shape of the waves as they exit the aperture follows a sinc function. For a sinc function, the half power, ($-3\,\mathrm{dB}$), beamwidth of the main lobe, $\theta_{sinc,-3\,\mathrm{dB}}$, is:

$$\theta_{sinc,-3\,\mathrm{dB}} = \frac{0.89\lambda}{D_a}. \tag{2.6}$$

2.1.5.2 Interaction with the atmosphere

There are many windows of transmission and absorption peaks in the frequency spectrum. Additionally, there is more refraction due to the atmosphere. Refraction is the bending of EM waves at the interference of two different dielectric materials. The index of refraction is given by:

$$n_{ir} = \frac{c_0}{v_{mat}}, \tag{2.7}$$

where v_{mat} is the speed of EM waves in the material. The effects must be taken into account when radar signals are transmitted into the atmosphere.

Refraction can be beneficial for surface-to-surface radars, as it can help the signal to propagate over the horizon, also known as ducting or atmospheric duct. The EM signal is sent towards the ionosphere; the refractive bending causes the wave to travel to the surface of the Earth, there it will hit the surface, many thousand miles away, and then it will bounce back to the receiver. This effect, called skip, is used in the over the horizon (OTH) radars.

2.1.5.3 Reflection

Scattering, or reflection, refers to the re-radiation of EM waves from a material surface. For conducting materials, the incident EM wave is almost entirely re-radiated due to the free electron response. In contrast, for dielectric materials, the incident energy is partially re-radiated, partially absorbed within the medium, and partially transmitted through it.

An important factor influencing reflection is the surface roughness, which describes the variation in surface height. Roughness is commonly quantified by the standard deviation of surface height relative to a reference plane. A surface is considered smooth when the incident wavelength is significantly larger than the roughness scale. In this case, the angle of incidence equals the angle of reflection, $\theta_i = \theta_r$, a phenomenon known

as specular scattering. Conversely, when the wavelength is much smaller than the roughness scale, the surface is regarded as rough. In this regime, scattering is locally specular over small surface regions but collectively results in diffuse scattering, where the incident energy is redistributed over a wide range of angles rather than concentrated in the specular direction.

Another measurable feature is the Radar Cross-Section (RCS), σ. It is measured in m^2 and used to quantify the scattering phenomenology. RCS is a function of the target viewing angle relative to the transmitting and receiving antenna and of frequency and polarization of the incident EM wave, which basically is interception, reflection and directivity. Regarding this theme, the concept of stealth targets is introduced. The aim of stealth targets is to be invisible to radar. For this purpose different techniques are applied:

- Minimize the physical cross section, which will minimize the EM wave energy intercepted.
- Minimize the amount of energy reflected intercepted using radar absorbing material (RAM).
- Minimize the shape of the target, which will decrease the amount of reflected energy directed towards the radar receiver.

2.1.6 Basic radar configurations and waveforms

2.1.6.1 Monostatic versus bistatic radar

In monostatic radar the transmitter and the receiver are collocated, which means that the antenna for transmission and reception are either the same or sufficiently close enough. One of the benefits of using the same antenna is that the transmitter and the receiver will be well isolated, avoiding feedback and false detection.

In a bistatic radar the transmitter and receiver are in two separate locations. The key feature of bistatic radars is the bistatic angle, β, shown in Figure 2.1. One special case of bistatic systems are pseudo-monostatic radars, in which the transmitter and

receiver are placed close enough so that $\beta \approx 0$ and it behaves as a monostatic radar.

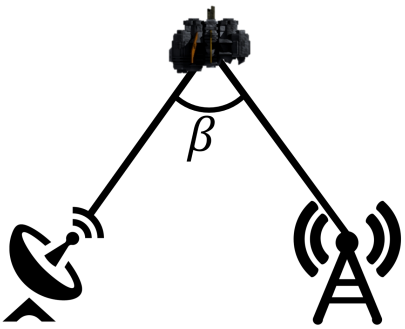

Figure 2.1: Bistatic angle of a bistatic radar

2.1.6.2 Active versus passive radar

Active systems are a type of radars that have a dedicated, and often exclusive, transmitter. Active systems can either be configured in a monostatic or bistatic way. In active radars, there is full control of the waveform parameters, introduced in Section 2.1.6.3, including the modulation, pulse width and pulse-repetition-interval; and the transmission parameters, these include the transmitted power and the operating frequency.

On the contrary, passive radars use an illuminator of opportunity (IO) as the transmitter. An IO is a transmitter that belongs to a third party. As such passive systems use exclusively bistatic configurations. IOs can be any kind of RF transmitters, from FM radio transmitters to telecommunications satellites. One of the main benefits of using passive radars are the reduced cost of the whole system, since there is no need for a transmitter. Another advantage would be that the receiver is hard to locate as it does not have and active RF signature. Nonetheless, it comes at a cost, since the radar signal processing is, usually, more complex. Moreover, a minimum level of knowledge of the transmitter must be had, such as the operating frequency or the location of the transmitter itself.

2.1.6.3 Continuous wave versus pulsed

Continuous wave (CW) systems transmit constantly a signal, which implies that the receiver is constantly hearing for echoes. Some problems that CW radars carry are:

- Isolation between the transmitter and the receiver. A bad isolation could lead to leakage. Some solutions for this problem involve using relatively low power, resulting in short range applications. Another solution is to use a bistatic configuration.

- As CW radars are always transmitting the estimation of the signal round trip time and the target range must be done by altering the features of the EM wave, with frequency or code modulation techniques.

Contrarily, the pulsed waveform systems emits a sequence of finite duration pulses, along with some periods where the receiver is receiving the reflections of the radar, period in which the transmitter is not transmitting. Next, some concepts involving pulsed waveforms will be introduced.

The pulse width, τ, of EW waves of pulsed waveforms have usually very short durations. During the transmitting time, the receiver is isolated or blanked from the antenna. The Pulse Repetition Interval (PRI) is the time that passes between the beginning of one pulse and the beginning of the next. The inverse of the PRI is the Pulse Repetition Frequency (PRF), measured in pulses per second or in Hz:

$$\mathrm{PRF} = \frac{1}{\mathrm{PRI}}. \tag{2.8}$$

The amount of pulse width over the PRI, or the pulse width multiplied by the PRF, is called the transmit duty factor, or duty cycle, d_t:

$$d_t = \frac{\tau}{\mathrm{PRI}} = \tau \cdot \mathrm{PRF}. \tag{2.9}$$

So, the average power, P_{avg}, of the transmitted EM wave is the product of the peak power, P_t, and the transmit duty factor:

$$P_{avg} = P_t \cdot d_t = P_t \cdot \tau \cdot \mathrm{PRF}. \tag{2.10}$$

An analogue to digital converter, (ADC), is used to sample the PRI. Each of the time

samples represents a different range increment, or range bin, at a certain found range.

As previously presented, the range is determined by the round-trip time, ΔT. However, problems appear when ΔT is bigger than the PRI. A time like this would be given by: $\Delta T = \text{PRI} + \Delta t$, which could be interpreted as a target at a short range related to Δt, or a target at a long range related to $PRI + \Delta t$. Therefore, it is desired to have the PRI be bigger than the time delay that would give the maximum range at which a target is being searched.

$$\text{PRI} \geq \Delta T_{max} = \frac{2 \cdot R_{max}}{c_0}. \tag{2.11}$$

This implies that the maximum range would be:

$$R_{max} \leq \frac{c \cdot \text{PRI}}{2} = \frac{c_0}{2 \cdot \text{PRF}}. \tag{2.12}$$

In the same way, the maximum range at which the range to a target can be measured unambiguously by the radar would be:

$$R_{ua} = \frac{c_0}{2 \cdot \text{PRF}}. \tag{2.13}$$

2.1.6.4 Non-coherent versus coherent radar

Non-coherent radar systems rely solely on the detection of signal amplitude, requiring the target return to exceed competing clutter in order to be discernible. In contrast, coherent radar systems exploit both the amplitude and the phase of the received signal. Access to phase information enables the measurement of phase variations, which can reveal target motion characteristics and facilitate imaging. In a pulsed coherent radar system, phase is measured on a pulse-to-pulse basis. The common phase reference for both transmission and reception is established through the use of a stable local oscillator.

Coherent systems form the basis of Doppler radars. The Doppler effect, arising from the relative motion between the radar and the target, causes the frequency of the electromagnetic wave reflected from the target to differ from the transmitted frequency. Consequently, the final received frequency would be the addition of the transmitted frequency and the Doppler frequency. The resulting frequency of the received waveform

would be:

$$f_r = f_t + f_D, \tag{2.14}$$

where f_r is the received frequency, f_t is the transmitted frequency and f_D is the Doppler frequency shift. The Doppler frequency shift, Doppler shift, or Doppler, is:

$$f_D \approx -\frac{2 \cdot v_r}{\lambda}, \tag{2.15}$$

where v_r is the radial component of the velocity of the target. This approximation only fulfils if v_r is much smaller than the speed of light.

The velocity vector of the target is typically defined relative to a reference frame centred on the radar. A positive radial velocity indicates that the target is receding, while a negative velocity indicates that it is approaching. This convention explains the negative sign in (2.15).

From (2.12), it can be concluded that if an increased maximum unambiguous range is desired, then the PRF must be decreased. However, by the Nyquist sampling theorem, the maximum Doppler frequency that can be unambiguously measured is:

$$f_{D,max} = \pm\frac{\text{PRF}}{2} \Rightarrow \text{PRF}_{min} = 2 \cdot f_{D,max} = \frac{4 \cdot v_{r,max}}{\lambda}. \tag{2.16}$$

Therefore, if the PRF is lowered to increase the maximum range, the maximum Doppler is decreased which may cause ambiguities in the Doppler domain. As a consequence, different PRF values should be chosen depending on the application.

2.1.7 Noise, signal-to-noise ratio (SNR) and detection

All objects radiate thermal noise EM waves in almost all frequencies, as a matter of fact, the receiver generates its own internal thermal noise. The SNR is the ratio of the useful received signal power to the noise power.

For target detection in the case of high SNR, a simple amplitude threshold can be set. If the amplitude of the power of a signal is above the threshold a target is detected. However, if the noise at a certain instant is above the threshold it can cause

false target detections. On the other hand, there also exists the possibility that the power of the signal plus the power of the noise would be smaller than the amplitude threshold, meaning that a target could be missed.

The probability of detection is the probability that the signal power plus the noise power is greater than the set amplitude threshold. Similarly, the probability of false alarm is the probability that the noise power is greater than the amplitude threshold. The perfect radar would have a $P_D = 1$, and a $P_{FA} = 0$. It can be noticed that the P_D and P_{FA} can be tuned with the amplitude threshold. If the threshold increases the P_D and P_{FA} decreases, and vice-versa.

2.1.8 Basic radar measurements

2.1.8.1 Target position

Target position is given in a 3D space, as radar estimates, the range in a certain azimuth angle and at a certain elevation angle. Additionally, these could be transformed into a Cartesian coordinate space. Modern radars can determine the following target parameters:

- Azimuth and elevation angles. These angles are determined by the pointing angle of the antenna main beam when detection occurs.
- Range, R, is measured by ΔT with (2.1). ΔT can be counted by numbers of ADC clock pulses between transmit time and receive time (if the first clock is the transmit pulse).
- Range rate, $\dot{R}$, is measured by the f_D, the Doppler frequency. The f_D can be estimated employing spectral analysis on the received signal in every range. f_D can be used to suppress clutter and determine multiple targets at the same range.

2.1.8.2 Resolution

Resolution describes the ability of the radar system to distinguish two or more targets that are closely spaced, whether in range, angle, or Doppler frequency. Therefore, two

targets are said to be resolved in range if they can be distinguished. The range resolution is given by:

$$\Delta R = \frac{c_0 \cdot \tau}{2}. \tag{2.17}$$

Since, generally, the bandwidth of a system can be approximated as: $B_W \approx 1/\tau$, then:

$$\Delta R \approx \frac{c_0}{2 \cdot B_W}. \tag{2.18}$$

Range resolution is proportional to the pulse width, and inversely proportional to the bandwidth of the radar signal. If the pulses are shorter the power decreases which will decrease the SNR and the chance of detection, if no other parameters are changed. A solution that could be implemented is pulse compression,a technique that maintains the desired energy while providing better range resolution by modulating the signal. Chirp pulses, a kind of pulse compression, sweep between two frequencies. Another type of pulse compression are the phase-coded pulses, which has a constant frequency and changes in the relative phase. For these waveforms the bandwidth no longer depends on the pulse duration but (2.18) is still valid.

2.2 The radar range equation (RRE)

The radar performance depends on the SNR at the receiver. The concept of SNR has been introduced but there are other similar concepts, such as the Signal-to-Clutter Ratio (SCR), and the Signal-to-Interference Ratio (SCR). The equation to estimate the SNR of the signal at the radar receiver is the Radar Range Equation (RRE). The RRE predicts the received power of the radio waves of the radar reflected from a target, the noise power level, and, thus, the SNR. It can also calculate the power received from surface and volumetric clutter.

2.2.1 Power density at a distance R

The power density at a certain distance R, if the antenna is isotropic, is mathematically given by:

$$Q_i = \frac{P_t}{4\pi \cdot R^2}, \tag{2.19}$$

where P_t, is the total peak power, R is the distance and Q_i is the power density. By looking at equation (2.19), it can be concluded that the total power divided by surface area of a sphere of radius R, measured in $\mathrm{W\,m^{-2}}$.

The antenna is usually not isotropic. The power density for a non-isotropic antenna is:

$$Q_i = \frac{P_t \cdot G_t}{4\pi \cdot R^2}, \tag{2.20}$$

where G_t is the gain of the antenna, which is the directivity of said antenna reduced by the losses the signal encounters as it travels from the input power to the point at which the signal enters into the air. In practice, the directivity can be used instead of the gain. In this case, the antenna losses are added to the system losses.

2.2.2 Received power from a target

The reflected power from a target is related to the amount of power that bounces back from the target. This power is directly related to the RCS, and mathematically is provided by:

$$P_{reft} = Q_i \cdot \sigma = \frac{P_t \cdot G_t \cdot \sigma}{4\pi \cdot R^2}. \tag{2.21}$$

Therefore, the power density back at the radar receiving antenna is:

$$Q_r = \frac{P_{reft}}{4\pi \cdot R^2} = \frac{P_t \cdot G_t \cdot \sigma}{(4\pi)^2 \cdot R^4}. \tag{2.22}$$

Thus, the received power from a target at a range R at the receiving antenna of effective area A_e is the power density at the antenna times the effective area of the antenna:

$$P_r = Q_r \cdot A_e = \frac{P_t G_t \sigma \cdot A_e}{(4\pi)^2 R^4}. \tag{2.23}$$

A_e is related to the antenna gain by:

$$G_r = \frac{4\pi A_e}{\lambda^2} = \frac{4\pi \eta_a A_{ant}}{\lambda^2}, \tag{2.24}$$

where η_a is the efficiency of the antenna, which takes values of $\eta_a \in [0, 1]$, and A_{ant} is the physical area of the antenna. Combining (2.23) and (2.24):

$$P_r = \frac{P_t G_t G_r \lambda^2 \sigma}{(4\pi)^3 R^4}, \tag{2.25}$$

where P_t is the peak transfer power measured in watts, G_t is the gain of the transmitter antenna in linear units, G_r is the gain of receiver antenna in linear units, λ is the carrier wavelength measured in meters, σ is the previous mentioned RCS of the target measured in m^2 and R is the range from the radar to the target measured in meters.

2.2.3 Receiver thermal noise

The noise can be modelled as white noise, meaning that the power spectral density is a constant uniform function across all the frequencies. The power P_n of the thermal noise in the radar receiver is proportional to the receiver bandwidth and is given by:

$$P_n = k_n \cdot T_s \cdot B = k_n \cdot T_0 \cdot F \cdot B_W, \tag{2.26}$$

where k is the Boltzmann constant, with $k_n = 1.38 \times 10^{-23} \mathrm{W\,s\,K^{-1}}$, T_0 is the standard temperature, with $T_0 = 290\,\mathrm{K}$, T_s is the system noise temperature, $T_s = T_0 \cdot F$, B_W is the instantaneous receiver bandwidth measured in Hz, F is the noise factor of the receiver subsystem measured in linear units.

From equation (2.26), it could be deduced that in order to reduce the noise, the receiver bandwidth could be reduced. Nonetheless, if the receiver bandwidth is smaller than the bandwidth of the signal, the range resolution suffers. The optimum bandwidth will be depend on both the transmitted bandwidth and the receiver filter.

2.2.4 SNR and the radar range equation

Taking into account (2.25) and (2.26), the SNR at the receiver for the monostatic radar can be computed as:

$$SNR = \frac{P_r}{P_n} = \frac{P_t G_t G_r \lambda^2 \sigma}{(4\pi)^3 R^4 k_n T_0 F B_W}. \tag{2.27}$$

Whereas, for the bistatic radar it would be:

$$SNR = \frac{P_t G_t G_r \lambda^2 \sigma_{bs}}{(4\pi)^3 R_1^2 R_2^2 k_n T_0 F B_W}. \tag{2.28}$$

2.2.5 Multiple pulse effects

Section 2.1.6.4 introduced coherent and non-coherent radars. These types of radars rely on multiple pulse integration, or multiple integration, methods. The SNR resulting from coherently integrating n_p pulses in white noise is:

$$SNR_c(n_p) = n_p \cdot SNR(1), \tag{2.29}$$

where $SNR_c(n_p)$ is the SNR for n_p pulses and $SNR(1)$ is the SNR for a single pulse. Consequently, the RRE when n_p pulses are coherently integrated for the monostatic radar is:

$$SNR_c(n_p) = n_p \cdot \frac{P_t G_t G_r \lambda^2 \sigma}{(4\pi)^3 R^4 k_n T_0 F B_W}. \tag{2.30}$$

Whereas, for the bistatic radar it will be:

$$SNR_c(n_p) = n_p \cdot \frac{P_t G_t G_r \lambda^2 \sigma_{bs}}{(4\pi)^3 R_1^2 R_2^2 k_n T_0 F B_W}. \tag{2.31}$$

The SNR for non-coherent integration is:

$$\sqrt{n_p} \cdot SNR(1) \leq SNR_{nc}(n_p) \leq n_p \cdot SNR(1). \tag{2.32}$$

For this reason, many times to estimate the SNR when non-coherent integration is used, the variable n_p is replaced by $\sqrt{n_p}$. Therefore, the RRE when n_p pulses are

non-coherently integrated for the monostatic radar is:

$$SNR_{nc}(n_p) = \sqrt{n_p} \cdot \frac{P_t G_t G_r \lambda^2 \sigma}{(4\pi)^3 R^4 k_n T_0 F B_W}. \tag{2.33}$$

Whereas, if it was a bistatic radar, it would be:

$$SNR_{nc}(n_p) = \sqrt{n_p} \cdot \frac{P_t G_t G_r \lambda^2 \sigma}{(4\pi)^3 R_1^2 R_2^2 k_n T_0 F B_W}. \tag{2.34}$$

2.2.6 Summary of losses

The total system loss is:

$$L_s = L_t \cdot L_a \cdot L_r \cdot L_{sp}, \tag{2.35}$$

where L_s is the system loss, L_a are the atmospheric losses, L_r are the receiver losses, L_{sp} are the signal processing losses and L_t are the transmit losses, it should be mentioned that the antenna losses will be part of the transmit losses.

The RRE with the losses for a monostatic radar with n_p pulses coherently integrated is:

$$SNR = \frac{P_t G_t G_r \lambda^2 \sigma n_p}{(4\pi)^3 R^4 k_n T_0 F B_W L_s}. \tag{2.36}$$

While for bistatic radar it would be:

$$SNR = \frac{P_t G_t G_r \lambda^2 \sigma_{bs} n_p}{(4\pi)^3 R_1^2 R_2^2 k_n T_0 F B_W L_s}. \tag{2.37}$$

If non-coherent radar was employed, the n_p variable would be substituted by $\sqrt{n_p}$.

The radar system is designed to search for targets in a given volume, defined by the range of elevation and azimuth angles to be considered and the range of distances from the nearest to the farthest. The radar can detect between $[R_{min}, R_{max}]$, but not in a continuous manner but with contiguous range movements of ΔR. Similarly, the Doppler frequency can be unambiguously determined from $-PRF/2$ to $PRF/2$.

2.2.7 RRE for other variables

The following RRE variations are given for monostatic radar systems with n_p pulses coherently integrated. If the system were bistatic, σ will have to be substituted by σ_{bs} and R^4 would have to be changed by the product between R_1^2 and R_2^2. Similarly, if the system were to integrate the pulses in a non-coherent way, n_p would have to be replaced by $\sqrt{n_p}$.

2.2.7.1 Range as a dependent variable

The detection range at which a given RCS can be detected with a given SNR is:

$$R_{det} = \left[\frac{P_t G_t G_r \lambda^2 \sigma n_p}{(4\pi)^3 k_n T_0 F B_W L_s \cdot SNR}\right]^{\frac{1}{4}}. \tag{2.38}$$

Note that some variables inside L_s are range-dependent.

2.2.7.2 Solving for minimum detectable RCS

The RRE is displayed supposing a minimum SNR, SNR_{min}, for a minimum RCS, σ_{min}:

$$\sigma_{min} = SNR_{min} \cdot \frac{(4\pi)^3 R^4 k_n T_0 F B_W L_s}{P_t G_t G_r \lambda^2 n_p}. \tag{2.39}$$

It should be noted that the higher the required minimum SNR, the higher the required RCS, which would probably translate into a bigger target.

2.2.7.3 Decibel form of the RRE

As it is known the decibel is a relative unit of measurement corresponding to the ratio of one value of a power or field quantity to another. In the decibel form multiplications are additions, and divisions are subtractions. So, the decibel form of the RRE is:

$$\begin{aligned} SNR[\text{dB}] =& P_t[\text{dB W}] + G_t[\text{dB}] + G_r[\text{dB}] + 20\log_{10}(\lambda) + \sigma[\text{dB}(\text{m}^2)] + 10\log_{10}(n_p) - 33 \\ & - 40\log_{10}(R) - (204[\text{dB W Hz}^{-1}] - F[\text{dB}] - 10\log_{10}(B_W)[\text{dB Hz}] - L_s[\text{dB}]). \end{aligned} \tag{2.40}$$

The -33 factor is $\approx 10\log_{10}\left[(4\pi)^3\right]$ and the -204 factor is $\approx 10\log_{10}(k_n T_0)$.

2.2.7.4 Average power form of the RRE

The average power form of the RRE is derived from the peak power, P_t, as:

$$T_d = n_{p,d} \cdot PRI = n_{p,d}/PRF \Rightarrow n_{p,d} = T_d \cdot PRF. \tag{2.41}$$

With T_d as the dwell time. The dwell time is the time that the antenna beam spends on a target. $n_{p,D}$ is the number of pulses, or hits per scan. Thus, the average power is derived from the duty cycle:

$$P_{avg} = P_t \cdot \frac{\tau}{PRI}. \tag{2.42}$$

The optimum receiver bandwidth, B_W, for a simple non-modulated pulse of width, τ, is:

$$B_W = \frac{1}{\tau}. \tag{2.43}$$

Combining (2.41), (2.42) and (2.43) yields in:

$$P_t = \frac{P_{avg} T_d B_W}{n_{p,d}}. \tag{2.44}$$

Combining (2.36) and (2.44), the average for of the RRE for coherent integration is:

$$SNR = \left(\frac{P_{avg} T_d B_W}{n_{p,d}}\right) \frac{G_t G_r \lambda^2 \sigma n_p}{(4\pi)^3 R^4 k_n T_0 F B_W L_s} \overset{1}{=} \frac{P_{avg} \cdot T_d \cdot G_t G_r \lambda^2 \sigma}{(4\pi)^3 R^4 k_n T_0 F L_s}. \tag{2.45}$$

In (2.45), equality 1 holds if $n_{p,d} = n_p$, which occurs if the dwell time equals the integration time under coherent processing. In this scenario, the integration time is referred to as Coherent Processing Interval (CPI). The CPI is the time duration over which the received radar pulses are collected and processed together to perform coherent integration and Doppler analysis. From (2.45), when coherent integration is applied over T_d and the receiver bandwidth matches the transmit bandwidth, the system SNR can be adjusted by changing T_d without any hardware modifications.

For non-coherent integration, the average form of the RRE is:

$$SNR = \left(\frac{P_{avg} T_d B_W}{n_{p,d}}\right) \frac{G_t G_r \lambda^2 \sigma \sqrt{n_p}}{(4\pi)^3 R^4 k_n T_0 F B_W L_s} \stackrel{1}{=} \frac{P_{avg} \cdot T_d \cdot G_t G_r \lambda^2 \sigma}{(4\pi)^3 R^4 k_n T_0 F L_s \sqrt{n_p}}, \tag{2.46}$$

where equality 1 holds if the dwell time is the same as the integration time when using non-coherent integration. For non-coherent processing, the integration time can be defined as the period during which the amplitudes of the received radar pulses are collected and summed.

In the hardware, generally, the average power, P_{avg}, the gain, $G_{t|r}$, the wavelength, λ, the noise factor, F, and the losses, L_s, are fixed, while the dwell time, T_d, is easily changed affecting the SNR. It is worth mentioning that aggressive RCS reduction efforts must be made to create significant reductions in radar detection range.

2.2.7.5 Pulse compression: intrapulse modulation

The origin of the pulse compression is the need of high bandwidth for good range resolution as well as the need of high pulse widths for good SNR. Intrapulse modulated waveforms are used to achieve fine range resolution while maintaining high average power.

The RRE for a system using pulse compression is:

$$SNR_{pc} = SNR_u \cdot G_{sp} = SNR_u \cdot \tau \cdot B_W. \tag{2.47}$$

where SNR_{pc} is the SNR for a modulated pulse with pulse compression, SNR_u is the SNR for an unmodulated pulse, G_{sp} is the signal processing gain, τ is the pulse width, and B_W is the pulse bandwidth.

Combining (2.36) and (2.47):

$$SNR_{pc} = \frac{P_t G_t G_r \lambda^2 \sigma n_p \cdot G_{sp}}{(4\pi)^3 R^4 k_n T_0 F B_W L_s} = \frac{P_t G_t G_r \lambda^2 \sigma n_p \cdot \tau \cdot B_W}{(4\pi)^3 R^4 k_n T_0 F B_W L_s}. \tag{2.48}$$

2.2.8 RRE for bistatic radar

The SNR expression for a monostatic radar system with pulse compression in (2.48) is reformulated for a bistatic radar configuration:

$$SNR_{bs} = \frac{P_t G_t G_r \lambda^2 \sigma_{bs} K_{mp} \cdot G_{sp}}{(4\pi)^3 R_1^2 R_2^2 k_n T_0 F B_W L_s}, \tag{2.49}$$

where σ_{bs} is the bistatic RCS of the target, R_1 is the range from the transmitter to the target, R_2 is the range from the target to the receiver and K_{mp} is the multiple integration factor, which is $K_{mp} = n_p$ for coherent integration and $K_{mp} = \sqrt{n_p}$ for non-coherent integration.

From the SNR expression in (2.49), the formulas for a bistatic radar without pulse compression or without multiple integration can be deduced. If pulse compression is not used, then $G_{sp} = 1$. Similarly, if neither coherent nor non-coherent multiple integration is applied, we have $K_{mp} = 1$.

2.2.9 RRE for multistatic radar

When the bistatic configuration is extended to multiple transmitters and/or receivers to form multiple bistatic pairs, a multistatic radar configuration is generated. The advantages of a multistatic radar lay on, not only the ability to increase the SNR, but also the capability of the radar to observe the target from different angles, which might increase the reflected RCS and decrease the ambiguity in the measurement.

The RRE presented in [1], can be extended for the multistatic case as:

$$\mathrm{SNR}_{\mathrm{ms}} = \sum_{a}^{N_{bs}} \sum_{b}^{M_{bs}} \mathrm{SNR}_{\mathrm{bs};a,b}, \tag{2.50}$$

for the coherent fusion the bistatic pair measurements, and as:

$$\mathrm{SNR}_{\mathrm{ms}} \approx \sqrt{\sum_{a}^{N_{bs}} \sum_{b}^{M_{bs}} \mathrm{SNR}_{\mathrm{bs};a,b}^{2}}, \tag{2.51}$$

for the non-coherent fusion. Where, $\mathrm{SNR}_{\mathrm{bs};a,b}$ is the SNR of the signal emitted from

transmitter a and received in the b receiver, and N_{bs} and M_{bs} are the number of transmitters and receivers.

2.3 Radar signal processing: non-coherent vs coherent integration

As seen in Section 2.2.5, there are two methods to integrate multiple pulses to increase the SNR: non-coherent and coherent integration.

In non-coherent integration only the magnitude of the echoed signal is used, whereas in coherent integration both the phase and magnitude, or the in-phase and quadrature components of the signal are employed to increase the SNR of the final signal.

The radar processing pipeline of the received signal would comprise of:

1. Amplify the received signals from the antenna using a low-noise amplifier (LNA) and down-convert them to baseband. By up-convert it is understood that the signal is modulated with a high-frequency RF signal from baseband, where the frequency spectrum or bandwidth of the signal is centred around the 0 Hz, to a higher frequency. After the up-conversion the bandwidth of the resulting signal will be centred around the frequency of the RF signal. Thus, by down-convert it is understood that the signal is converted from a higher frequency to the 0 Hz frequency using the RF signal. Generally, the RF signal consists of a single frequency component.

   Most of the radar signals are up-converted, as the necessary antenna would be too big for the signal to be transmitted. For instance, if a monopole antenna of size $\lambda/4$ [33] were used, its theoretical length would be infinite; though in practice, it would simply be extremely large.

2. The received signals are passed through a matched filter. The matched filter maximizes the SNR in the presence of Additive White Gaussian Noise (AWGN) by correlating the received radar signal with the original transmitted signal. The matched filtering process can be described as:

$$s_{MF}(t) = s_R(t) * s^*_{BB}(-t), \tag{2.52}$$

where s_{MF} is the matched filter output, s_R is the received and amplified down-converted signal, $s^*_{BB}(-t)$ is complex conjugate of the original sent signal in base-band, s_{BB}, which has been reversed in time, $*$ is the convolution operation. The discrete-time convolution is defined as [1]:

$$s_1[n] * s_2[n] = \sum_{-\infty}^{\infty} s_1[a] \cdot s_2[n-a]. \tag{2.53}$$

The matched filter provides the processing signal gain, G_{sp}, in (2.47).

3. If non-coherent processing is chosen, the received pulses are integrated by adding the magnitude of the received pulses as such:

$$s_{NC} = \sum_{a=0}^{n_p-1} |s_{MF,a}|, \tag{2.54}$$

where $s_{MF,a}$ are the different received signals after the matched filter and $|\cdot|$ is the magnitude operation.

An example of non-coherent integration is shown in Figure 2.2. In this case, the target is stationary at a range of 86.55 km, and an Linear Frequency Modulation (LFM) chirp is transmitted. The LFM chirp is a modulated waveform in which the frequency linearly increases or decreases with time. The transmitted signal has a pulse width of 50 µs, the sampling frequency is 10 MHz, and PRF is 1 kHz. The post-antenna SNR is $SNR = -5$ dB. The corresponding propagation delay places the target at sample index 5774. The outcome of the non-coherent integration reveals a dominant peak at range bin 5774, indicating the correct estimation of the location of the target. Because phase information is discarded, only the range of the target can be estimated. The effect of the matched filter is also evident, producing a peak in the range bin associated with the target.

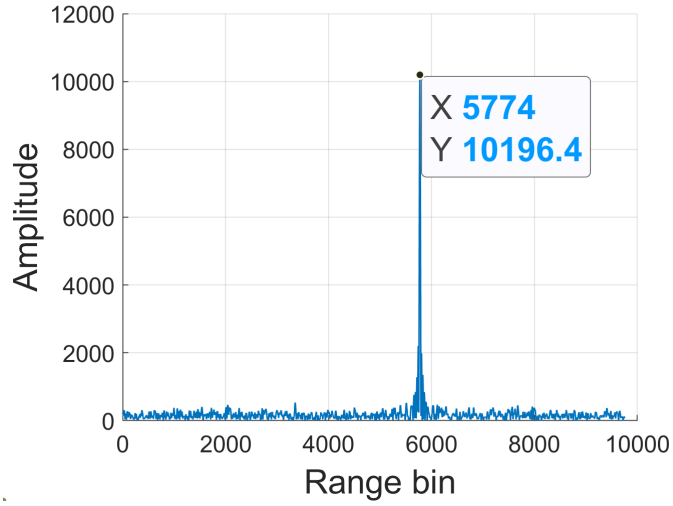

Figure 2.2: Non-coherent integration, target position=86.55 km, sampling frequency=10 MHz

Coherent processing can be achieved by Doppler processing. The resulting pulses are arranged into rows resulting in the range-slow time matrix or fast-time slow-time matrix, or map. Depending on the number of pulses to be integrated, the number of rows will vary. Finally, the Fourier Transform (FT) is applied along the slow time axis, and the range-Doppler map is computed. The K_f-point discrete Fourier Transform (DFT) for discrete-time signals is defined as [34]:

$$S_D[k_f] = \sum_{n=0}^{K-1} x[n] e^{-j2\pi n \frac{k_f}{K_f}}, \quad \text{with} \quad k_f = 0, \ldots, K_f - 1. \tag{2.55}$$

While the inverse DFT (IDFT) is defined as:

$$s_D[n] = \frac{1}{K_f} \sum_{k_f=0}^{K-1} X[k_f] e^{j2\pi n \frac{k_f}{K_f}}, \quad \text{with} \quad n = 0, \ldots, K_f - 1. \tag{2.56}$$

A fast version of the DFT, called fast Fourier Transform (FFT), is found in [35].

Figure 2.3 shows an example of Doppler processing and coherent integration. More concretely, Figure 2.3a shows the target marked in red, while Figure 2.3b shows the target, in yellow. Range-Doppler maps are useful tools when dealing with

multiple targets in the same range bin but with different speeds, as it will result in different Doppler shifts.

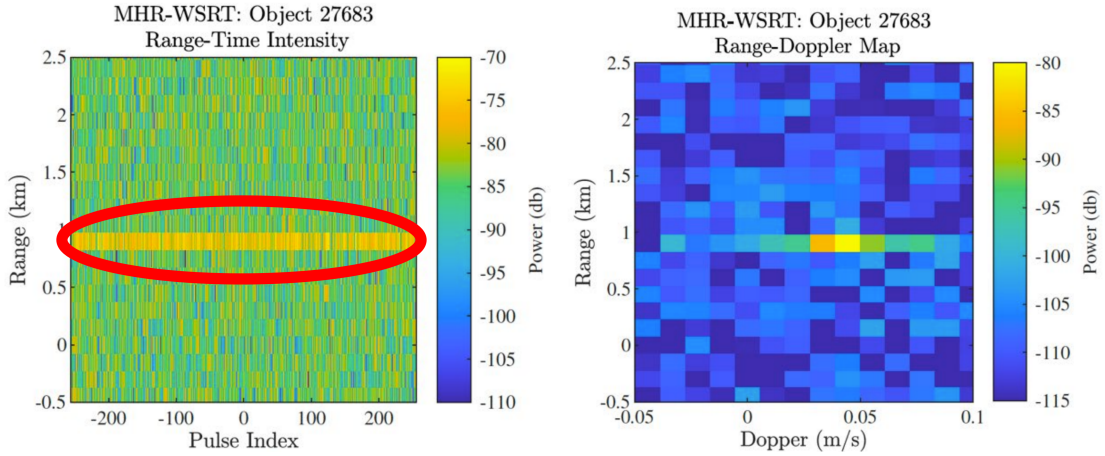

(a) Fast-time slow-time map taken from [36] (b) Range-Doppler map taken from [36]

Figure 2.3: Examples of fast-time slow-time and range-Doppler maps

The advantages of using coherent integration over non-coherent integration is the higher integration gain, which would yield better results, as the SNR would be higher. Nonetheless, the gain comes with the disadvantage of having a more complex receiver or signal processing. Similarly, signal coherency must be ensured. This means that the phase must be known, accurately timed and is consistent through the received signals. Conversely, the non-coherent integration has a simpler processing pipeline and is more straightforward. Since, only the magnitude is needed, the radar receiver is simpler.

As discussed in Section 2.2.7.4, the achievable multiple integration gain is constrained by the integration time, referred to as the CPI in the coherent case, and equally named integration time in the non-coherent case. The integration time in the non-coherent case is restricted by the relative position of the target with respect to the radar. If the displacement of the target causes it to move into a different range bin, the resulting change in delay leads to corrupted signals. Similarly, the CPI is constrained by the motion parameters of the target. If the target changes range bin or its velocity during the CPI, coherent integration will not be possible. As mentioned, a change in range introduces different delays, while a change in velocity results in variations in

Doppler frequency and phase, both of which distort the coherently integrated signal.

The CPI and integration time for non-coherent processing can be calculated as:

$$\begin{aligned} CPI &= n_{cp} \cdot PRI, \\ T_{nc} &= n_{ncp} \cdot PRI, \end{aligned} \tag{2.57}$$

with n_{cp} and n_{ncp} being the number of coherent and non-coherent pulses to be integrated, respectively. They are both related to the dwell time as [32]:

$$\begin{aligned} CPI &\leq T_d, \\ T_{nc} &\leq T_d. \end{aligned} \tag{2.58}$$

2.4 Summary

This chapter provided an introduction to radar concepts. Specifically, radar configurations were discussed, covering monostatic and bistatic setups, as well as the distinctions between active and passive radar systems. Additionally, key concepts such as SNR, range, range resolution, and Doppler frequency shift were reviewed.

A central concept in radar systems is the RRE, which offers insight into the signal quality at the receiver. The chapter also explored the impact of different multiple integration techniques, such as non-coherent and coherent integration, on the RRE.

In summary, this chapter introduced the radar theory, essential for the development and analysis of radar systems discussed in this thesis. The concepts introduced here form the basis for further exploration into radar performance, system design, and processing techniques in the following chapters.

Chapter 3

Preliminary knowledge and established techniques

This chapter comprises a comprehensive literature review focusing on spaceborne and ground-based radar, alongside the mathematical tools that, despite not being directly related to radar, have been utilized in this thesis. The review examines existing studies, technologies, and advancements pertaining to radar relevant to SSA and the developed novelties. By synthesizing this knowledge, the chapter seeks to establish a theoretical framework and contextual understanding for the novelty developments of the research.

3.1 Spaceborne radar for space situational awareness

Several radar technologies have been developed for SSA, yet only a limited number have been implemented on spaceborne platforms. Spaceborne radar offers distinct advantages, although these depend on the specific mission geometry and constraints. In certain configurations, such as the one presented in this thesis, the reduced distance between the platform and the target can lower signal power requirements. However, depending on the orbital geometry, the radar may at times be positioned farther from its target than a ground-based system. Moreover, spaceborne systems must operate under strict onboard power limitations, unlike most ground-based installations. A clear advantage, nonetheless, is the absence of atmospheric losses and the need for atmospheric

compensation techniques.

There are spaceborne radars that are used to perform imaging tasks using Synthetic Aperture Radar (SAR) techniques. Spaceborne SAR is utilized to image the globe.

Continuing with the spaceborne radar for SSA, in the literature active systems have been proposed. The main benefit of using an active spaceborne radar is that it does not depend on any IOs, which in the space might be scarce. In [37], a sub-THz inverse synthetic aperture radar, which would image space objects, was introduced. There is also an on-going project [38] that explores distributed spaceborne radars and employs the sub-THz radar. Similarly, in [39], a feasibility study was conducted on the possibility of a phased array antenna, low PRF and processing techniques to feed an on-board tracker. At last, in [40], an ontological framework for spaceborne radars with the purpose of SSA was provided, which itself assumed an active radar scenario.

There are proposed spaceborne radar systems that are passive as well, such as in [12, 24, 41]. The main advantage of using a spaceborne passive system for SSA is that only a receiver is required, making the RF system significantly simpler. Additionally, as the number of satellite constellations is increasing, there are a high amount of standardized IOs. This implies a larger coverage area, thereby increasing the probability of target detection. However, the processing solutions in the passive case are more complex.

3.1.1 Forward scatter passive bistatic radar for SSA

In this section the study found in [12] is reviewed as it is the baseline for the novelties presented in the thesis. In [12], a CubeSat-based Passive Bistatic Radar (PBR) was introduced. The PBR relies on the FS configuration. In the FS configuration, the bistatic angle is $\beta \approx 180°$, as in Figure 3.1, with the target crossing between the transmitter and the receiver.

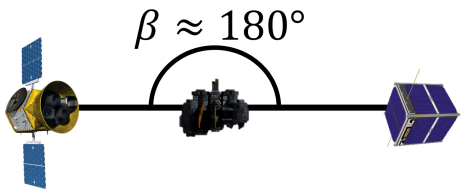

Figure 3.1: Forward scatter configuration

FS applications have been found useful in many fields thanks to its advantages over monostatic radar systems. According to [16], the RCS in FS is enhanced, see Figure 3.2. Therefore, this configuration could be used to detect low flying objects, such as winged missiles, and stealth coated aircrafts. More recently, as reported in [12], it was explained that it was viable to use Forward Scatter Radar (FSR) for space situational awareness, to track and detect space objects. As a consequence, if FSR is used along with Shadow Inverse Synthetic Aperture Radar (SISAR) algorithms, space objects could be imaged. Additionally, SISAR techniques can be used to extract the localization of the possible target.

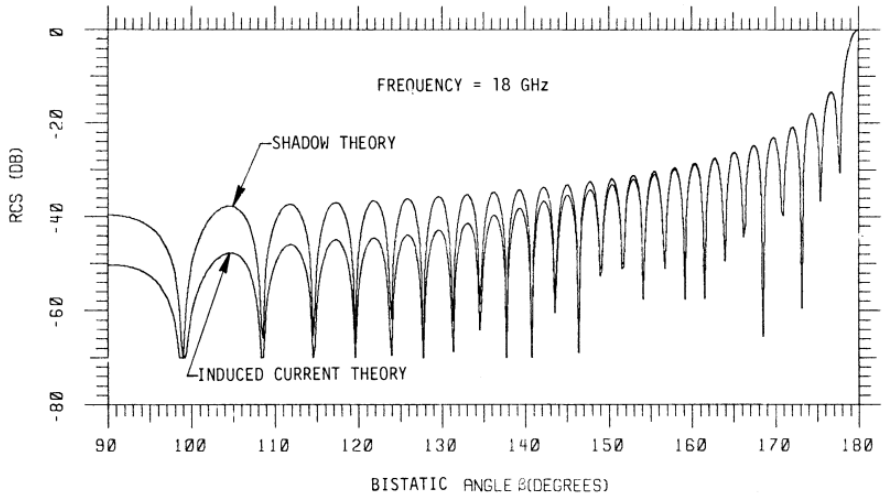

Figure 3.2: RCS of a target at $f_0 = 18\,\text{GHz}$ from [42]

3.1.2 Fundamentals of SISAR

First, it is important to know about the fundamental functioning of SAR. Typical SAR [32] relies on a large antenna synthetic aperture. The synthetic aperture, which would allow for a higher spatial resolution, could be formed by using the motion of the radar platform. The signals are sent and received while the radar antenna is moving, and using the information from the motion of the antenna they are processed. There is a variation of SAR called Inverse Synthetic Aperture Radar (ISAR), which instead of relying on the relative motion of the radar antenna to the target it relies on the relative motion of the target to the radar antenna to create the synthetic aperture. It must be

added that a phased array antenna could be used to expand the synthetic aperture.

In [43], the SISAR technique is explained as being an ISAR technique that exploits the shadow or forward scattering geometry. When using SISAR, the Radio Holographic Signal (RHS) is reconstructed. The RHS is a coherent radar signal whose phase and amplitude are fully recorded over multiple spatial positions to allow for the reconstruction of the target. Since, at the receiver, both the target signal and the direct signal of the transmitter are present, the RHS can be characterized as an interference signal which would be the one-dimensional shadow radio hologram synthesized coherently in time. The RHS, also referred to as the FS signal, is processed using a matched filter to extract the motion parameters of the target. In this approach, the FS signal is replicated at the receiver for different assumed motion parameters. Then, it is correlated with the received FS signal through the matched filter to estimate the range and velocity of the target.

It is evident that the FS signal is a crucial component for successful processing in SISAR. Certainly, without the FS signal the algorithm would not work. The receiving, or reconstruction, of the FS signal is itself a topic that is being investigated to this day. Since, in a real scenario it is difficult to achieve the synchronous processing needed [44] to retrieve the FS signal, in most of the cases an amplitude detector [45] is used to obtain one of the quadrature components. The other component is recovered via RHS reconstructions methods. Several of these methods, as reported in [44, 41], are based on the Hilbert transform. Since the topic is out of the scope of this thesis, in the pertinent chapters it is assumed that the full complex FS signal has been successfully retrieved.

In [41], the fundamentals of the Moving-Ends (ME) SISAR are laid out, which takes into account the movement of the transmitter and receiver. In [24], it was explained how the ME-SISAR could be implemented and applied for SSA in a spaceborne radar scenario. The ME-SISAR geometry is shown in Figure 3.3, where TX is the transmitter, RX is the receiver and P is the target. The three elements of the scenario, transmitter, receiver and target, are moving with speeds of $\mathbf{v_T}$, $\mathbf{v_R}$ and $\mathbf{v}$, respectively.

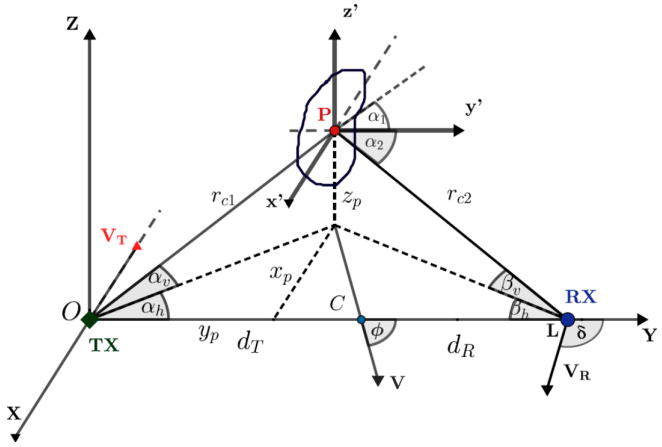

Figure 3.3: SISAR geometry

The SISAR algorithm is applied to the FS signal, the signal is emitted from the transmitter, scattered by the target and captured at the receiver. For modelling the FS signal, as for [46], it is assumed that the dimension of the target is comparably larger than λ, the wavelength, so the Fresnel-Kirchhoff diffraction formula can be applied. If the target were in the same order, or bigger, than the wavelength, the diffraction formula would become invalid. The Fresnel-Kirchhoff formula is expressed as:

$$E_{FS}(t) = \frac{-jA_{FS}}{2\lambda} \int\int \epsilon_\tau(x', z') \frac{e^{jk(r_1+r_2)}}{r_1 r_2} (\cos(\alpha_1) + \cos(\alpha_2)) dx' dz', \tag{3.1}$$

with $E_{FS}(t)$ being the FS signal, A_{FS} the amplitude of the transmitted signal and $k = \frac{2\pi}{\lambda}$. r_1 describes the distance from the transmitter to every point of the target, whereas r_2 describes it from every point of the target to the receiver:

$$r_1 = \sqrt{\{X_T(t) - [X_p(t) + x']\}^2 + \{Y_T(t) - [Y_p(t) + y']\}^2 + \{Z_T(t) - [Z_p(t) + z']\}^2}, \tag{3.2}$$

$$r_2 = \sqrt{\{X_R(t) - [X_p(t) + x']\}^2 + \{Y_R(t) - [Y_p(t) + y']\}^2 + \{Z_R(t) - [Z_p(t) + z']\}^2}, \tag{3.3}$$

where $(X, Y, Z)|_{T,R,p}$ are the transmitter, receiver and target coordinates in time; and

ϵ_τ is the function of the shadow profile of the target:

$$\epsilon_\tau = \begin{cases} 1 & (x', z') \in S_{FS} \\ 0 & (x', z') \notin S_{FS} \end{cases} .$$

If it is assumed that the target is moving near the baseline in both X and Z directions, and that L, from Figure 3.3, is not comparable to the size of the target, r_1 and r_2 can be approximated as:

$$r_1 \approx r_{c1} + \frac{x'^2 + 2x'[X_p(t) - X_T(t)] + z'^2 + 2z'[Z_p(t) - Z_T(t)]}{2r_{c1}}, \tag{3.4}$$

$$r_2 \approx r_{c2} + \frac{x'^2 + 2x'[X_p(t) - X_R(t)] + z'^2 + 2z'[Z_p(t) - Z_R(t)]}{2r_{c2}}, \tag{3.5}$$

$$r_{c1} = \sqrt{(X_T - x_p)^2 + y_p^2 + z_p^2}\ , \quad r_{c2} = \sqrt{(X_R - x_p)^2 + (Y_R - y_p)^2 + z_p^2}\ ,$$

with r_{c1} and r_{c2} being the distance from the transmitter and the receiver to the target when $t = 0$. As $\alpha_1 \approx \alpha_2 \approx 0$, then: $\cos\alpha_1 + \cos\alpha_2 \approx 2$. Combining (3.1) with (3.4) and (3.5), the FS signal for the ME scenario is:

$$E_{FS}(t) = \frac{A_{FS} e^{jk(r_{c1}+r_{c2})}}{j\lambda r_{c1} r_{c1}} \int_{S_{FS}} H(x') e^{jkx'^2\left(\frac{1}{2r_{c1}}+\frac{1}{2r_{c2}}\right)} e^{jkx'\left(\frac{X_p(t)-X_T(t)}{r_{c1}}+\frac{X_p(t)-X_R(t)}{r_{c2}}\right)} dx', \tag{3.6}$$

with $H(x')$ is the Complex Profile Function (CPF) of the target, defined as:

$$H(x') = \int \epsilon_\tau(x', z') e^{jkz'^2\left(\frac{1}{2r_{c1}}+\frac{1}{2r_{c2}}\right)} e^{jkz'\left(\frac{Z_p(t)-Z_T(t)}{r_{c1}}+\frac{Z_p(t)-Z_R(t)}{r_{c2}}\right)} dz'. \tag{3.7}$$

Two parameters are introduced, $h(x')$ and $m(x')$, the height difference and the median line of the target. They are related as:

$$m(x') = \frac{h(x')}{2}. \tag{3.8}$$

The limits of the CPF can be set from $m(x') - h(x')/2$ to $m(x') + h(x')/2$ as:

$$H(x') = \int_{m(x')-\frac{h(x')}{2}}^{m(x')+\frac{h(x')}{2}} e^{jkz'^2\left(\frac{1}{2r_{c1}}+\frac{1}{2r_{c2}}\right)} e^{jkz'\left(\frac{Z_p(t)-Z_T(t)}{r_{c1}}+\frac{Z_p(t)-Z_R(t)}{r_{c2}}\right)} dz'. \tag{3.9}$$

As per [24], by ignoring the second order variation of z' and computing the integral, the CPF can be approximated as:

$$H(x') \approx h(x')\text{sinc}\left[kh(x')\left(\frac{Z_p(t)-Z_T(t)}{2r_{c1}}+\frac{Z_p(t)-Z_R(t)}{2r_{c2}}\right)\right] e^{jkm(x')\left(\frac{Z_p(t)-Z_T(t)}{r_{c1}}+\frac{Z_p(t)-Z_R(t)}{r_{c2}}\right)}. \tag{3.10}$$

The position vector of a space object in an assumed circular orbit can be determined from Figure 3.4 using (3.11a). The orbital angular velocity of the object, denoted by ω_{spc}, is obtained from (3.11b), where $\mu \approx 3.99 \times 10^{14}\text{m}^3/\text{s}^2$ represents the standard gravitational parameter of the Earth, and R denotes the radial distance between the centre of the Earth and the space object. The parameter α_{spc} corresponds to the orbital inclination angle in the XY-plane, which may alternatively be interpreted as the trajectory angle of the space object.

$$P_{spc}(t) = \begin{bmatrix} X(t) \\ Y(t) \\ Z(t) \end{bmatrix} = R_{spc} \begin{bmatrix} \sin(\omega_{spc}t)\cos(\alpha_{spc}) \\ \cos(\omega_{spc}t) \\ \sin(\omega_{spc}t)\sin(\alpha_{spc}) \end{bmatrix}, \tag{3.11a}$$

$$\omega_{spc} = \sqrt{\frac{\mu}{R_{spc}^3}}. \tag{3.11b}$$

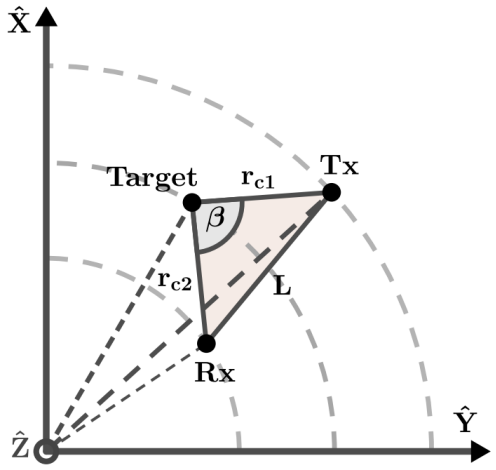

Figure 3.4: Space geometry

If ω_{spc} is small enough for the small angle approximation to be used. The position vector (3.11a) can be approximated as:

$$P_{spc}(t) = \begin{bmatrix} X(t) \\ Y(t) \\ Z(t) \end{bmatrix} \approx R_{spc} \begin{bmatrix} \omega_{spc}\cos(\alpha_{spc})t \\ 1 - \frac{(\omega_{spc}t)^2}{2} \\ \omega_{spc}\sin(\alpha_{spc})t \end{bmatrix}. \tag{3.12}$$

Combining (3.6) and (3.12) yields in:

$$E(t) = Q\int_S H(x')e^{j\eta x'^2}e^{j\gamma x' t}dx'; \tag{3.13}$$

$$Q = \frac{Ae^{jk(r_{c1}+r_{c2})}}{j\lambda r_{c1}r_{c2}}; \quad \eta = k\left(\frac{1}{2r_{c1}} + \frac{1}{2r_{c2}}\right); \tag{3.14}$$

$$\gamma = k\sqrt{\mu}\,\Gamma_p\left(\frac{1-\frac{\Gamma_T}{\Gamma_p}}{r_{c1}} + \frac{1-\frac{\Gamma_R}{\Gamma_p}}{r_{c2}}\right); \quad \Gamma_{T|R|p} = \frac{\cos\alpha_{T|R|p}}{\sqrt{R_{T|R|p}}}. \tag{3.15}$$

To be able to extract the CPF with SISAR, the inverse transform is applied to (3.13):

$$\dot{H}(x') = \frac{\gamma}{2\pi Q}e^{-j\eta x'^2}\int_{t_{obs}} E(t)e^{-j\gamma x' t}dt, \tag{3.16}$$

with $\dot{H}(x')$ being the reconstructed CPF, $E(t)$ the received FS signal and t_{obs} the observation time. As a consequence, to be able to extract the CPF, the Q, γ and η variables from (3.14) and (3.15) must be estimated. Similarly, a target with a certain shape and size is assumed for the $H(x')$ in (3.13).

The study in [24] showed that errors in altitude and trajectory angle estimation can lead to a corrupted CPF reconstruction. In the considered scenario, the receiver was at an altitude of 400 km, the target at 700 km, and the transmitter at 963 km. Altitude errors of up to 200 m still allowed for accurate reconstruction, whereas errors greater than 2 km produced an incorrect profile. In contrast, even small trajectory angle errors, as low as 3°, resulted in an unreliable CPF. In terms of SNR, even relatively low values, such as −10 dB, are sufficient to identify the target shape from the CPF.

3.1.2.1 Extraction of the motion parameters of the target from the FS signal

According to [24], to extract the motion parameters of the target from the FS signals a bank of matched filters can be used. The received FS signal is down-converted to baseband, and correlated with several reference FS signals previously created with different target altitudes and inclination angles. The FS signals are created using (3.6) and correlated using a matched filter as in (3.17).

$$y_{MF}(t) = s_{MF}(t) * x^*_{MF}(-t) = \int_{-\infty}^{\infty} s_{MF}(\nu) \cdot x^*_{MF}(\nu - t) d\nu, \tag{3.17}$$

where, $y_{MF}(t)$ is the output of the matched filter, $s_{MF}(t)$ is the reference FS signal, $x_{MF}(t)$ is the received FS signal, $*$ is the convolution operation and * is the complex conjugate.

The matched filter could be expanded to be used in a bank of correlators, Figure 3.5. Once the received signal has been correlated with the different reference signals, the maximum is chosen. From those maxima, the highest value is selected, and the respective altitude and inclination angle are extracted.

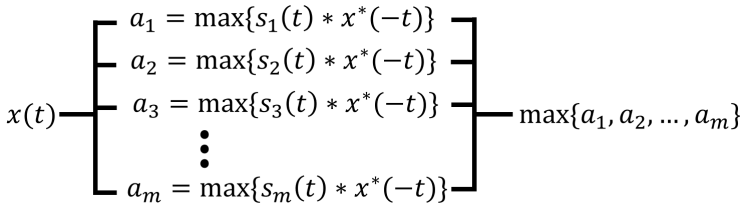

Figure 3.5: Bank of correlators of motion parameters extraction

The main problem with this approach is that it is very time-consuming and, in some cases, not feasible. This is because the search grid step needs to be small, requiring many correlators to reduce the error in the estimation, which would require of a large memory to store all of them, and a considerable amount of time to correlate them all. Similarly, as deduced from [24], the SNR also plays an important role in the algorithm. Therefore, two of the challenges are increasing the SNR to ensure the correct functioning of the SISAR algorithm and developing an improved method for extracting the motion

parameters, which will be introduced in Chapter 5.

3.1.3 Comparison with ISAR

For reference on the computational load, SISAR will be compared to ISAR. To create the ISAR image the standard method is a 2D-IFFT algorithm [47]. First, an IFFT is applied across each row (fast-time) to compress the radar pulses, resolving scatterers in the range dimension based on their time delay. Subsequently, a FFT is applied across each column (slow-time) of the range-compressed data. This second transform analyses the Doppler frequency shift induced by target rotation, effectively resolving scatterers in the cross-range dimension. The final output of this efficient process is a high-resolution 2D image where the intensity of each pixel represents the radar brightness of a scatterer at a specific range and cross-range location on the target.

Assuming a size target of 1 m, the possible ISAR computational time will be computed. For this size, the range resolution of the radar should be 1 cm, the bandwidth 1.5 GHz and the sampling frequency 3 GHz. The cross-range resolution is defined as [47]:

$$\Delta CR = \frac{\lambda}{2 \cdot \Delta\theta} \tag{3.18}$$

with ΔCR being the cross-range resolution and $\Delta\theta$ the angular rotation of the target. For an operational frequency of 10 GHz, the angular rotation should be: $\Delta\theta = 0.15\,\text{rad}$.

If the angular rotation of the target is $0.01\,\text{rad}\,\text{s}^{-1}$, the time to rotate by $\Delta\theta$ would be 15 s. For a PRF of 1 kHz, the number of collected pulses is: $PRF \cdot t_{\Delta\theta} = 15\,000$. At this PRF, the received signal would contain 3 000 000 samples, or range bins. After range compression, only the bins corresponding to the target are selected. Using an FFT size of 2048, the resulting matrix would have a dimension of 2048×15000. On an i9 CPU, processing this matrix would take approximately 45 ms.

For comparison, in the SISAR scenario, the receiver is at an altitude of 400 km, the transmitter at 963 km, and the target at 702 km with a trajectory angle of 68°. To extract the motion parameters of the target, the correlation map generated by the bank of correlators should use a step size of 1 km in altitude and 1° in the trajectory angle.

This results in a correlation map of size 563×360, corresponding to 202 680 FS signals to be processed. Assuming a correlation time of 5 ms per signal, the total computation time would be 16.89 min, which is significantly longer than for ISAR.

3.1.4 Summary

In summary, spaceborne radar technologies offer significant advantages for SSA, enabling the localization and imaging of space objects. Both active and passive spaceborne radar systems have been reviewed. Active systems provide the advantage of total control over the transmitted signals, while passive systems benefit from using large satellite constellations as transmitters, offering greater coverage.

A key development in spaceborne radar for SSA is the use of the FS configuration. Forward scattering systems enhance the RCS of targets, resulting in a higher SNR compared to monostatic systems. The integration of SISAR techniques with FSR provides a powerful tool for imaging space objects and extracting motion parameters. Some of the challenges with SISAR are the high computational cost of extracting the motion parameters, as well as having high enough SNR for the accurate extraction of them.

The FS system could be combined with a conventional monostatic radar to improve localization performance. In this configuration, the monostatic radar provides an initial estimation of the motion parameters, while the FS system, making use of this prior information, refines the result by performing a more accurate localization within the reduced search space. Some issues that the system will face would be how to mitigate the effect of the monostatic signal on the FS signal and vice-versa. In addition, the final radar solution would be more complex, and would require higher power capabilities. Similar systems, referred to as Reverse Forward Scatter (RFS) radars, have been proposed in [48, 49]. In an RFS configuration, a reflector is placed behind the target, while a monostatic radar transmits the signal. The FS signal is then generated by the reflection of the monostatic signal.

3.2 Ground-based radar for space situational awareness

In 1946, the US Army Signal Corps conducted an experiment in which electromagnetic signals were reflected off the Moon and received by an Earth-based antenna [2, 3]. It was the first experiment of radar astronomy, and it proved that radar could be a viable way to perform SSA. Ever since then, radar has been widely used for SSA to detect and track cooperative objects orbiting around the Earth, such as satellites, or uncooperative objects, such as space debris. Lately there has been an encouragement to develop space-based SSA radar [37, 12]. However, most of the radar SSA systems are Earth-based. While most SSA radars work in a monostatic configuration in some cases the bistatic configuration has been proposed [50].

Many of the SSA systems use radio telescopes, mainly as receivers as they have better sensitivity, improving the detection of targets with smaller RCS, and possibly smaller targets, for a given range [51, 52]. However, the bistatic angle is not large enough so that the bistatic advantages can be exploited and most of these systems work in a quasi-monostatic configuration [1]. Examples of radio telescopes that have been used are the Sardinia Radio Telescope (SRT) [53], the Millstone Hill Radar (MHR) [54, 36, 55] at the Haystack Observatory, the Tracking and Imaging Radar (TIRA) [56, 57, 55] located at the FGAN research institute, the Effelsberg Radio Telescope [58], the Westerbork Synthesis Radio Telescope (WSRT) [36, 55].

The BIstatic RAdar for LEo Tracking (BIRALET) configuration was introduced in [53]. On the experiment, two satellites, one CubeSAT and space debris of the Cosmos-2237 satellite were tracked. The radar was configured in a bistatic way. The Flight Termination System (FTS), part of the Italian Air Force, was transmitting the radar signals, and the SRT was the receiver. The FTS has an output power of 4 kW, it can transmit from 400 to 455 MHz. The SRT has a 64 m parabolic antenna, with an operating frequency from 0.3 to 116 GHz. The baseline for this bistatic radar was 40 km.

The MHR, along with the Haystack and Haystack Auxiliary (HAX), was employed to detect different satellites and space debris [54]. With the different radio telescopes multi-frequency RCS data was collected. Each space object was tracked at multiple

elevation angles, and the radar data were used to extract the RCS values and target sizes.

In [56] it was explained how the TIRA could use its 34 m parabolic antenna with its mono-pulse L-band tracking radar for detect and track space objects, while its Ku-band imaging radar could be used to image them. The detection and tracking would be used to determine the orbit of said space objects and characterize them. In one hand, because of its 13 kW peak power and low noise amplifiers (LNA), the L-band radar is sensitive enough to detect down to 2 cm sized objects at a distance of 1000 km. If the TIRA transmits radar signals while the Effelsberg radio telescope [58] acts as a receiver, the objects that could be detected were as small as 0.9 cm at 1000 km. More importantly, [58] proved that a bistatic radar could be adopted to perform SSA tasks. On the other hand, the Ku-band radar can be used to image space objects such as satellites to provide support of Launch and Early Orbit Phases (LEOPs) and as a diagnosis tool to determine attitude and shape of the possible target. More concretely, the study in [57] showed how the TIRA could be operated to characterize de-orbiting satellites and space debris.

When multiple transmitter-receiver bistatic pairs are combined, multistatic systems are created. Regarding the role of multistatic systems in SSA, there have been some studies on multistatic radars [59, 60] for detecting space objects, but a limited number of them used long baseline bistatic pairs. In this thesis, by *long baseline*, it is understood a distance from transmitter to receiver of 5000 km, or greater. Additionally, following [59, 60], a radar system is considered bistatic if it produces a bistatic angle, β, greater than 10°. In [59], as part of the German Experimental Surveillance and Tracking Radar (GESTRA), transmitter and receiver units were built and assessed to create a multistatic system with a maximum baseline of 500 km to detect a target at an altitude of 1000 km. The configuration resulted in a bistatic angle of 14°. In [60] a baseline of 250 km was employed to create a bistatic system to perform SAR imaging on a target at 627 km. This system utilized a bistatic angle of 11°. A more recent experiment was conducted on [61], where a transmitter in Millstone Hill, USA, was used along with two receivers, placed in Westerbork, Netherlands, and Sardinia, Italy, which created a bistatic angle of around 8° and 10°, respectively, with baselines of 5650 km and 5500 km,

respectively. However, the multistatic capabilities and performance have not yet been evaluated using real measurements.

A long baseline will enable the system to better exploit the bistatic capabilities in a multistatic configuration and reduce the ambiguity in the target location derived from the radar measurements. Configuring the system to work in a bistatic way, instead of a monostatic or quasi-monostatic configuration, will allow distributing sensing and to capture different target returns from the same transmission. Hence, if one of the bistatic pairs returns an incorrect location detection of the target because of its low signal-to-noise ratio (SNR), the other readings could help to locate it correctly, as it is going to be seen in Section 6.5. Moreover, multistatic radars can offer better behaviour characterization of the space object [62]. Being able to have multiple receivers in the multistatic radar will open the possibility of increasing the SNR of the target if the fusion of the radar data is performed with proper methods, such as the multiple-input-multiple-output (MIMO) ambiguity function (AF), introduced in Section 6.2.

One key issue, not addressed in the thesis, is the synchronization problems that might arise from having receivers and transmitters in different continents. Nevertheless, several solutions have been proposed to synchronize digital systems, principally using GNSS signals [63, 64].

In [36], it was shown how to detect GEO satellites. The MHR and the TIRA were the transmitters and the SRT, the Westerbork Synthesis Radio Telescope (WSRT), and the e-MERLIN array radio telescope situated in the United Kingdom (UK) were the receivers. The e-MERLIN is a particular case since it has 7 antennas working together as a single receiver. To achieve it, the 7 antennas, which have diameters from 25 m to 76 m and are 10 km to 220 km apart, are connected by a dedicated optical network and the coherence between the different transmitted or received signals is maintained by radiofrequency (RF) timing signals on those same fibres. Table 3.1 shows the parameters used in [36]. The peak power and bandwidth on TIRA is dependent on N_{mod}, the Binary phase shift keyed (BPSK) modulation number. The pulse width itself is 1 ms divided into N_{mod} subpulses, therefore the bandwidth will be proportional to N_{mod} and, assuming a fixed SNR at the receiver, the peak power will also be proportional to N_{mod}.

On the contrary, the MHR uses a linear frequency modulated (LFM) chirp.

	MHR	TIRA
Modulation type	LFM	BPSK
Peak power	3000 kW	Depends on N_{mod}
Operating freq.	1295 MHz	1333 MHz
Bandwidth	8 MHz	Depends on N_{mod}
Pulse width	Maximum: 1 ms	1 ms divided into N_{mod} subpulses
PRF	Algorithmically determined	30 Hz

Table 3.1: MHR and TIRA parameters

The results demonstrated that GEO targets can be detected, tracked, and their RCS extracted from radar returns. Range–Doppler maps, shown in Figure 3.6, confirm that coherent processing is achievable. The number of coherently integrated pulses reached up to 4000 when the MHR served as the transmitter and up to 2000 when TIRA was used as the illuminator. Assuming comparable PRFs for both transmitters and applying (2.57), the resulting CPIs are 133.33 s for the MHR and 66.67 s for TIRA. These results indicate that high integration gains are achievable for GEO targets, ensuring sufficient SNR for reliable detection and accurate motion estimation. Moreover, the CPI values confirm that GEO targets maintain coherence over relatively long time intervals.

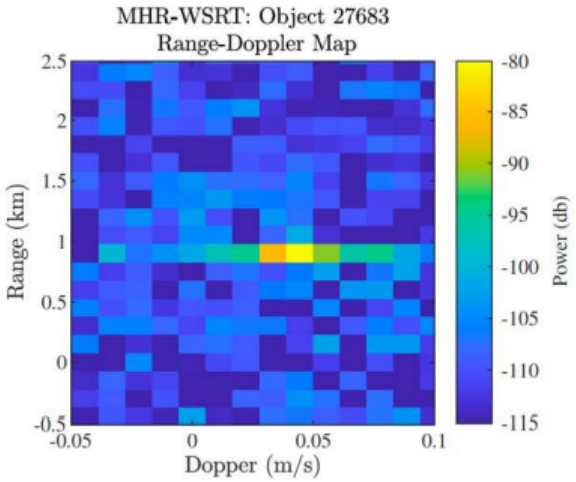

Figure 3.6: Range-Doppler maps extracted in [36]

3.2.1 Bistatic radar for SSA

This section covers some of the peculiarities of the bistatic configuration when applied in a SSA scenario. In a classical radar system, the transmitter and receiver are situated in the same locations and, many times, use the same antenna for transmission and reception purposes, forming the aforementioned monostatic configuration as seen on Section 2.1.6.1.

On the contrary, a bistatic radar would use a transmitter and a receiver in different locations. In SSA, due to their high sensitivity, radio telescopes are often used as receivers in conjunction with radar transmitters to form bistatic pairs. Nevertheless, due to the relatively small distance between the transmitter and receiver compared to the target location, most bistatic SSA systems do not form large enough bistatic angles and can be considered quasi-monostatic.

Indeed, a key property of a bistatic radar is its bistatic angle, β, which is the angle with vertex at the location of the target and rays at the transmitter-target and target-receiver paths. Figure 3.7 shows the basic bistatic configuration. The transmitter, Tx, and receiver, Rx, are separated by a distance, $L_{Tx,Rx}$, also called the baseline, the target travels at a speed, v, while the distance from the transmitter to the target is denoted by d_{Tx} and the distance from the receiver to the target by d_{Rx}. A system can be considered bistatic if $\beta > 0$. There is an exception though if $\beta \approx 10$ while $L_{Tx,Rx} \neq 0$, then the system is considered quasi-monostatic. For example, in [50] a bistatic system was used to detect a satellite at 800 km with a baseline of about 10 km. The estimated bistatic angle of this configuration was 0.72°, an angle associated with quasi-monostatic configurations.

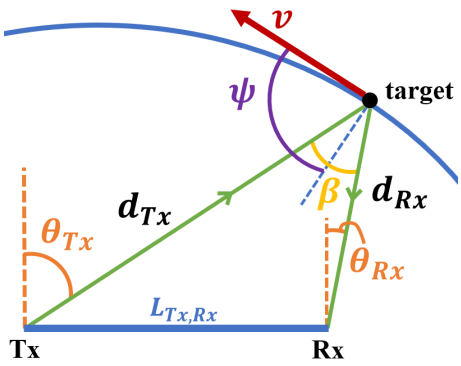

Figure 3.7: Bistatic configuration

When considering earth-to-space observations, for a big enough bistatic angle to be achieved, which according to [59, 60] should be around 10°; the transmitter and receiver will have to be separated by hundreds or thousands of kilometres, depending on the intended maximum altitude to be observed. For example, assuming a bistatic angle of 10° and $d_{Tx} \approx d_{Rx}$, if the target is at an altitude of 1000 km, a LEO satellite, the transmitter and receiver should be separated by 175 km, which is the distance between Nottingham and London. On the other hand, if the observed object is orbiting at 35 786 km, a geostationary (GEO) satellite, the minimum distance between transmitter and receiver for the radar system to be considered bistatic should be 6261 km, the distance between Amsterdam and Washington DC. An example of a radar for SSA with a big bistatic angle was shown in [65]. For the study a system with a baseline of 916 km was used to detect a target at 620 km, which created an estimated bistatic angle of 72°.

One of the key features of the bistatic radar is the bistatic angle, β. The bistatic angle affects the bistatic RCS, $\mathrm{RCS}_{\mathrm{bs}}$, of the target. Here the bistatic RCS will be modelled as [42]:

$$\mathrm{RCS}_{\mathrm{bs}} \approx \mathrm{RCS}\ \cos\frac{\beta}{2}, \tag{3.19}$$

where RCS is the monostatic RCS and β is the bistatic angle. The bistatic Doppler frequency is given by [66]:

$$f_D = -\frac{2v}{\lambda}\cos\psi\cos\frac{\beta}{2}. \tag{3.20}$$

While the Doppler resolution is calculated as [1]:

$$\Delta f_D = \frac{1}{T_d} = \frac{1}{n_p \,\mathrm{PRI}}, \tag{3.21}$$

where T_d and n_p are observation time and number of pulses, respectively.

Furthermore, the bistatic range is computed as [67]:

$$r_{bs} = R_1 + R_2, \tag{3.22}$$

with R_1 and R_2 being the distance from the transmitter to the target and the target to the receiver, respectively.

Following the bistatic range, in frequency-modulated radar the bistatic range resolution can be deduced as [67]:

$$\Delta r_{bs} = \frac{\Delta r}{\cos(\beta/2)\cos(\psi)} = \frac{c_0}{2B_W \cos(\beta/2)\cos(\psi)}, \tag{3.23}$$

with Δr being the range resolution for monostatic radar.

3.2.2 Summary

Ground-based radar systems have been crucial in advancing SSA technologies. The majority of ground-based SSA radar systems utilize monostatic or quasi-monostatic configurations to detect and track space objects. Advanced bistatic configurations could offer enhanced target characterization and reduced localization ambiguities. However, there are issues to consider when using bistatic radars for SSA, such as synchronization over long baselines and achieving optimal bistatic angles. Multistatic systems could further enhance detection reliability by fusing data from multiple transmitter-receiver pairs. The challenge remains in how to effectively fuse the bistatic data.

3.3 Classification of radar signals using Artificial Intelligence (AI)

In AI, Neural Network (NN) architectures are used to perform a variety of tasks. Neural networks consist of neurons, mathematical functions designed to approximate the

behaviour of biological neurons [68]. Among the most common architectures are Convolutional Neural Network (CNN), which use the convolution to hierarchically extract spatially localized features, making them well-suited for image processing. Generative Adversarial Networks (GANs), by contrast, are primarily used for data generation. A GAN consists of a Generator, which produces synthetic data, and a Discriminator, which distinguishes real data from generated outputs. Through this adversarial process, the Generator progressively produces highly realistic data. In this thesis, Recurrent Neural Network (RNN) are employed, an architecture tailored for sequential data that maintains a memory of previous inputs.

The output of a network depends on its training objective. For tasks typically handled by CNNs and RNNs, outputs generally fall into two categories:

- Classification: a probability distribution over a set of discrete classes, obtained via a softmax activation [69]. The predicted class is assigned to the one with the highest probability. This value, often called the confidence score, represents the estimated certainty of the model that the input belongs to that specific class.

- Regression: a continuous, scalar or vector-valued estimate of a variable. The reliability of a regression output is not encapsulated by a single score for that prediction but is instead evaluated globally using error metrics like Mean Squared Error on a validation set.

AI, and in particular deep learning architectures such as CNN and RNN, has found increasing application in the radar domain. Most commonly, these methods are employed for classification tasks, including the identification of different targets [70, 71, 72, 73] or human activities [74]. In addition, they are also widely used for the extraction of radar signal parameters, such as modulation type, pulse repetition interval (PRI), or pulse width [75, 76, 77, 78, 79]. These applications demonstrate the versatility of AI methods in handling complex, high-dimensional radar data, where conventional signal processing techniques may be limited in scalability or adaptability.

3.3.1 Recurrent neural network (RNN) functioning

A RNN is a type of neural networks for processing sequential data [80], such as signals or text. In this thesis, RNNs are going to be used to classify FS signals, therefore the functioning of RNNs will be explained next.

The main advantage of RNNs when using them for signals is its memory. RNNs have a hidden state that is used as a memory. This allows them to store and employ information from previous time intervals. Thus, RNN would be very useful when processing signals, as past data points would affect the current or future points. RNNs can be used to predict the next step of the sequential data, to estimate how the data will behave or to classify said sequential data into given classes.

The layers of a basic RNN architecture are [80]:

- Input: input feature signal, represented by $x_{NN}(t)$ in Figure 3.8.
- Hidden state: serving as the network memory. It is denoted by $h_{NN}(t)$ in Figure 3.8 and computed from the current input and the previous hidden state as:

$$h_{NN}(t) = f_a(b_{NN} + U_{NN} \cdot x_{NN}(t) + W_{NN} \cdot h_{NN}(t-1)), \tag{3.24}$$

  where t is the unit time, $f_a(\cdot)$ is the activation function, which is a non-linear function, that would be more adequate to map non-linear dependencies, U_{NN}, W_{NN} are matrix weights, and b_{NN} is a bias term. The bias term enables the layer to model data distributions that are not centred at zero.

- Outputs: output of the network, represented by $o_{NN}(t)$ in Figure 3.8. It can be mathematically expressed as:

$$o_{NN}(t) = c_{NN} + V_{NN} \cdot h_{NN}(t), \tag{3.25}$$

  where $o_{NN}(t)$ denotes the output and c_{NN} the bias term. The output $o_{NN}(t)$ may serve as the input to a $softmax(\cdot)$ function, yielding a probability vector that quantifies the likelihood of the input belonging to each class.

- Weights: the input to hidden connections are parametrized by the weight matrix U_{NN}, the hidden to hidden recurrent connections are parametrized by the weight matrix W_{NN} and the hidden to output connections are parametrized by the weight matrix V_{NN}. The weights are updated using gradients, which indicate how much the weight has to change in order to reduce the error.

  Gradients are computed using the back-propagation method. Once the error is computed for a set of weights and bias terms, it is back-propagated to each neuron in the hidden layer to compute the gradient. The gradient is the vector of partial derivatives of $e_{NN,\mathfrak{t}}$ with respect to the Θ_{NN} evaluated at the time step $\mathfrak{t}$ [81]:

$$G_{NN,\mathfrak{t}} = \nabla_{\Theta_{NN}} e_{NN,\mathfrak{t}}(\Theta_{NN}), \tag{3.26}$$

  where Θ is the variable representing the $U_{NN}, V_{NN}, W_{NN}, b_{NN}, c_{NN}$ parameters, $e_{NN,\mathfrak{t}}(\cdot)$ is the error at time step $\mathfrak{t}$, that could itself be interpreted as a random stochastic function that is differentiable with respect to the parameters and $\mathfrak{t}$ is the vector of time step, the discrete time vector.

  The back-propagation method computes the gradient of the error with respect to each layer of the neural network, starting from the output and finishing with the top layers [82]. Therefore, the weights are updated from the bottom of the layers to the top of them.

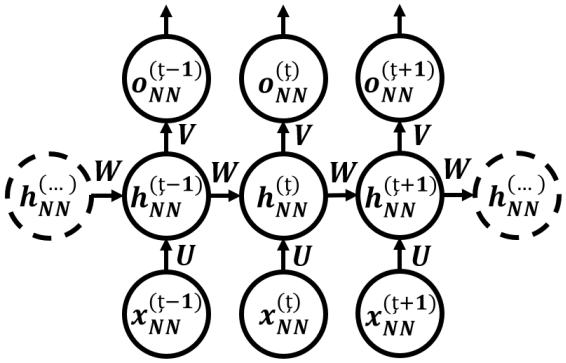

Figure 3.8: Basic architecture of a RNN as studied in [80]

3.3.1.1 Long Short Term Memory (LSTM)

Introduced in 1997, the LSTM provided a solution for Back-Propagation Through Time (BPTT) learning [83]. This was a challenge faced by early RNNs. For the BPTT, the error signals, the error between the estimations and the real values, when back-propagated could cause [84]:

- Increase dramatically, leading to oscillating weight values. Also called the Exploding Gradient Problem.
- Decrease down to small values. However, if the the input signal is very long, the learning process of the RNN could take an insurmountable amount of time. This is called the Vanishing Error Problem. As the aim is to minimize the error, a gradient descent method is employed. The method relies on following the descending gradient. Since the gradient is basically a derivative, it can be easily understood how following the descending gradient would be similar to following a decreasing slope, thus minimizing the error.

  The gradient of the weights will decrease quickly with each iteration and with back-propagation, specially if there are lots of layers. The very small values of the gradients will make very hard for the network to find the gradient that descends, and it will take longer to find the optimal result. This is specially true if the signals are long, as the computation of the gradients and back-propagation will take longer.

3.3.1.1.1. Constant Error Carousel

The Constant Error Carousel (CEC) [84] solution is used to prevent the Vanishing Error Problem. CEC ensures that a constant error flow through each neuron in the RNN is made. Mathematically, it is achieved by [85]:

$$f_{NN,u_{NN}}(z_{NN,u_{NN}}(\text{ţ})) = \frac{z_{NN,u_{NN}}(\text{ţ})}{W_{NN,[u_{NN},u_{NN}]}}, \tag{3.27}$$

where ţ is a time unit, $z_{NN,u_{NN}}$ is the weighted input of the unit u_{NN}, $W_{NN,[u_{NN},u_{NN}]}$ is the weight that connects the unit u_{NN} to itself, $f_{NN,u_{NN}}$ is the squashing function

of the unit, neuron, u_{NN}. It is called squashing function because it can squash a large input to a small output.

From (3.27), it can be deduced that $f_{NN,u_{NN}}$ is a linear function. Additionally, the activation of the unit u_{NN} must remain constant over time to have a constant error flow:

$$\begin{aligned} y_{NN,u_{NN}}(t+1) &= f_{NN,u_{NN}}(z_{NN,u_{NN}}(t+1)) \\ &= f_{NN,u_{NN}}(y_{NN,u_{NN}}(t)W_{NN,[u_{NN},u_{NN}]})) \\ &\overset{1}{=} y_{NN,u_{NN}}(t). \end{aligned} \tag{3.28}$$

In (3.28), $y_{NN,u_{NN}}$ is the output of unit u. For the equality 1 in (3.28) to hold, $f_{NN,u_{NN}}$ must be the identity function, and by setting $W_{NN,[u_{NN},u_{NN}]} = 1$.

3.3.1.1.2. LSTM architecture

An LSTM block is illustrated in Figure 3.9, following the description in [85]. The block consists of a single cell incorporating a constant error carousel (CEC) and a self-recurrent connection with a fixed weight of 1. The state of the c_{NN}-th cell in memory block m_{NN} is denoted as $s_{NN,m_{NN},c_{NN}}$.

The write operation to the cell state is controlled by the input gate, $y_{NN,in}$, while the read operation from the cell state is governed by the output gate, $y_{NN,out}$, with their respective activation functions $f_{NN,in}$ and $f_{NN,out}$. The update of the internal cell state proceeds by first computing the product of the input gate activation and the transformed input, obtained via the squashing function $g_{NN,a}(\cdot)$. This product is then added to the previous cell state, $s_{NN,m_{NN},c_{NN}}(t)$, yielding the updated cell state $s_{NN,m_{NN},c_{NN}}(t+1)$.

Prior to being transmitted to the output gate, the updated cell state is passed through a squashing activation function $h_{NN,a}(\cdot)$. The final cell output, $y_{NN,m_{NN},c_{NN}}$, is obtained by multiplying this squashed cell state by the output gate activation. It should be noted that $y_{v_{NN}}(t)$ represents the output of unit v_{NN}.

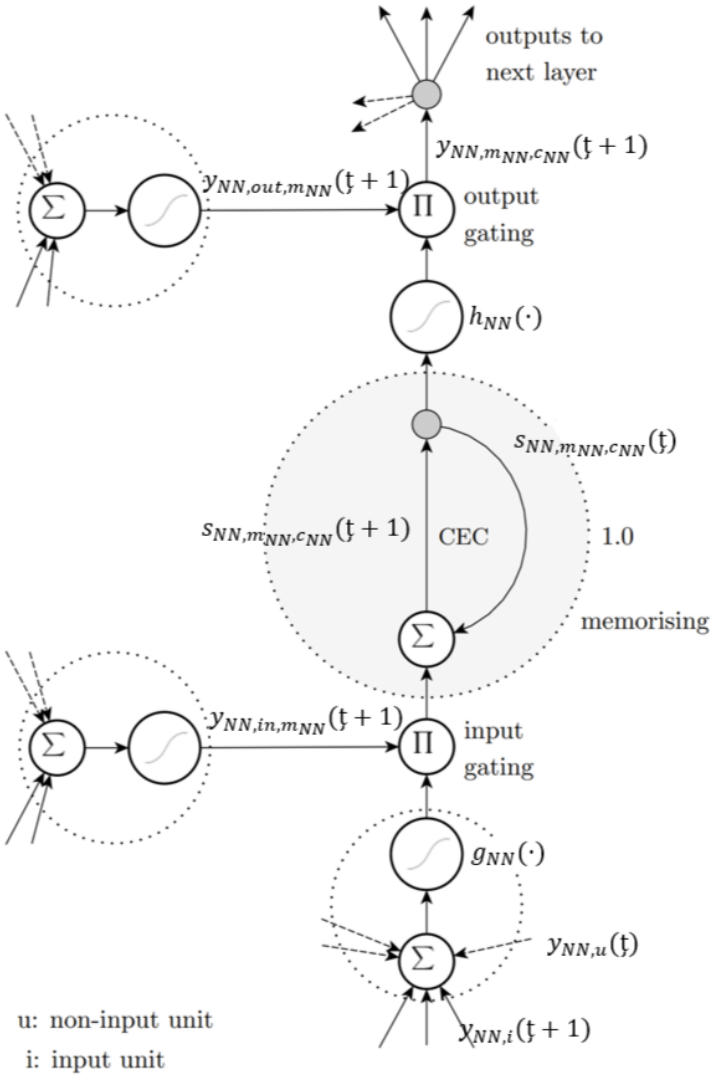

Figure 3.9: LSTM architecture as per [85]

3.3.2 ADAptive Moment estimation (ADAM)

The gradient g_t, a vector of partial derivatives of the error with respect to the parameters, is central to error minimization. Since the gradient points in the direction of steepest ascent, parameters are updated opposite to this direction to reduce error: a positive gradient component indicates the parameter should be decreased, while a negative component indicates it should be increased. Although many gradient-based optimizers exist, AdaM [81], or simply Adam or ADAM, is used here and will be described.

Adam is an algorithm for first-order gradient-based optimization of stochastic objective functions, based on adaptive estimates of lower-order moments [81]. The advantages of Adam include its straightforward implementation, computational efficiency with minimal memory requirements, and suitability for problems involving large datasets or a high number of parameters.

The pseudo-code of the Adam algorithm is:

1	$\Theta_{NN,0}$;	Initialize parameter vectors, typically at random.
2	$m_{A,0} = 0$;	Initialize first moment (mean) vector
3	$v_{A,0} = 0$;	Initialize second moment (variance) vector
4	$\mathfrak{t} = 0$;	Initialize time-step
5	**while** $\Theta_{NN,\mathfrak{t}}$ does not converge	
6	$\quad \mathfrak{t} = \mathfrak{t} + 1$;	Next step for next iteration
7	$\quad G_{NN,\mathfrak{t}} = \nabla_{\Theta_{NN}} e_{NN,\mathfrak{t}}(\Theta_{NN,\mathfrak{t}})$;	Compute the gradient of $e_{NN,\mathfrak{t}}$, the error
8	$\quad m_{A,\mathfrak{t}} = \beta_{A,1} \cdot m_{A,\mathfrak{t}-1} + (1 - \beta_{A,1}) \cdot g_{NN,\mathfrak{t}}$;	Update bias first moment estimate
9	$\quad v_{A,\mathfrak{t}} = \beta_{A,2} \cdot v_{A,\mathfrak{t}-1} + (1 - \beta_{A,2}) \cdot g^2_{NN,\mathfrak{t}}$;	Update bias second raw moment estimate
10	$\quad \hat{m}_{A,\mathfrak{t}} = m_{A,\mathfrak{t}}/(1 - \beta_{A,1,\mathfrak{t}})$;	Compute bias-corrected first moment estimate
11	$\quad \hat{v}_{A,\mathfrak{t}} = v_{A,\mathfrak{t}}/(1 - \beta_{A,2,\mathfrak{t}})$;	Compute bias-corrected second raw moment estimate
12	$\quad \Theta_{NN,\mathfrak{t}} = \Theta_{NN,\mathfrak{t}-1} - \alpha_A \cdot \hat{m}_{A,\mathfrak{t}} / \left(\sqrt{\hat{v}_{A,\mathfrak{t}}} + \epsilon_A\right)$;	Update parameters
13	**end**	
14	**return** $\Theta_{NN,\mathfrak{t}}$	

In the pseudocode, the parameters that control the learning process, called hyper-

parameters, are:

- α_A: step-size.
- $\beta_{A,1}, \beta_{A,2} \in [0, 1)$: exponential decay rates for the moment estimates.
- ϵ_A: the denominator offset. It is usually a small value, on the order of 10^{-8}. If the estimated variance for the next step, $\hat{v}_{A,k_t}$, computed in line 11, equals zero, it would cause a computational error in line 12.

3.3.3 Some activation functions

This section delves into some of the activation functions that are commonly used in RNNs. Three sigmoid functions are going to be introduced as the activation functions. A sigmoid function is a mathematical function with a S-shaped curve [86]. Some of the most common sigmoid functions are:

- Hyperbolic tangent, which is defined as:

$$\tanh \varphi = \frac{\sinh \varphi}{\cosh \varphi} = \frac{e^{2 \cdot \varphi} - 1}{e^{2 \cdot \varphi} + 1}. \tag{3.29}$$

  The $tanh(\cdot)$ has a lower limit of -1 and an upper limit of 1.

- The logistic function, also simply called the sigmoid function, is mathematically defined as [87]:

$$\sigma_l(\varphi) = \frac{1}{1 + e^{-\varphi}}. \tag{3.30}$$

  Contrary to the tanh function, the logistic function has an lower limit of 0 and an upper limit of 1.

- A hard-sigmoid function is a linear approximation of a sigmoid function. A common definition is [88]:

$$\sigma_H(\varphi) = \begin{cases} 0 & \text{if} \varphi < 2.5 \\ 0.2\varphi + 0.5 & \text{if} -2.5 \leq \varphi \leq 2.5 \\ 1 & \text{if} \varphi > 2.5 \end{cases}. \tag{3.31}$$

The advantages of a hard-sigmoid is the simpler mathematical operations to compute its output and derivative. The disadvantages would be the inaccurate approximation to the logistic function, which would impact the overall performance of the neural network.

Classification activation functions are used in the last layer of a neural network. They provide a value between $[0, 1]$ that is used to classify the input into the different classes. The two most common classification functions are:

- Logistic function. This has already been explained and is mathematically expressed by (3.30).
- Softmax activation function. Firstly introduced in [69], it computes a probability distribution of the input to be of a certain class. The function preserves the rank order of its input values, meaning that it provides a vector in which the first value is the most probable class of the input, the second value is the second most probable class and so forth.It is a generalization of the *winner-takes-all* approach of picking the maximum value. Mathematically, it is expressed as [69]:

$$Q_{a_f}(\varphi) = \frac{e^{V_{a_f}(\varphi)}}{\sum_{b_f=0}^{N_{cl}-1} e^{V_{b_f}(\varphi)}}, \tag{3.32}$$

with φ being the input vector to the softmax function, Q_{a_f} is class membership indicator of the a_f-th class, V_{a_f} and V_{b_f} are the outputs of the neural network associated with the a_f and b_f classes, and N_{cl} is the number of classes.

3.4 Conclusion on the preliminary knowledge

This chapter has provided an overview of existing radar systems, as well as signal processing models and solutions proposed for both spaceborne and ground-based applications. Although numerous active spaceborne radar systems have been developed, relatively few passive systems exist. The passive system considered in this thesis is that presented in [12, 24], which operates using a FS configuration. For ground-based

radar, the focus of this thesis is on long-baseline multistatic systems. While many bistatic ground radars are reported in the literature, only the system described in [36] employs a long baseline. Section 3.2.1 discusses some of the distinctive characteristics and challenges associated with bistatic radar operation. The chapter concludes with an introduction of the RNN, specifically the LSTM architecture, and the Adam training algorithm, which will be applied in Chapter 5.

Chapter 4

Radar system and payload design for the spaceborne segment

The increasing number of space objects orbiting the Earth has created the need for systems that can detect space objects to prevent space collisions. Ground-based radar systems, such as the Tracking and Imaging Radar (TIRA) of FGAN, use both radar and optical techniques to detect and track space objects. However, these systems are costly and often not accessible to all potential users, academic or commercial. Additionally, many of the antennas employed for space surveillance are primarily used for radio astronomy, making the integration of dedicated radar systems less practical.

The high cost and limited accessibility of ground-based systems create the demand for alternative solutions. A viable solution could be spaceborne radar systems, which would be more affordable and widely accessible compared to current ground-based systems, as studied on [12]. A spaceborne system, such as a radar mounted on a CubeSat acting as the receiver, coupled with a commercial satellite serving as the illuminator of opportunity and transmitter, offers a cost-effective and practical alternative. This approach would provide an easily accessible and feasible solution for detecting space objects. Moreover, the system will be positioned in an orbit, it will have shorter distances to the possible targets, which will lead to more suitable SNRs. Furthermore, since there is no active transmitter, the solution itself would be cheaper. Moreover,

the system described in [12], consisted of a passive bistatic radar (PBR) equipped with software defined radio (SDR), and, of course, an antenna so that the radars tasks for space surveillance could be performed. The study proved that the system could be a low budget solution and could detect space objects of even a few centimetres. In addition, the increasing number of satellites, namely commercial constellations, contributes to improved coverage. Besides, at those altitudes the effects of the atmosphere in the radar signals can be ignored. Therefore, the choice of the PBR seems appropriate.

In this chapter, the payload antenna and the radar system will be designed. It will be seen how the design of the antenna will be conditioned by the IOs, the size of the CubeSat and its ability to complete the radar tasks. Similarly, to justify the choice of the design, a RRE analysis will be conducted.

4.1 Antenna design and RRE analysis

This section will introduce the system design, more concretely how the spaceborne radar could be coupled with a phased array of monopoles, and a RRE analysis. Why the phased array of monopoles is chosen would be justified, by comparing the advantages and disadvantages of other possible antennas, and by using the RRE analysis. Similarly, the different possible IOs are analysed. Once the most suitable antenna is chosen, the bandwidth of the antenna will be computed. This task is left at the end of the study. The last analysis will ensure that the antenna is able to receive the full bandwidth of the signal from the IO. With the results of the RRE analysis, the observation time of the possible target will be computed.

4.1.1 Introduction

As introduced in [12], the system would be a passive bistatic radar (PBR) mounted on a CubeSat. In [12], the proposed radar sensor was a uniformly illuminated aperture, without getting into which antenna would be suitable for the task. In this chapter different antenna designs will be presented and the most suitable will be chosen. Similarly, in [12], two satellites were considered as the IOs: the HY2A and the GSTAR. This chapter examines more modern satellite constellations. The main advantage over

the previous IOs is the higher number of satellites per constellation. Furthermore, the service of the HY2A was terminated in December 2021, which would render its usage in the analysis useless.

The CubeSat would be placed at a lower orbit than the satellite used as the IO and the possible targets would be orbiting between them, Figure 4.1. The CubeSat will be receiving the signal from the satellite with a bistatic angle of nearly $\beta_{bs} \approx 180$, the FS configuration. The main advantage of using the FS configuration is the enhanced radar cross section (RCS) [16] that will improve the SNR, as it was studied in Section 3.1.

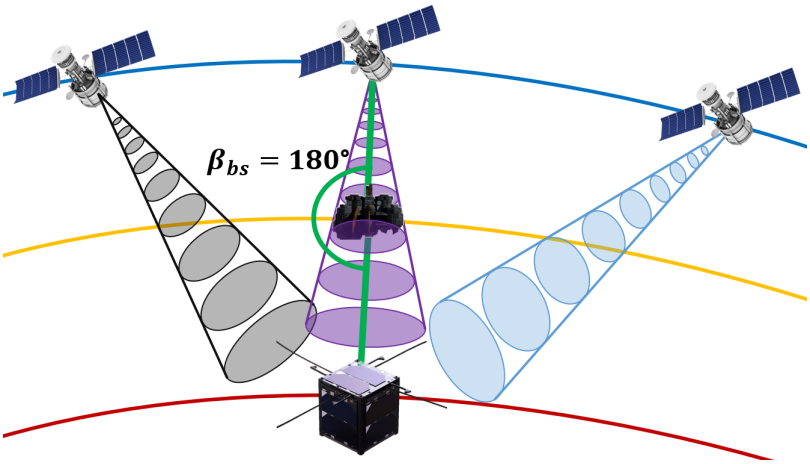

Figure 4.1: PBR configuration for a constellation of satellites

The maximum RCS in FS, also known as forward scatter cross section (FS-CS), is [42, 16]:

$$\sigma_{FS,max} = \frac{4\pi A_{trg}^2}{\lambda^2}, \tag{4.1}$$

where A_{trg} is the forward scatter area, the area of silhouette of the target, and λ is the wavelength. It can be observed that the smaller the λ, the higher $\sigma_{FS,max}$, so an IO, a passive transmitter, working at relatively high frequencies will be more desirable than one working a lower frequencies.

Figure 4.2 compares the FS-CS with the monostatic RCS of a perfectly conductive sphere of radius 25 cm. While the monostatic RCS asymptotically approaches -7 dB as the frequency increases, the FS-CS continues to grow with frequency. Consequently, at higher frequencies, the FS configuration offers a significant advantage for detecting

small targets.

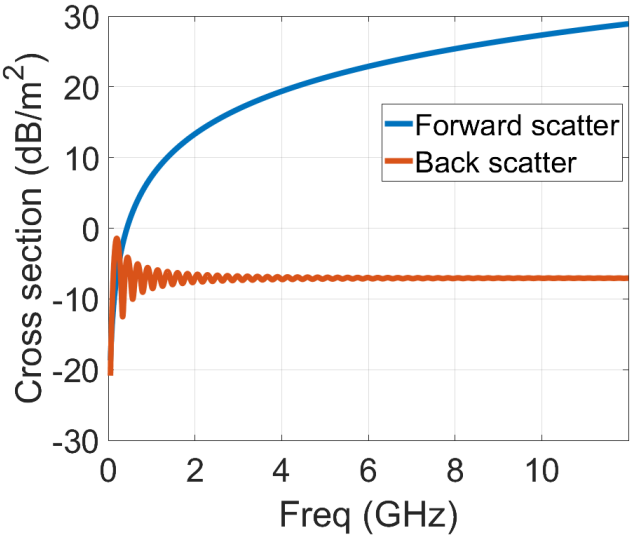

Figure 4.2: FS vs back scatter for a perfectly conductive sphere of a 25 cm radius

4.1.2 Illuminator of opportunity

The ideal IOs would be satellite constellations, as the large number of standardized transmitters would enhance the capability to detect space objects. Dedicated sensing satellites already exist, such as the Sentinel missions [89], which observe the atmosphere, oceans, and land using radar and optical sensors; EarthCARE [90], primarily focused on cloud and aerosol observation; and Haiyang-2 (HY-2) [91], dedicated to ocean monitoring and regional environmental trends. Each of these platforms carries radar transmitters that could, in principle, support the task at hand. However, with only a single satellite available per mission, passive radar operations are limited to narrow time windows. By contrast, satellite constellations provide a larger number of transmitters, thereby increasing detection opportunities and maximizing observation coverage.

Four constellations are considered: Starlink, Iridium, Globalstar and OneWeb. Iridium and Globalstar are used for phone satellite and low-speed data communications. Meanwhile, Starlink and OneWeb are used for high-speed data communications. The specifications relevant for the passive radar sensing task of each constellation considered is shown in Table 4.1 as per [92, 93, 94, 95, 96].

	f_0	B_W	Altitude	EIRP	Number of satellites
Starlink	10.7-12.7 GHz	250 MHz	550 km	37.7 dBW	4519
Iridium	1616-1626.5 MHz	35 kHz	783 km	30.9 dBW	66
GlobalStar	2.5 GHz	16.5 MHz	1400 km	37 dBW	48
OneWeb	10.7-12.7 GHz	250 MHz	1200 km	38.3 dBW	634

Table 4.1: Parameters of the different IOs

From these options the most useful ones are the Starlink and OneWeb constellations because:

- Their operating frequencies, f_0, are the highest, and, consequently, the FS CS will also be higher.
- The large bandwidth which gives a high signal processing gain after the matched filter, depending on the chosen pulse width of the received communications signal.
- The amount of satellites, which will increase the possibility of receiving a signal and detecting space objects.

The final parameter to consider when selecting an IO is altitude. Although the lower altitude of Starlink enhances the SNR due to the shorter distance between the CubeSat and the transmitter, it significantly reduces the number of space objects that can be detected. In contrast, the higher altitude of the OneWeb constellation offers broader coverage, making it more suitable for the proposed design. Accordingly, OneWeb is selected for the following analysis. In practice, both constellations could be employed since they share the same bandwidth and frequency band; however, for clarity and simplicity, the results presented in the next sections focus solely on OneWeb.

The pulse width of the IOs is not included in the analysis. In the proposed method, as seen in Section 3.1.2, the reconstructed FS signal is treated as an interference signal. This approach does not require prior knowledge of the waveform parameters. Instead, the receiver can independently define the start and stop times for data collection. This

interval, known as the observation or integration time, serves the same role as a pulse width and is therefore a parameter chosen by the radar platform. It is assumed that the communication satellite IOs are transmitting during this observation period. Although, in practice, these satellites do not operate with a 100% duty cycle and their activity depends on user demand, this variability does not affect the ability of the receiver to set its own effective pulse width, or observation time.

4.1.3 Payload design

One of the primary constraints on the size, weight, and power consumption of a CubeSat is the antenna. In the absence of such limitations, a promising candidate would be a massive array of Vivaldi antennas [97]. The key advantage of this design lies in the exceptionally wide bandwidth of the Vivaldi elements, which would allow a single radar system to simultaneously receive signals across multiple frequency bands transmitted by different OneWeb constellation satellites. Capturing a greater number of FS signals from diverse IOs would markedly enhance the SSA capabilities of the system by enabling multi-static, multi-perspective, and multi-frequency observations, leading to richer target characterization and improved localization accuracy. Vivaldi arrays typically suffer from lower aperture efficiency, meaning that their physical size is large relative to their directivity. They also produce higher side lobes than narrowband arrays, which increases the complexity of beamforming. Nevertheless, in the absence of hardware constraints, the benefit of simultaneous multi-band reception could outweigh these limitations. The physical size of such arrays ultimately prevents their integration into a CubeSat platform.

To meet the size limitations of a 1U CubeSat, the antennas will be designed accordingly. They will operate at 11.075 GHz, which corresponds to the centre frequency of the second 250 MHz channel of the OneWeb constellation. Additionally, a steering beam For this analysis the following antennas will be considered:

- Patch antenna
- Array of patch antennas

- 3-Dimensional Phased Array Antenna (3D-PAA)
- Phased Array of Monopoles (PAM)

It must be mentioned that the patch antenna, the array of patch antennas and the PAM are analysed using the antenna toolbox from MATLAB, which uses the theory in [98], and the mathematical formulas for the antennas, introduced in Section 4.1.3.1. The 3D-PAA is going analysed only using the mathematical formulas due to its more complex design.

The design and characterization of patch antennas and monopoles, as well as their array implementations, are well established and not novel in themselves. Numerous examples of array designs employing patches and monopoles can be found in [99, 100, 101, 102]. However, the analysis of the novel 3D-PAA and PAM in a spaceborne scenario has not yet been conducted. This study seeks to address that gap and to demonstrate that monopole arrays are strong candidates for spaceborne applications.

4.1.3.1 Antenna theory

As some of the antennas have been designed using MATLAB, to check and cross-validate the results, the parameters of the antennas are also going to be calculated using the mathematical formulas for the antennas and numerical methods.

4.1.3.1.1. Image theory for the ground plane

A common method to decrease the antenna size is to use a ground plane. The ground plane mirrors the currents of the real antenna [97]. It would be similar to having a *mirror* antenna. For a perfect electric conductor ground plane, the image currents are created by mirroring in $z = 0$ [97]:

$$\mathbf{r}'_{\text{image}} = (x, y, -z), \tag{4.2}$$

with the current phase conjugation and sign reversal being:

$$\begin{aligned} I_{x,\text{image}} &= -\text{conj}(I_x), \\ I_{y,\text{image}} &= -\text{conj}(I_y), \\ I_{z,\text{image}} &= -\text{conj}(I_z). \end{aligned} \tag{4.3}$$

4.1.3.1.2. Computation of radiations fields

Once the currents of the antenna have been computed, the radiation pattern of the electric field is calculated. The radiation pattern is given in Cartesian components using the discretized radiation integral as [98]:

$$\mathbf{E_{rad}}(\hat{r}) = \frac{j\eta k}{4\pi} \sum_{n=1}^{N} I_n \Delta l_n \Big[(\hat{\mathbf{l}}_n \times \hat{r}) \times \hat{r} \Big] e^{jk\hat{r}\cdot\mathbf{r}_n}, \tag{4.4}$$

where:

- I_n is the complex current of segment n,
- Δl_n is the segment length $(\Delta x, \Delta y, \Delta z)$,
- $\hat{\mathbf{l}}_n$ is the segment direction vector $(\hat{x}, \hat{y}, \hat{z})$,
- $\mathbf{r}_n$ is the segment position,
- $\hat{\mathbf{r}}$ is a unitary vector in the observation direction.

The electrical field is computed in Cartesian using the currents in the x component. The process is repeated for the y component of the currents and the images of the x and y currents. The total electric field is a result of adding all the electrical fields. The electrical field is then projected from the Cartesian basis to the spherical basis:

$$\begin{aligned} E_\theta &= E_x \cos\theta \cos\phi + E_y \cos\theta \sin\phi - E_z \sin\theta, \\ E_\phi &= -E_x \sin\phi + E_y \cos\phi, \\ E_r &= 0. \end{aligned} \tag{4.5}$$

It should be noted that as the far field approximation is being used: $E_r = 0$

4.1.3.1.3. Finite Ground Plane Effect

The finite ground plane effect is modelled using aperture diffraction theory [103]:

$$G(\theta, \phi) = \text{sinc}\left(\frac{L_g k \sin\theta\cos\phi}{2\pi}\right) \cdot \text{sinc}\left(\frac{W_g k \sin\theta\sin\phi}{2\pi}\right), \tag{4.6}$$

with L_g and W_g are length and width of the ground plate. The total fields are modified as:

$$E_{\theta,G} = E_\theta \cdot G(\theta, \phi), \qquad E_{\phi,G} = E_\phi \cdot G(\theta, \phi). \tag{4.7}$$

Naturally, the component in the radial axis will still be 0. Then, the Cartesian components of the electric field are computed again, as:

$$\begin{aligned} E_x &= E_{\theta,G}\cos\theta\cos\phi - E_{\phi,G}\sin\phi, \\ E_y &= E_{\theta,G}\cos\theta\sin\phi + E_{\phi,G}\cos\phi, \\ E_z &= -E_{\theta,G}\sin\theta. \end{aligned} \tag{4.8}$$

4.1.3.1.4. Radiation Intensity and Directivity

The radiation intensity is computed as [98]:

$$U_{ant}(\hat{r}) = \frac{1}{2\eta_{ant}}\left(|E_x(\hat{r})|^2 + |E_y(\hat{r})|^2 + |E_z(\hat{r})|^2\right), \tag{4.9}$$

where η_{ant} is the impedance in the free space, which values is: $376.730\,313\,412\,\Omega$. The total radiated power is:

$$P_{rad} = \int_{\hat{r}} |U_{ant}(\hat{r})|^2 \, d\hat{r}. \tag{4.10}$$

The directivity pattern is:

$$D_{ant}(\hat{r}) = \frac{U_{ant}(\hat{r})}{\frac{1}{4\pi}P_{\text{rad}}}. \tag{4.11}$$

4.1.3.1.5. Radiation array factor

The directivity pattern of the antenna is going to be calculated using a two-step process that starts with the Radiation Array Factor (RAF). The RAF approach is valid if the following conditions are met [98]:

1. All the antenna elements are the same.

2. All the antenna elements are oriented in the same direction.

3. The signal phase shift between antenna elements is constant.

The RAF is computed as [98]:

$$RAF(\hat{r}) = \sum_{a=0}^{N_{el}-1} c_a e^{jk\hat{r}\,\vec{r}_a}, \tag{4.12}$$

where, $\hat{r}$ is the unit position vector pointing to the position of interest, N_{el} is the number of elements in the array, $\vec{r}_A$ is the position vector of element a, k is the wavenumber, $k = \frac{2\cdot\pi}{\lambda}$, and c_a is the complex-valued excitation coefficient of element a.

For a uniform linear array, where the elements are equally spaced and aligned along a straight line, the RAF can be expressed as [97].:

$$RAF_{ul} = \sum_{a=1}^{N_{el}} e^{j(a-1)(kd_{ul}\cos\theta_{ul}+\beta_{ul})}, \tag{4.13}$$

k denotes the wavenumber, d_{ul} the spacing between antenna elements, θ_{ul} the elevation angle at which the RAF is evaluated, and β_{ul} the inter-element phase shift. From (4.13), it can be deduced that the maxima of the RAF occur when:

$$\psi_{ul} = kd_{ul}\cos\theta_{ul} + \beta_{ul} = 2\pi \cdot m_{ul}, \tag{4.14}$$

with m_{ul} being an integer. Consequently, the main lobe is obtained at $\psi_{ul} = 0$, while the first grating lobes appear at $\psi_{ul} = \pm 2\pi$.

If the main lobe is required in the broadside direction of the antenna, i.e. $\theta_{ul} = 90°$, then $\beta_{ul} = 0$. This implies that no phase shift is needed to place the main lobe along the antenna normal. Conversely, if the main lobe is to be steered to a different elevation angle, a phase shift of $-kd_{ul}\cos\theta_{st}$ must be applied, where θ_{st} denotes the desired steering angle. In general, the first grating lobes are set at $\theta_{ul} = \{0, \pi\}$, to avoid unwanted interference. Consequently, the maximum steering angle can be determined

by solving for θ_{st} such that the first grating lobe coincides with π.:

$$\begin{aligned} kd_{ul}\cos\pi - kd_{ul}\cos\theta_{st,max} = -2\pi \rightarrow \cos\theta_{st,max} = \frac{\lambda}{d_{ul}} - 1 \rightarrow \\ \rightarrow \theta_{st,max} = \arccos\left(\frac{\lambda}{d_{ul}} - 1\right). \end{aligned} \tag{4.15}$$

(4.15) has been derived with respect to the elevation angle. If instead it is expressed in terms of the inclination angle, i.e., the angle measured relative to the antenna normal, then the relation can be written as:

$$\cos\left(\frac{\pi}{2} - \vartheta_{st,max}\right) = \sin\vartheta_{st,max} = \frac{\lambda}{d_{ul}} - 1 \rightarrow \vartheta_{st,max} = \arcsin\left(\frac{\lambda}{d_{ul}} - 1\right) \tag{4.16}$$

To compute the radiation pattern of the array antenna, the RAF is multiplied by the radiation pattern of one of the elements [98]:

$$U_a(\hat{r}) = D_{el}(\hat{r}) \cdot RAF(\hat{r}), \tag{4.17}$$

where U_a is the beam pattern of the array, D_{el} is the directivity patter of a single element and RAF is the radiation array factor. The final the directivity is computed using (4.11).

Now that the mathematical elements for computing the directivity from the currents in the antenna elements are known. The models of the currents for different antennas are going to be introduced.

4.1.3.1.5.1. Grating lobes

Grating lobes are the side lobes of the directivity pattern

4.1.3.1.6. Patch antenna

To estimate the size of the patch antenna first the dielectric and the height of the patch antenna must be selected. In [98] the height is chosen to be:

$$h_p \ll \lambda. \tag{4.18}$$

To fulfil this condition, the height is going to be chosen as 1% of the wavelength:

$$h_p = 0.01 \cdot \lambda. \tag{4.19}$$

The width and length of the patch are computed as [98]:

$$\begin{aligned} W_p &= \frac{c}{2f_r}\sqrt{\frac{2}{\epsilon_r + 1}}, \\ L_p &= \frac{c}{2f_r\sqrt{\epsilon_{reff}}} - 2\Delta L_p, \end{aligned} \tag{4.20}$$

with:

- f_r is the resonance frequency, or the desired transmitting or receiving frequency of the antenna,
- ϵ_r is the relative permittivity,
- ϵ_{reff} is the effective permittivity, calculated as [98]:

$$\epsilon_{reff} = \frac{\epsilon_r + 1}{2} + \frac{\epsilon_r - 1}{2}\left[1 + 12\frac{h_p}{W_p}\right]^{-1/2}, \tag{4.21}$$

- ΔL is length extension that accounts for the fringing fields that electrically elongate the patch. It is computed as [98]:

$$\Delta L = 0.412\ h_p \frac{(\epsilon_{reff} + 0.3)\left(\frac{W_p}{h_p} + 0.264\right)}{(\epsilon_{reff} - 0.258)\left(\frac{W_p}{h_p} + 0.8\right)}, \tag{4.22}$$

If $kh_p \ll 1$, then electrical field of the patch antenna can be computed as [98]:

$$E_{p,\phi} \approx j\frac{2V_0 e^{-jkr_p}}{\pi r_p}\left\{\sin\theta_p \frac{\sin\left(\frac{kW_p}{2}\cos\theta_p\right)}{\cos\theta_p}\right\}\cos\left(\frac{kL_{eff}}{2}\sin\theta_p \sin\phi_p\right), \tag{4.23}$$

where

- $V_{p,0} = h_p \cdot E_{p,0}$ is the voltage across the slot,

- ϕ_p and θ_p are the azimuth and inclination angles,
- r_p is the distance from the antenna to the observation point.

4.1.3.1.7. Dipole antenna

As per [98], the size of the monopole is chosen to be comparable to half of the size of the wavelength:

$$L_{dp} \approx \frac{\lambda}{2}. \tag{4.24}$$

The current distribution on a thin, centre-fed dipole of length L_{dp} is given by:

$$I_{dp}(z) = I_0 \sin\left[k\left(\frac{L_{dp}}{2} - |z|\right)\right], \quad \text{for } |z| \leq \frac{L_{dp}}{2}, \tag{4.25}$$

where:

- $I_{dp}(z)$ is the current at position z,
- I_0 is the current maximum,
- L_{dp} is the total length of the dipole.

4.1.3.1.8. Inverted-L monopole antenna

The inverted-L monopole is comprised of the ground plane, the vertical arm of size h_m connected to the feed, and the horizontal arm of size L_m connected to top of the vertical arm. Since it is a monopole, the total size of the antenna will be [98]:

$$L_m + h_m \approx \frac{\lambda}{4}. \tag{4.26}$$

As stated in [104], to achieve maximum directivity at higher elevation angles, the lengths of the vertical and horizontal arms are chosen as 33% and 67% of the total antenna length, respectively:

$$\begin{aligned} L_m &\approx 0.67 \cdot \frac{\lambda}{4}, \\ h_m &\approx 0.33 \cdot \frac{\lambda}{4}. \end{aligned} \tag{4.27}$$

The current in an inverted-L monopole is modelled for a wire of radius a_m as [105]:

$$\begin{aligned} I_{z,m}(z) &= I_o\left(1-\frac{|z|}{h_m+L_m}\right) \text{ for } -h_m \le z \le h_m, \\ I_{x,m}(x) &= \pm I_o\left(1-\frac{x-a_m+h_m}{h_m+L_m}\right) \text{ for } -a_m \le z \le L_m+a_m, \end{aligned} \tag{4.28}$$

with the $\pm$ sign also models the currents in the monopole and its mirror.

4.1.3.2 Patch antenna

The patch antenna consists of a single rectangular metal patch. The advantages of using a patch antenna include low volume, size, weight, cost and processing power. Additional advantages include easier design and fabrication and a robust mounting. In the radar processing side the design will be more simple, since only one receiving structure is needed. The overall antenna will have an area of $10 \times 10\,\text{cm}^2$, Figure 4.3, which would fit into a 1U CubeSat. The radiating part of the antenna has an area of $4 \cdot W_p \times 4 \cdot L_p$, where W_p and L_p have been taken from (4.20). The patch is several times more the theoretical width and length, so the directivity of the antenna is comparable to the directivity of the other cases. Therefore, the final size of the antenna is: $5.24 \times 5.4\text{cm}^2$.

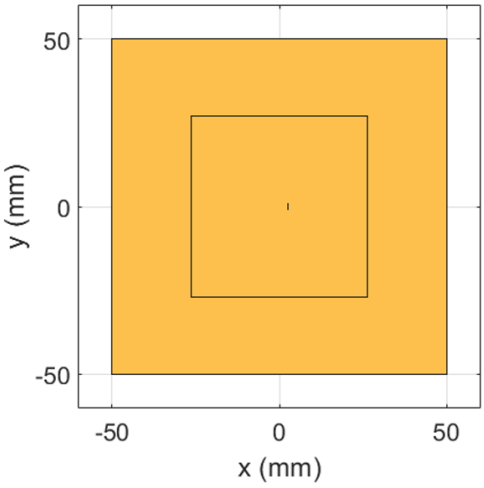

Figure 4.3: Single patch antenna

The maximum directivity gain for this antenna design is 12.54 dBi. Figure 4.4 shows that there are six main lobes, four on the crest-like shape and two to the sides of it.

The multiple illuminators of the constellation in combination with the multiple lobes will contribute to a higher probability of detecting space objects. However, if there were multiple space objects, the shape of the directivity could lead to a higher ambiguity in the detection and motion parameter estimation of the targets.

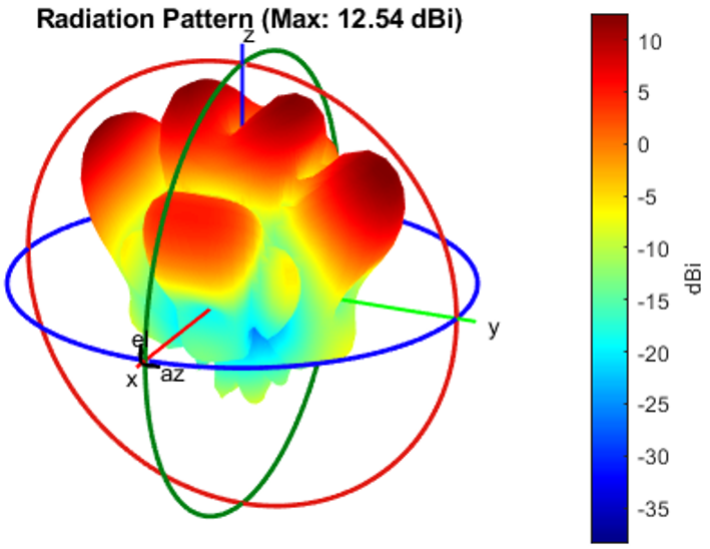

Figure 4.4: Directivity pattern of the patch antenna using MATLAB

The directivity is recomputed using the formulas from Section 4.1.3.1, and the resulting pattern is shown in Figure 4.5. For clarity of observation and analysis, this figure and the following ones derived from the formulas are plotted on a sphere. The maximum directivity is 10.29 dBi, 2.25 dBi less than the result from MATLAB. However, unlike the MATLAB simulation, the pattern exhibits five main lobes, there is one wide lobe at the top of the pattern, while the MATLAB pattern shows two. If this antenna were selected, a more detailed study would be required to understand the discrepancies between the two results and to obtain a reliable directivity model.

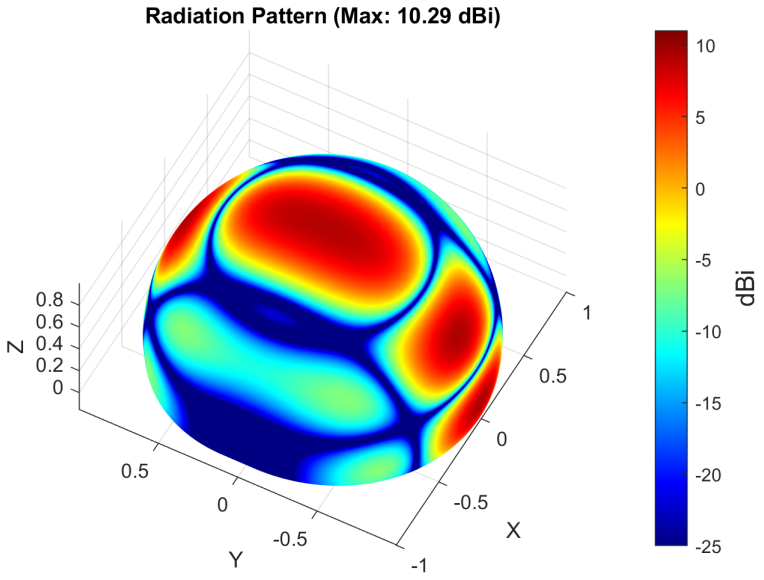

Figure 4.5: Directivity pattern of the patch antenna using the formulas

4.1.3.3 Array of patch antennas

The array is composed of 16 patch antennas arranged in a 4×4 configuration, as illustrated in Figure 4.6. This design retains several advantages of a single patch antenna, such as low profile, compact size, light weight, and cost efficiency. Like the single patch, it also ensures mechanical robustness and ease of fabrication. Moreover, the array offers an additional advantage, its ability to electronically or digitally scan the surrounding environment.

As shown in Figure 4.6, the antenna array occupies an area of $10 \times 10\,\mathrm{cm}^2$, making it suitable for integration into a 1U CubeSat. Each patch element measures $1.31 \times 1.35\,\mathrm{cm}^2$ with a height of $270.69\,\mu\mathrm{m}$, calculated using (4.19) and (4.20). According to [106], a spacing of 0.7λ enhances the maximum directivity at higher elevation angles. In this design, a slightly smaller spacing of 0.67λ was selected as a trade-off to suppress the sidelobes. Consequently, the row and column spacing between adjacent patches is $1.8\,\mathrm{cm}$, measured from the centre of one patch to the centre of the next. The directivity pattern is evaluated for two steering angles: $0°$ and $30°$. The latter was derived using (4.16) with $d_{ul} = 0.67\lambda$ and also ensures compliance with the tracking capabilities

required by the system.

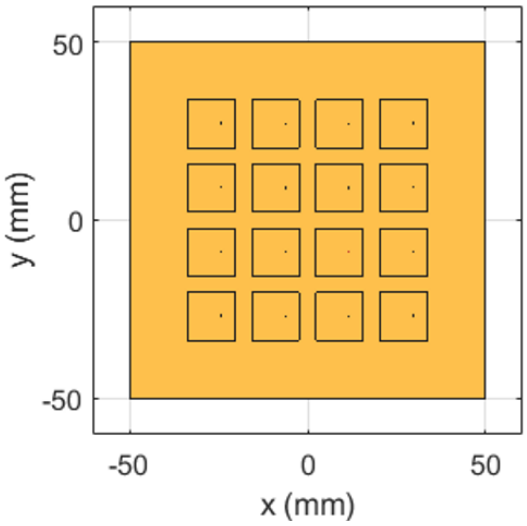

Figure 4.6: Array of patch antennas

Figure 4.7 presents the directivity patterns obtained using MATLAB. The maximum directivity gain is 19.77 dBi for a 0° steering angle, and 18.36 dBi for a 30° steering angle, indicating a small loss of only 1.41 dB due to beam steering. Unlike a single patch antenna, the array exhibits a single main lobe, reducing ambiguity in the target location. It should be noted, however, that implementing a phase shift increases the sidelobe levels.

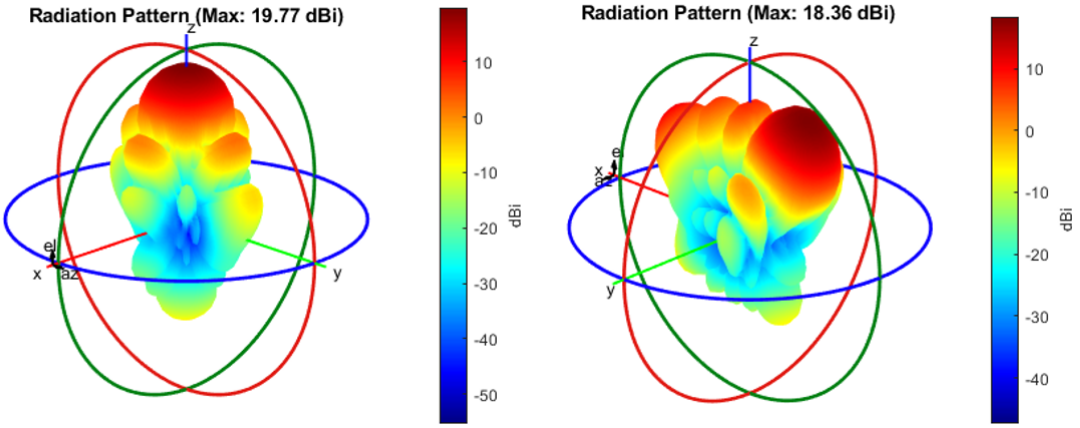

(a) No beam steering (b) Beam steering of 30°

Figure 4.7: Directivity patterns for array of patch antennas using MATLAB

Figure 4.8 presents the directivity patterns of the patch antenna array for different steering angles. The formula-based results yield maximum directivities of 20.52 dBi without beam steering and 19.10 dBi with beam steering, corresponding to errors of 0.62 dBi and 0.70 dBi, respectively. For both the non-steered case, Figure 4.8a, and the steered case at 30°, Figure 4.8b, the sidelobe levels are consistent between MATLAB and the analytical formulas. Since the beam shapes agree and the directivity differences are minor, the MATLAB results can be considered validated.

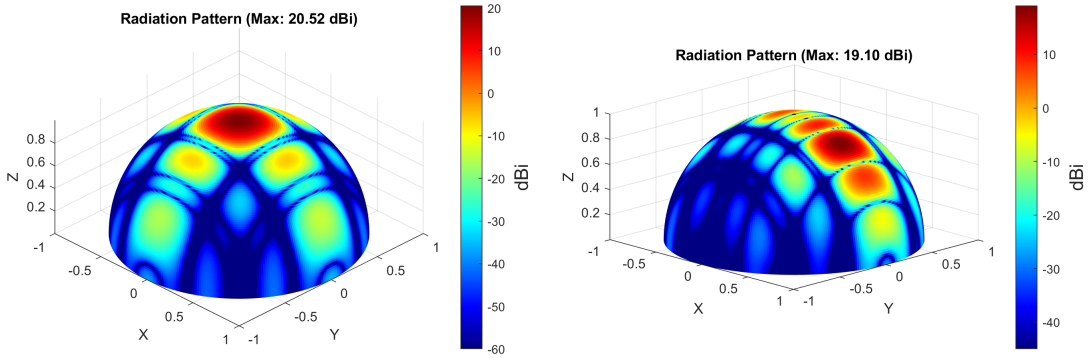

(a) No beam steering (b) Beam steering of 30°

Figure 4.8: Directivity patterns for array of patch antennas using formulas

4.1.3.4 3-dimensional phased array antenna (3D-PAA): dipoles within poles

This is a novel antenna developed by Nobuyuki Kaya [107]. Originally, it was designed to be used as a ground-based antenna to receive different communications signals from multiple satellites, as per [107], using digital beamforming, Figure 4.9a. Some advantages of using such antenna will be that it can electronically or digitally scan the environment. Additionally, in theory, the 3D-PAA has an improved directivity compared to the other examined antennas.

The designed antenna occupies a volume of 1U, measuring $10 \times 10 \times 10\,\text{cm}^3$, and consists of 49 elements arranged as shown in Figure 4.9b. A hexagonal base shape has been selected to ensure uniform separation between all poles. It should be noted that, in Figure 4.9b, the poles shown in blue are not connected to the feed; only the horizontal dipoles, highlighted in red, are fed. It is assumed that each dipole receives the same

feed without any delay or unwanted phase mismatch. Furthermore, although the poles are made up of dipoles, they do not constitute Yagi antennas, as the dipoles act as radiating antenna elements and not as reflector or director rods.

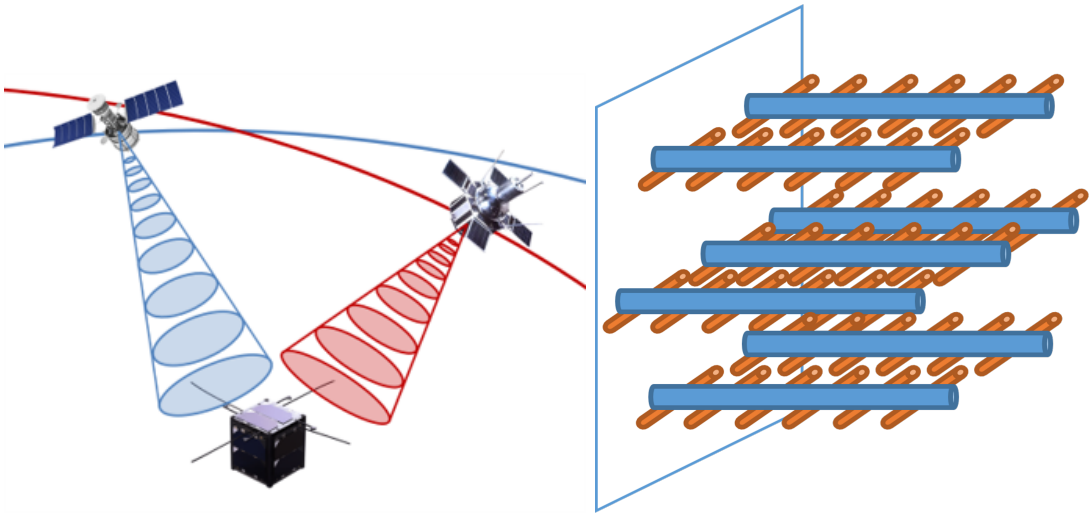

(a) Digital beamforming technology (b) 3D-PAA design

Figure 4.9: 3D-PAA design with digital beamforming technology

The dipoles have a length of 12.81 mm, calculated using (4.24). Due to the novelty of the antenna, the maximum directivity was evaluated for different spacing values, and the configuration that provided the highest directivity while fitting within 1U was selected, as shown in Figure 4.10. Consequently, the separation between dipoles within a pole is $0.6\lambda = 1.62$ cm, and the separation between poles, i.e. the side of the hexagonal base, is $1.85\lambda = 5$ cm. The spacing of 1.9λ from Figure 4.10 was not selected, as it would exceed the 1U volume constraint; therefore, the spacing was slightly reduced.

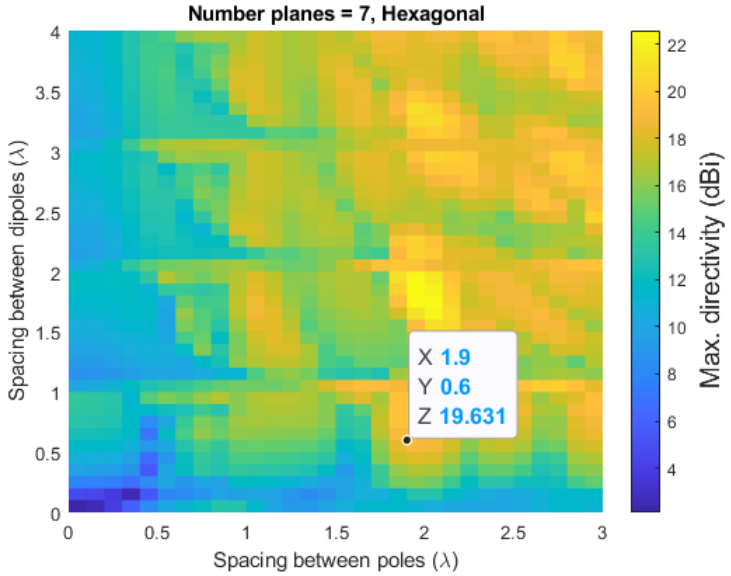

Figure 4.10: Maximum directivity for different spacing values

The directivity of the 3D-PAA is calculated as described in Section 4.1.3.1, where the RAF approach is applicable since the required conditions are satisfied. The maximum directivity without beam steering is 19.5 dB, while steering the beam to 30° reduces the directivity to 17.3 dB, corresponding to a loss of 2.2 dB. Unlike the patch antenna array, this loss is relatively high. As shown in Figure 4.11a and Figure 4.11b, the antenna exhibits noticeably high back lobes. These are partly attributable to the fact that the CubeSat structure was not included in the simulation, even though its presence would clearly influence the radiation pattern. Nevertheless, the back lobes are not expected to cause significant issues, as no signals of interest are anticipated from behind the antenna. If the 3D-PAA were selected, however, the radiation pattern would need to be recalculated with the CubeSat included in the model. Should the back-lobe issue persist, an additional mitigation strategy could involve placing electromagnetic absorbing material on the rear side of the antenna to suppress unwanted signals.

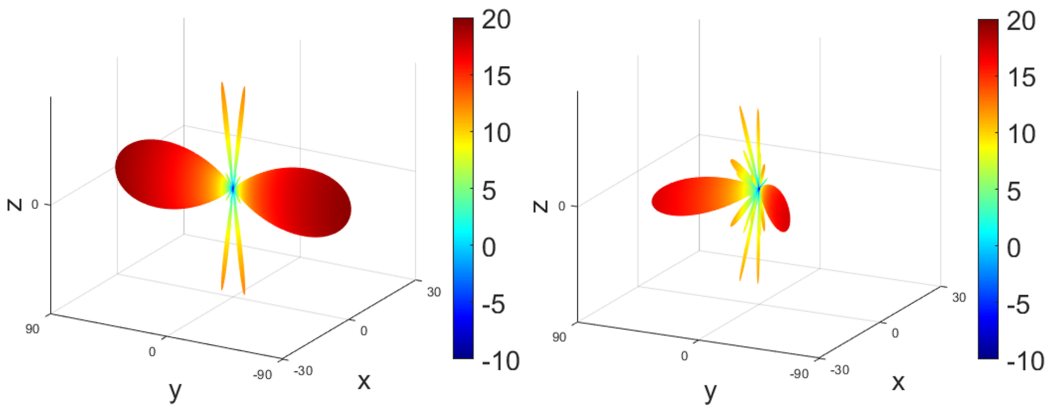

(a) No beam steering (b) Beam steering of 30°

Figure 4.11: Directivity pattern of 3D-PAA

4.1.3.5 Trade-off: phased array of monopoles (PAM)

A trade-off between the 3D-PAA and the array of patches is the phased array of monopoles (PAM). For the design of the PAM, the chosen antenna elements of the array are inverted-L monopole antennas [108, 109]. Some of the advantages of the inverted-L monopole over the simple monopole are the compact design and tunability [110]. A detailed view on the size of the used inverted-L antenna can be found in Figure 4.12.

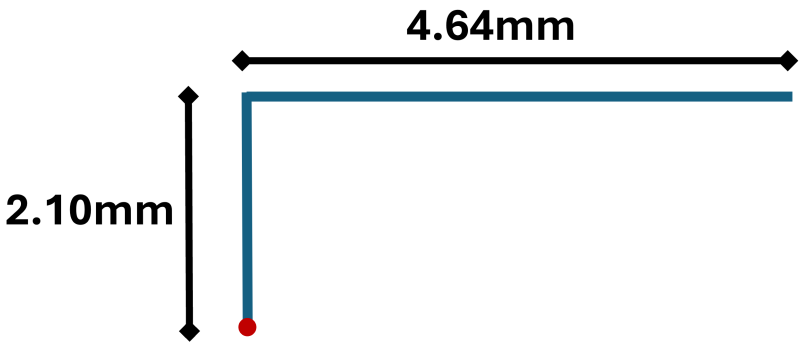

Figure 4.12: Measurements of the inverted-L monopole

The monopole features a height of 2.10 mm and a length of 4.64 mm, as specified by (4.27). Its width is 299.44 µm, a dimension chosen to be significantly smaller than the operating wavelength. 49 inverted-L antennas, Figure 4.13b, have been arranged in a 7×7 matrix as in Figure 4.13a. The antenna will have a total volume of $10\times10\times0.21\,\text{cm}^3$.

Since, there are many elements, it is expected to have a higher gain than the array of patches, therefore the row and column spacing between the elements is $\lambda/2 = 1.35\,\text{cm}$.

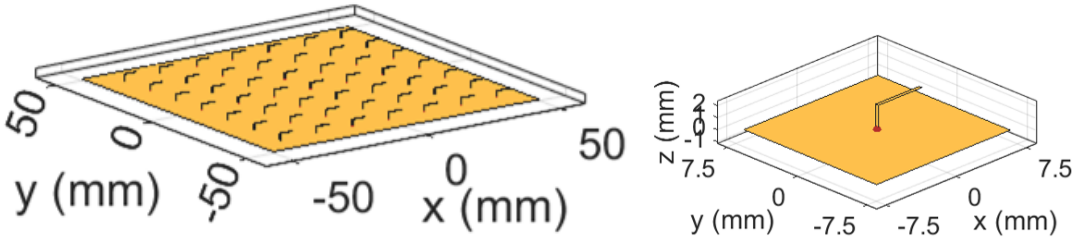

(a) PAM (b) Element of PAM

Figure 4.13: PAM

Similarly to the patch antenna, the inverted-L array antenna has been designed using the Antenna Toolbox from Matlab, which uses the theory of [98]. A beam steering angle of 30° is going to be implemented to be able to scan the environment.

Figure 4.14a and Figure 4.14b show the directivity pattern of the PAM. The computations show that without a phase shift, the directivity is 20.19 dBi. If there is a phase shift of 30°, the directivity is 19.58 dBi, a degradation of 0.6 dB, practically unnoticeable. The advantages over the rest of antennas are the improved directivity and the smaller sidelobes, which would increase the accuracy of the position of the detected target.

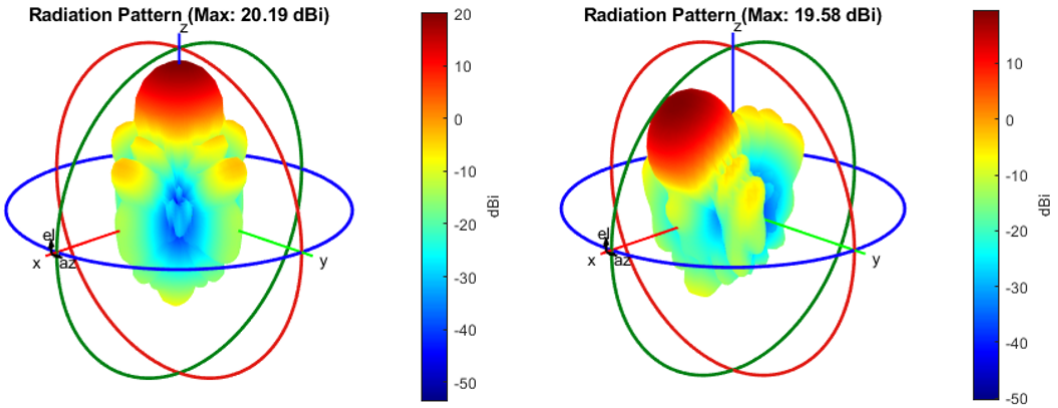

(a) No beam steering (b) Beam steering of 30°

Figure 4.14: Directivity pattern of PAM

As in the previous cases, the directivity patterns are recalculated using the formulas in Section 4.1.3.1, with the results shown in Figure 4.15. The maximum directivity is 20.33 dBi without beam steering and 19.49 dBi with a steering angle of 30°. The corresponding errors, 0.14 dB and 0.10 dB, are negligible. The overall shapes closely match those obtained in MATLAB. Although the sidelobe levels are higher than in the patch array case, they remain between 0 dB and −10 dB, which indicates minimal impact on the overall performance of the antenna. As these results are consistent with the MATLAB results, the antenna directivity pattern is validated.

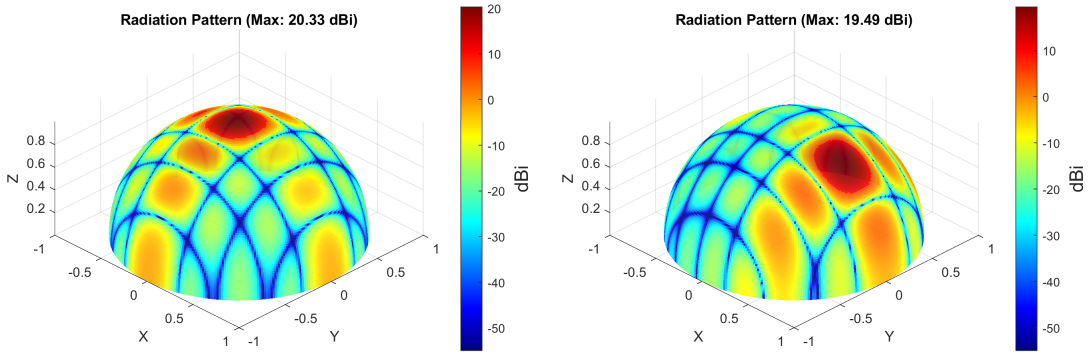

(a) No beam steering (b) Beam steering of 30°

Figure 4.15: Directivity pattern of PAM using the formulas

Similarly to the array of patches, the advantages of the PAM over the 3D-PAA are the simpler design, easier to manufacture and mount robustness. Since the PAM is used as a trade-off, the PAM is going to be used in the RRE analysis instead of the 3D-PAA.

	Beam steering angle	
	0°	30°
Patch antenna	12.54 dBi	-
Array of patch antennas	19.77 dBi	18.36 dBi
3D-PAA	19.5 dBi	17.3 dBi
PAM	20.19 dBi	19.58 dBi

Table 4.2: Directivity gain for different antennas and beam steering angles

4.1.4 RRE analysis

In order to assess the detection capabilities of the proposed spaceborne system, in which we consider the payload selected in the previous section, the RRE is used. Since a bistatic approach is being used, the RRE from Section 2.2.5 is going to be employed with some changes:

$$SNR = \frac{EIRP\ G_r\ G_{sp}\ \lambda^2\ \sigma_{FS}}{(4\pi)^3\ R_1^2\ R_2^2\ k_n\ T_0\ F\ B_w\ L_s} \cdot K_{np}, \tag{4.29}$$

where:

- $EIRP$ is the effective isotropic radiated power, which is $EIRP = P_t \cdot G_t$.
- G_r is the receiver gain. Defined as the directivity gain of the receiver antenna, $G_{r,ant}$, and the low noise amplifier (LNA) gain, G_{LNA}.
- G_{sp} is the signal processing gain. This is approximately given by the product between the transmitted pulse length and the transmitter bandwidth as seen in (2.47). Since the IOs are the OneWeb constellation satellites, assuming that the satellites are constantly transmitting, a pulse length of 0.5 s is chosen.
- K_{np} is the multiple integration factor, which is either n_p or $\sqrt{n_p}$, depending on whether the multiple integration, as shown in Section 2.2.5, is coherent or non-coherent, respectively.
- σ_{FS} is the forward scatter cross section as defined in (4.1).

4.1.4.1 SNR fluctuations

Before examining the minimum detectable size, it is important to first consider how fluctuations in the bistatic ranges and the FS-CS influence the SNR. In a monostatic radar, the integration time is essentially the period during which the target remains within the same range bin and, for coherent integration, within the same Doppler bin. In this case, however, the signal of interest is not a conventional radar signal but an interference signal, which means that standard range bin analysis cannot be applied.

Instead, a more suitable approach is to study how variations in the target altitude affect both the SNR and the observation time. The observation time, which depends on the antenna used, will be examined in Section 4.1.6.

For a SNR variation of $\pm 3\,\mathrm{dB}$, the product $R_1 R_2$ would have to be reduced or incremented by a factor of $\sqrt{2}$:

$$\begin{aligned} SNR_{FS} \cdot 2 \rightarrow 2 \cdot \frac{1}{R_1^2 R_2^2} &= \frac{1}{\left(\frac{R_1 R_2}{\sqrt{2}}\right)^2}, \\ SNR_{FS} \cdot \frac{1}{2} \rightarrow \frac{1}{2} \cdot \frac{1}{R_1^2 R_2^2} &= \frac{1}{\left(\sqrt{2} R_1 R_2\right)^2}. \end{aligned} \tag{4.30}$$

To determine how much the altitude must change to produce a variation of either $\sqrt{2}$ or $\left(\sqrt{2}\right)^{-1}$, the altitude is first fixed and then variated. The ratio is then obtained by comparing the original product $R_1 R_2$ with the modified product $(R_1 + \Delta R)(R_2 - \Delta R)$.

Figure 4.16 shows the ratio results for different altitude changes. The blue region marks where the ratio drops below $1/\sqrt{2}$, while the red region indicates where it exceeds $\sqrt{2}$. For example, at an altitude of 882 km, a decrease of 308 km increases the product $R_1 R_2$ by a factor of 2.62, leading to an equivalent reduction in the SNR. Conversely, at 588 km, an increase of 231 km raises the SNR by a factor of $1/0.44 = 2.27$. The figure also shows that substantial altitude variations are generally required to cause large SNR fluctuations. However, when the target is orbiting close to either the receiver or the transmitter, even relatively small altitude changes, on the order of 3.5 km, can produce significant effects on the SNR. For the assumed integration time of 0.5 s, this would correspond to an altitude change rate of about 7 km/s, which is unrealistic for LEO orbits given their typically very low eccentricity.

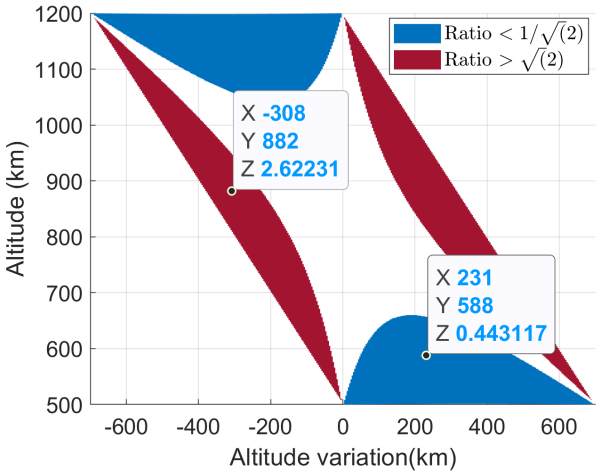

Figure 4.16: Variation ratios resulting from changes in altitude

The FS-CS would be affected by the type of target. Certainly, if the target is spheric, the FS-CS will not change. Therefore, the target to analyse will be a cube, more concretely it will be analysed how a rotating cube influences σ_{FS} and, consequently, the SNR. To this end, the scenario shown in Figure 4.17 is considered, where the target is modelled as a cube rotating with angular velocity ω_{rot} in the xy-plane of Figure 3.3. In this configuration, the receiver consistently perceives a rectangular area, Figure 4.17b.

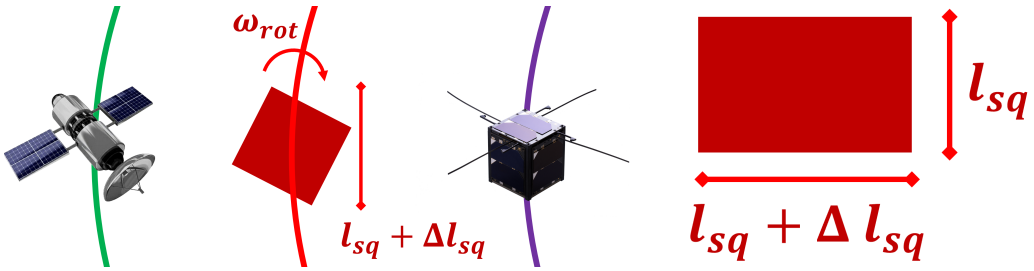

(a) Rotating target (b) Perceived shape and size

Figure 4.17: Perceived shape and size when a cube target is rotating

The base of the rectangle can be computed as:

$$b_{trg} = l_{sq} + \Delta l_{sq} = l_{sq} \cdot (\sin \alpha_{rot} + \cos \alpha_{rot}), \tag{4.31}$$

where l_{sp} is the side of the cube, and α_{rot} is the angle of rotation. Consequently, the

perceived area can be computed as:

$$A_{trg} = l_{sq} \cdot b_{trg} = l_{sq}^2(|\sin\alpha_{rot}| + |\cos\alpha_{rot}|). \tag{4.32}$$

If a variation of $\pm 3\,\mathrm{dB}$ of the FS-CS is considered large enough for the RRE analysis to become invalid, then, as the wavelength is constant, the area would have to increase by a factor of $\sqrt{2}$, as in:

$$\sigma_{FS} \cdot 2 = \frac{4\pi\left(A_{trg}\sqrt{2}\right)^2}{\lambda^2}. \tag{4.33}$$

An increment of $\sqrt{2}$ would correspond to an angle of 45°. As the integration time is 0.5 s, the target would have to be rotating at $\omega_{rot} = 45/0.5 = 90\,\mathrm{deg/s} = \frac{\pi}{2}\mathrm{rad/s}$.

4.1.4.2 Minimum detectable size

For the RRE analysis, for the sake of simplicity, it will be assumed that the directivity of the antenna will be the same as the antenna gain, and the target is modelled as a perfect conductive sphere. In this case, the silhouette of the sphere corresponds to the area of a circle:

$$A_c = \pi r_c^2. \tag{4.34}$$

Combining (4.1), (4.29) and (4.34), the minimum detectable size is obtained:

$$r_{trg} = 2\sqrt[4]{\frac{SNR\ R_1^2\ R_2^2\ k\ T_0\ F\ B_w\ L_s}{EIRP\ G_r\ G_{sp}\ K_{np}}}, \tag{4.35}$$

where r_{trg} is the radius of the assumed sphere. The parameters used for the calculation of the minimum detectable size are summarized in Table 4.3. The target SNR is set at 20 dB, which is sufficient to guarantee reliable detection. The LNA gain is 40 dB, a value reported as achievable in spaceborne implementations [111, 112]. System noise characteristics, including the noise figure and associated losses, are adopted from [113], resulting in a total noise temperature of 3570 K. Using (4.36), where T_s denotes the system temperature and T_0 the reference temperature, this corresponds to a noise figure of 11.24 dB. Operating in the space environment eliminates atmospheric losses; therefore,

total losses account only for system and polarization effects, with a combined value of $L_s = 2.5\,\text{dB}$. The number of pulses is set to $n_p = 6$, a choice that will be justified in Section 4.2.

$$F = 10 \cdot \log_{10}\left(\frac{T_s}{T_0} + 1\right). \tag{4.36}$$

EIRP	f_0	B_W	**Tx alt.**	**Rx alt.**	**Target alt.**
38.3 dBW	11.075 GHz	250 MHz	1200 km	500 km	500-1200 km

SNR	n_p	F	L_s	G_{LNA}	$G_{r,ant}$
20 dB	6	11.24 dB	2.5 dB	40 dB	[12.54; 19.77; 20.19]dB

Table 4.3: Minimum detectable size computing parameters

According to (4.35), if either $R_1 \approx 0$ or $R_2 \approx 0$, the minimum detectable size approaches zero. This implies that when the target is located near the transmitter or the receiver, the minimum detectable size becomes very small. The product $R_1^2 \cdot R_2^2$ reaches its maximum when $R_1 = R_2$, corresponding to the case where the target is near the midpoint between the transmitter and receiver orbits. Integration also influences the minimum detectable size. Since $\sqrt{n_p} \ll n_p$, non-coherent integration will yield a smaller minimum detectable size, whereas coherent integration results in a larger one for the same system parameters.

Regarding the influence of the antennas on the minimum detectable size, a higher antenna gain leads to a smaller detectable size. Consequently, the PAM, which provides the highest gain, yields the smallest minimum detectable size, followed by the patch array and the single patch antenna. Considering all factors in the RRE analysis, the smallest detectable size occurs when coherent integration is applied with the PAM. For a beam steering angle of 30°, the directivity is lower than in the case without steering, resulting in a larger minimum detectable size. Finally, since the directivities of the patch array and the PAM are similar, their minimum detectable sizes are also expected to be comparable.

Figure 4.18, Figure 4.19, Figure 4.20 and Figure 4.21 show the minimum detectable

diameter for the theoretically perfectly conductive sphere. All the cases display the maximum values of the minimum detectable sizes at an altitude of 850 km, with the receiver being at 500 km and the transmitter being at 1200 km. The plots prove that near the transmitter and the receiver the detectable sizes are very small, theoretically 0 cm.

In the non-coherent integration without beam steering, Figure 4.18, the largest minimum detectable sizes are 25 cm for the PAM and 39 cm for the patch antenna. By contrast, the coherent integration without beam steering, Figure 4.19, reduces the minimum detectable sizes to 20 cm for the PAM and 31 cm for the patch antenna. Overall, the PAM consistently achieves smaller detectable sizes, whereas the patch antenna results in larger ones, making it the less effective option.

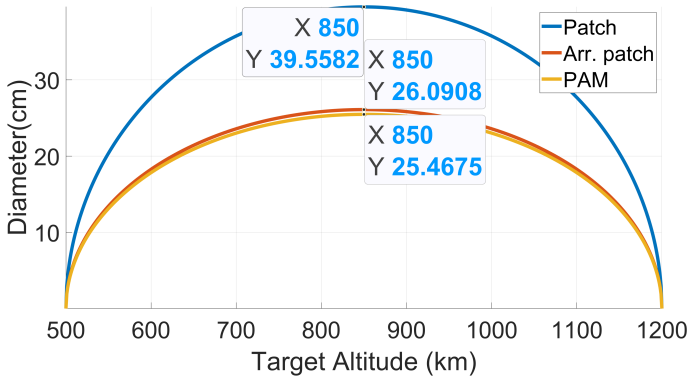

Figure 4.18: Minimum detectable size for different antennas with non-coherent integration

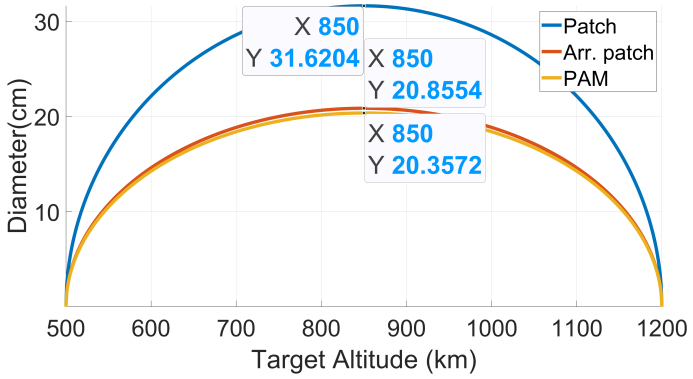

Figure 4.19: Minimum detectable size for different antennas with coherent integration

Figure 4.20 and Figure 4.21 show the minimum detectable sizes for the case where the steering of the beam is performed. As expected, the minimum detectable size has increased with respect to the previous cases. For the non-coherent integration, the value is 26.36 cm for the PAM and 28.23 cm for the array of patch antennas. In the case of coherent integration, the size is 21.07 cm for the PAM and 22.57 cm for the array of patch antennas. With the beam steering, the differences between the two antennas are more noticeable, with a difference of 1.87 cm and 1.5 cm between them.

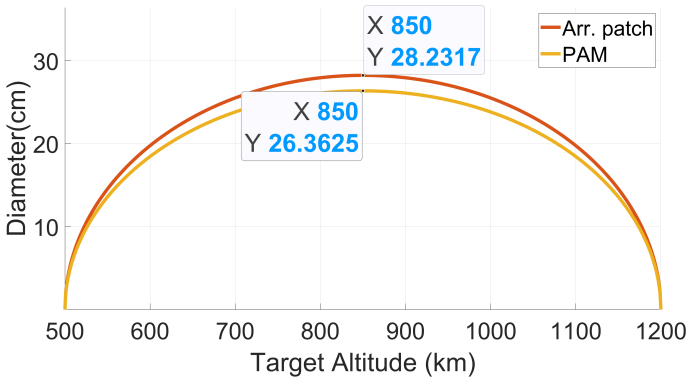

Figure 4.20: Minimum detectable size for non-coherent integration with a 30° steering

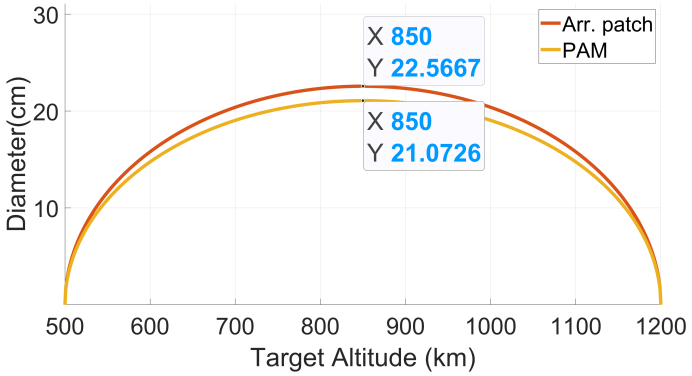

Figure 4.21: Minimum detectable size for coherent integration with a 30° steering

4.1.5 Antenna bandwidth and beamwidth

The antenna bandwidth is estimated using the reflection coefficient, the S11 parameter [114]. The S11 measures how much of the signal is returned to the antenna. The

frequency values of S11 $< -10\,\mathrm{dB}$ are generally accepted as the bandwidth [114]. As per [114], the S11 parameter is computed using the impedance of the antenna as:

$$\begin{aligned} \Gamma_{ant} &= \frac{Z_{ant} - Z_0}{Z_{ant} + Z_0}, \\ \mathrm{S}_{11}(\mathrm{dB}) &= 20 \cdot \log_{10}\left(\Gamma_{ant}\right), \end{aligned} \tag{4.37}$$

where $Z_0 = 50\Omega$, the reference impedance, Z_{ant} is the antenna impedance, and Γ_{ant} is the voltage reflection coefficient.

The closed form of the impedance of the antenna can be found in [105]. The impedance is going to be calculated for various frequencies to find the S11 for this values. As all the elements are the same, only one S11 will be computed. The value of the resistance is:

$$R_m = 15\,(k\,h_m)^2 \cdot \left(2 - \frac{h_m}{h_m + L_m}\right) \cdot \left[2 - \frac{10}{9} \cdot \frac{h_m^2 + \frac{3}{5}L_m^2 + \frac{6}{5}h_m(L_m + a_m)}{(h_m + L_m)^2}\right]. \tag{4.38}$$

Similarly, the reactance of the antenna is:

$$\begin{aligned} X_{\mathrm{in}} = \frac{-60\,h_m\left(2 - \frac{h_m}{h_m + L_m}\right)}{k\,(h_m + L_m)^2} \Bigg[& \ln\frac{\sqrt{3}\,h_m}{a_m} - \frac{1}{3} - \frac{20a_m}{9h_m} + \frac{L_a T_m - h_m/4}{\sqrt{L_a^2 + h_m^2/4}} \\ & + \frac{L_a T_m/3 - 3h_m/4}{\sqrt{L_a^2 + 9h_m^2/4}} - \frac{3k^2h_m^2}{8} + \frac{k^2h_m^2}{2}\left[\frac{1}{4} - \left(1 + \frac{L_m}{h_m}\right)^2\right]\ln\frac{\sqrt{3}\,h_m}{a_m} \\ & + \frac{k^2h_m^2}{8}\sqrt{\frac{1}{4} + \frac{L_a^2}{h_m^2}} + \frac{3k^2h_m^2}{8}\sqrt{\frac{9}{4} + \frac{L_a^2}{h_m^2}} + \frac{T_m k^2 h_m^2}{8}\ \ln\frac{L_a + \sqrt{L_a^2 + h_m^2/4}}{a_m + h_m/2} \\ & + \frac{3T_m k^2 h_m^2}{8}\ \ln\frac{L_a + \sqrt{L_a^2 + 9h_m^2/4}}{a_m + 3h_m/2}\Bigg], \end{aligned} \tag{4.39}$$

with $L_a = L_m + a_m$ and $T_m = 1 - \frac{a_m}{h_m}$.

The primary issue with the inverted-L antenna is the impedance mismatch caused by the bend. This mismatch results in a high reflection coefficient, leading to a low S11 and a reduced bandwidth. To address this problem, a matching impedance can be introduced. At $f_0 = 11.075\,\mathrm{GHz}$, the resulting impedance is: $Z_m = 8.40 - 0.72j\ \Omega$. For a reference impedance of $50\,\Omega$, the corresponding matching impedance would be:

$Z_{\text{match}} = 41.60+0.72j\ \Omega$. One straightforward approach is to use a series combination of a resistor and an inductor. While the inductor is lossless, the resistor dissipates power, which reduces the radiated power. An alternative approach is to design a transmission line with a stub [115]. At such high frequencies, the transmission line and stub are physically small, making this a practical solution.

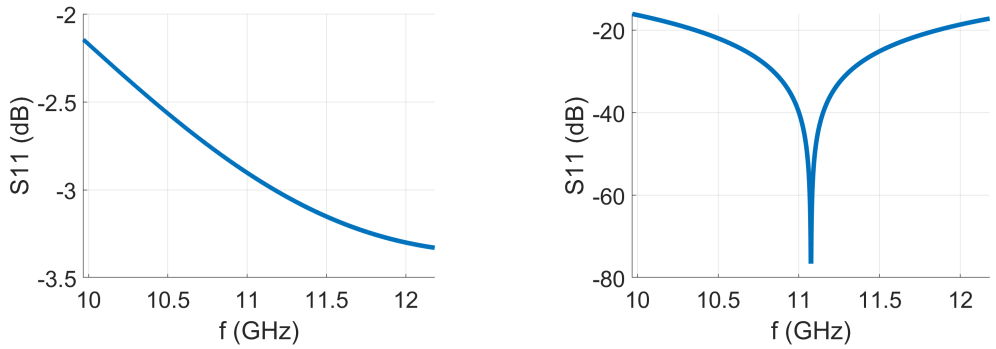

(a) No impedance matching (b) With impedance matching

Figure 4.22: S11 parameter for the PAM

Figure 4.22 shows the S11 parameter for the antenna element, both with and without impedance matching. Without matching, Figure 4.22a, the S11 is approximately $-3\,\text{dB}$. With the matching impedance, Figure 4.22b, the S11 improves significantly, ranging from $-20\,\text{dB}$ to $-70\,\text{dB}$, resulting in a substantial increase in bandwidth. This demonstrates that impedance matching is an effective method for enhancing the bandwidth of the antenna. In addition, the antenna will be capable to receive the full 250 MHz bandwidth from OneWeb. A band-pass filter should be implemented to avoid interferences from the neighbouring bands.

For measuring the antenna beamwidth the zero azimuth cut of the directivity pattern is going to be shown. From it, the $-3\,\text{dB}$ beamwidth will be estimated. The cases of $0°$ and $30°$ steering will be shown.

Figure 4.23 shows the zero azimuth beam patterns for the chosen PAM antenna. Figure 4.23a shows the case where there is no beam steering, whereas Figure 4.23b shows a $30°$ beam steer. For the first case, the $-3\,\text{dB}$ beamwidth is $20°$, and for the second case, the the $-3\,\text{dB}$ beamwidth is $22°$.

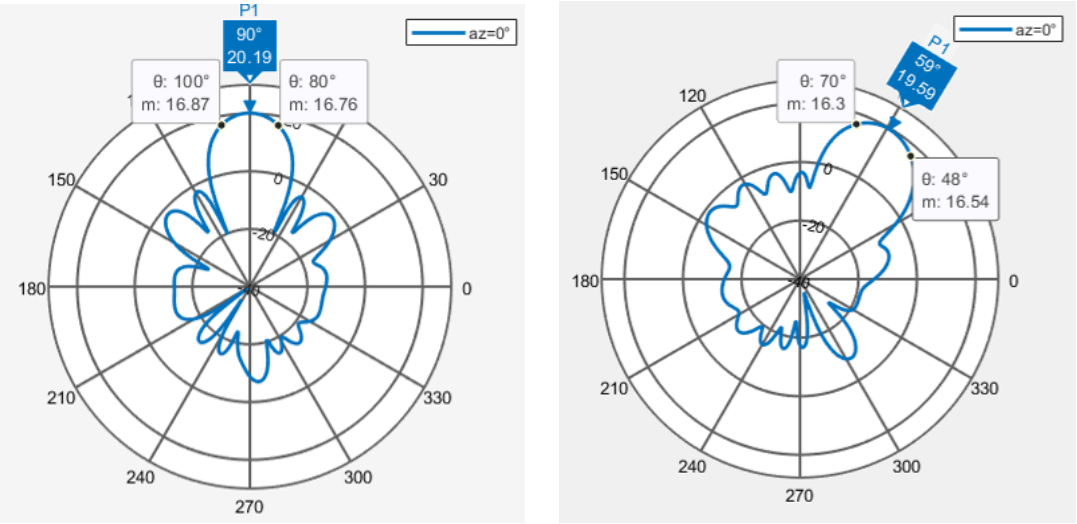

(a) Zero azimuth directivity pattern without steering

(b) Zero azimuth directivity pattern for 30° steering

Figure 4.23: Zero azimuth directivity pattern for PAM

4.1.6 Observation time

Once the antenna has been selected, the observation time can be computed. It is assumed that, given the amount of OneWeb satellites and the steering capabilities of the antenna, the receiver can maintain uninterrupted signal availability. The target is assumed to remain within the $-3\,\mathrm{dB}$ beamwidth of the receiving PAM antenna, which, as shown in Section 4.1.5, is a reasonable assumption.

The FS main lobe (FSML) is the angle in which the FS signal is scattered in the forward direction. For the computation, the observation time is the time in which the receiver is in FSML of the target, as the receiver will be able to receive the resulting FS signal. The FSML is defined as [24]:

$$\theta_{FS} = \frac{\lambda}{D_{trg}}, \tag{4.40}$$

where θ_{FS} is the main lobe of the forward scatter measured in radians and D_{trg} is the diameter of the simulated sphere. In (4.40), it can be seen that the larger the target, the smaller the FSML, which would decrease the observation time.

To compute the observation time, the scenario illustrated in Figure 4.24a is consid-

ered. The field of view is assumed to be conical, and its angle can be approximated as:

$$\alpha_{FV} \approx \theta_{FS} + \theta_{-3\,\mathrm{dB}} + \theta_{st} \tag{4.41}$$

with $\theta_{-3\,\mathrm{dB}}$ being the $-3\,\mathrm{dB}$ beamwidth, and θ_{st} the steering angle. The distance from the centre of the Earth to the receiver is R_{Rx}, and to the target is R_{trg}. The orbits are assumed to have very low eccentricity, and are therefore approximated as circular. The corresponding field of vision angle relative to the centre of the Earth, Λ_{FV}, can be obtained by resolving the green triangle from Figure 4.24a using the law of sines:

$$\begin{aligned}\Lambda_{FV} &= 2\left\{\pi - \left(\pi - \frac{\alpha_{FV}}{2}\right) - \arcsin\left[\frac{R_{Rx}\sin\left(\pi - \frac{\alpha_{FV}}{2}\right)}{R_{trg}}\right]\right\} \\ &= 2\left\{\frac{\alpha_{FV}}{2} - \arcsin\left[\frac{R_{Rx}\sin\left(\pi - \frac{\alpha_{FV}}{2}\right)}{R_{trg}}\right]\right\}.\end{aligned} \tag{4.42}$$

The receiver and target move with angular velocities $\vec{w_{Rx}}$ and $\vec{w_{trg}}$, respectively, computed using the angular escape velocity from (3.11b). The relative angular velocity is then given by $\vec{w_{trg}} - \vec{w_{Rx}}$. Accordingly, the observation time can be expressed as:

$$t_{obs} = \Lambda_{FV} \cdot |\vec{w_{trg}} - \vec{w_{Rx}}| = \Lambda_{FV} \cdot \sqrt{|\vec{w_{Rx}}|^2 + |\vec{w_{trg}}|^2 - 2|\vec{w_{Rx}}||\vec{w_{trg}}|\cos\alpha_{rel}}, \tag{4.43}$$

with $|\cdot|$ being the magnitude of the vector, and α_{rel} the relative trajectory angle from Figure 4.24b.

To obtain a comprehensive assessment of the observation time, the target will be simulated at different altitudes, from the receiver to the transmitter, and will travel with a relative angle of $\alpha_{rel} = [0, 360]^\circ$ with respect to the trajectory of the receiver, as in Figure 4.24b. The target is modelled as a sphere, and two diameters will be considered: 5 cm, which has been shown to be detectable in Section 4.1.4.2, and 2 m.

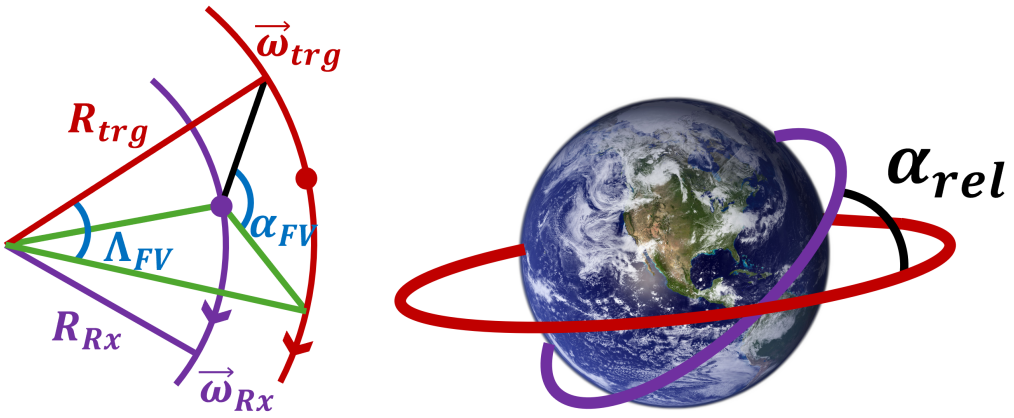

(a) Observation time diagram (b) Relative angle between target and receiver

Figure 4.24: Observation time diagram and relative trajectory angle

Figures 4.25 and 4.26 present the observation times for two different target sizes, altitudes, and relative angles, both with and without beam steering. The blank regions in the plots correspond to observation times shorter than 0.5 s, which is the integration time assumed in the RRE analysis of Section 4.1.4. The plots exhibit symmetry because, as the relative angle increases beyond 180° and approaches 360°, the trajectory angles of the target and transmitter coincide. Observation time increases with altitude, as the area covered by the FSML expands accordingly.

Figure 4.25b and Figure 4.26b show that larger targets result in fewer instances where the observation time exceeds 0.5 s, thereby limiting the ability to detect the space object. By contrast, smaller targets, as illustrated in Figure 4.25a and Figure 4.26a, are preferable as their larger FSML will increase α_{FV} and the observation time. For larger targets, observation is more effective when the target follows the trajectory of the receiver, since this reduces relative velocity and consequently increases observation time. Finally, beam steering further improves observation time by enlarging the effective field of view.

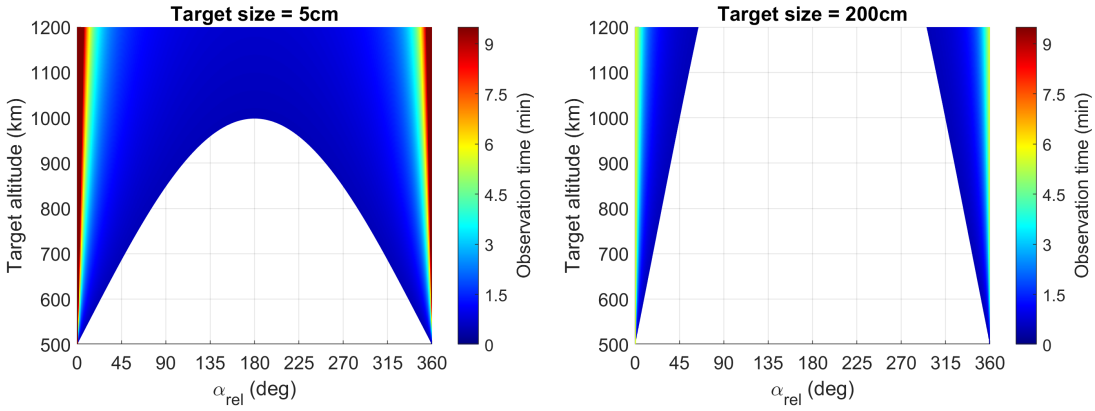

(a) Observation time for a target of 5 cm of diameter

(b) Observation time for a target of 2 m of diameter

Figure 4.25: Observation time at different altitudes and angles without steering

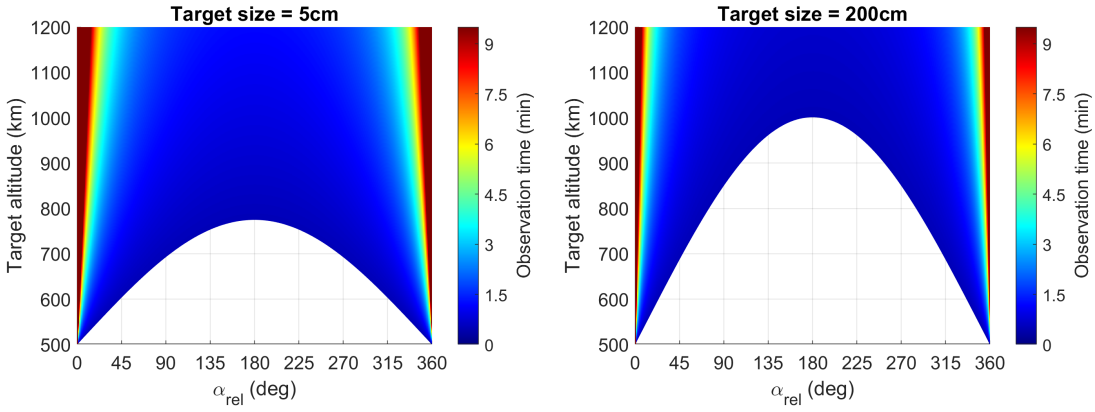

(a) Observation time for a target of 5 cm of diameter

(b) Observation time for a target of 2 m of diameter

Figure 4.26: Observation time at different altitudes and angles with 30° steering

4.1.7 Conclusion on the payload antenna design and the RRE analysis

In this chapter, the payload has been designed, and the altitude of the CubeSat has been set. Different antennas, appropriate for mounting on a CubeSat, have been studied and to help choose between the proposed antennas, an RRE analysis has been conducted.

There are multiple IOs that could be used in the spaceborne radar. However, as presented in Section 4.1.2, the best option is the OneWeb constellation satellites. The combination of a high number of standardized satellites with favourable parameters and

the high altitude would increase the number of possible space objects to be detected.

Four antennas have been presented and discussed: a patch antenna, an array of patch antennas, the 3D-PAA, and the trade-off PAM. The flat nature of the patch antenna and the array of patches is ideal because it does not increase the volume of the CubeSat. The use of the 3D-PAA would be very useful for the task of detecting space objects. It has the ability to scan the environment, and its directivity is better than that of the array of patches. The trade-off antenna, the PAM, combines the best characteristics of both, has an almost flat surface, and offers improved directivity.

Among the considered options, the single patch antenna exhibits the lowest power consumption, cost, and weight. A more advanced alternative is the array of patch antennas, which offers the additional capability of scanning the environment through beam-steering technology. The 3D-PAA, consisting of nearly 50 elements, presents significant power demands, not only for processing signals from each element but also for steering the main beam during target tracking. Furthermore, due to the large number of elements, the 3D-PAA occupies the greatest volume and contributes the highest weight. An additional limitation is the presence of a pronounced back-lobe in the beam pattern, which would require suppression. Considering these factors, the PAM emerges as the most suitable choice for integration on the CubeSat. This antenna provides superior directivity when beam steering is employed, while maintaining minimal weight and volume and offering a robust mounting solution. Moreover, as demonstrated in the minimum detectable size analysis, the PAM achieves the best performance for detecting the smallest targets. Compared to the array of patch antennas, the PAM exhibits higher directivity and reduced sidelobes during beam steering, thereby minimizing the likelihood of detection errors. Although the PAM alone would not be able to cover the full signal bandwidth, the inclusion of a matching transmission line and stub can significantly enhance its bandwidth, enabling reception of the complete signal spectrum.

The analysis of observation time presented in Section 4.1.6 indicates that a reduction in target size is advantageous, as it corresponds to an increased FSML and, consequently, a longer observation time. Furthermore, when the target trajectory closely aligns with that of the receiver, the observation time is further extended. Additional gains can be

achieved through beamwidth steering, which effectively enlarges the perceived field of view and thereby increases the duration of target observation.

4.2 Multiple frequencies system with forward scattering configuration for the integration of multiple observations

While on Section 4.1 the main focus was on designing a payload suitable for the CubeSat and for performing SSA tasks, the focus of this chapter, is to address the challenge of reducing the noise of the FS signal. In the chapter, a multiple frequency radar system is proposed that permits the integration of multiple observations.

4.2.1 Introduction

As explained on Section 3.1.2.1, part of the SISAR algorithm is the extraction of the motion parameters in order to replicate the FS signal. To be able reduce the possibility of erring when the motion parameters from the FS signals are extracted, the SNR from the received signals has to be improved.

A way of increasing the SNR for the FS scenario is to increase the signal processing gain by increasing the integration time. However, if the integration time is too long, the algorithm will computationally costly, as the integration time increases, the number of samples to be processed in the SISAR algorithm increases. In addition, achieving relatively large integration times in a spaceborne scenario could be difficult to achieve. Another issue is that the FS signal is generated when the target crosses the baseline. In a space environment, even with a steering antenna, this crossing would occur only a few times. This would difficultate the usage of common multiple integration methods, such as coherent integration and non-coherent integration. To be able to surpass these issues the multiple frequency system is proposed. The system would allow the integration of multiple observations from different frequency channels, thus increasing the overall SNR.

4.2.2 Multiple frequency system with FS configuration for SSA

The multiple frequency radar system allows the system to receive several signals at different frequencies at the same time, which opens the possibility of performing the integration of multiple observations. This could be achieved by using an illuminator that uses multiple frequencies simultaneously and a receiver that could detect the emitted frequencies. The receiver could either have an antenna with a very large bandwidth or an antenna for each frequency band, Figure 4.27. Additionally, a software defined radio (SDR) receiver could be used for such a system as its adaptability and, above all, wideband capabilities would make it a suitable candidate. In Figure 4.27, the antenna beams for the various channels are depicted as an example, their directions are illustrative and do not represent specific antenna steering angles. The figure aims to demonstrate the concept of different beams operating at distinct transmitting and receiving frequencies.

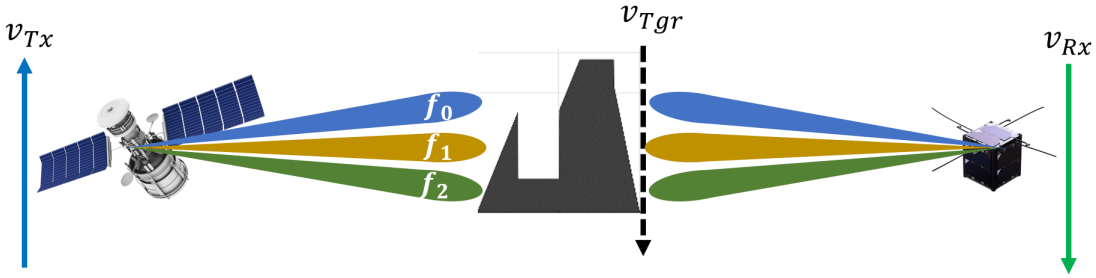

Figure 4.27: Multiple frequency transmitter and receiver

4.2.2.1 SISAR multiple observation integration method

The scenario presented for the method consists of an illuminator of opportunity, which will operate on N_f number of channels with a different carrier frequency per channel, such as $f_i \in \{f_0, f_1, \ldots, f_{N_f-1}\}$; a CubeSat with the radar receiver mounted on it, with the proper antennas to receive the transmitted frequencies; and the target crossing between them.

The multiple observation method simply consists on retrieving the FS signals the different channels and averaging them. Essentially, the performed operation is a coherent averaging. The formulation of these the proposed averaging is shown in (4.44).

$$\hat{E}_{fs}(t) = \frac{1}{N_f} \sum_{a=0}^{N_f-1} E_{fs,a}(t), \tag{4.44}$$

where $\hat{E}_{fs}$ is the averaged FS signal, $E_{fs,a}$ is the down-converted FS signal from channel a and N_f is the number of frequency channels.

As described, the FS signals would be received through different channels, each channel having a different operating frequency. As each channel has a different carrier the resulting FS signal would be different, since, as seen on (3.13), the FS signal is frequency dependent. Therefore, an analysis of the FS signal in (3.13) would be conducted to find out which is the best compensation operation that can be used.

4.2.2.1.1. FS signal analysis for multiple frequencies

The FS signal in (3.13) has three variables that are frequency-dependent: Q and η from (3.14) and γ from (3.15).

First, from (3.14), it can be deduced that the Q would be affected very little with the changes in the operational frequency. This is because the result of the product of r_{c1} and r_{c2} in the denominator is very large, therefore, if the changes in the frequency are not very large, the Q function will remain practically the same for different values of the frequency.

Secondly, in the η function from (3.14) and γ function from (3.15) the fraction addition of $\frac{\cdot}{r_{c1}} + \frac{\cdot}{r_{c2}}$ would result in some bigger variation in their values compared to the previous Q function. Nonetheless, if this is combined with the fact that both appear in a complex exponential, it is safe to assume that the effect of these variations in the values could be ignored in the final FS signal.

As a consequence, it is safe to assume that, despite the different frequencies and if these are not very different in value, there is no need to use any kind of compensation operation. Therefore, the received baseband FS signals from the different frequency channels could be averaged without any kind of further processing, as shown in Figure 4.28. The reason for averaging the signals is to not affect the CPF of the target.

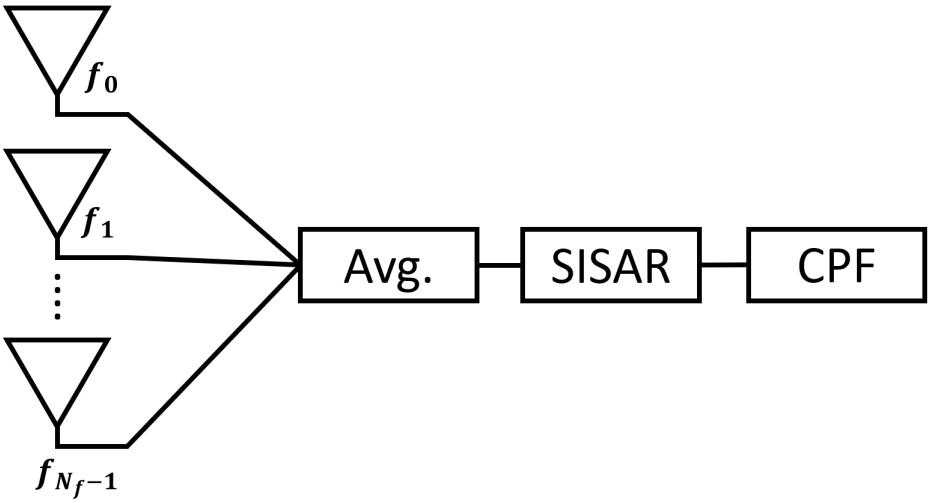

Figure 4.28: Multiple observation averaging receiver scheme

4.2.3 Methodology

To asses the system two analysis are conducted. One analysis relies on the visual inspection of the CPF as it is a good indicator on the quality of the signal to recreate the profile of the target. The other analysis will involves the mean square error (MSE). The MSE between the CPF without any noise and the CPF recreated from the averaged FS signals will be computed, (4.45). For proving that the signals are similar enough to be directly averaged, the MSE will be computed between the FS signal generated using the first channel and the averaged signals using a different number of channels, (4.46). Since the aim of (4.46) is to see how the quality of the averaged signal degrades, no noise is going to be introduced.In summary, (4.45) is a measure of error between the reconstructed and the true CPF and (4.46) measures the error between the signal from the first channel and the averaged signal with different number of channels.

$$\mathrm{MSE}_{SNR,a} = \frac{1}{n_{CPF}} \sum_{n_{CPF}} \left| H(x') - \hat{H}_a(x') \right|^2 . \tag{4.45}$$

$$\mathrm{MSE}_{FS,b} = \frac{1}{n_{sFS}} \sum_{n_{sFS}} \left| E_{fs,1}(t) - \hat{E}_{fs,b}(t) \right|^2 . \tag{4.46}$$

Please note that in (4.45), $\text{MSE}_{SNR,i}$ is the MSE for the a-th value of SNR, H is the CPF without any noise, $\hat{H}_a$ is the reconstructed CPF for the a-th value of the SNR, and n_{CPF} is the number of samples from the CPFs. Meanwhile, in (4.46), $\text{MSE}_{FS,b}$ is the MSE when the first b channels are averaged, $E_{fs,1}$ is the FS signal for the first channel, $\hat{E}_{fs,b}$ is the averaged signal when the first b channels are used, and n_{sFS} is the number of samples from the FS signals.

The geometry of [24] is simulated. This assumes a spaceborne scenario. On the analysis the target is assumed to be in the 3 dB beamwidth of the transmitting antennas and the reflected power from the target is the same for all the observations. The IOs are the OneWeb constellation satellites. OneWeb is a constellation that provides telecommunication services and operates between $[10.7, 12.7]$GHz with bandwidths of 250 MHz. The receiver has six PAM, as this antennas has proven to be the most suitable in Chapter 4, tuned between $[10.7, 12.2]$GHz and is situated at an altitude of 500 km. As the frequency increases the antenna becomes smaller. As a consequence, if 10.7 GHz antenna could fit into a $10 \times 10\,\text{cm}^2$, it is safe to assume that the 12.2 GHz would fit as well. Another safe assumption is that the bandwidth of a single antenna, although enough to receive one channel from OneWeb, would struggle to capture two consecutive channels, as seen in Section 4.1.5, thus the need for an antenna per channel. Altogether, the system would fit into a 6U, $30 \times 30 \times 20\,\text{cm}^3$, CubeSat, Figure 4.29. Summarizing, 6 different channels are simulated, each with a different operating frequency. The SNR after the multiple averaging is considered within the interval -30 dB to 20 dB. The noise is assumed to be AWGN.

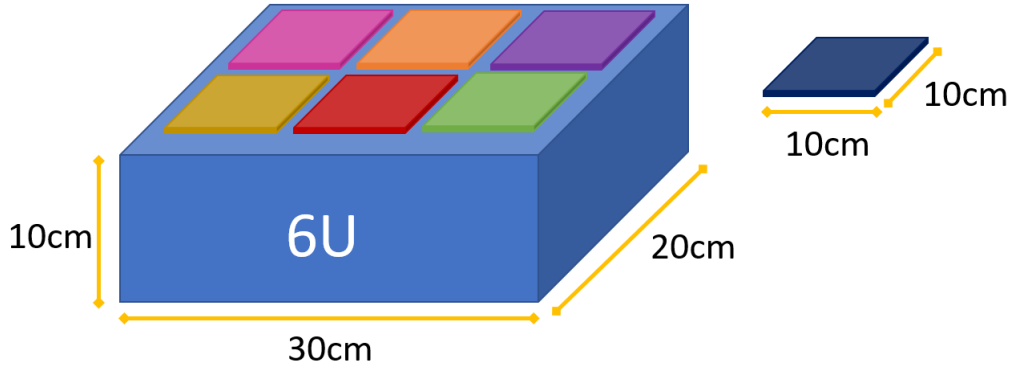

Figure 4.29: 6U radar receiver scheme

The transmitter and receiver have the same angle of trajectory, 0°. The simulated target is a perfectly conductive sphere. For the visual analysis, the target has a trajectory angle of 180°, a radius of 75 cm and an altitude of 850 km. For the MSE analysis, 100 different scenarios will be simulated. For each scenario the altitude, angle and size of the target will be taken from a uniformly random generated variable. A summary of the parameters can be found in Table 4.4.

	Visual analysis	**MSE analysis**
Operational frequency	[10.7, 12.2] GHz	
SNR	[-30, 20] dB	
Receiver altitude	500 km	
Transmitter altitude	1200 km	
Target altitude	850 km	[500, 1200]km
Target angle	180 deg	[0, 360] deg
Target radius	75 cm	[5, 200] cm
Integration time	0.5 s	
Number of channels	6	
Number of iterations	-	100

Table 4.4: Simulation parameters

4.2.4 Results

Figure 4.30 shows the CPF with no noise. Figure 4.31 shows the retrieved CFPs for the single channel and multichannel cases for different values of SNR. While Figure 4.31a has been computed with an SNR of −30 dB, Figure 4.31b has been computed with a SNR of 20 dB. A notable difference can be observed in the case of −30 dB, as the CPF resulting from the multiple observation method is different in height and, if the edges of the CPF are looked at, different in shape. Figure 4.31a shows the most differences, as it has the lowest SNR. Whereas the CPF retrieved from the SNR of 20 dB, Figure 4.31b, is the most similar. For this last case, the CPF from the single channel and the multiple observation are identical and almost indistinguishable from the true CPF on Figure 4.30.

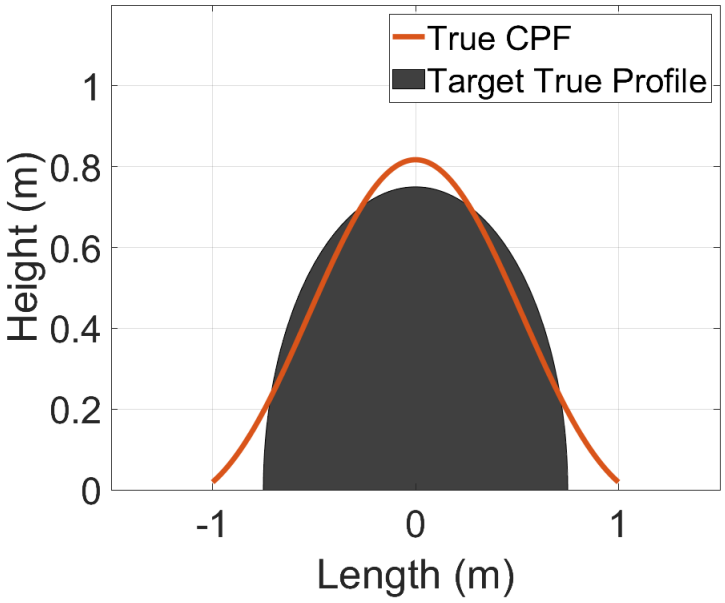

Figure 4.30: CPF with no noise

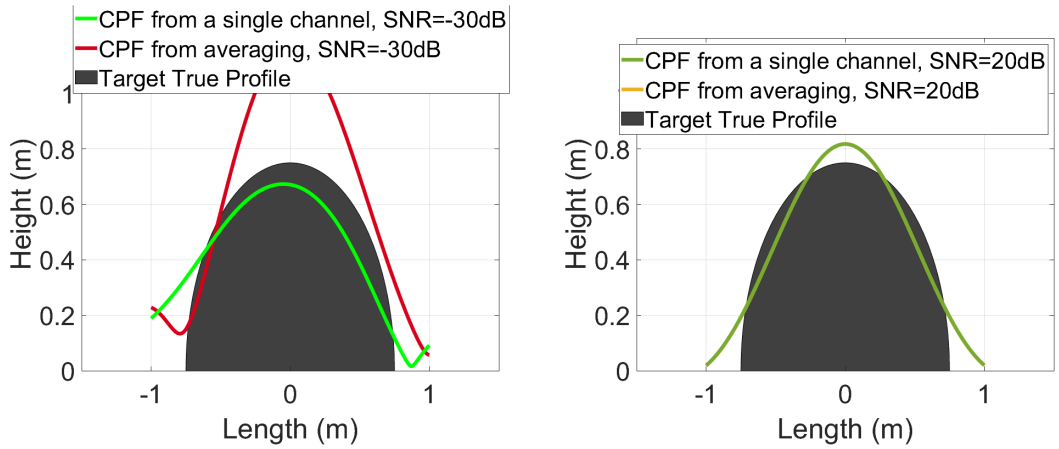

(a) Reconstructed CPF with a $SNR = -30\,\text{dB}$ (b) Reconstructed CPF with a $SNR = 20\,\text{dB}$

Figure 4.31: Retrieved CPFs for different values of SNR

Figure 4.32 displays the MSE of the reconstructed CPFs. It can be seen that as the SNR increases the error between the retrieved profile using the averaging method and the CPF without any noise decreases from 2 cm to almost 0 m, which means that the error is not noticeable.

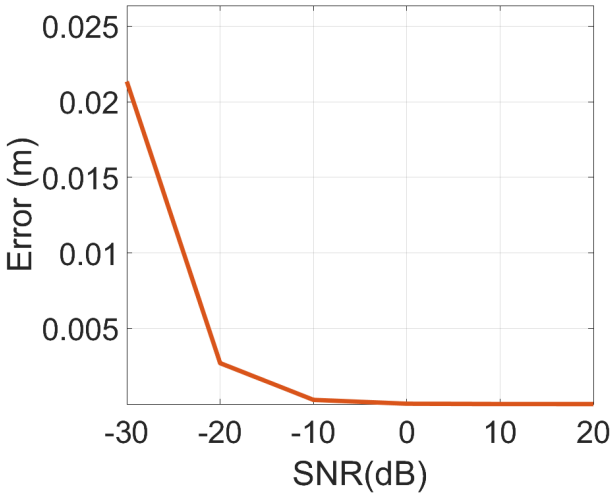

Figure 4.32: MSE of the reconstructed CPF with multiple averaging for different values of SNR

In Figure 4.33, it is assumed that the FS signal is measured in volts (V), and, thus, the MSE of the FS signals will also be measured in volts. Before computing the MSE, the FS signals were normalized to ensure comparable magnitudes. It can be perceived

that as the number of signals to be averaged increases, the error increases. Additionally, if a few signals are averaged the error is almost zero. Despite that, the error no matter how many signals are averaged is very small, in the order of 10^{-33}, practically 0.

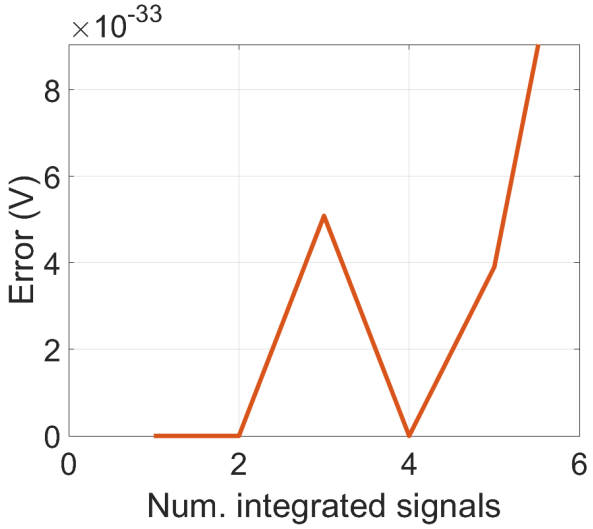

Figure 4.33: MSE of the averaged FS signals for different number of channels

4.2.5 Conclusion on the multiple frequency system with FS configuration

The multiple observation integration method that should be applied for SISAR imaging is, in essence, an averaging of the obtained FS signals from the different frequency channels. In a real world scenario, the target might be tumbling which would produce different profiles and different FS signals. This method overcomes that problem by coherently averaging the received signals.

To validate the method three analysis have been completed, The first one is a visual analysis of the resulting CPF, which was proven to be similar to the CPF without any noise. The second analysis showed how the method behaved under different SNR scenarios. Finally, the MSE for the synthesized FS with different number of channels proved that the error between a FS signal and an averaged FS signal was minimal.

The benefits of using such a system are that there would not be any need for an extra memory to store the FS signals to be integrated and that the integration is a more

straightforward operation. Also, if the target is tumbling or rotating, different observation periods are used to perform multiple integration. As a result, the FS signals would be created from different profiles of said target, producing different signals, leading to a worse quality signal. This situation is avoided by simultaneously receiving all the FS signals that will be averaged at a given time.

4.3 Conclusion on the radar system design

In this chapter, the radar system for the spaceborne segment have been designed. The OneWeb constellation was selected as is the best choice for the IO due to its high-altitude coverage and standardized satellite parameters, which will enhance the detection capabilities. The payload design included setting the altitude of the CubeSat and evaluating different antenna options capable of completing the radar tasks and being suitable to be mounted on the CubeSat. The analysis proved that the PAM antenna is the optimal choice due to its balance between directivity, beam-steering capability, low weight, and compact size.

Additionally, a multiple observation integration system and method were introduced for the FS signal processing. The system averages the received FS signals across multiple frequency channels, improving the SNR. The results demonstrated that the method preserves the CPF quality, improving the obtained CPF under low SNR conditions. Similarly, it ensures minimal error between the FS signal for one of the channels and the averaged FS signals. Furthermore, the approach eliminates the need for additional memory storage, making it an efficient and practical solution for spaceborne radar applications.

The system has thus far been evaluated under a single-target scenario. Extending the analysis to a multi-target environment introduces additional complexities that are dependent on the relative timing of baseline crossings, as well as the altitude and trajectory angle of each target. At the receiver, the observed signal constitutes a superposition of FS components generated by targets with distinct motion parameters, geometrical shapes, and physical dimensions. To address this, array processing methods such as beamforming may be employed to estimate the direction of arrival of each

component, thereby facilitating the separation of individual target contributions. Nevertheless, in cases where two or more targets cross the baseline simultaneously, the existing FS signal model becomes inadequate and requires reformulation to explicitly account for multi-target interference. Moreover, variations in SNR present a further challenge, as targets at different altitudes may yield signals of substantially different power levels. This necessitates pre-processing strategies, such as gain normalization, to equalize signal amplitudes prior to the extraction of motion parameters.

In conclusion, this chapter presents a comprehensive system design that combines an optimized payload with an advanced signal processing method. This will ensure a high-quality FS signal acquisition for the subsequent stages of the spaceborne pipeline.

Chapter 5

Novel signal processing methods and algorithms for spaceborne radar with the purpose of SSA

This chapter will introduce the appropriate signal processing methods and algorithms for the extraction of the motion parameters of the detected space objects. It should be noted that processing tools from Section 3.3 and Section 5.3.2.1.1 will be employed here. Throughout all this chapter the system described in Chapter 4 is assumed.

5.1 Introduction

The overall aim in this chapter is to reduce the computational time of the motion parameter extraction algorithm. The most straight-forward way is to use a matched filter approach [24], where different values are employed to generate the FS signal locally and then passed through a matched filter, a correlator, to find which one is the most comparable. The main problem is the small step size needed in the search grid, This would lead to a high density multi-dimensional grid, which is computationally costly.

To reduce the processing time, a combination of a recurrent neural network and the zoom-in matched filter algorithm is used. The neural network is used as a classifier, to reduce the computational load on the zoom-in algorithm. The algorithm consists on an

iterative process of find and *zoom-in* around the grid points with highest correlation.

To asses the performance of the developed algorithms, the uncertainty, the error, in the extracted motion parameters will be calculated. This will provide a comprehensive understanding of the reliability, accuracy, and limitations of the algorithms. It will quantify its accuracy and evaluate its robustness. An additional benefit of modelling the error of the methods is that it can be used in the computation of probability of collision with other space objects [116] or other SSA estimations.

5.2 Zoom-in matched filter algorithm

This section will introduce the concept of zoom-in matched filter algorithm for the extraction of the motion parameters needed for the SISAR algorithm. This algorithm is an improvement over the matched-filter approach proposed in [24].

5.2.1 Introduction

For the successful extraction of the CPF in the SISAR algorithm, as described in [24], the correct FS signal must be estimated. The matched-filter (MF) approach in [24], explains that for the estimation, several FS signals are replicated using different angle and altitude values. The values of altitudes and angles used to generate the FS signals, are chosen using a grid-like solution, which would create pairs of altitudes and angles. These result in a correlation map, or MF map, similar to an ambiguity function (AF) [1]. Later, these replicated signals are passed through a matched filter or correlator with the received signal to find which one has the highest correlation. The pair of altitude and angle with the highest correlation is chosen.

Figure 5.1 shows the output of the estimation process without any noise. A 1 km altitude step and a 1° angle step have been used. The target in Figure 5.1 is orbiting at an altitude of 701 km and an angle of 21°. The motion parameters have been correctly estimated, marked in red. However, the reason of the successful estimation is that the simulated altitude has a value that is part of the search grid, which will not be the case in a real scenario. Figure 5.1 also shows that there are lots of angle and altitude pairs that are highly correlated, marked in white. In fact, in the FS scenario, the correlation map

consistently exhibits this aspect: a curve along which all values are highly correlated, while correlations outside this curve are very weak.

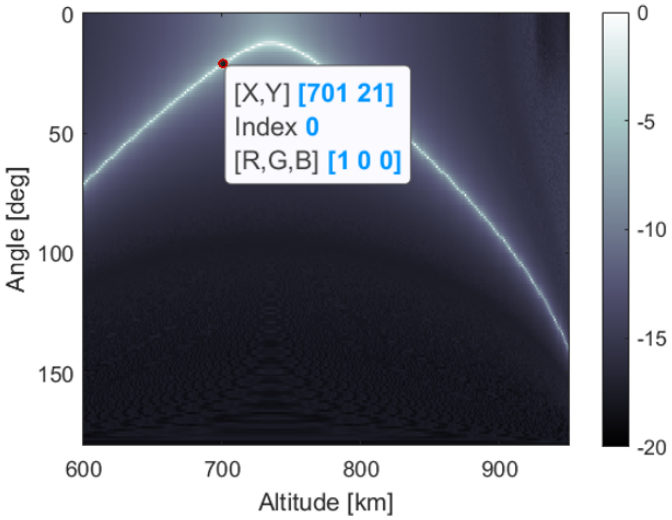

Figure 5.1: Altitude and angle estimation

Problems arise when the altitude of the target is not on the proposed altitudes and angles. For example, in Figure 5.2, the altitude has been estimated using a step of 10 km; and the angle has been estimated with a step of 20°. The estimated values for the same target of Figure 5.1 are 810 km for the altitude and 40° for the angle.

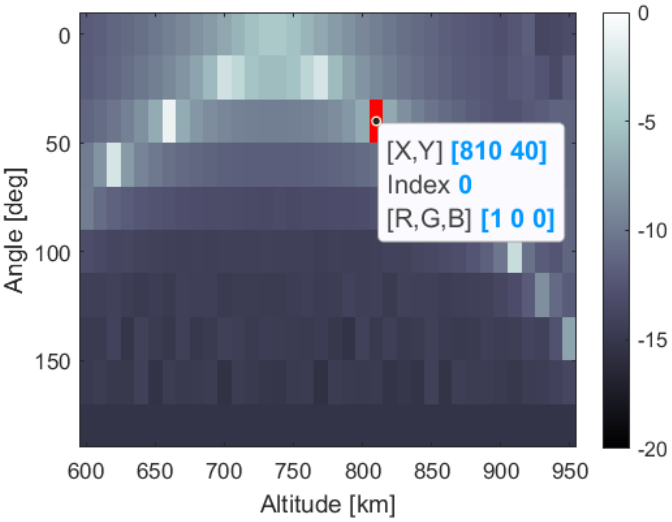

Figure 5.2: Estimation of the altitude and angle using a smaller grid

Certainly, a way to increase the accuracy is to decrease the size of the step, but it would come at a cost of computational time and power consumption. Therefore, a better approach is needed to estimate the altitude and angle. Ultimately, this is a maximization problem: if the search grid is not sufficiently dense, a local maximum may be mistaken for the point of highest correlation.

The usual method of constructing the correlation map in the FS scenario consists of a bank of correlators [21, 22, 23, 24]. Adaptive optimization methods could, in principle, offer a more efficient alternative. In signal processing, methods that minimize error are often preferred when a matched filter solution is not feasible. Approaches such as Bayesian optimization [117] and gradient-based techniques, including Adam [81], would serve to minimize the error between the received and replicated signals. However, in the presence of noise and with a large number of highly correlated candidate signals, Figure 5.1, these optimization strategies would face challenges. The gradient-based algorithms would converge to a local minimum corresponding to an incorrect pair of altitude and angle, rather than the true solution. Bayesian optimization, while more global in nature, relies on the acquisition function to balance exploration and exploitation. When the search space contains many highly correlated signals, the marginal gain from exploring new candidates becomes statistically insignificant. This would make identifying the true global maximum computationally impractical. For these reasons, a more brute force strategy is adopted to refine the search from a *coarse* grid to a *finer* grid: the zoom-in matched filter algorithm.

5.2.2 Zoom-in MF algorithm description

As discussed in Section 5.2.1, the correlation map exhibits a curve-like structure, where the points along the curve are highly correlated. Consequently, the primary objective of the algorithm is to reconstruct the MF map with sufficient accuracy to ensure that all maxima are correctly identified. The zoom-in MF algorithm addresses this objective through an iterative procedure, in which each iteration progressively *zooms in* on the maxima obtained in the preceding step, thereby refining their localization. The approach works as follows:

1. Create an initial grid of $M_{ang} \times M_{alt}$ around a certain area of interest. To compute the FS signal for the MF map, as seen in Section 3.1.2, the shape and size of the target must be selected. So, a spherical target is assumed with a diameter of D_{trg}. The area of interest will most possibly be between $[0, 360]$ for the angle of trajectory and $[alt_{rx}, alt_{tx}]$ for the altitude.

2. Compute the MF map and normalize the output. To calculate the replicated CPF for the FS signal in (3.13) a number of N_{sz} points are computed as the profile of the target.

3. Use a threshold level, κ_{i_L}, to select the highest values.

4. Use a smaller grid of $N_{ang,i_L} \times N_{alt,i_L}$ to zoom-in on the values.

5. Repeat steps 2, 3 and 4 until the a certain number of iterations, L, have passed.

Please note that $M_{alt|ang}, N_{alt|ang,i_L}, i_L, L \in \mathbb{N}$ and $0 < \kappa_{i_L} \leq 1$. $N_{alt|ang,i_L}$ is the number of altitude or angle values for the new grid around the threshold values for the iteration i_L. The values of these parameters are chosen to ensure that the estimation process is completed within a reasonable time while maintaining sufficient grid density to minimize errors. The target is assumed to remain the same across all iterations of the algorithm. Although the shape and size of the target could vary between iterations, accounting for such variations would substantially increase the algorithm complexity and computational time of the algorithm, which the design aims to avoid.

Figure 5.3 illustrates several stages of the zoom-in MF algorithm for a scenario in which the receiver is located at an altitude of 500 km and the transmitter belongs to the OneWeb constellation at an altitude of 1200 km. The angles were computed within the range $[-50°, 50°]$. The altitude and angle of the target, highlighted in red, are approximately 600 km and 40°, respectively. The inclusion of these values among the resulting parameter pairs confirms that the MF map is being correctly computed. The zoom-in algorithm progressively refines the MF output around the highly correlated points, narrowing the search region at each iteration.

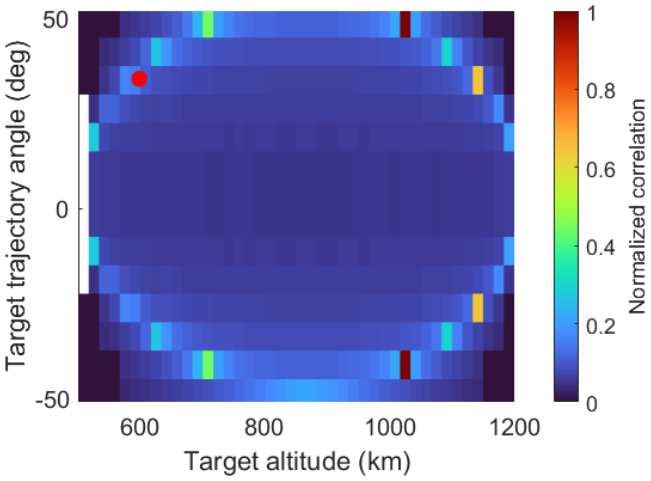

(a) MF map of zoom-in algorithm after first iteration

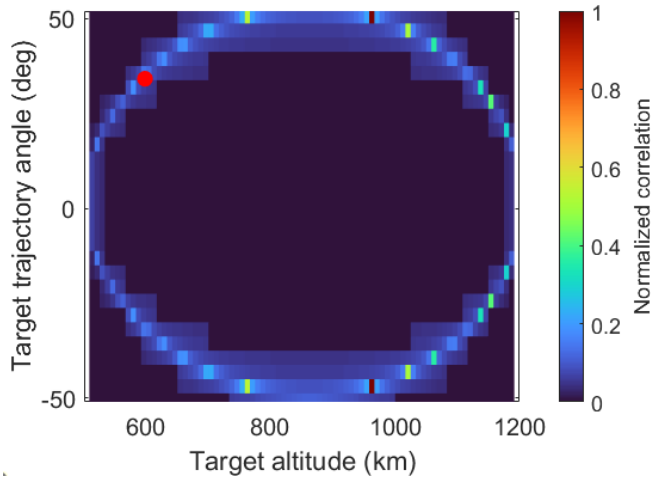

(b) MF map of zoom-in algorithm output after second iteration

Figure 5.3: MF map of the zoom-in MF algorithm at different stages

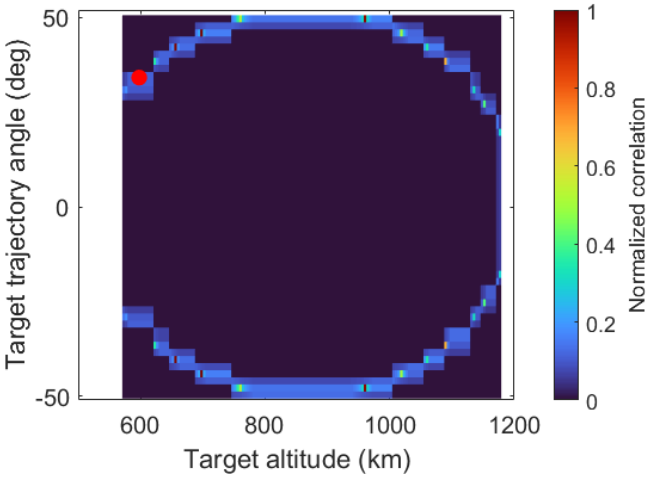

(c) MF map of zoom-in algorithm after third iteration

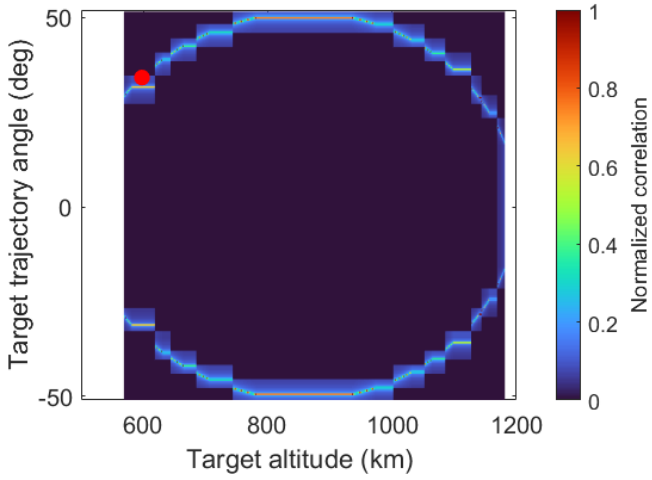

(d) MF map of zoom-in algorithm after fourth iteration

Figure 5.3: MF map of the zoom-in MF algorithm at different stages

The observed symmetry in altitude is expected, as the bistatic range remains identical for symmetric points, leading to nearly equivalent correlation values. Moreover, the plots provide clear evidence of the statement in Section 5.2.1, namely that the correlation maps form a curve of highly correlated points. Although an absolute maximum exists, locating it using conventional adaptive grid methods is computationally imprac-

tical, as previously discussed. Consequently, reconstructing the entire curve of highly correlated points becomes a necessary objective.

It is assumed that the target will cross the baseline at least twice, this would be possible thanks to the steering capabilities of the antenna. These crossings will enable the creation of a track of altitudes that could be used to estimate the speed and trajectory of the space object. For this reason, the analysis focuses solely on altitude.

Some implications of the symmetry in altitude will be that two different sets of results could be passed onto the orbit propagation module, from which collision probability could be computed. The first set of results, Figure 5.4, will be the altitude from the maximum of the MF map and the uncertainty, or error, model that is derived from it. The second set, Figure 5.5, will include two altitudes: the altitude corresponding to the maximum value of the MF map and its symmetrical counterpart. The parameters for the error model are obtained based on the assumption that the altitude with the smallest error is selected. Including these two altitudes in the second set ensures that the altitude with the smallest error is captured within the set.

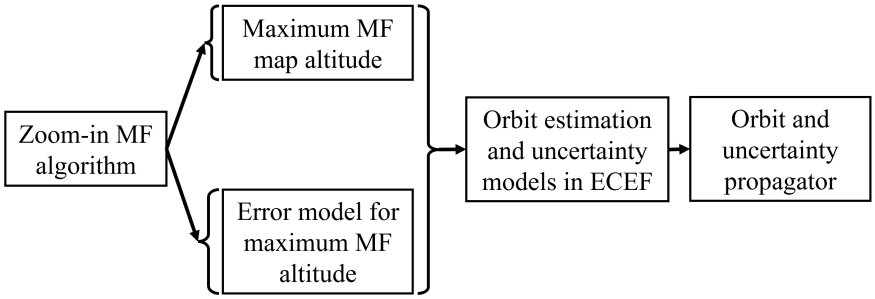

Figure 5.4: First set of altitudes passed onto the next stages

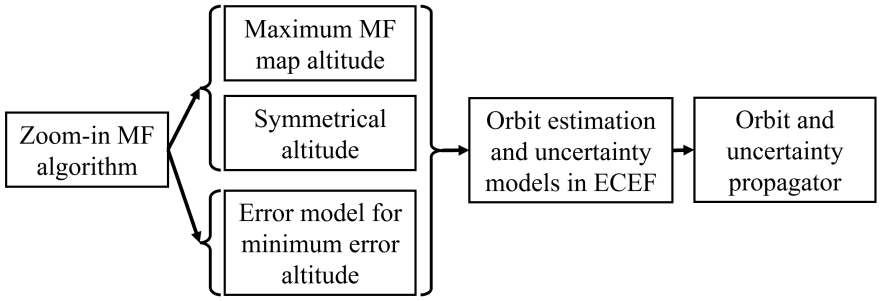

Figure 5.5: Second set of altitudes passed onto the next stages

5.2.3 Methodology

For analysing the performance of the estimation and to model the uncertainty in the algorithm a Monte Carlo simulation will be conducted. The system in Chapter 4 is assumed, and since, as it has been demonstrated in Section 4.2, the error in the final FS signal is minimum if multiple frequency channels are integrated, only the first frequency channel is simulated. In each iteration a different target will be simulated, while the transmitter and the receiver will be the same. Besides, both transmitter and receiver will have the same orbit inclination, the same angle of trajectory. In the simulated scenarios, the parameters of the target, altitude, angle and size; are going to be chosen from a uniform random variable.

The target will be a perfectly conductive sphere, the diameter will be chosen randomly between 0.2 m to 2 m, taken from Section 4.1.4.2. The angles of trajectory of the target are going to be picked from a uniform random variable between $[0°, 360°]$. The altitude of the target will be randomly chosen between the altitudes of the receiver and the transmitter. The altitude of the receiver will be 500 km and the altitude of the transmitter will be 1200 km, the altitude for the OneWeb constellation satellites. The SNR of the FS signal after the receiver chain will be 20 dB, which is achievable as seen in Section 4.1.4.

Several preliminary tests were conducted to select the optimal parameters for the algorithm. The primary objective of these tests was to identify parameter sets capable of generating the MF map in under 10 min while preserving the highest possible level of detail. The 10 min constraint was imposed to ensure that, when the algorithm is executed repeatedly within the Monte Carlo simulation framework, the overall computational cost remains manageable. The tests involved processing 10 FS signals randomly generated according to the parameters listed in Table 5.1a, using different combinations of $M_{alt|ang}$, L, $N_{alt|ang,i_L}$, and κ_{i_L}. The final parameters selected for the zoom-in MF algorithm are summarized in Table 5.1b, while Table 5.1 provides an overview of both the simulation and zoom-in parameters. It should be noted that 100 iterations were completed, and the simulations were performed in MATLAB on a PC equipped with

16 GB of RAM and an Intel i9-9900K CPU.

		Target			
Rx. alt	**Tx. alt**	**Altitude**	**Angle**	**Size**	**SNR**
500 km	1200 km	[500, 1200]km	[0°, 360°]	[0.2, 2]m	20 dB

(a) Parameters for the receiver, transmitter and target

$\mathbf{M_{alt\|ang}}$	**L**	$\mathbf{N_{alt\|ang,i_L}}$	$\boldsymbol{\kappa_{i_L}}$
10	3	5, 3, 3	0.1, 0.15, 0.17

(b) Parameters for zoom-in MF algorithm

Number of iterations
100

(c) Number of iterations for the Monte Carlo simulation

Table 5.1: Parameters for the Monte Carlo simulation

The parameters in Table 5.1b give an insight into the functioning of the algorithm. It can be seen that while, at first, it is necessary to have a higher amount of altitude and angle values for the grid, with each iteration the number decreases, as the maxima have been found and the process of zoom-in is being performed around them. Similarly, the number of maxima that is chosen is less with each iteration as seen by the threshold value, κ_{i_L}, which increases with each passing iteration.

5.2.4 Results

Two errors are going to be presented: the altitude error and the absolute of the altitude error. To illustrate them, histogram are displayed. In the same graph, the probability density function of a Gaussian random variable is shown, to prove that, at least visually, they fit into it. Similarly, a mathematical proof of its fit is going to be given ensuring that the error can be modelled as a random Gaussian variable.

The histogram in Figure 5.6a show that with the maximum MF map altitude the algorithm results in over 60 cases where the error is less than 174 km. In Figure 5.6b, it can be observed that the cases where the error is below 182 km is around 90, the

majority of them. The reason for this is that, naturally, the minimum error altitude will result in a higher estimation accuracy. One more notable difference between both cases is that the error for the maximum MF altitude, Figure 5.6a, is contained within 0 km and 580 km, which would include the whole search area. Meanwhile, the histogram for the minimum error altitude, Figure 5.6b, shows that the maximum achieved error is 260 km.

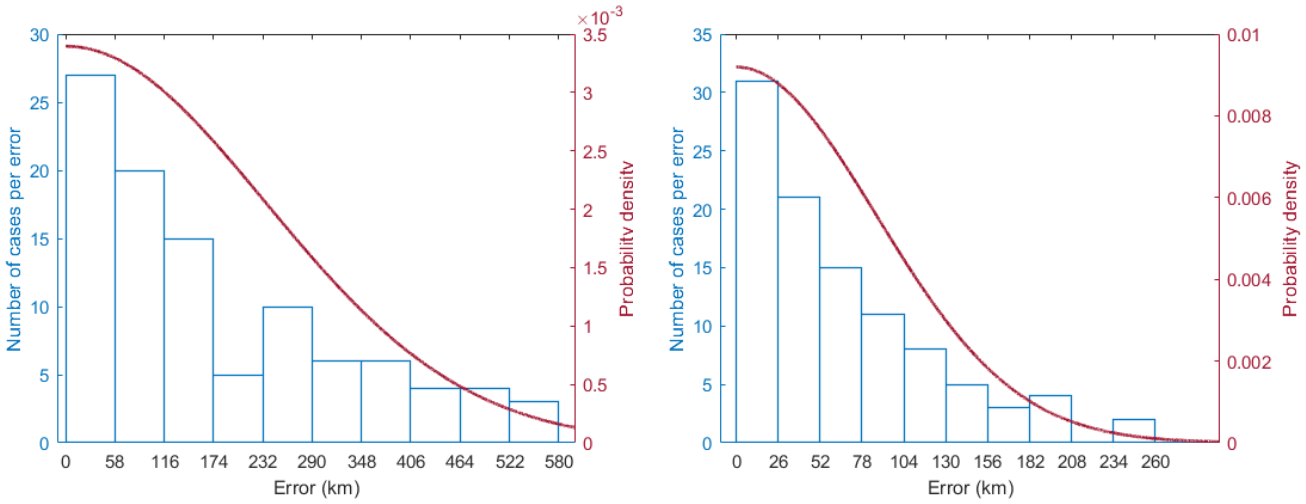

(a) Histogram for the maximum MF map altitude

(b) Histogram for minimum error altitude

Figure 5.6: Absolute error in the estimation of the altitude

Figure 5.6 shows that the error distributions for both altitude estimates can be represented by two distinct random Gaussian variables. More specifically, they are well described by a folded normal distribution. The error data also pass the Chi-Square goodness-of-fit test [118] at the 5% significance level, confirming that the Gaussian model is appropriate. Table 5.2 summarizes the results, where $\bar{\mu}_{err,alt,|MaxMF,MinErr}$ denotes the mean of the extracted absolute errors, $\sigma_{err,alt,|MaxMF,MinErr}$ the variance of the corresponding Gaussian variables, and t_{ite} the time per iteration. As expected, the parameters associated with the minimum-error altitude are smaller. The mean errors are 177.77 km and 64.58 km, respectively. This indicates that, although the error is modelled as a folded Gaussian variable with zero mean, the average error remains 177.77 km and 64.58 km, depending on the chosen error model. The total runtime of the Monte Carlo simulation was 24 h, corresponding to an average of 14.40 min per

iteration. This exceeds the target runtime by approximately 40%.

$\bar{\mu}_{\mathbf{err,alt,MaxMF}}$	$\bar{\mu}_{\mathbf{err,alt,MinErr}}$	$\sigma_{\mathbf{err,alt,MaxMF}}$	$\sigma_{\mathbf{err,alt,MinErr}}$	$\mathbf{t_{ite}}$
177.77 km	64.58 km	234.95 km	86.80 km	14.40 min

Table 5.2: Mean of errors, variances for the Gaussian variables and time per iteration

5.2.5 Computational complexity of the algorithm

To demonstrate that the zoom-in MF algorithm provides an improvement in terms of computational load compared to the MF approach presented in [21, 22, 23, 24], the analytical computational complexities of both algorithms are derived and compared.

5.2.5.1 Computational complexity of the zoom-in MF algorithm

For analysing the computational complexity of the algorithm it is assumed that both MF and zoom-in MF algorithms will compute the same amount of points, N_{sz}, for the CPF, therefore this variable will be ignored. Similarly, it is assumed that both algorithms will compute the same amount of points when replicating the FS signal.

As described in Section 5.2.2, the computational complexity grows as follows:

1. The first step, which consists of the creating the initial grid will result in:

$$O(1)_{zoom-in} = M_{ang} \times M_{alt}. \tag{5.1}$$

2. The next operation that increases the computational complexity is the zoom-in around the threshold values:

$$O(2)_{zoom-in} = O(1)_{zoom-in} + \sum_{N_{i_L}} N_{ang,i_L} \times N_{alt,i_L}, \tag{5.2}$$

   where, N_{i_L} will be the number of threshold values.

3. Since the operation is repeated L times, the final computational complexity will

be:

$$\begin{aligned} O_{zoom-in} &= O(1)_{zoom-in} + \sum_{L} \sum_{N_{i_L}} N_{ang,i_L} \times N_{alt,i_L} \\ &= M_{ang} \times M_{alt} + \sum_{L} \sum_{N_{i_L}} N_{ang,i_L} \times N_{alt,i_L}. \end{aligned} \tag{5.3}$$

5.2.5.2 Algorithm comparison

As per [24], the computational complexity of the MF algorithm is:

$$O_{MF,FS} = [3L_n \log L_n \times L_n] \times \frac{\Delta_R}{m_s} \times \frac{\Delta_\phi}{n_s} = [3L_n \log L_n \times L_n] \times M_{corr} \times N_{corr}, \tag{5.4}$$

where, L_n is the length of the FS signal, Δ_R is the length of the search area of the altitudes, Δ_ϕ is the length of the search area of the angles, and m_s and n_s are the altitude and angles steps, respectively.

$3L_n \log L_n \times L_n$ is the amount of operations related to replicating and correlating the FS signals. As both zoom-in and MF algorithms will have to replicate and correlate the signals, this term can be ignored for the comparison, resulting in:

$$O_{MF} = M_{corr} \times N_{corr}. \tag{5.5}$$

At first, it can be observed that the computational complexity is less in the MF algorithm, as the only operation to do will be to setup the search grid. However, if it is assumed that:

$$M_{ang} \times M_{alt} \ll M_{corr} \times N_{corr}, \tag{5.6}$$

then, it is safe to assume that:

$$\sum_{N_{i_L}} N_{ang,i_L} \times N_{alt,i_L} \ll M_{corr} \times N_{corr}, \tag{5.7}$$

because the number of threshold points is smaller than the total number of points in the grid for the MF algorithm.

Therefore, if the number of loops is not large, (5.6) and (5.7) yield in:

$$M_{ang} \times M_{alt} + \sum_{L} \sum_{N_{i_L}} N_{ang,i_L} \times N_{alt,i_L} \ll M_{corr} \times N_{corr}, \qquad O_{zoom-in} \ll O_{MF}. \tag{5.8}$$

5.2.6 Conclusion on the zoom-in matched filter algorithm

This section has introduced a novel zoom-in approach for estimating the altitude of space objects using the FS configuration. Additionally, it explained how the results of the algorithm could be passed on to the next stages of the SSA pipeline. Two sets of results were considered: the altitude corresponding to the maximum value of the MF and two altitudes, one from the maximum of the MF and its symmetrical counterpart.

An analysis was conducted to evaluate the accuracy of the algorithm and to model the error, providing insight into its performance, which is crucial for the next stages of the SSA pipeline. The presented analysis of the zoom-in algorithm demonstrates that the absolute error in altitude can be modelled as a folded normal distribution. Both visual analysis, through histograms in Figure 5.6, and mathematical analysis, using the Chi-Square goodness-of-fit test, confirm that the error follows a Gaussian distribution. The algorithm achieves mean altitude errors of 177.77 km and 64.58 km. However, the time per iteration, 14.4 min, exceeds the intended iteration time.

From a broader perspective, the mean positioning error of 177.77 km represents approximately 25.4% of the total baseline distance of 700 km. In relative terms, this indicates a 74.6% reduction over the possible maximum error, the baseline length. The mean error of 64.58 km corresponds to only 9.23% of the baseline, reflecting a 90.77% reduction. Although these relative improvements are substantial, the error in the altitude estimation remains too large to enable accurate CPF reconstruction. Furthermore, the obtained errors appear considerably higher than those reported in [22, 23]. However, it is important to note that the baselines in those studies were on the order of 500 m, whereas the baseline in this study is 700 km, three orders of magnitude larger.

Section 5.2.5 provides a detailed comparison between the analytical computational complexity of the zoom-in MF algorithm and that of the conventional MF approach based on a bank of correlators. The results demonstrate that, as long as the number of iterations in the zoom-in MF algorithm remains within a reasonable number, its computational requirements are lower than those of the bank of correlators method. This reduction in computational time highlights the efficiency of the iterative zoom-in strategy, which focuses resources on progressively refined regions of interest rather than exhaustively searching the entire parameter space.

5.3 RNN-zoom-in MF algorithm for the altitude estimation of space objects

This section introduces and analyses the performance of the RNN-zoom-in MF algorithm. It provides an overview of the RNN architecture and the various versions of the zoom-in MF algorithm when coupled with the RNN, detailing their design and differences. The section also discusses the reasoning behind these design choices and their impact on the performance.

5.3.1 Introduction

Although the zoom-in MF algorithm has been shown to be computationally more efficient than the conventional MF approach, it nevertheless remains computationally demanding. For example, the total runtime for the 100 simulated scenarios reported in Section 5.2.4 amounted to 24 h, corresponding to an average of 14.4 min per signal. This still exceeds the target runtime of 10 min per signal. To further reduce computational time, a hybrid strategy is proposed that integrates a RNN classifier with the zoom-in MF algorithm. As illustrated in Figure 5.7, the RNN is applied prior to the zoom-in stage to classify key parameters of the target, such as altitude, trajectory angle, or size, directly from the FS signal. This information is subsequently provided to the zoom-in algorithm, thereby constraining the search space and reducing the overall computational burden. The innovation and novelty of this approach lie in the introduction of a dedicated signal pre-processing stage and the integration of the RNN into the

signal processing pipeline. These elements optimize the dataset for the chosen architecture and enhance the effectiveness of the zoom-in algorithm by guiding its search more efficiently.

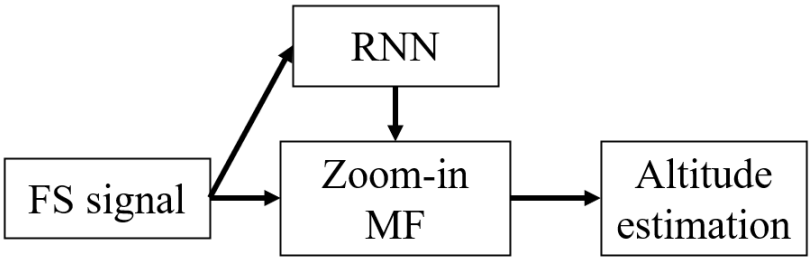

Figure 5.7: Estimation of the altitude using the RNN aided zoom-in approach

5.3.2 Recurrent neural network

A RNN was chosen as the neural network as it has proven to be able to *remember* better the time dependencies [119], making it more suitable for the classification of time signals. In Section 5.2 there are two variables of the target that could be estimated: the angle of trajectory and the altitude. In order to reduce the computational load on the zoom-in MF algorithm, the area of search of these two variables could be divided into subsets. Then, the RNN could classify the FS signals into these subsets, reducing the area of search for the zoom-in MF approach. In the proposed framework, only the angle of trajectory is going to be classified. The reason for not classifying the altitude is that, while different altitudes of the target will result in different FS signals, the signals are not different enough so that the RNN can distinguish them. This becomes evident when the symmetrical shape of MF map, Figure 5.3, is taken into account, there is too much ambiguity between them.

A reasonable assumption would be to divide the angle search area into N_C equal classification fields. For the proposed framework, $N_C = 4$ such as the classification fields are: $\{[-45°, 45°); [45°, 135°); [135°, 225°); [225°, 315°]\}$. The reason for choosing these four fields, and not a higher number, is that they result in different enough FS signals so that the RNN can differentiate them. However, there exists one issue with the angles of $[225°, 315°]$ and $[45°, 135°]$, as they produce the same cosine values. If this is taken

into account in (3.15), it can be noted that $\Gamma_{T|R|p}$ will be the same for these angles, resulting in the same FS signals. Therefore, the angles from 225° to 315° are ignored as the RNN would not be able to distinguish between $[225°, 315°]$ and $[45°, 135°]$. So the final selected classification fields are $\{[-45°, 45°); [45°, 135°); [135°, 225°]\}$.

5.3.2.1 Signal pre-processing

The magnitude and the unwrapped phase are fed into the RNN to classify their corresponding signals into the different subsets. Phase unwrapping is performed by adding or subtracting integer multiples of 2π whenever the phase difference between consecutive samples is greater than or equal to π radians, thereby ensuring phase continuity. Incorrect unwrapping can lead to errors, as the resulting wrapped phase of the signal will no longer accurately represent the true phase. Additionally, as the signal will be noisy, the fed signals will also have noise. The noise is assumed to be AWGN. A SNR = 20 dB is chosen, as it has proven to be attainable in Section 4.1.4. To have a better classification accuracy, the signal will be cleaned using the Fractional Fourier Transform.

5.3.2.1.1. Fractional Fourier Transform

The Fractional Fourier Transform (FrFT) is an operator that can rotate a signal in the time-frequency plane. As it was seen in [41], the FS signal is similar to a linear chirp, making the FrFT a very useful tool for the case at hand. The FrFT is a generalization of the traditional Fourier transform. Being $x[n']$ a discrete signal of length N, the α-th order discrete FrFT is defined as [120]:

$$X_{\alpha_{FrFT}}[n] = \sum_{a=-N/2}^{N/2} K_{\alpha_{FrFT}}[n, a]\, x[a], \tag{5.9}$$

where $X_{\alpha_{FrFT}}[n]$ denotes the FrFT of order α_{FrFT} of the discrete signal $x[n]$. The fractional order, α_{FrFT}, is:

$$\alpha_{FrFT} = \frac{2\phi_{FrFT}}{\pi},$$

$K_{\alpha_{FrFT}}[n, n']$ is the FrFT kernel, defined as [120]:

$$K_{\alpha_{FrFT}}[n, a] = \begin{cases} A_{FrFT,0}\, e^{j\pi\left(n^2+a^2\right)\cot\phi_{FrFT} - j\pi 2na\csc\phi_{FrFT}} & \text{if } \phi_{FrFT} \neq m_{FrFT}\cdot\pi \\ \delta_D[n-a] & \text{if } \phi_{FrFT} = 2\cdot m_{FrFT}\cdot\pi \\ \delta_D[n+a] & \text{if } \phi_{FrFT} i = 2\cdot m_{FrFT}\cdot\pi + \pi \end{cases},$$

where, $\delta_D(\cdot)$ is the Dirac delta function; $j = \sqrt{-1}$, the imaginary unit; $m_{FrFT} \in \mathbb{Z}$, an integer; and $A_{FrFT,0}$ is defined as:

$$A_{FrFT,0} = \frac{e^{j\frac{\phi_{FrFT}}{2}}}{\sqrt{j\sin\phi_{FrFT}}}.$$

An interpretation of the FrFT is the clockwise rotation of the signal in the time-frequency plane by an angle, ϕ_{FrFT}. Therefore, as seen on Figure 5.8, as the order increases, the time duration decreases. It can be intuitively deduced that the inverse of the FrFT of order α_{FrFT}, which has an angle ϕ_{FrFT} associated to it, is the FrFT of order $-\alpha_{FrFT}$, which would have an angle $-\phi_{FrFT}$ associated.

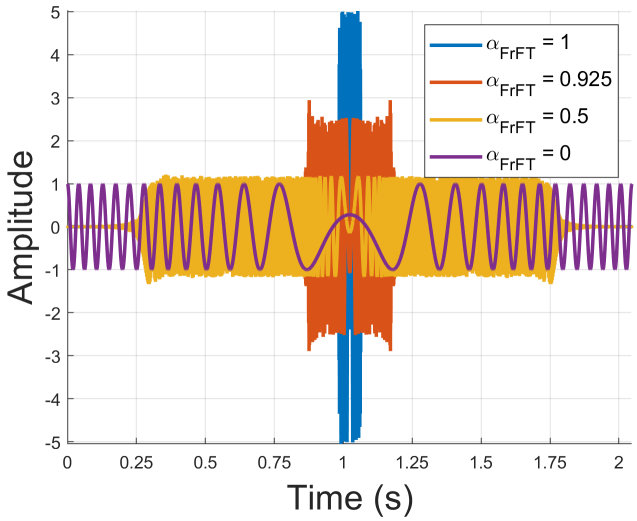

Figure 5.8: Real part of the output of the FrFT with different values of α_{FrFT} for a linear chirp starting at -250 kHz and ending at 250 kHz

Some of the properties of the FrFT are [121]:

1. Zero rotation: $FrFT_{\alpha_{FrFT}=0}\{x[n]\} = x[n]$.

2. Consistency with Fourier transform: $FrFT_{\alpha_{FrFT}=1}\{x[n]\} = \mathcal{F}\{x[n]\}$.

3. Additivity of rotations:

$$FrFT_{\alpha_{FrFT}=\alpha_{FrFT,1}}\{FrFT_{\alpha_{FrFT}=\alpha_{FrFT,2}}\{x[n]\}\} = FrFT_{(\alpha_{FrFT,1}+\alpha_{FrFT,2})}\{x[n]\} \tag{5.10}$$

4. Whole (2π) rotation: $FrFT_{\alpha_{FrFT}=4}\{x[n]\} = x[n]$.

From property (5.10) it can deduced that, indeed, there exists a inverse Fourier Transform (IFrFT). The inverse FrFT of the fractional Fourier transform of order α_{FrFT} is the fractional Fourier transform of order $-\alpha_{FrFT}$: $IFrFT_{\alpha_{FrFT}} = FrFT_{-\alpha_{FrFT}}$.

5.3.2.1.2. Fractional Fourier Transform cleaning

The spectrogram in Figure 5.9 demonstrates that the FS signal exhibits characteristics similar to those of a complex LFM chirp. Although direct cleaning of the signal using a low-pass filter is possible, the application of the FrFT prior to filtering provides a more effective means of obtaining a cleaner signal. As outlined in Section 3.1.2, multiple approaches exist for extracting FS signals, several of which rely on constructing the analytical signal via the Hilbert transform. In the present study, the signal depicted in Figure 5.9 corresponds to the full complex FS signal reported in [24]. Accordingly, it is assumed that the complete FS signal has been successfully acquired and is available for subsequent processing.

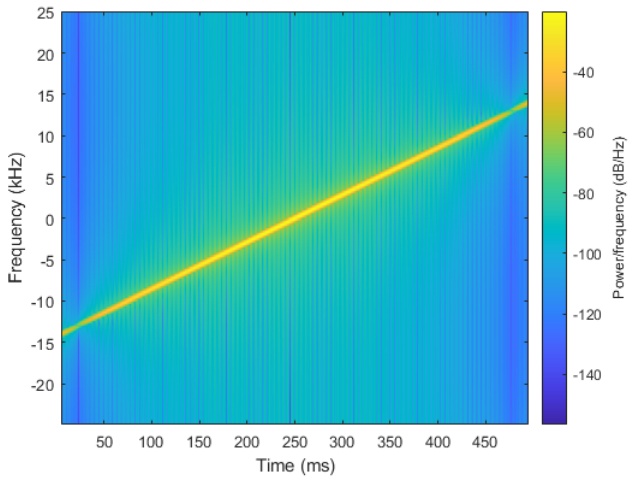

Figure 5.9: Spectrogram of the FS signal generated with a receiver at 500 km, a transmitter at 1200 km, and a spherical target at 700 km altitude, radius 1.5 m, moving at a trajectory angle of 180°. Both receiver and transmitter share a trajectory angle of 0°.

The FrFT cleaning process is as follows:

1. Estimate the angle that maximizes the time response using the instantaneous frequency of the signal and its duration.

2. Rotate the signal in the frequency-time plane using said angle and the FrFT.

3. Remove the noise of the signal by digitally filtering it. The filter employed in this step is an *ideal* filter. The rotated FS signal is first transformed into the frequency domain, after which only the frequency components within the interval ±2 kHz are retained, while all remaining components are suppressed. As this operation is carried out in post-processing, issues of non-causality do not arise. In contrast, for real-time implementation, a Finite Impulse Response (FIR) filter with the corresponding characteristics would need to be designed.

4. Rotate the signal back to its original position.

The FS signals in Figure 5.10 have been created using the same parameters as in Figure 5.9. As it can be seen in Figure 5.10, the FS signal can be properly cleaned with the FrFT approach. The cleaned signal, in Figure 5.10b, is similar to the signal in

5.9, except for the edges, that, due to the FrFT, have been removed. Because of this, it is preferable to use the noisy FS signal, Figure 5.10a, in the zoom-in algorithm, as the removal of the edges could lead to errors in the correlation. The new processing structure is shown in Figure 5.11.

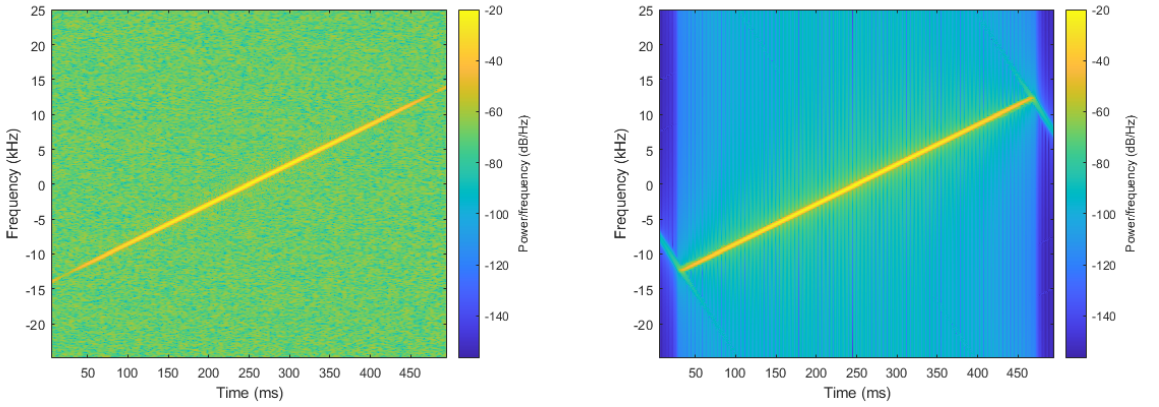

(a) Spectrogram of the FS signal with noise

(b) Spectrogram of FS signal cleaned with the FrFT

Figure 5.10: FrFT cleaning example

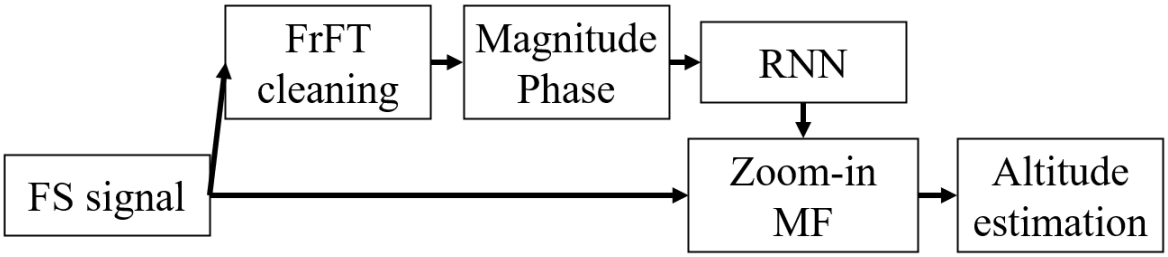

Figure 5.11: Estimation of the altitude and angle using RNN aided zoom-in MF algorithm with FrFT cleaning

5.3.2.2 RNN design and training

The RNN was implemented using the artificial intelligence toolbox from MATLAB. As illustrated in Figure 5.12, the network consists of eight layers. The sequence input layer receives two features: the magnitude and the unwrapped phase of the FS signal. Both bi-LSTM layers [122] contain 256 hidden units. The dropout layers employ a dropout rate of 0.5. Finally, the softmax layer outputs three classes, corresponding to the predefined classification fields.

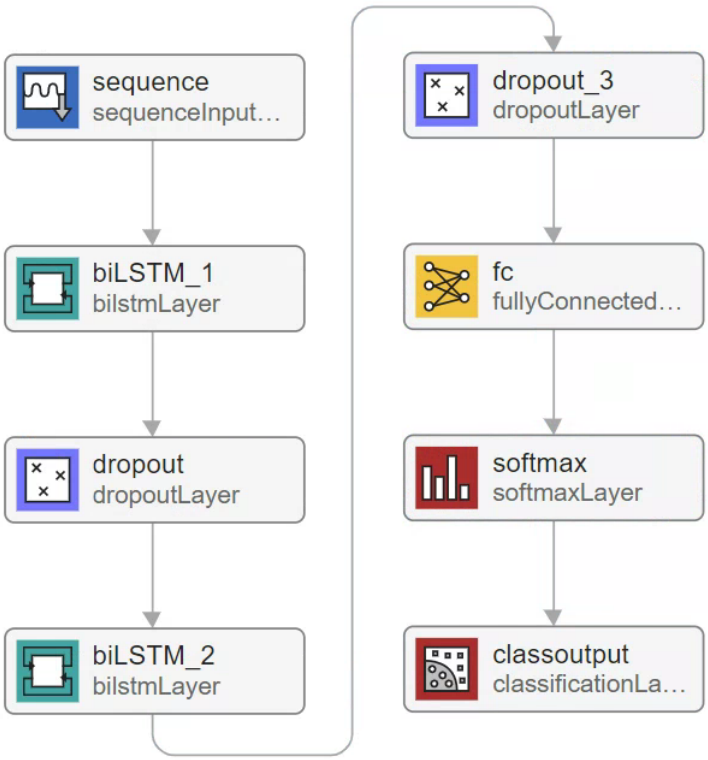

Figure 5.12: RNN structure

The RNN will be trained using the Adam optimization method, Section 3.3.2. FS signals will be generated for the three previously defined subsets, $[-45°, 45°)$; $[45°, 135°)$; $[135°, 225°]$. The target parameters used to generate the FS signals will be randomly assigned. The receiver altitude is set to 500 km, while the transmitters correspond to satellites from the OneWeb constellation at an altitude of 1200 km. The target is modelled as a perfectly conductive sphere, with diameters from 20 cm, shown in Section 4.1.4.2 to be detectable, up to 2 m. All generated signals assume a SNR of 20 dB. The trajectory angles are randomly generated within the defined subsets, and 1000 signals are produced for each subset, per class. Of these, 7.5%, 75 signals, are reserved for validation. A summary of the training parameters is provided in Table 5.3.

			Target			
SNR	**Rx. alt.**	**Tx. alt.**	**Diameter**	**Altitude**	**Angle**	**# of signals per class**
20 dB	500 km	1200 km	[0.2, 2]m	[500, 1200]m	$[-45°, 45°)$	1000
					$[45°, 135°)$	1000
					$[135°, 225°]$	1000

Table 5.3: Parameters for RNN training

Figure 5.13 illustrates the training accuracy for the case without FrFT cleaning, where the RNN classifier achieves an accuracy of 84%. For comparison, the corresponding training progress with FrFT cleaning is shown in Figure 5.14, reaching an accuracy of 85.33%, which is slightly higher than in the case without FrFT cleaning. In both scenarios, the accuracy eventually converges to a similar level, indicating that the two RNNs produce comparable outputs. A closer look at the progression of the training process reveals a notable distinction. Without FrFT cleaning, the RNN requires approximately 10 000 iterations before surpassing the 80% accuracy. In contrast, when FrFT cleaning is applied, the RNN reaches an accuracy of about 85% in only 100 iterations. This behaviour suggests that the dataset processed with FrFT cleaning provides a more optimized input, enabling the RNN to learn more effectively and achieve high accuracy much faster. Consequently, it can be inferred that the RNN benefits from the application of FrFT cleaning. To further substantiate this conclusion, the confusion matrices for both cases will be analysed and compared.

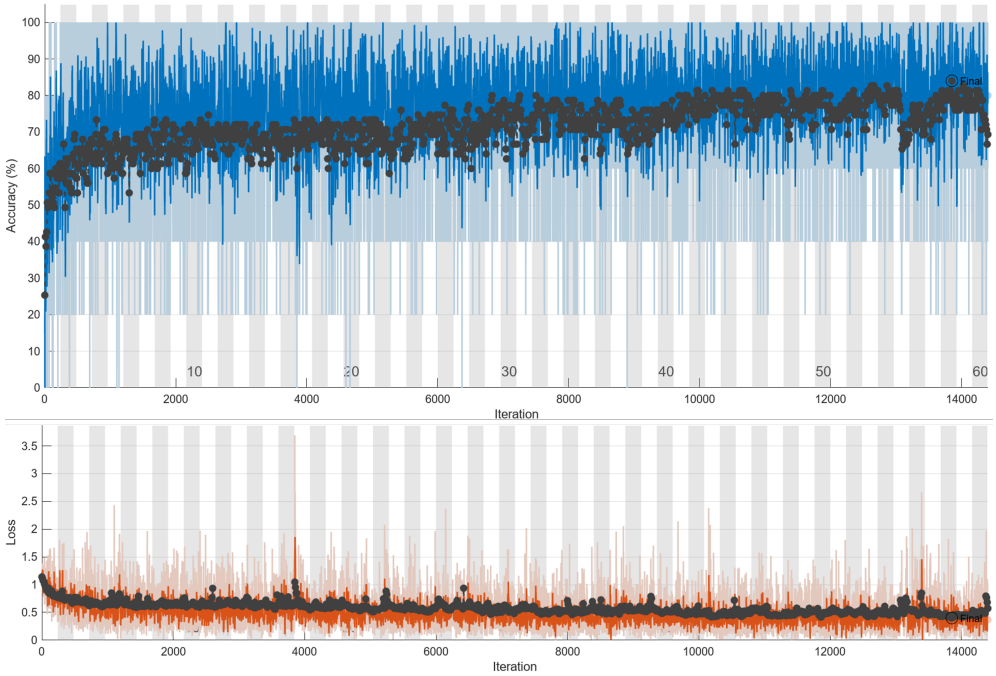

Figure 5.13: Training accuracy and loss for the RNN without FrFT cleaning

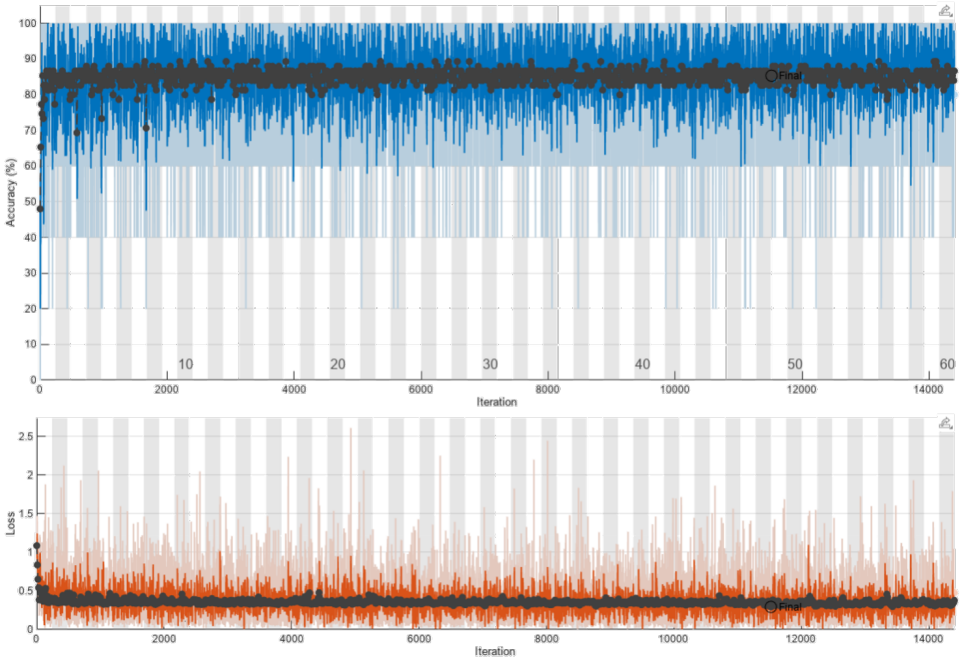

Figure 5.14: Training accuracy and loss for the RNN with FrFT cleaning

The confusion matrix in Figure 5.15a shows that the RNN classifies the -45deg

and 135deg classes with relatively high accuracy but encounters difficulties with the 45deg class. This challenge arises because the FS signals associated with 45deg closely resemble those of 135deg, which leads to frequent misclassifications. Specifically, the classification accuracy is 90.67% for the -45deg class, 78.67% for the 135deg class, and only 49.33% for the 45deg class, resulting in an overall accuracy of 72.89%.

When FrFT cleaning is applied, the results presented in Figure 5.15b indicate a clear improvement. In this case, the RNN classifies signals generated by targets within $[-45°, 45°)$ and $[135°, 225°)$ with accuracies of 96% and 98.67%, respectively. For signals in the range $[45°, 135°)$, the accuracy improves compared to the unprocessed case but remains lower at 60%, primarily due to confusion between the 45deg and 135deg classes. Averaging across all three classes results in an overall accuracy of 84.89%, which is consistent with the validation accuracy. As a consequence, the RNN with FrFt cleaning will be chosen, as it has proven to have higher accuracy.

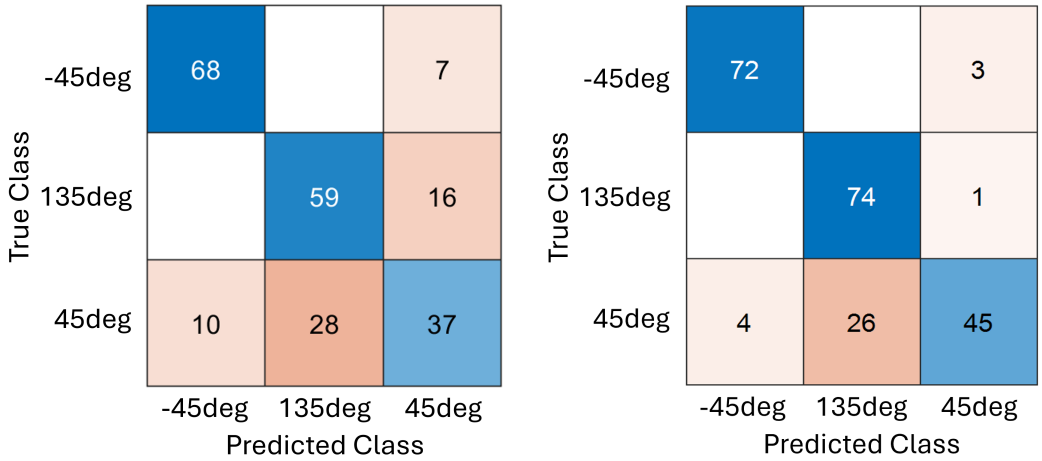

(a) Without FrFT cleaning (b) With FrFT cleaning

Figure 5.15: Confusion chart for the trained RNN using the validation signals

5.3.3 Zoom-in MF algorithm calibration for the different RNN classes

It is important that the zoom-in algorithm is calibrated for the different RNN classes, or subsets, to ensure that the full potential of the algorithm is reached and that the estimation is completed in under 10 min. The way of calibrating the algorithm is to use a Monte Carlo simulation in a similar manner to Section 5.2.3, but instead of using 50

iterations, for sake of time, 10 iterations will be employed. Table 5.4 shows summarizes the Monte Carlo parameters.

		Target				
Rx. alt.	**Tx. alt.**	**Altitude**	**Angle**	**Size**	**SNR**	**Num. ite.**
500 km	1200 km	[500, 1200] km	$[-45°, 45°)$	[0.2, 2]m	20 dB	10
			$[45°, 135°)$			
			$[135°, 225°]$			

Table 5.4: Monte Carlo parameters for the calibration of each of the tailored zoom-in algorithms

The chosen zoom-in parameters for the algorithm are shown in Table 5.5. The table also shows the time per iteration and the mean absolute error. While most of the calibration parameters are the same for the different classes, the $N_{alt|ang,i_L}$ are different. If the iteration time and the mean absolute errors are taken into consideration along with the $N_{alt|ang,i_L}$ values, it would imply that the tailored zoom-in algorithm for the 135deg is able to reconstruct the MF map with high level of detail under less time and with less number of computations.

Class	$\mathbf{M_{alt\|ang}}$	**L**	$\mathbf{N_{alt\|ang,i_L}}$	$\boldsymbol{\kappa_{i_L}}$
-45deg	10	3	[3, 5, 5]	[0.1, 0.15, 0.17]
45deg	10	3	[3, 5, 5]	[0.1, 0.15, 0.17]
135deg	10	3	[3, 3, 5]	[0.1, 0.15, 0.17]

(a) Parameters for tailored zoom-in MF algorithms

Class	$\mathbf{t_{ite}}$	$\boldsymbol{\bar{\mu}_{err,alt,MaxMF}}$	$\boldsymbol{\bar{\mu}_{err,alt,MinErr}}$
-45deg	13.06 min	198.68 km	76.20 km
45deg	9.70 min	171.89 km	55.91 km
135deg	6.50 min	76.15 km	21.75 km

(b) Time per iteration, mean error for the altitudes

Table 5.5: Tailored zoom-in algorithm parameters, time per iteration and mean errors

5.3.3.1 FrFT compensation method

It is evident that it would be most advantageous if all of the targets had an angle trajectory in [135°, 225°]. To accomplish it, a possible solution could be to somehow add a compensation for the $\Gamma_{T|R|p}$ term in (3.13), which would not be possible. Another solution involves analysing the FrFT angle that maximizes the time response of the FS signals of the different subsets. For the analysis 100 signals will be created for each subset using the parameters in Table 5.4, and the FrFT angle will be estimated.

The analysis of the FrFT angle, Figure 5.16 shows that, within the subsets, most of the FrFT angles remain confined to a set of values. With this information, a FrFT compensation technique is proposed. Specifically, the compensation involves adjusting the FrFT angle for each subset. The adjustment is calculated as the mean FrFT angle of the 135deg class minus the mean FrFT angle of the respective subset. This adjustment is then applied to the frequency-time representations, ensuring that the resulting FrFT angles closely align with the angle of the 135deg class. The mean angles from the analysis and compensation angles, $\phi_{FrFT,comp}$, are shown in Table 5.6.

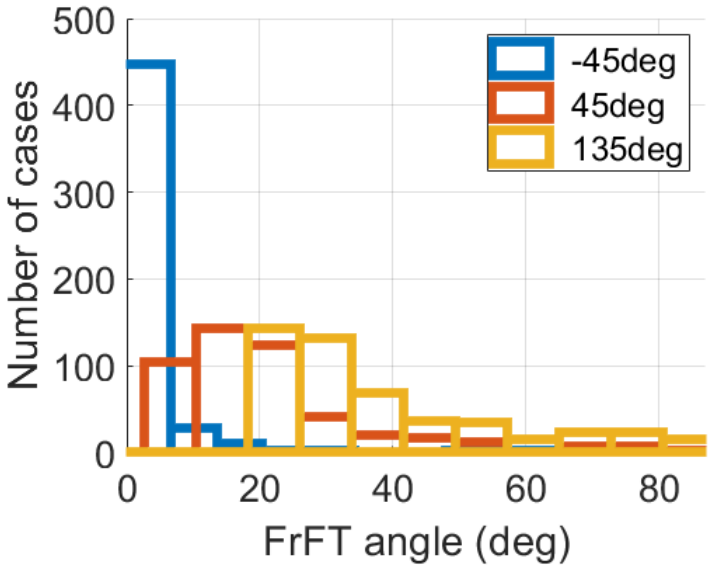

Figure 5.16: Histograms for the FrFT angles for different classes

Class	Mean FrFT angle	$\phi_{\mathbf{FrFT,comp}}$
-45deg	3.27°	33.11°
45deg	22.17°	14.21°
135deg	36.38°	0°

Table 5.6: Mean FrFT angles and compensation angles

5.3.4 RNN-zoom-in algorithm performance analysis

From Section 5.3.3, two different processing frameworks can be designed: one for the case where the tailored zoom-in algorithms are used, Figure 5.17, and one for the case where the FrFT compensation is used, Figure 5.18.

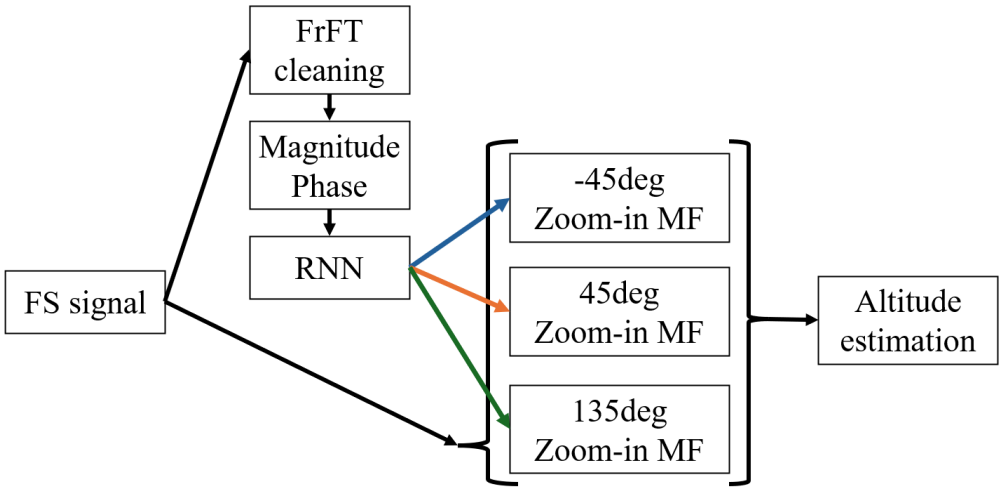

Figure 5.17: Diagram for the processing framework with tailored zoom-in MF algorithms

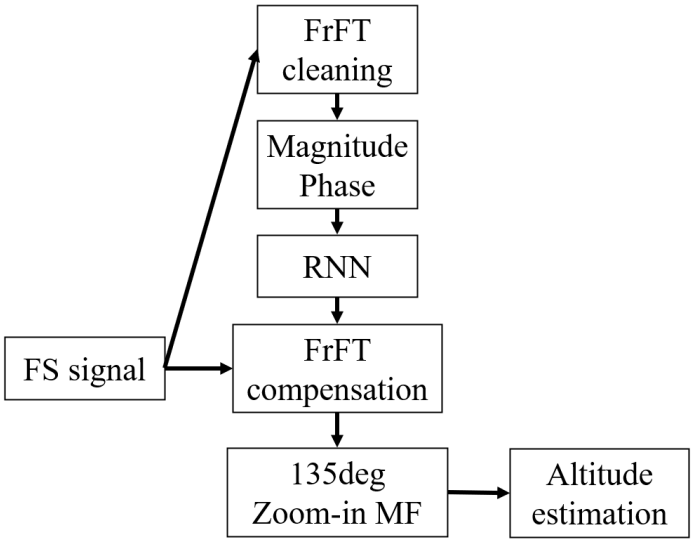

Figure 5.18: Diagram for the processing framework with FrFT compensation

5.3.4.1 Methodology

To evaluate the performance of the RNN–zoom-in MF algorithm, a Monte Carlo simulation will be conducted. The primary metric of interest is the error in estimating the target altitude, as it represents the most critical target parameter. Additionally, the score of the output of the RNN can be incorporated into the algorithm. As described in Section 3.3, the output score corresponds to the probability that a given input belongs to a particular class, providing a measure of confidence. Two approaches are taken to extract the altitude of the target:

1. Use a threshold of 85%, the accuracy from Figure 5.14, for the scores of the classification and pass it onto the zoom-in algorithm. If the score lowers from the threshold, the zoom-in approach will be employed without the classificator information.

2. Use the RNN without taking into account the scores and pass the information onto the zoom-in algorithm. The score of a classification is the probability that a certain signal is part of the predicted class. It is an indicator of how accurate the classification is for the processed signal.

The parameters listed in Table 5.5, Table 5.6, and Table 5.7 were used in the Monte Carlo simulations. To ensure that all simulations were conducted under consistent conditions, the FS signals were generated in advance, stored, and subsequently loaded into the simulation framework. A total of 100 iterations were completed, with all simulations performed in MATLAB on a PC equipped with 16 GB of RAM and an Intel i9-9900K CPU.

		Target				
Rx. alt	**Tx. alt**	**Altitude**	**Angle**	**Size**	**SNR**	**Num. ite.**
500 km	1200 km	[500, 1200]km	[0°, 360°]	[0.2, 2]m	20 dB	100

Table 5.7: Monte Carlo parameters for the receiver, transmitter and target

5.3.4.2 Results

This section presents the results obtained from the different proposed solutions that integrate the RNN with the zoom-in MF algorithm. The analysis focuses on evaluating both the accuracy and computational performance of these combined methods. In particular, the discussion emphasizes the role of the RNN in alleviating the computational burden of the zoom-in MF algorithm, demonstrating how it can guide the search process and reduce the number of computations required to achieve high-resolution correlation maps.

5.3.4.2.1. Results for the RNN-zoom-in MF algorithm with tailored parameters

Figure 5.19 Figure 5.20 show the histograms for the maximum MF map and minimum error altitude. The histogram for the maximum MF map, Figure 5.19a and Figure 5.20a, show a maximum error of 560 km. While the maximum error in Figure 5.19b and Figure 5.20b is 270 km. Moreover, the errors in the minimum altitude error lowers when the scores are used compared to when they are not. This is evident from the number of errors below 27 km, which is 30 when the scores are used, versus 35 when the scores are not considered. Regarding the observed distribution of errors for the maximum MF altitude, the distribution of errors is more spread if the scores are not considered than

if the scores are considered. The number of errors below 56 km is 30 and 25 for the case with scores and the case without scores.

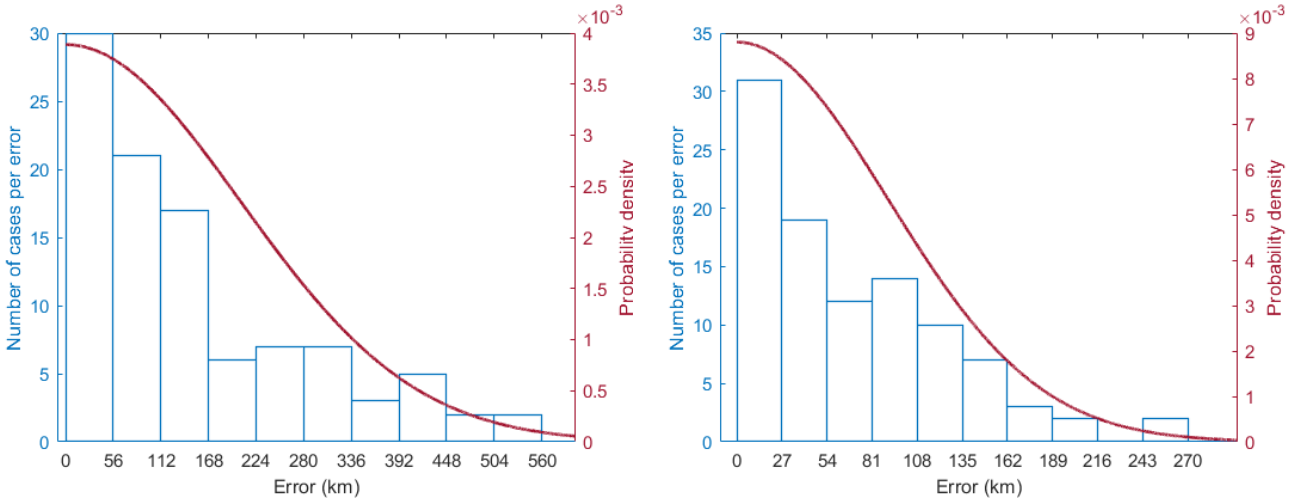

(a) Histogram of the maximum MF map altitude (b) Histogram of the minimum error altitude

Figure 5.19: Histograms of the errors for the RNN-zoom-in MF algorithm when using the scores

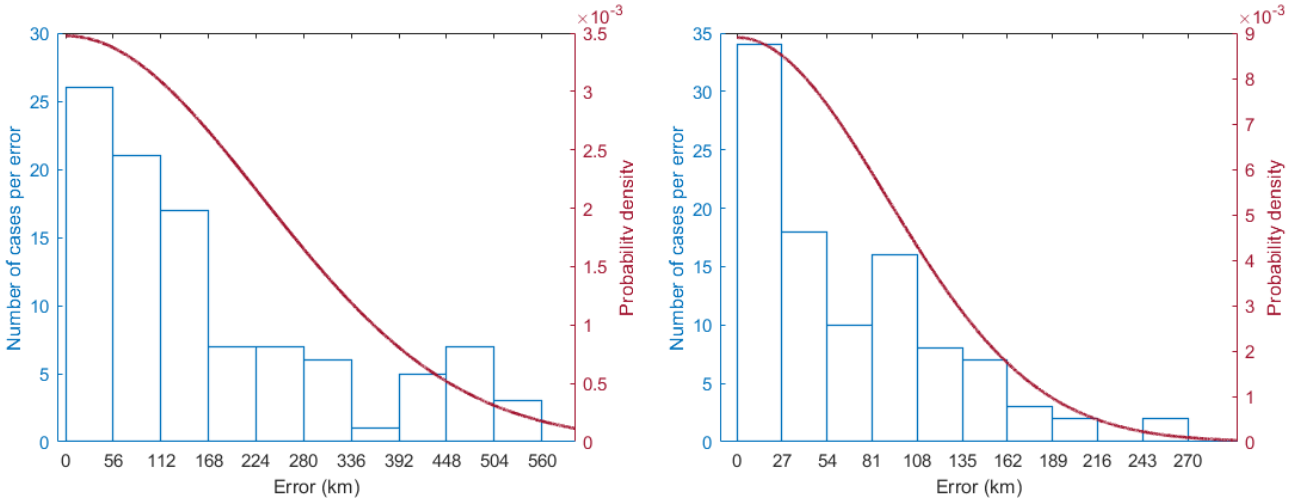

(a) Histogram of the maximum MF map altitude (b) Histogram of the minimum error altitude

Figure 5.20: Histograms of the errors for the RNN-zoom-in MF algorithm without using the scores

The error datasets pass the Chi-square goodness-of-fit test at the 5% significance level. The time per iteration, shown in Table 5.8, are 11.08 min and 9.06 min if the

scores are used and if the scores are not used, respectively. By looking at the values from Table 5.2 it can be noticed that compared to the zoom-in MF algorithm the algorithm with the RNN is faster. The mean and variance, $\bar{\mu}_{err,alt,MaxMF|MinErr}$ and $\sigma_{err,alt,MaxMF|MinErr}$, for the maximum MF map altitude and the minimum error altitude mathematically prove the deduced features about the distribution of errors observed in the histograms. It should be noted that the obtained parameters for the minimum error altitude, $\bar{\mu}_{err,alt,MinErr}$ and $\sigma_{err,alt,MinErr}$, are similar to the zoom-in MF algorithm, but with less computational time needed.

Case	$\bar{\mu}_{\mathbf{err,alt,MaxMF}}$	$\bar{\mu}_{\mathbf{err,alt,MinErr}}$	$\sigma_{\mathbf{err,alt,MaxMF}}$	$\sigma_{\mathbf{err,alt,MinErr}}$	$\mathbf{t_{ite}}$
1	152.78 km	68.71 km	205.27 km	90.67 km	11.08 min
2	171.41 km	66.87 km	229.54 km	89.63 km	9.06 min

Table 5.8: Mean of errors, variances for the Gaussian variables and time per iteration for the RNN-zoom-in MF algorithm

5.3.4.2.2. Results for the RNN-zoom-in MF algorithm with FrFT compensation

The histograms in Figure 5.21 and Figure 5.22 show the errors for the RNN-zoom-in MF algorithm with FrFT compensation. No major differences can be observed in the error distributions between the case when the scores are utilized and the case where the scores are ignored. An observation worth noting is the maximum value for the minimum error altitude, which is 250 km. This value would imply that, for the minimum altitude error, the algorithm is more precise than in the previous presented processing frameworks.

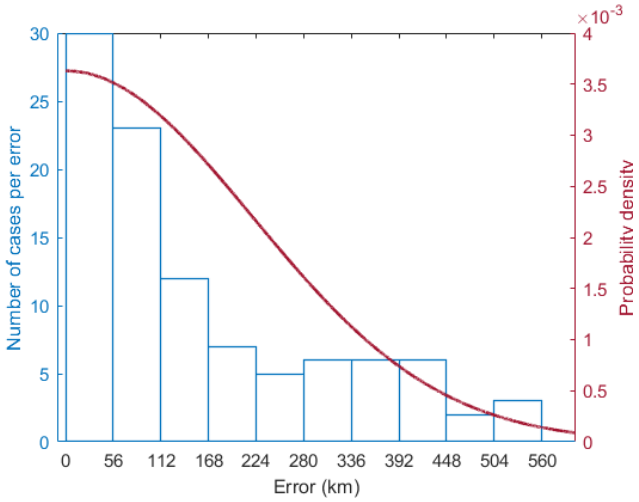

(a) Histogram of the maximum MF map altitude

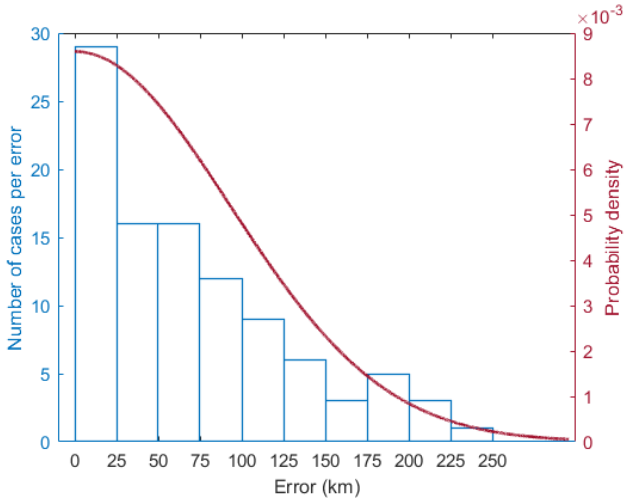

(b) Histogram of the minimum error altitude

Figure 5.21: Histograms of the errors for the RNN-zoom-in MF algorithm with FrFT compensation when using the scores

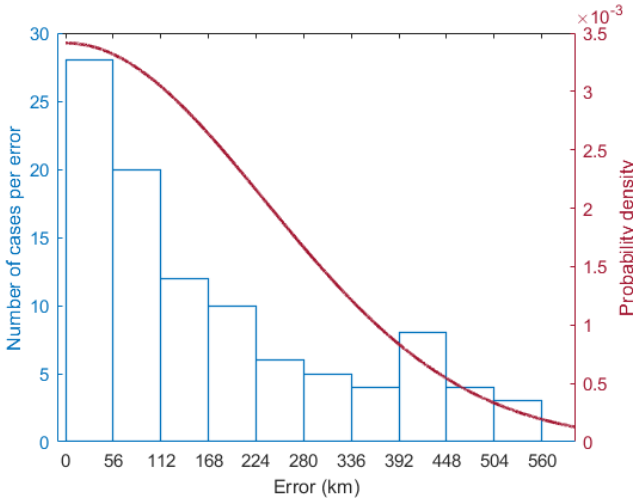

(a) Histogram of the maximum MF map altitude

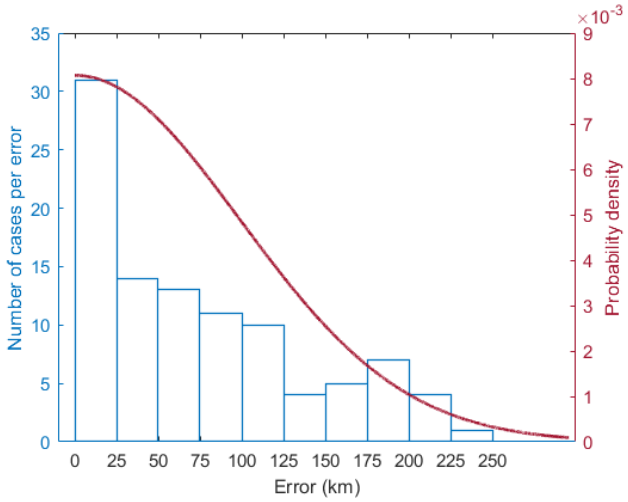

(b) Histogram of the minimum error altitude

Figure 5.22: Histograms of the errors for the RNN-zoom-in MF algorithm with FrFT compensation and without using the scores

Compared to the previous cases, the results in Table 5.9, demonstrate that algorithm for when the RNN is employed along the zoom-in MF algorithm with the FrFT compensation is faster. The mean and variance parameters, $\bar{\mu}_{err,alt,MaxMF|MinErr}$ and $\sigma_{err,alt,MaxMF|MinErr}$, are bigger than the previous case where no FrFT compensation

was implemented. However, the values are similar to the zoom-in MF algorithm but with less computational time, 5 min less if the scores are used and 7 min if the scores are neglected.

Case	$\bar{\mu}_{\mathbf{err,alt,MaxMF}}$	$\bar{\mu}_{\mathbf{err,alt,MinErr}}$	$\sigma_{\mathbf{err,alt,MaxMF}}$	$\sigma_{\mathbf{err,alt,MinErr}}$	$\mathbf{t_{ite}}$
1	161.87 km	70.75 km	219.81 km	92.84 km	9.05 min
2	174.22 km	74.70 km	233.67 km	98.89 km	7.19 min

Table 5.9: Mean of errors, variances for the Gaussian variables and time per iteration for the RNN-zoom-in MF algorithm with FrFT compensation

5.3.5 Conclusion on the RNN-zoom-in MF algorithm

The novel RNN-zoom-in MF algorithm improves upon the zoom-in MF approach. As demonstrated, the newly proposed processing frameworks are both faster and more accurate than using only the zoom-in MF algorithm. The RNN reduces the search grid of the zoom-in MF algorithm by classifying the received FS signal into three different angle subspaces. Additionally, the RNN consists of two bi-LSTM layers and is trained with random diameters, random altitudes, and random angles within the defined angle subspaces.

Two different strategies were considered for integrating the RNN with the zoom-in MF algorithm. In the first approach, the zoom-in MF algorithm was tailored to each subset of outputs provided by the RNN. In the second approach, the RNN outputs were used to rotate the FS signal in the time–frequency plane via the FrFT, producing a signal aligned with the 135deg class. The error analysis indicates that FrFT-based compensation yields the lowest computational time. Conversely, the combination of the RNN with tailored zoom-in MF algorithms provides superior accuracy if the minimum altitude error is selected. Furthermore, incorporating the RNN output scores improves estimation accuracy compared to using only the class labels. Although this approach increases computational time, by approximately 2 min per signal, the mean error is reduced, demonstrating a favourable trade-off between accuracy and computational cost.

To place the proposed approach into perspective, it is instructive to compare its performance with that of the conventional MF method. As shown in Sections 5.2.4 and 5.3.4.2, the final altitude resolution achieved was approximately 42.80 m, and the final angular resolution was 0.0066°. Over a search space of 700 km in altitude and 360° in angle, this corresponds to nearly 8.9210×10^8 signals that would need to be generated and correlated using the standard MF approach. In [24], it is assumed that the signals are pre-generated, thereby avoiding regeneration for each received signal. Even with this assumption, and with a correlation time of 5.051 ms per signal, the computation time required to estimate the motion parameters from a single FS signal would be on the order of 52 days, which is clearly impractical.

Introducing an RNN to reduce the search grid decreases the number of required correlations to approximately 2.2302×10^8, lowering the computation time to about 13 days per signal. However, this process would still need to be repeated for 100 signals and would require substantial memory to store the large number of FS signals. By contrast, the RNN–zoom-in algorithm achieves the same level of accuracy in a fraction of the time, demonstrating its clear advantage over the conventional MF approach in terms of computational feasibility.

5.4 Conclusion on the novel signal processing methods and algorithms for spaceborne radar

In conclusion, this chapter has explored the developed novelties in signal processing for the spaceborne segment, presenting improvements in the estimation of the altitude of space objects. First, in Section 5.2, the novel zoom-in MF algorithm was introduced, which improves upon the traditional MF algorithm by creating MF maps more efficiently.

In Section 5.3, the RNN-based zoom-in MF algorithm was presented, further enhancing the zoom-in approach. By incorporating an RNN classifier, the search grid is reduced, alleviating the computational load. The results show that integrating the RNN significantly improves computational efficiency, which is crucial when processing large amounts of FS signals. The FrFT-based approach is particularly effective for min-

imizing altitude error, while the tailored zoom-in MF algorithm performs better when the maximum MF map altitude is passed to the orbit propagator.

Section 5.2.5 has shown that, due to the increased complexity of the zoom-in algorithm, the estimation is completed faster than with the MF algorithm, as it focuses on computing the area around the maxima of the MF maps, provided that the number of loops in the algorithm is not excessively high.

Table 5.10 summarizes the results of the algorithm for the extraction of the altitude of the target. The different solutions that have been proposed are:

A. **Zoom-in MF algorithm without using the RNN.** This represents the simplest case, where only the zoom-in algorithm is employed, without involving the RNN.

B. **RNN-zoom-in MF algorithm with tailored parameters and scores.** A decision threshold is set for the classification output. If the score falls below this threshold, the zoom-in MF algorithm is applied without utilizing any information from the RNN. Conversely, if the score exceeds the threshold, the information provided by the classifier is incorporated into the tailored zoom-in MF algorithm corresponding to the predicted class.

C. **RNN-zoom-in MF algorithm with tailored parameters and without scores.** The zoom-in MF algorithm, which has been specifically designed to correspond to the predicted class, is employed in every instance, independent of the obtained scores.

D. **RNN-zoom-in MF algorithm with FrFT compensation and with scores.** As in Case B., a threshold is defined. When the score falls below this threshold, the zoom-in MF is applied directly, without any additional information. If the score exceeds the threshold, the FrFT compensation is performed, and the FS signal is passed through the 135deg class–specific zoom-in MF algorithm.

E. **RNN-zoom-in MF algorithm with FrFT compensation and without scores.** The FrFT compensation is employed with the information of the RNN

regardless of the value of the scores. Then, the compensated FS signal is passed through the zoom-in MF algorithm corresponding to the 135deg class.

Case	$\bar{\mu}_{\mathbf{err,alt,MaxMF}}$	$\bar{\mu}_{\mathbf{err,alt,MinErr}}$	$\mathbf{t_{ite}}$
A.	177.77 km	65.58 km	14.40 min
B.	152.78 km	68.71 km	11.08 min
C.	171.41 km	68.87 km	9.06 min
D.	161.87 km	70.75 km	9.05 min
E.	174.22 km	74.70 km	7.19 min

Table 5.10: Mean of errors and time per iteration for the various proposed solutions

If the maximum MF map altitude is chosen as the algorithm output, the optimal solution is Case B., corresponding to the RNN–zoom-in MF algorithm with tailored parameters and the use of scores. This approach is also less computationally demanding than the zoom-in–only algorithm. Conversely, if the priority is to minimize computation time, the most suitable solution is Case E., which employs the RNN–zoom-in algorithm with FrFT compensation and without scores. This strategy likewise requires less computational effort than the zoom-in–only approach. When the output is the minimum error altitude, Case A., corresponding to the zoom-in–only approach, achieves the best accuracy. However, Case C. provides a comparable level of accuracy while reducing computational time, making it a more efficient alternative. Similarly, Case D. offers a favourable trade-off between accuracy and computational cost for the maximum MF altitude case.

Chapter 6

Advanced signal processing techniques for long baseline ground-based distributed systems for SSA

This chapter covers the novel signal processing techniques that have been used for the data fusion and the ambiguity assessment in the radar measurements of multi-static long-baseline ground-based radars. One of the main characteristics of this system is that it is a single-input-multiple-output (SIMO) radar with long bistatic baselines. This means that there is one transmitter and multiple receivers, in which each bistatic pairs has a long baseline. The novelty in this chapter is the use of the MIMO AF from Section 6.2 when solving the localization problem of long baseline bistatic pairs.

6.1 Introduction

With the development of multi-static ground-based radars there is the need of developing a way of fusing the different radar measurements from the different bistatic pairs. A very useful tool is the MIMO AF. In a similar way to the multiple integration, the MIMO AF is able to non-coherently or coherently add the individual AFs sourced from the different bistatic pairs.

6.2 Multiple-input-multiple-output (MIMO) ambiguity function (AF)

Because of the architecture in this chapter, the MIMO AF is going to be introduced, as it is a useful processing tool that can be used to combine different bistatic signals.

A way to assess the performance and limits of a radar system is the Ambiguity Function (AF). In classic radar, the AF for a single transmitter and single receiver system is defined as the output of a matched filter for a certain waveform and different values of delay and Doppler shift [1]. Since the matched filter is in essence a correlation filter, the AF could also be interpreted as how similar the transmitted signal is with respect to signals with different ranges and Doppler shift. Mathematically can be expressed as:

$$AF(\tau_\Delta, f_D) = \int_{-\infty}^{\infty} s(t) \cdot s^*(t - \tau_\Delta) e^{j2\pi f_D t} dt, \tag{6.1}$$

with τ_Δ being the delay of the signal and f_D the Doppler shift.

The MIMO AF approach employed in this study was originally presented in [123], naturally, it has been adapted for the case at hand. In a similar way as in [124], the radar parameters of range and Doppler rate are replaced by its Cartesian equivalents of position and speed. The reason behind using Cartesian coordinates is that it will be more helpful for performing later SSA tasks [62] and is easier to visualize, having similar plots as in [125]. In the paper, a AF is introduced for multiple-inputs-single-outputs (MISO) systems. If the MISO AF is generalized, the MIMO AF can be deduced. First, the AF of one of the bistatic pairs is described as:

$$AF_{a,b}(\vec{p}, \vec{v}) = \int_{-\infty}^{\infty} s_{a,b}(t, \vec{p}_c, \vec{v}_c) \cdot s^*_{a,b}(t, \vec{p}, \vec{v}) dt, \tag{6.2}$$

where $\vec{p} = (p_x, p_y, p_z)$ is the position vector, $\vec{v} = (v_x, v_y, v_z)$ the speed vector, $s_{a,b}(t, \vec{p}_k, \vec{v}_k)$ is a signal transmitted from the transmitter a and received at the receiver b assuming a target at the position $\vec{p}_c = (p_{c,x}, p_{c,y}, p_{c,z})$ with a speed of $\vec{v}_c = (v_{c,x}, v_{c,y}, v_{c,z})$. Note that compared to the traditional definition in (6.1), here the delay and Doppler have been replaced with the 3-dimensional position and velocity parameters which allows us to use a common space for all sensor pairs.

Combining the AF of the different transmitter-receiver pairs, the MIMO AF can now be defined as:

$$AF(\vec{p},\vec{v}) = \sum_{a=1}^{N_{bs}} \sum_{b=1}^{M_{bs}} AF_{a,b}(\vec{p},\vec{v}). \tag{6.3}$$

Hence, here the MIMO AF is defined as the sum of the AF of the different bistatic pairs. In (6.3) this sum is done coherently, also called coherent fusion, which implies that good synchronization between the different sensors is necessary. An alternative approach is to sum the AF from the different pairs non-coherently, non-coherent fusion:

$$AF(\vec{p},\vec{v}) = \sum_{a=1}^{N_{bs}} \sum_{b=1}^{M_{bs}} |AF_{a,b}(\vec{p},\vec{v})|. \tag{6.4}$$

6.2.1 Different forms of the MIMO AF

To reduce complexity, the MIMO AF in (6.2) can be simplified if the different speed component values are replaced by the Doppler shift resulting from the perceived speed:

$$AF_{i,j}(\vec{p}; f_{D;a,b}) = \int_{-\infty}^{\infty} s_{a,b}(t;\vec{p}, f_{D;a,b;k}) \cdot s^*_{a,b}(t;\vec{p} f_{D;a,b}) dt, \tag{6.5}$$

where $f_{D;a,b}$ is the Doppler frequency shift perceived from transmitter a at receiver b.

As different Doppler shifts are perceived from each bistatic pair, the $f_{D;a,b}$ returning the maximum response in each AF can be used to synthesise the MIMO AF:

$$AF(\vec{p}) = \sum_{a=1}^{N_{bs}} \sum_{b=1}^{M_{bs}} \max_{f_{D;a,b}} |AF_{a,b}(\vec{p}, f_{D;a,b})|, \tag{6.6}$$

$$AF(\vec{p}) = \sum_{a=1}^{N_{bs}} \sum_{b=1}^{M_{bs}} \max_{f_{D;a,b}} AF_{a,b}(\vec{p}, f_{D;a,b}). \tag{6.7}$$

It should be noted that in (6.6) the AF from the different pairs are added non-coherently. Further, this definition can only be applied in the single target scenario or the multiple target scenario where the targets are at different positions but have similar velocity parameters.

6.3 Radar system characterization

For the system characterization various components and properties of the employed radar system are introduced. These are going to be used in later simulations and analysis. At the current, stage the system would only be able to detect small satellites in LEO, around half the size of a Starlink satellite, and large satellites in GEO, as discussed on Section 6.4.2.

The radar system will not be a search radar, and, as such, it will not be scanning the whole space, from horizon to horizon. Since many space objects, from satellites to space debris, have two-line element (TLE) sets [126], the ephemerides, the trajectories, of these could be calculated. The position of said space objects could be estimated and, using this prior knowledge, the radio telescopes could be pointed to that location. Once this is completed, the signal processing, using the MIMO AF, could be performed and a constant false alarm rate (CFAR) detector [127] could be used to detect the possible targets.

As a reminder, the configuration described in Section 3.2.1 is used in this chapter. For reference, the configuration is shown again in Figure 6.1. In this setup, β represents the bistatic angle, Tx and Rx denote the transmitter and receiver, respectively, and $L_{Tx,Rx}$ corresponds to the baseline. In this case, the bistatic range is given by:

$$R_{bs} = d_{Tx} + d_{Rx} \tag{6.8}$$

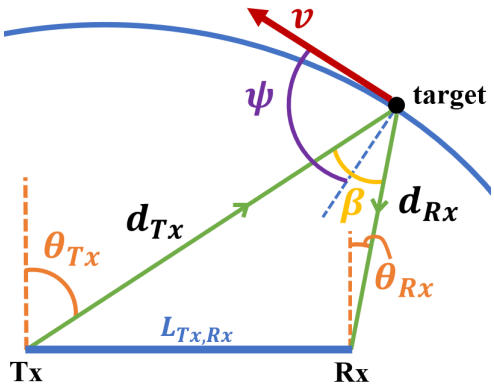

Figure 6.1: Bistatic configuration

6.3.1 Long baseline multistatic radar challenges in SSA

In SSA, the expected operating ranges are very large. This could result in aliasing problems in the Doppler processing specially when working with long baseline bistatic systems. For instance, assuming a transmitter in the Haystack Observatory, Massachusetts, USA, and a receiver near Westerbork, Netherlands, as in [61], if the target to be detected is at an altitude of 600 km, the PRI should be at least 20.02 ms, an equivalent PRF of 49.96 Hz. This means that the maximum speed that the radar would be able to detect, assuming an operational frequency of 1.24 GHz is $v_{max} = PRF \cdot \lambda/4 = 3.02\,\mathrm{m\,s^{-1}}$. The orbital escape speed is [128]:

$$v_{esc} = \sqrt{\frac{2G_c M_{earth}}{r_{trg}}}, \tag{6.9}$$

with G_c being the gravitational constant of the Earth, M_{earth} the mass of the Earth, and $r_{trg} = R_{earth} + h_{tgr}$, R_{earth} being the radius of the Earth, and h_{tgr} the altitude of the satellite. Using (6.9), the resulting speed of the target should be at least $v_{esc} = 10.69\,\mathrm{km\,s^{-1}}$. If the angular speed of the rotation of the Earth is considered, $72.92\,\mu\mathrm{rad\,s^{-1}}$, the relative speed of the target is $10.19\,\mathrm{km\,s^{-1}}$. By using (3.20), with $\beta = 47.98°$, from the configuration in [61] and $\psi = 80°$, so that the Doppler is not zero, the perceived Doppler shift is $f_D = 13.73\,\mathrm{kHz}$ Thus, the PRF needed to detect the target would produce aliasing in Doppler. Consequently, a correct Doppler processing scheme must be adopted to avoid aliasing. In [129, 130] solutions have been presented to solve the aliasing in space environments. Additionally, in [131] a two step solution is presented for high speed targets, and a similar approach could be taken to overcome the Doppler aliasing.

On one hand, regarding coherent integration processing for LEO targets, as they have high speeds, the target would change between range bins and the coherent processing interval (CPI) would be small. Range compensation techniques would be needed to have larger CPIs. On the other hand, when it refers to the coherent fusion processing, by examining (3.20) it is easy to see how different bistatic pairs will generate different Doppler shifts. To be able to implement coherent multiple fusion Doppler compensation

will be needed. The main implication for this issue is that between the bistatic pairs there must be good synchronization and that the systems must be properly defined to account for phase errors or different Doppler frequencies.

In cases of GEO targets, the relative speed is almost zero [132], as it matches the rotation of the Earth, so the multiple coherent integration, in this case, would be much simpler and less pre-processing for it will be necessary. The perceived zero-speed allows for longer integration times without range compensation, since the target does not change range bin. In addition, coherent multiple sensor fusion when using the MIMO AF is also more direct, as there is no need for Doppler compensation since the perceived speed is zero.

6.4 Radar system validation

To validate the proposed radar system configuration, a series of simulations are going to be reproduced to assess the feasibility of the multistatic system. It must be mentioned that most of the results that are going to be shown are the outcomes of one of the bistatic pairs, since the rest of the results for the bistatic pairs are going to be similar. For the results to be as most realistic as possible, transmitter and receiver parameters of known radio telescopes are chosen.

6.4.1 Transmitter and receiver

The transmitter used in the simulation is located in MIT Haystack Observatory, USA, and uses the Millstone Hill Radar (MHR). MHR is a 25.6 m radius full steerable mechanical antenna. The location of the receiver is in Cambridge, United Kingdom, and uses one of the antennas of the Mullard Radio Astronomy Observatory (MURA). MURA is comprised of several radio telescopes with antennas of different sizes and for the sake of comparison, it is assumed that the antenna has a radius of 25 m. The gain values of the antennas are shown in Table 6.1. Knowing the radius of the antenna and assuming

an efficiency of 70%, the antenna gain can be computed using [133]:

$$G_{pa} = e_A \left(\frac{\pi d_{pa}}{\lambda} \right)^2, \tag{6.10}$$

where e_A is the antenna efficiency, d_{pa} is the antenna diameter and λ the operating wavelength.

	Gain
MHR	55.29 dB
MURA	55.08 dB

Table 6.1: Gain values for MHR and MURA

As discussed on Section 6.3 the transmitted waveform is a LFM chirp. The rest of the parameters for the simulation are presented on Table 6.2 as per [134, 135].

Center frequency (f_0)	1.295 GHz
Bandwidth (B_W)	2 MHz
Peak power	3000 kW
Pulse width (τ)	1 ms
Pulse Repetition Interval (PRI)	25 ms
Pulse Repetition Frequency (PRF)	40 Hz
Max. average power	120 kW

Table 6.2: Transmitter parameters

Circular polarization was selected for this study because it reduces power losses caused by the Faraday rotation effect in the L-band, which arises due to ionospheric interactions [136]. Beyond polarization effects, the ionosphere introduces additional challenges, such as phase distortions and frequency shifts, which must also be mitigated to ensure accurate signal processing. In [137], a method based on the *map drift* algorithm was proposed to correct ionospheric anomalies in spaceborne radar observations without requiring prior knowledge of the total electron content. This approach offers a significant advantage over methods that depend strongly on electron content estimation.

For instance, in [138], the study demonstrated that artifacts in the received signal could be minimized in a dawn–dusk sun-synchronous orbit and subsequently corrected using a background ionospheric model. While such techniques were originally developed for radar systems transmitting from space toward Earth, analogous approaches could be adapted and applied to the bistatic radar configuration investigated in this work.

6.4.2 Targets

To assess the feasibility of the proposed system, targets at different orbital altitudes were simulated. For the LEO case, synthetic orbits were generated at several altitudes, while for the GEO case, the orbit of the Alcomsat-1 satellite was replicated. The corresponding orbital parameters are listed in Table 6.3. The semi-major axis was calculated as the sum of Earth radius and the altitude provided in the parameter table. For the Alcomsat-1 satellite, orbital parameters were extracted from Two-Line Elements (TLEs) dated 16 January 2020. TLEs are standardized data files containing orbital elements from which the position of a satellite can be calculated and propagated over time [126].

In terms of physical dimensions, Alcomsat-1 has a size of $2.36 \times 2.1 \times 3.6\,\mathrm{m}^3$, whereas the synthetic LEO satellite was modelled as approximately half the size of a Starlink satellite, with dimensions of $75 \times 30 \times 20\,\mathrm{cm}^3$, excluding the solar panels. These dimensional assumptions are necessary to provide RCS estimates for the analysis. The monostatic RCS values were obtained using the *rcs* function from MATLAB, which implements the physical optics (PO) method [139]. RCS values were estimated across all azimuth and elevation angles of the cuboid models, and the mean value was then calculated. To account for modelling uncertainties and potential errors, 3 dB were subtracted from the mean before applying the result. Then, the bistatic RCS was computed using (3.19). The values of the bistatic RCS where used in the link budget calculations presented in Section 6.4.3.

	Alcomsat 1	LEO target
Norad ID	43039	-
Inclination (°)	12×10^{-3}	52
Eccentricity	2.16×10^{-4}	2.54×10^{-4}
Epoch year	2020	2020
Epoch day	16.7935	16.7935
Mean anomaly	98.993°	98.993°
Ascending node	302.9646°	302.9646°
Argument of periapsis	334.5991°	334.5991°
Altitude (km)	35 794.72	$[1200 - 2200]$
RCS	$15.17\,\mathrm{dB\,m^{-2}}$	$-17.61\,\mathrm{dB\,m^{-2}}$

Table 6.3: Orbit parameters and RCS for targets

6.4.3 Link budget and visibility analysis

This section evaluates the possible observation time and the expected SNR of the proposed system for the selected targets. These two aspects are essential, as the observation time defines the duration for which a target can be monitored, while the SNR determines the quality of the received signal and the likelihood of successful detection. The evaluation is carried out using the parameters defined in Section 6.4.1, ensuring consistency across all scenarios.

With respect to target visibility, the observation time for a GEO satellite can be considered theoretically infinite, as its apparent position remains essentially constant relative to the observer. By contrast, the visibility of LEO targets was determined by propagating their orbits over a 24-hour period. A target was assumed to be observable when it simultaneously was within the beamwidths of both the transmitting and receiving antennas and when the antenna pointing elevation exceeded 8.1°. This minimum elevation threshold was selected in accordance with the operational constraints of the Effelsberg Radio Telescope [140].

Figure 6.2 illustrates the target visibility time over a 24-hour period. More specif-

ically, Figure 6.2a presents the maximum, mean, and minimum visibility times per observation instance, while Figure 6.2b depicts the cumulative visibility time across the full 24 h. As expected, the observation time increases with target altitude. At lower altitudes, the target may fall below the effective horizon of either the transmitter or the receiver, thereby reducing the overall visibility time. At an orbital altitude of 1100 km, the cumulative observation time amounts to only 43 s, with a mean of 21.6 s per instance, which may be insufficient for reliable detection. By contrast, at 1200 km, the cumulative visibility time reaches 3.03 min, with an average of 1 min per instance—generally adequate to ensure detection. At higher altitudes, visibility times continue to increase, with a maximum cumulative duration of approximately 30 min and up to 7.98 min per instance observed at 2200 km. It can be observed that the variations in maximum and minimum visibility times exhibit a periodic-like behaviour as the altitude increases. Furthermore, the cumulative observation time at 1800 km is greater than that at 1900 km. This occurs because the orbit propagation was limited to 24 h, making the results dependent on the specific simulated scenario. Nonetheless, the simulation provides a useful overview of the expected observation times.

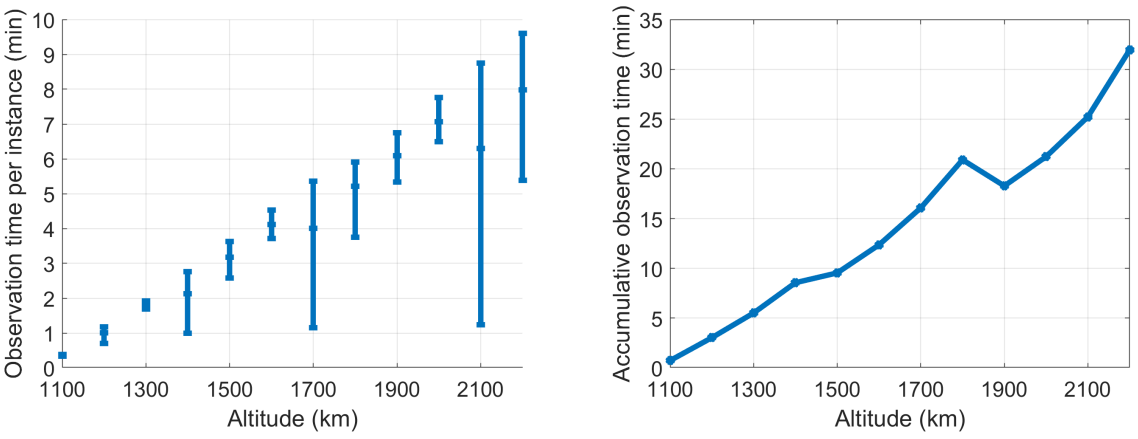

(a) Observation time per instance

(b) Accumulated observation time in 24 h

Figure 6.2: Observation time for different altitudes

The SNR is computed using the RRE in for a bistatic configuration assuming co-

herent integration [1, 32] from during the periods where the target is visible:

$$\mathrm{SNR}_{\mathrm{bs}} = n_p \frac{P_t G_t G_r G_{sp} \lambda^2 \ \mathrm{RCS}_{\mathrm{bs}}}{(4\pi)^3 \, R_1^2 R_2^2 k T_0 F B_W L_s}, \tag{6.11}$$

where

- n_p is the number of coherently integrated pulses. For the simulations $n_p = 25$ for the LEO target and $n_p = 50$ for the GEO target.
- P_t is the transmitting power.
- G_t is the transmitter antenna gain.
- G_r is the receiver antenna gain.
- G_{sp} is the signal processing gain, defined as:

$$G_{sp} = \tau \cdot B_W. \tag{6.12}$$

- λ is the operating wavelength.
- R_1 is the distance from the transmitter to the target.
- R_2 is the distance from the target to the receiver.
- k is the Boltzmann constant.
- T_0 is the reference noise temperature, 290 K.
- F is the noise factor. In this case, $F = 3.62$ dB, derived from the 150 K system temperature from the technical notes of the MHR [141].
- The losses, L_s, comprise four different categories:
  - System losses, which are 6 dB, accounting for 3 dB per path.
  - Dry air atmospheric losses. Which for a two-way path are estimated at 2.4 dB.

- Atmospheric losses for air containing vapour water, to account for any cloud or humid environment assumed at 2.6 dB.
- Tropospheric losses, assumed at 1.6 dB.

Atmospheric and tropospheric losses will vary with range, which can affect the resulting SNR. In this analysis, these losses were calculated for the longest slant range, considering the altitude of the troposphere and the atmosphere. As such, the computed values correspond to a worst-case scenario. The resulting loss, 6.6 dB*, is relatively modest and can be regarded as an error margin, ensuring that performance requirements are satisfied even under the most unfavourable conditions.*

The mean SNR for the geostationary target is 19.60 dB, with a variation of only $\pm 5.72 \times 10^{-6}$dB. Since the relative position of the Alcomsat satellite remains nearly constant, the resulting SNR shows negligible fluctuations during the observation period. In contrast, the SNR of the LEO target, shown in Figure 6.3, exhibits significant variations, particularly at higher altitudes. This effect arises because longer visibility times at greater altitudes allow for more pronounced fluctuations in the received signal. Furthermore, the mean SNR decreases with increasing altitude, as the satellite is located farther from both the transmitter and the receiver. As with the observation time, the SNR variations follow a repeating pattern determined by the simulated scenario.

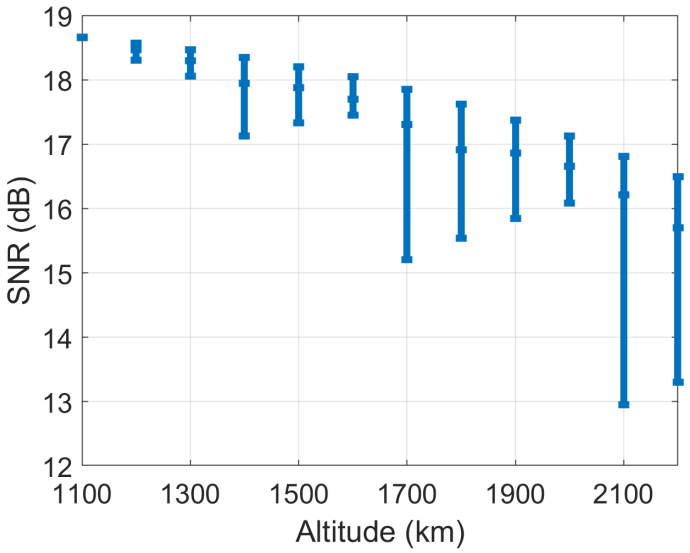

Figure 6.3: SNR variation for 24 hours for LEO target

6.5 System performance

Having assessed the feasibility of the radar system, this section investigates the performance of the proposed long baseline radar under different sensor and target configurations. For measuring the ambiguity of the radar measurements the multiple-input-multiple-output (MIMO) ambiguity function (AF), introduced in Section 6.2, will be used.

6.5.1 Simulated scenarios

The different radar configurations examined in this analysis are summarised as:

- **Monostatic case**. In the case of the monostatic configuration, the transceiver will be placed in the same location as the MHR antenna.
- **Bistatic case**. In the case of the bistatic case, the receiver will be placed depending on which multistatic receiver configuration is being studied. The different receiver configuration cases are presented in the next point.
- **Multistatic case**. In the multistatic case, only one transmitter is assumed,

located in MHR, while several receiver configurations are considered:

- **Case 1**: cluster of receivers. The main advantage of the cluster, or any of the multiple receiver configurations, is that the overall SNR would increase by the number of receivers. Also, it would be easier to synchronize and manage the receivers if they are closer. The cluster of receivers takes its location from the eMerlin radio telescope network based in the UK. The chosen locations are:
  - Jodrell Bank:
    - Lovell telescope. Coordinates (53.2366, −2.3085, 10)
    - Mark II telescope. Coordinates (53.2339, −2.3039, 10)
  - Pickmere. Coordinates (53.2886, −2.4453, 10)
  - Darnhall. Coordinates (53.1563, −2.5357, 10)
  - Knockin. Coordinates (52.7902, −2.9971, 10)
  - Defford. Coordinates (52.1005, −2.1443, 10)
- **Case 2**: receivers spread throughout the world. The spread configuration would allow to decrease the ambiguity as the target is observed from different angles. However, separating the receivers so far from each other, would make synchronization challenging. The positions of these receivers are based on pre-existing radio telescopes or observatories. Evidently, many of these pre-existing radio telescopes function at a different operating frequency than the one used in MHR, but it is assumed in the simulation that every receiver works at the same frequency. The locations of the receivers are:
  - Azores archipelago. The receiver is located in the RAEGE station in the island of Santa Maria. Coordinates (36.9852, −25.1259, 276)
  - Spain. This receiver is located in the Yebes Observatory. Coordinates (40.5241, −3.0893, 980)
  - Canary Islands. The receiver would be based in the Teide Astronomic Observatory. Coordinates (28.2986, −16.5106, 2400)

    - Ghana. The receiver in Ghana is located in the Ghana Radio Astronomy Observatory. Coordinates (5.7503, −0.3051, 70)
    - Guyana. Although there is no radio telescope, it is assumed that the receiver would be located in the rocket launch facilities of the French Guyana. Coordinates (5.2264, −52.7774, 2)
    - Puerto Rico. The antenna would be located in the old Arecibo Observatory. Coordinates (18.3442, −66.7526, 498)

- **Case 3**: combination of both Case 1 and Case 2. For this case there would be two receivers per cluster. The distance between the receivers in the cluster is around 200 km. The locations of the receivers are:
    - Azores archipelago. One of the receivers will be placed in the RAEGE Santa Maria station and the other one is located at SATCOM Earth Station. The coordinates are:
        - Azores I: (36.9852, −25.1259, 276)
        - Azores II: (37.7908, −25.6649, 238)
    - Ghana. The first receiver will be placed in the same place as in the previous configuration, the Ghana Radio Astronomy Observatory, the second one 200 km away from there. The coordinates are:
        - Ghana I: (5.7503, −0.3051, 70)
        - Ghana II: (7.4244, −0.8833, 70)
    - Spain. One of the receivers will be placed on the Yebes Observatory and the other one will be placed on the Javalambre Astrophysics Observatory. The coordinates of the receivers would be:
        - Spain I: (40.5241, −3.0893, 980)
        - Spain II: (40.0419, −1.0162, 1957)

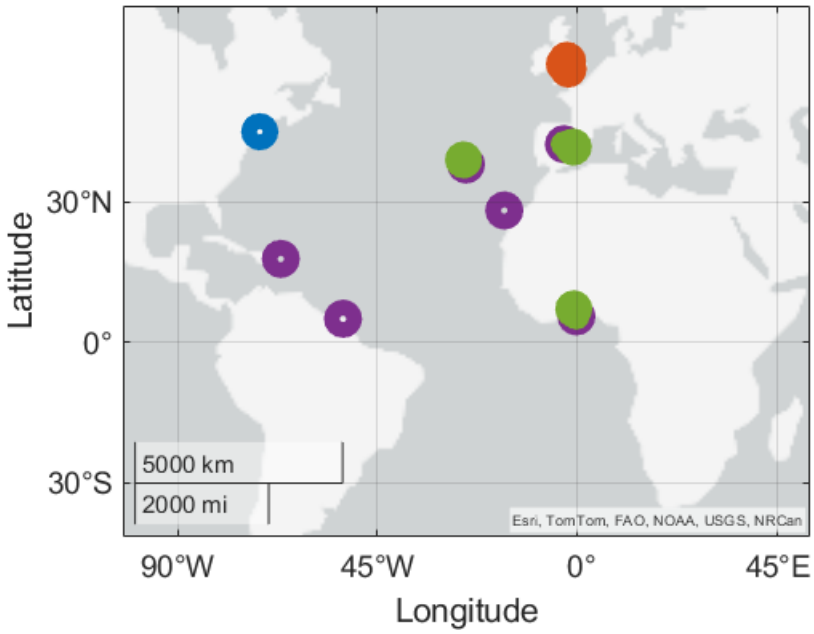

Figure 6.4: Position of the transmitter (blue) and receivers (orange for Case 1, purple for Case 2 and green for Case 3)

6.5.1.1 Receiver and transmitter parameters

By virtue of simplicity, an SNR of 22 dB and 19.60 dB is assumed for the LEO and GEO targets, respectively, at the receiver after the matched filter and multiple integration. The SNR after the matched filter and the multiple coherent integration can be calculated as:

$$\begin{aligned} SNR_{n_p} &= SNR_{ant} + 10\log(n_p) + 10\log(G_{sp}) - 3\,\text{dB} \\ &= SNR_{ant} + 10\log(n_p) + 10\log(T_p \cdot B_W) - 3\,\text{dB}, \end{aligned} \tag{6.13}$$

where the extra 3 dB are to account for estimation or processing errors. So, using parameters from Table 6.2, for achieving $SNR_{LEO} = 22\,\text{dB}$ and $SNR_{GEO} = 19.60\,\text{dB}$, the SNR before the antenna should be $SNR_{ant,LEO} = -18.01\,\text{dB}$ and $SNR_{ant,GEO} = -23.30\,\text{dB}$, respectively.

6.5.1.2 Targets

Two targets at different altitudes will be simulated for the examined scenarios: one target at LEO and another target at GEO, at altitudes of 1200 km and 35 795 km, respectively. Since it is assumed that the SNR is fixed, the targets are not considered to have a particular size or RCS.

6.5.2 Results and discussion

As discussed, two satellites are going to be simulated at altitudes 1200 km and 35 795 km. The MIMO AF will be computed for the monostatic case, for one of the bistatic pairs, (6.5), and for the coherent and non-coherent multistatic cases. It should be noted that the coordinates $(0, 0, 0)$ correspond to the position of the target, such that the actual location of the target over time is represented at the origin of the MIMO AF plot. Furthermore, it is assumed that the antennas continuously point to the target throughout the entire observation period. The graphs will show the (x, y) cut of the $z = 0\,\text{m}$ plane.

6.5.2.1 MIMO AF with Doppler shift estimates

For this set of results, the MIMO AF is computed using (6.6) for the non-coherent fusion and (6.7) for the coherent fusion. Some of the results that are going to be displayed present some errors in the Doppler estimation. Nonetheless, because of the multiple fusion the final MIMO AF still presents the target in the correct position. It is worth mentioning that only the results of the (x, y) cut of the LEO target are shown, since the results of the GEO target are very similar to the results observed when no Doppler processing was done.

In the following figures, the red lines represent the $-3\,\text{dB}$ limits. The $-3\,\text{dB}$ lines will define the the uncertainty or ambiguity in the measurement. Similarly, the $-3\,\text{dB}$ levels will give a measure on the possible location and the resolution of the system and not a detection threshold. Moreover, the detection performance will also depend on the chosen detector, which is out of the scope of this thesis.

6.5.2.1.1. Case 1: cluster of receivers

Figure 6.5 shows the (x, y) cut for the $z = 0$ plane of the MIMO AF for the GEO case. First, it must be noted that the ridge in all the graphs is similar because the bistatic range also similar due to the configuration of the receivers. It can be noticed that the introduction of multiple readings from different receivers reduces the uncertainty for the multistatic cases, whether it is coherent or non-coherent. The multistatic case for the non-coherent fusion, Figure 6.5b, shows that the main lobe has absorbed the sidelobes. The AF in the coherent case, Figure 6.5c, presents lower floor levels, the surroundings around the $-3\,\mathrm{dB}$ levels are darker, and also lower uncertainty.

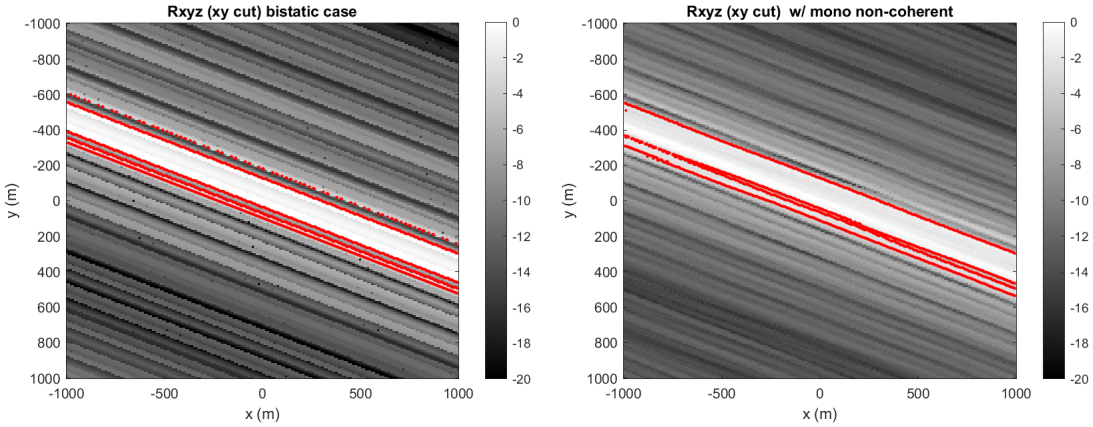

(a) Bistatic case (b) Non-coherent fusion

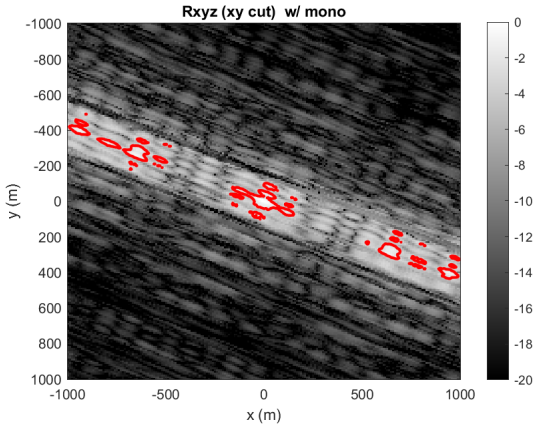

(c) Coherent fusion

Figure 6.5: Case 1, (x,y) cut, alt. $= 35\,795\,\mathrm{km}$

In Figure 6.6 the MIMO AFs after applying Doppler approach are shown. The

first feature to notice is the decrease in ambiguity. Specifically, compared to the GEO target, the ridge has been replaced by a main lobe, Figure 6.6a. The non-coherent fusion, Figure 6.6b, has a similar same shape as the bistatic case, while the coherent fusion, Figure 6.6c, shows how the ambiguity has been highly reduced. One last thing to notice is that some of the bistatic pairs have had their Doppler estimated incorrectly, which results in some higher side lobe levels around the main lobe. However, because of the fusion of the different bistatic readings with the MIMO AF, these do not affect the $-3\,\mathrm{dB}$ levels.

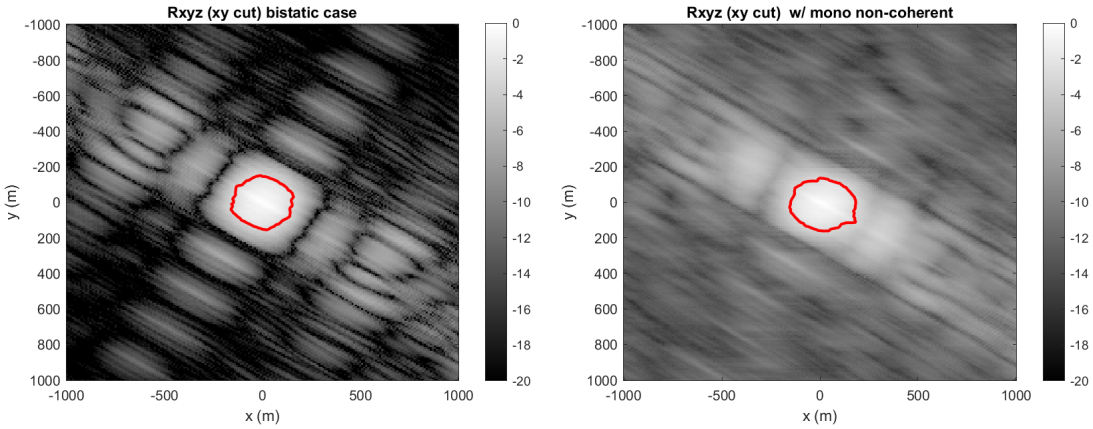

(a) Bistatic case

(b) Non-coherent fusion

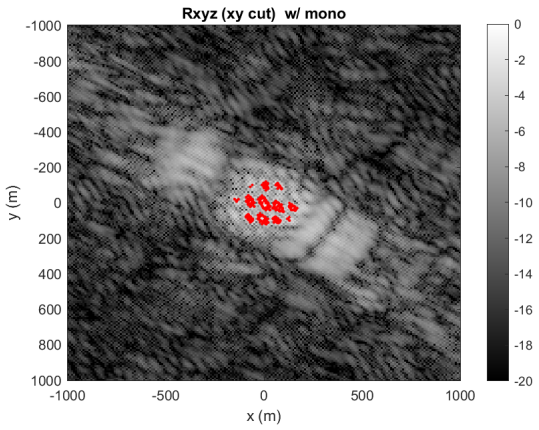

(c) Coherent fusion

Figure 6.6: Case 1, (x,y) cut, alt. $= 1200\,\mathrm{km}$

6.5.2.1.2. Case 2: receivers spread throughout the world

Similarly, as in Case 1, the bistatic AF for a GEO altitude target, see Figure 6.7a, presents a ridge. This is due to the GEO altitude diminishing the effect of the bistatic configuration, as the bistatic angle, around 8°, is small. However, as each MIMO AF is different for each bistatic pair, when fusion is applied, see Figure 6.7b and Figure 6.7c, the ambiguity in the final MIMO AF is reduced. For the coherent fusion, Figure 6.7c, although it seems not to show major peaks are present, a maximum peak is present in (0, 0). The ambiguity for these case has been reduced when compared to the previous scenario, Figure 6.5c.

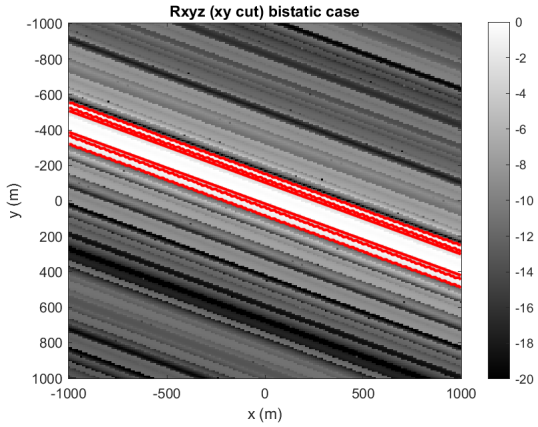

(a) Bistatic case

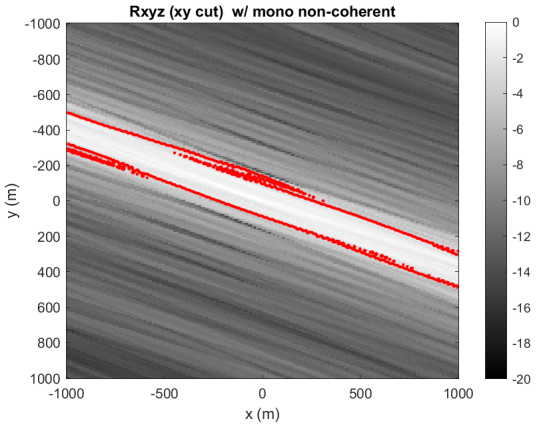

(b) Non-coherent fusion

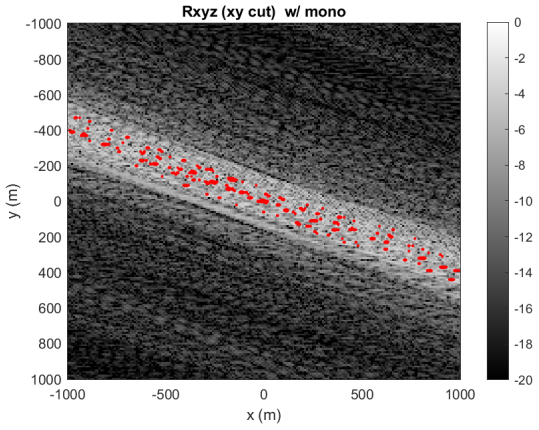

(c) Coherent fusion

Figure 6.7: Case 2, (x,y) cut, alt. = 35 795 km

For the LEO case, the Doppler in the presented bistatic case, Figure 6.8a, has been

incorrectly estimated. This has resulted in the maximum changing position and the target perceived on another location. However, due to the monostatic and the rest of the bistatic readings, the maximum of the multiple fusion occurs in the correct position of the target, Figure 6.8b and Figure 6.8c. At the same time, because of this error, and some other miscalculations in the other bistatic AFs in both the coherent and non-coherent fusion, there are some inconsistencies in the -3 dB levels that might led to a wrong estimation of the location. The coherent fusion, Figure 6.8c, presents smaller ambiguity than the non-coherent case, Figure 6.8b. However, compared to Case 1, the ambiguity seems to be more spread along smaller lobes, instead of several thicker lobes, Figure 6.6c.

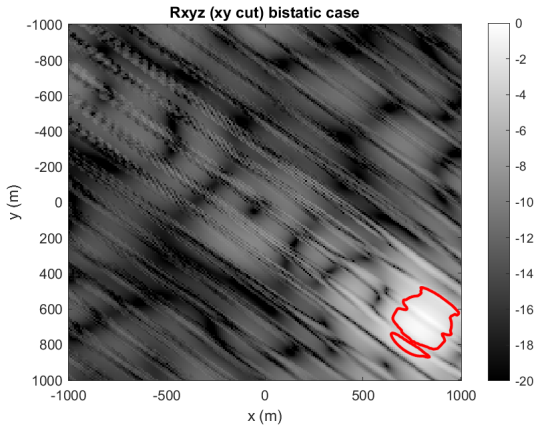

(a) Bistatic case

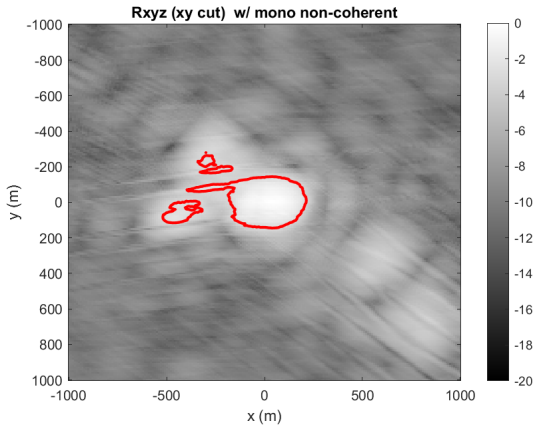

(b) Non-coherent fusion

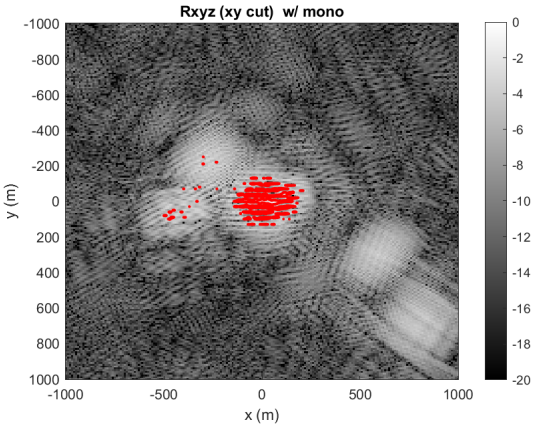

(c) Coherent fusion

Figure 6.8: Case 2, (x,y) cut, alt. = 1200 km

6.5.2.1.3. Case 3: clusters spread throughout the world

For the third and final case, the multistatic AF of the coherent case, Figure 6.9b, presents lower ambiguity than the ridge shaped AF of the non-coherent case, Figure 6.9a. No major improvements have been observed from Case 2.

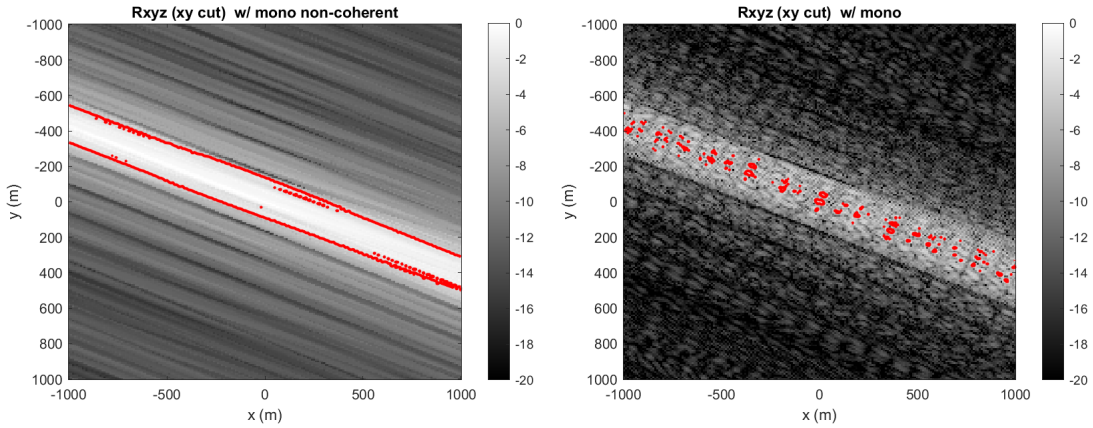

(a) Non-coherent fusion (b) Coherent fusion

Figure 6.9: Case 3, (x,y) cut, alt. = 35 795 km

Case 3 does not present any significant changes from the previous cases for the LEO target. The multiple fusion plots, Figure 6.10a and Figure 6.10b, show almost identical outcomes as in Case 1 and Case 2 for the non-coherent fusion. In the case of the coherent fusion, as in Case 2, the ambiguity is spread throughout multiple thin main lobes, although these seem to be less, and more concentrated around the true position of the target. As with Case 2, the higher values of the side lobes, appearing in a brighter round patch around the true position of the target, come from bad estimations of the other bistatic measurements. Although, the fusion of all of them result in the correct position of the target.

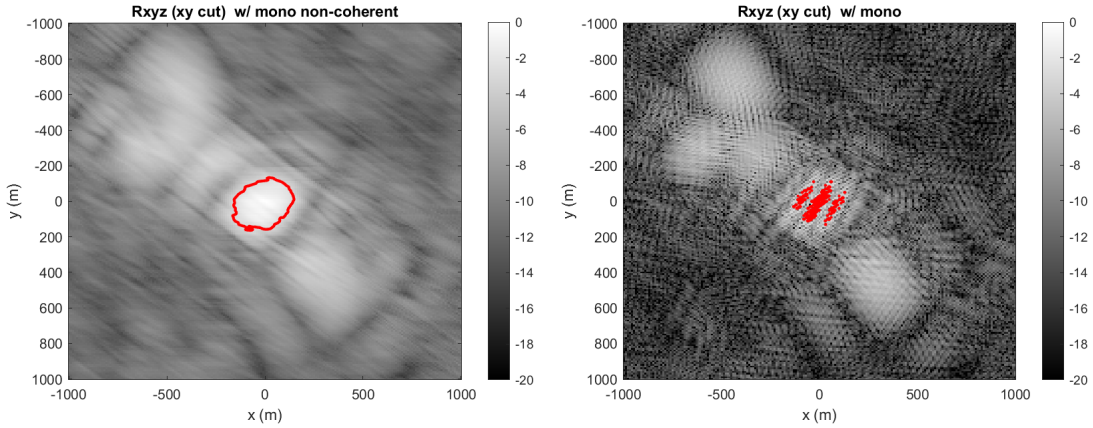

(a) Non-coherent fusion (b) Coherent fusion

Figure 6.10: Case 3, (x,y) cut, alt. = 1200 km

6.6 Conclusion on the long-baseline distributed ground-based radar

In this chapter a long baseline multistatic radar system was proposed as a potential solution for SSA. The results from the feasibility analysis have proven that the SNR would be enough for the detection of certain targets. Further, the results MIMO AF analysis for the multistatic system shows that the extension from bistatic to multistatic gives advantages in localisation performance and reduction in the ambiguity measurement. Using the MIMO AF, the system was assessed under different target-receivers configurations. Results demonstrated that distributed scenarios generally outperform co-located receivers however accounting for synchronisation challenges in remote receivers, clusters of receivers operating coherently can be a good alternative. While coherent fusing performs significantly better than non-coherent in all scenarios, proper synchronisation between all the sensors can be very challenging, especially in highly distributed geometries.

Moreover, comparing the results for different target-sensor configurations it was demonstrated that distributed systems have an advantage over swarms of receivers. This becomes more apparent for targets in lower altitudes where the bistatic angle increases even more. The target is observed from different sides, which results in different bistatic AFs and, when combined, produces an AF with less ambiguity. Nevertheless, in terms

of system implementation, it should be noted that having access to several receivers in different countries and continents can be very challenging. Hence, the cluster of receivers (Case 1) might be more applicable. Furthermore, as the altitude of the target increases, see GEO, the advantages of spread receivers start to diminish and therefore a clustered configuration where coherence fusion could be achieved would be more desirable. It must be noted that the results in Case 3 were more accurate and presented less ambiguity than on the previous two cases. The reason is that compared to Case 1, since all the receivers are in the same location, many of them will present similar processing errors, and compared to Case 2, having less receivers spread through the world will lead to less possible errors. As a consequence, Case 3 is the optimal case.

Chapter 7

Conclusions and future work discussion

This thesis has introduced and analysed novel radar system architectures and advanced signal processing techniques for SSA. As the number of space objects orbiting the Earth continues to grow, the risk of collisions increases. Therefore, it is essential to deploy systems that monitor the space environment to prevent such incidents. While traditional ground-based radar systems play a crucial role in SSA, emerging technologies, such as spaceborne PBR systems, as studied in [12], and long-baseline ground-based distributed radar systems, offer additional advantages, including improved coverage and enhanced location accuracy.

Chapter 2 provided a comprehensive exposition of fundamental radar principles, covering monostatic and bistatic configurations, active and passive radars, and the RRE. These fundaments served as the basis for developing advanced systems and algorithms designed to address the challenges of SSA. Meanwhile, Chapter 3 explored various established techniques and preliminary knowledge employed throughout the thesis.

Regarding spaceborne radar, Chapter 4 introduced the design of the payload of the CubeSat platform, utilizing the OneWeb constellation satellites as an IOs. Section 4.1 examined various antennas. It was concluded that the PAM antenna was the optimal choice, providing a balance between directivity, beam-steering capabilities, and the minimum detectable size. To enhance the performance of the system, an novel multiple observation integration technique was developed in Section 4.2. The technique relied

on the system being able to receive different signals from different frequency channels, which would then be averaged. This technique increases the SNR, which would be essential in later stages of the processing pipeline.

To optimize the estimation method of the altitude of the space objects when the PBR is used, Chapter 5 introduced the zoom-in MF algorithm and the RNN-zoom-in MF algorithm, which improved on the MF approach in [24]. In Section 5.3, the computational load was decreased with the zoom-in algorithm, which computed the MF map by zooming-in on the relevant search points. Additionally, in Section 5.3, a RNN classifier was introduced into the processing pipeline, which reduces the search space, decreasing computational time while maintaining, or in same cases surpassing the accuracy of the zoom-in solution. Two key approaches were explored in this context: the first method tailored the zoom-in MF algorithm for specific RNN classification subspaces; the second approach used the FrFT to produce FS signals that were similar to the $[135, 225]$ subset. The results confirmed that the error could be modelled as a folded Gaussian variable.

Regarding the future work for the spaceborne radar, in [142, 143], strategies for multi-node FSR were explored to extract motion parameters. Similar principles could be adapted to the multi-frequency solution presented in Section 4.2.2. Furthermore, although the proposed solutions in Chapter 5 demonstrate improvements over the established MF approach, the resulting estimation errors could be further reduced. The key challenge lies in narrowing the search space prior to the extraction of target parameters. One straightforward strategy is to exploit ephemerides to constrain the search grid, with a RNN could be employed to select the most appropriate ephemerides from the FS signal. Following, the AI solutions, the proposed RNN in Section 5.3 could be extended with a regression layer, providing direct estimates of altitude and trajectory angle. The associated estimation error may subsequently be modelled and used to refine the search space.

An alternative approach is to employ the derived error models from Section 5.3.4.2 directly, applying them to reduce the search space for altitude estimation before re-estimating the motion parameters. Further reduction of the search space could also be

achieved through beamforming and bistatic configurations, since bistatic measurements would provide preliminary information about the position and velocity of the target prior to FS signal processing. If the search space is sufficiently reduced, gradient-based or Bayesian methods could then be applied for motion parameter estimation.

In the longer term, several developments are required to enable a practical implementation of the FSR system. First, an appropriate SDR platform, as discussed in [12] must be selected to ensure that the system can meet both processing and operational requirements. Parallel to this, dedicated detection strategies for FS signals must be designed and validated. Existing approaches, such as those proposed in [144, 145], provide useful foundations, but further adaptation and refinement will be necessary to accommodate the specific constraints of the envisaged application. Finally, the physical hardware must also be addressed: the antenna will need to be fabricated and experimentally tested to guarantee adequate performance under realistic operational conditions. Collectively, these steps represent the essential pathway toward a robust and deployable FSR solution.

Chapter 6 proposed a long-baseline multistatic radar architecture, processing the different bistatic signals with the MIMO AF to locate the target and reduce measurement errors. The feasibility analysis established the sufficient SNR levels to result in reliable localization results. The comparison between the different receiver configurations proved that distributed receiver systems present an improvement over co-located receiver setups, particularly for LEO targets, where larger bistatic angles significantly enhance the observation diversity.

Future work on the long-baseline distributed radar will primarily focus on the development of Doppler compensation techniques for scenarios in which different receivers observe varying Doppler shifts. Given the high velocities of LEO targets and the associated large Doppler shifts, additional signal processing will also be required to mitigate potential aliasing effects. Accurate Doppler estimation in the presence of multiple targets represents another critical challenge. As discussed in Section 6.5.2, the MIMO AF exhibits a distinguishable absolute maximum, suggesting that a gradient-based approach could be employed to compute the function more efficiently. For operational

deployment, potential synchronization issues must be addressed to ensure reliable performance. Furthermore, similarly to the spaceborne case, an appropriate detection strategy must be implemented to reliably determine the presence of targets within the observation area.

With respect to the state of the art, current SSA radar systems are predominantly implemented as ground-based monostatic or pseudo-monostatic configurations [146, 147], with no operational long-baseline or spaceborne radar systems presently deployed. Because of the considerable costs associated with deployment and maintenance, these ground-based radars are not readily accessible to all individuals or institutions. In this context, the spaceborne PBR offers a potential alternative. In the proposed configuration, the reduced distance between the space object and the receiver, combined with the bistatic arrangement that relies on IOs to collect the radar signals, could render the system more cost-effective and accessible. Furthermore, long-baseline distributed radars provide the additional advantage of enabling observations of a target from multiple perspectives. By exploiting the bistatic angle, such systems may also achieve the capability to detect stealth targets, should they be deployed in the future.

When compared with spaceborne radars, ground-based radars are subject to observational constraints due to their fixed terrestrial location. Conversely, spaceborne radars benefit from orbital motion, which facilitates broader coverage of space regions as they are unconstrained by geographical limitations. From a performance standpoint, long-baseline radars have demonstrated superior localization accuracy, as multiple bistatic baselines provide more robust results even when individual bistatic measurements produce erroneous position estimates. Nevertheless, ground-based radars face difficulties in detecting low-altitude LEO targets, since their observation windows are often too short to guarantee reliable detection. In contrast, spaceborne systems are particularly well-suited to monitoring such targets and, when operating in FS configurations, exhibit enhanced sensitivity to small objects owing to the increased FSML. Additionally, the FS-CS relative to the monostatic RCS is bigger at sufficiently high frequencies. Despite this potential, spaceborne radars employing FS configurations remain at the research stage, with several technical challenges yet to be addressed. Meanwhile, long-

baseline ground-based systems benefit from the maturity of existing monostatic radar technologies, which have been extensively developed and deployed over several decades.

References

[1] Mark A. Richards, ed. *Principles of Modern Radar: Basic principles*. Radar, Sonar and Navigation. Institution of Engineering and Technology, 2010.

[2] J.H. Dewitt and E.K. Stodola. "Detection of Radio Signals Reflected from the Moon". In: *Proceedings of the IRE* 37.3 (1949), pp. 229–242. DOI: 10.1109/JRPROC.1949.231276.

[3] Tom Gootée. "Radar reaches the moon". In: *Radio News* (1946), pp. 25–27.

[4] R. Qashoa, M. Driedger, R. Clark, P. Harrison, M. Berezin, R. Lee, and A. Howarth. "SPACEDUST-Optical: Wide-FOV Space Situational Awareness from Orbit". In: *Proceedings of the Advanced Maui Optical and Space Surveillance (AMOS) Technologies Conference*. Ed. by S. Ryan. Sept. 2023, 160, p. 160.

[5] Tanner Campbell, Adam Battle, Dan Gray, Om Chabra, Scott Tucker, Vishnu Reddy, and Roberto Furfaro. "Stingray Sensor System for Persistent Survey of the GEO Belt". In: *Sensors* 24.8 (2024). ISSN: 1424-8220. DOI: 10.3390/s24082596. URL: https://www.mdpi.com/1424-8220/24/8/2596.

[6] Xuguang Zhang, Yunmeng Liu, Huixian Duan, and E Zhang. "Weak Spatial Target Extraction Based on Small-Field Optical System". In: *Sensors* 23.14 (2023). ISSN: 1424-8220. DOI: 10.3390/s23146315. URL: https://www.mdpi.com/1424-8220/23/14/6315.

[7] Paloch Vasudhara, Wasanchai Vongsantivanich, Pitch Jantawichayasuit, and Supatcha Chaimatanan. "Initial Orbit Determination for Space Situational Awareness System using Triangulation Method". In: *2022 International Conference on Electrical, Computer and Energy Technologies (ICECET)*. 2022, pp. 1–5. DOI: 10.1109/ICECET55527.2022.9872842.

[8] *ESA'S ANNUAL SPACE ENVIRONMENT REPORT*. Tech. rep. ESA Space Debris Office), 2024.

[9] Tico Times. *Costa Rica becomes a space watchman with powerful radar*. 2021. URL: https://ticotimes.net/2021/04/24/costa-rica-becomes-a-space-watchman-with-powerful-radar-2.

[10] LeoLabs Inc. *LeoLabs Accelerates Radar Coverage in Europe with Commissioning of the Azores Space Radar*. 2023. URL: https://www.prnewswire.com/news-releases/leolabs-accelerates-radar-coverage-in-europe-with-commissioning-of-the-azores-space-radar-301844777.html.

[11] J.M. Wallace and P.V. Hobbs. *Atmospheric Science: An Introductory Survey*. International Geophysics Series. Elsevier Academic Press, 2006. ISBN: 9780127329512.

[12] Adriano Rosario Persico, Paul Kirkland, Carmine Clemente, John J. Soraghan, and Massimiliano Vasile. "CubeSat-Based Passive Bistatic Radar for Space Situational Awareness: A Feasibility Study". In: *IEEE Transactions on Aerospace and Electronic Systems* 55.1 (2019), pp. 476–485. DOI: 10.1109/TAES.2018.2848340.

[13] Lewis Creed, Julie Graham, Ciarán Jenkins, Sebastian Diaz Riofrio, Andrew Wilson, and Massimiliano Vasile. "STRATHcube: the design of a CubeSat for space debris detection using in-orbit passive bistatic radar". English. In: 72nd International Astronautical Congress, IAC 2021 ; Conference date: 25-10-2021 Through 29-10-2021. Oct. 2021. URL: https://iac2021.org/,%20https://www.iafastro.org/events/iac/iac-2021/.

[14] Hank Heidt, Jordi Puig-Suari, Augustus S. Moore, Shinichi Nakasuka, and Robert J. Twiggs. "CubeSat: A New Generation of Picosatellite for Education and

Industry Low-Cost Space Experimentation". In: 2000. URL: https://api.semanticscholar.org/CorpusID:33175707.

[15] European Space Agency. *CubeSat Concept and the Provision of Deployer Services*. 2012. URL: https://www.eoportal.org/other-space-activities/cubesat-concept#npscul-naval-postgraduate-school-cubesat-launcher.

[16] Jerome I. Glaser. "Bistatic RCS of Complex Objects near Forward Scatter". In: *IEEE Transactions on Aerospace and Electronic Systems* AES-21.1 (1985), pp. 70–78. DOI: 10.1109/TAES.1985.310540.

[17] Yihua Qin, Abdollah Ajorloo, and Fabiola Colone. "Feasibility Study for a Multichannel Forward Scatter Radar Exploiting Amplitude-based Array Processing". In: *2024 International Radar Conference (RADAR)*. 2024, pp. 1–6. DOI: 10.1109/RADAR58436.2024.10993543.

[18] A.V. Myakinkov, D.M. Smirnova, and R.S. Fadeev. "Space-time processing in multi-static forward scatter radar with moving airborne transmitters". In: *2015 16th International Radar Symposium (IRS)*. 2015, pp. 622–627. DOI: 10.1109/IRS.2015.7226241.

[19] Nabilah Ripin, Ahmad Asari Sulaiman, Nur Emileen Abd Rashid, M. F Hussin, and Nor Najwa Ismail. "Simulation Study of a Small UHF Printed Monopole Antenna for Forward Scatter Radar Network". In: *Advanced Science Letters* 23.5 (2017), pp. 4454–4457. ISSN: 1936-6612. DOI: doi:10.1166/asl.2017.8971. URL: https://www.ingentaconnect.com/content/asp/asl/2017/00000023/00000005/art00140.

[20] M. Gashinova, V. Sizov, N.A. Zakaria, and M. Cherniakov. "Signal detection in multi-frequency Forward Scatter Radar". In: *The 7th European Radar Conference*. 2010, pp. 276–279.

[21] Cheng Hu, V. Sizov, M. Antoniou, M. Gashinova, and M. Cherniakov. "Optimal Signal Processing in Ground-Based Forward Scatter Micro Radars". In: *IEEE Transactions on Aerospace and Electronic Systems* 48.4 (2012), pp. 3006–3026. DOI: 10.1109/TAES.2012.6324674.

[22] A. De Luca, L. Daniel, M. Gashinova, and M. Cherniakov. "Target parameter estimation in moving transmitter moving receiver forward scatter radar". In: *2017 18th International Radar Symposium (IRS)*. 2017, pp. 1–7. DOI: 10.23919/IRS.2017.8008190.

[23] Nertjana Ustalli, Debora Pastina, and Pierfrancesco Lombardo. "Kinematic parameters extraction from a single node Forward Scatter Radar configuration". In: *2018 19th International Radar Symposium (IRS)*. 2018, pp. 1–10. DOI: 10.23919/IRS.2018.8448024.

[24] Ilias Theodorou, Christos Ilioudis, Carmine Clemente, Massimiliano Vasile, and John Soraghan. "SISAR imaging for space debris based on nanosatellites". English. In: *IET Radar Sonar and Navigation* 14.8 (Aug. 2020), pp. 1192–1201. ISSN: 1751-8784. DOI: 10.1049/iet-rsn.2019.0574.

[25] Davide Cataldo, Luca Gentile, Selenia Ghio, Elisa Giusti, Sonia Tomei, and Marco Martorella. "Multibistatic Radar for Space Surveillance and Tracking". In: *IEEE Aerospace and Electronic Systems Magazine* 35.8 (2020), pp. 14–30. DOI: 10.1109/MAES.2020.2978955.

[26] Jun Wang, Zhaotao Qin, Yanxian Bi, Shaoming Wei, and Feixiang Luo. "Target localisation in multistatic radar using BR, TDOA, and AOA measurements". In: *The Journal of Engineering* 2019.19 (2019), pp. 6052–6056. DOI: https://doi.org/10.1049/joe.2019.0128. eprint: https://ietresearch.onlinelibrary.wiley.com/doi/pdf/10.1049/joe.2019.0128. URL: https://ietresearch.onlinelibrary.wiley.com/doi/abs/10.1049/joe.2019.0128.

[32] M.I. Skolnik. *Radar Handbook, Third Edition*. Electronics electrical engineering. McGraw-Hill Education, 2008. ISBN: 9780071485470. URL: https://books.google.es/books?id=76uF2Xebm-gC.

[33] "II - Antenna Elements and Arrays". In: *The Electrical Engineering Handbook*. Ed. by WAI-KAI CHEN. Burlington: Academic Press, 2005, pp. 569–583. ISBN: 978-0-12-170960-0. DOI: https://doi.org/10.1016/B978-012170960-0/

50043-8. URL: https://www.sciencedirect.com/science/article/pii/B9780121709600500438.

[34] A.V. Oppenheim and R.W. Schafer. *Discrete-time Signal Processing*. Prentice-Hall signal processing series. Pearson, 2010. ISBN: 9780131988422. URL: https://books.google.es/books?id=mYsoAQAAMAAJ.

[35] E. O. Brigham and R. E. Morrow. "The fast Fourier transform". In: *IEEE Spectrum* 4.12 (1967), pp. 63–70. DOI: 10.1109/MSPEC.1967.5217220.

[36] Sarah Welch, Gregory Hogan, Delphine Cerutti-Maori, Simon Garrington, Robert Morrison, Matern Otten, Cees Bassa, Nick Pallecaros, Philip van Dorp, Paul Harrison, Tonino Pisanu, and Marco Martorella. "Long Baseline Bistatic Radar for Space Situational Awareness". In: *NATO, STO-MP-SET-SCI-297* ().

[37] Emidio Marchetti, Andrew G. Stove, Edward G. Hoare, Mikhail Cherniakov, David Blacknell, and Marina Gashinova. "Space-Based Sub-THz ISAR for Space Situational Awareness - Laboratory Validation". In: *IEEE Transactions on Aerospace and Electronic Systems* 58.5 (2022), pp. 4409–4422. DOI: 10.1109/TAES.2022.3160985.

[38] University of Birmingham. *University of Birmingham at the forefront of space-borne radar research*. 2023. URL: https://www.birmingham.ac.uk/news/2023/space-borne-radar-research.

[39] Marco Maffei, Augusto Aubry, Antonio De Maio, and Alfonso Farina. "Space-borne Radar Sensor Architecture for Debris Detection and Tracking". In: *IEEE Transactions on Geoscience and Remote Sensing* 59.8 (2021), pp. 6621–6636. DOI: 10.1109/TGRS.2020.3029384.

[40] Marco Maffei, Augusto Aubry, Antonio De Maio, and Alfonso Farina. "An Ontology for Spaceborne Radar Debris Detection and Tracking: Channel-Target Phenomenology and Motion Models". In: *IEEE Aerospace and Electronic Systems Magazine* 36.6 (2021), pp. 18–42. DOI: 10.1109/MAES.2021.3055958.

[41] I. Theodorou, C. V. Ilioudis, C. Clemente, and M. Vasile. "SISAR Imaging - Radio Holography Signal Reconstruction Based on Receiver-Transmitter Motion". In: *2019 IEEE Radar Conference (RadarConf)*. 2019, pp. 1–6. DOI: 10.1109/RADAR.2019.8835596.

[42] R.E. Kell. "On the derivation of bistatic RCS from monostatic measurements". In: *Proceedings of the IEEE* 53.8 (1965), pp. 983–988. DOI: 10.1109/PROC.1965.4077.

[43] V. V. Chapurskiy and V. N. Sablin. "SISAR: shadow inverse synthetic aperture radiolocation". In: *Record of the IEEE 2000 International Radar Conference [Cat. No. 00CH37037]*. 2000, pp. 322–328. DOI: 10.1109/RADAR.2000.851854.

[44] Cheng Hu, Changjiang Liu, Rui Wang, and Tao Zeng. "Improved Reconstruction of Radio Holographic Signal for Forward Scatter Radar Imaging". In: *Sensors* 16.5 (2016). ISSN: 1424-8220. DOI: 10.3390/s16050651. URL: https://www.mdpi.com/1424-8220/16/5/651.

[45] A.B. Blyakhman, A.G. Ryndyk, and A.V. Myakinkov. "Basic Principles of Forward-Scattering Radars". In: *Bistatic Radar*. John Wiley & Sons, Ltd, 2007. Chap. 15, pp. 393–415. ISBN: 9780470035085. DOI: https://doi.org/10.1002/9780470035085.ch15. eprint: https://onlinelibrary.wiley.com/doi/pdf/10.1002/9780470035085.ch15. URL: https://onlinelibrary.wiley.com/doi/abs/10.1002/9780470035085.ch15.

[46] Max Born, Emil Wolf, A. B. Bhatia, P. C. Clemmow, D. Gabor, A. R. Stokes, A. M. Taylor, P. A. Wayman, and W. L. Wilcock. *Principles of Optics: Electromagnetic Theory of Propagation, Interference and Diffraction of Light*. 7th ed. Cambridge University Press, 1999. DOI: 10.1017/CBO9781139644181.

[47] Victor C. Chen and Marco C. Martorella. *Inverse Synthetic Aperture Radar Imaging: Principles, Algorithms and Applications*. The Institution of Engineering and Technology, 2014. DOI: 10.1049/SBRA504E. eprint: https://digital-library.theiet.org/doi/pdf/10.1049/SBRA504E. URL: https://digital-library.theiet.org/doi/abs/10.1049/SBRA504E.

[48] J. Taylor, L. Daniel, E. Hoare, M. Gashinova, and M. Cherniakov. "Reverse Forward Scatter Radar Power Budget Analysis". In: *2021 21st International Radar Symposium (IRS)*. 2021, pp. 1–10. DOI: 10.23919/IRS51887.2021.9466212.

[49] J. Taylor, L. Daniel, E. Hoare, M. Gashinova, and M. Cherniakov. "Reverse forward scatter radar signal simulation with reflectors of opportunity". In: *International Conference on Radar Systems (RADAR 2022)*. Vol. 2022. 2022, pp. 113–118. DOI: 10.1049/icp.2022.2301.

[50] Stéphane Saillant. "Bistatic space-debris surveillance radar". In: *2016 IEEE Radar Conference (RadarConf)*. 2016, pp. 1–4. DOI: 10.1109/RADAR.2016.7485184.

[51] *Technical Report on Space Debris*. Tech. rep. United Nations, 1999.

[52] *Scanning and observing*. URL: https://www.esa.int/Space_Safety/Space_Debris/Scanning_and_observing2.

[53] Giacomo Muntoni, Luca Schirru, Tonino Pisanu, Giorgio Montisci, Giuseppe Valente, Francesco Gaudiomonte, Giampaolo Serra, Enrico Urru, Pierluigi Ortu, and Alessandro Fanti. "Space Debris Detection in Low Earth Orbit with the Sardinia Radio Telescope". In: *Electronics* 6.3 (2017). ISSN: 2079-9292. DOI: 10.3390/electronics6030059. URL: https://www.mdpi.com/2079-9292/6/3/59.

[54] R Lambour, N Rajan, T Morgan, I Kupiec, and E Stansbery. "Assessment of orbital debris size estimation from radar cross-section measurements". In: *Advances in Space Research* 34.5 (2004). Space Debris, pp. 1013–1020. ISSN: 0273-1177. DOI: https://doi.org/10.1016/j.asr.2003.02.043. URL: https://www.sciencedirect.com/science/article/pii/S0273117704000778.

[55] Alexander Serrano, Alexander Kobsa, Faruk Uysal, Delphine Cerutti-Maori, Selenia Ghio, Andrew Kintz, Robert L. Morrison Jr., Sarah Welch, Philip van Dorp, Gregory Hogan, Simon Garrington, Cees Bassa, Chris Saunders, Marco Martorella, Miguel Caro Cuenca, and Isaac Lowe. "Long baseline bistatic radar imaging of tumbling space objects for enhancing space domain awareness". In: *IET Radar, Sonar & Navigation* n/a.n/a (). DOI: https://doi.org/10.1049/rsn2.12511. eprint: https://ietresearch.onlinelibrary.wiley.com/doi/

pdf/10.1049/rsn2.12511. URL: https://ietresearch.onlinelibrary.wiley.com/doi/abs/10.1049/rsn2.12511.

[56] D. Mehrholz, Flury W. Leushacke, R. Jehn, H. Klinkrad, and M. Landgraf. "Detecting, tracking and imaging space debris". In: *ESA Bulletin* 109 (Feb. 2002), pp. 128–134.

[57] Vassilis Karamanavis, Heinrich Dirks, Lars Fuhrmann, Frank Schlichthaber, Nora Egli, Thomas Patzelt, and Jens Klare. "Characterization of deorbiting satellites and space debris with radar". In: *Advances in Space Research* 72.8 (2023), pp. 3269–3281. ISSN: 0273-1177. DOI: https://doi.org/10.1016/j.asr.2023.07.033. URL: https://www.sciencedirect.com/science/article/pii/S0273117723005689.

[58] Klemens Letsch, L. Leushacke, R. Jehn, and R Keller. "First results from the multibeam bistatic beampark experiments at FGAN". In: *5th European Conference on Space Debris* 5 (2009).

[59] Christoph Reising, Markus Gilles, Rudolf Hoffmann, Steven Horstmann, and Stephan Schneider. "GESTRA - upgrading to future distributed phased array radar networks for space surveillance". In: *2022 IEEE International Symposium on Phased Array Systems and Technology (PAST)*. 2022, pp. 1–8. DOI: 10.1109/PAST49659.2022.9975037.

[60] Federica Bordoni, Marwan Younis, Marc Rodriguez-Cassola, Pau Prats-Iraola, Paco López-Dekker, and Gerhard Krieger. "SAOCOM-CS SAR imaging performance evaluation in large baseline bistatic configuration". In: *2015 IEEE International Geoscience and Remote Sensing Symposium (IGARSS)*. 2015, pp. 2107–2110. DOI: 10.1109/IGARSS.2015.7326218.

[61] Sarah Welch, Gregory Hogan, Robert Morrison, Cees Bassa, and Tonino Pisanu. "Long Baseline Radar Bistatic Measurements of Geostationary Satellites". In: *2022 19th European Radar Conference (EuRAD)*. 2022, pp. 1–4. DOI: 10.23919/EuRAD54643.2022.9925016.

[62] Simão da Graça Marto, Massimiliano Vasile, Sebastian Diaz Riofrio, Christos Ilioudis, and Carmine Clemente. "Survey of manoeuvre detection methods and their application to multi-static radar". English. In: AMOS 2022 ; Conference date: 27-09-2022 Through 30-09-2022. Sept. 2022.

[63] R. Píriz, P. Roldán, D. Sanz, J. Díaz, A. González, T. Polewka, and A. Bauch. "A cost-efficient regional synchronization system". In: *2017 Joint Conference of the European Frequency and Time Forum and IEEE International Frequency Control Symposium (EFTF/IFCS)*. 2017, pp. 683–685. DOI: 10.1109/FCS.2017.8089000.

[64] Eduardo Rodrigues Silva Filho and Marc Rodriguez Cassola. "Experimental Evaluation of GNSS-Based Frequency Synchronization for SAR Applications". In: *IGARSS 2022 - 2022 IEEE International Geoscience and Remote Sensing Symposium*. 2022, pp. 7164–7167. DOI: 10.1109/IGARSS46834.2022.9883501.

[65] F. Laghezza, F. Berizzi, A. Capria, E. Dalle Mese, G. Pupillo, S. Montebugnoli, E. Salerno, and M. Di Martino. "Italian bistatic radar system for surveillance of space debris in Low Earth Orbit". In: *2010 IEEE Radar Conference*. 2010, pp. 220–224. DOI: 10.1109/RADAR.2010.5494621.

[66] Victor Chen. *The Micro-Doppler Effect in Radar, Second Edition*. 2019.

[67] Nicholas J. Willis. *Bistatic Radar*. Radar, Sonar and Navigation. Institution of Engineering and Technology, 2004.

[68] J J Hopfield. "Neural networks and physical systems with emergent collective computational abilities." In: *Proceedings of the National Academy of Sciences* 79.8 (1982), pp. 2554–2558. DOI: 10.1073/pnas.79.8.2554. eprint: https://www.pnas.org/doi/pdf/10.1073/pnas.79.8.2554. URL: https://www.pnas.org/doi/abs/10.1073/pnas.79.8.2554.

[69] John Bridle. "Training Stochastic Model Recognition Algorithms as Networks can Lead to Maximum Mutual Information Estimation of Parameters". In: *Advances in Neural Information Processing Systems*. Ed. by D. Touretzky. Vol. 2.

Morgan-Kaufmann, 1989. URL: https://proceedings.neurips.cc/paper_files/paper/1989/file/0336dcbab05b9d5ad24f4333c7658a0e-Paper.pdf.

[70] Hongliang Zhu, Nan Lin, Howard Leung, Rocky Leung, and Segios Theodoidis. "Target Classification From SAR Imagery Based on the Pixel Grayscale Decline by Graph Convolutional Neural Network". In: *IEEE Sensors Letters* 4.6 (2020), pp. 1–4. DOI: 10.1109/LSENS.2020.2995060.

[71] Sangtae Kim, Kwangjin Lee, Seungho Doo, and Byonghyo Shim. "Automotive Radar Signal Classification Using Bypass Recurrent Convolutional Networks". In: *2019 IEEE/CIC International Conference on Communications in China (ICCC)*. 2019, pp. 798–803. DOI: 10.1109/ICCChina.2019.8855808.

[72] Zhongsheng Sun, Jun Wang, Peng Lei, and Zhaotao Qin. "Multiple Walking People Classification with Convolutional Neural Networks Based on Micro-Doppler". In: *2018 10th International Conference on Wireless Communications and Signal Processing (WCSP)*. 2018, pp. 1–4. DOI: 10.1109/WCSP.2018.8555912.

[73] Jihoon Kwon, Seungeui Lee, and Nojun Kwak. "Human Detection by Deep Neural Networks Recognizing Micro-Doppler Signals of Radar". In: *2018 15th European Radar Conference (EuRAD)*. 2018, pp. 198–201. DOI: 10.23919/EuRAD.2018.8546605.

[74] Homa Arab, Iman Ghaffari, Lydia Chioukh, Serioja Ovidiu Tatu, and Steven Dufour. "A Convolutional Neural Network for Human Motion Recognition and Classification Using a Millimeter-Wave Doppler Radar". In: *IEEE Sensors Journal* 22.5 (2022), pp. 4494–4502. DOI: 10.1109/JSEN.2022.3140787.

[75] Fatih Cagatay Akyon, Yasar Kemal Alp, Gokhan Gok, and Orhan Arikan. "Classification of Intra-Pulse Modulation of Radar Signals by Feature Fusion Based Convolutional Neural Networks". In: *2018 26th European Signal Processing Conference (EUSIPCO)*. 2018, pp. 2290–2294. DOI: 10.23919/EUSIPCO.2018.8553176.

[76] Victoria Clerico, Jorge González-López, Gady Agam, and Jesús Grajal. "LSTM Framework for Classification of Radar and Communications Signals". In: *2023 IEEE Radar Conference (RadarConf23)*. 2023, pp. 1–6. DOI: 10.1109/RadarConf2351548.2023.10149618.

[77] Abdulrahman Al-Malahi, Omar Almaqtari, Walid Ayedh, and Bin Tang. "Radar Signal Sorting Using Combined Residual and Recurrent Neural Network (CR-RNN)". In: *2021 18th International Computer Conference on Wavelet Active Media Technology and Information Processing (ICCWAMTIP)*. 2021, pp. 21–27. DOI: 10.1109/ICCWAMTIP53232.2021.9674097.

[78] Marta Walenczykowska and Adam Kawalec. "Radar signal recognition using Wavelet Transform and Machine Learning". In: *2022 23rd International Radar Symposium (IRS)*. 2022, pp. 492–495. DOI: 10.23919/IRS54158.2022.9905015.

[79] Seok-Jun Hong, Yearn-Gui Yi, Jeil Jo, and Bo-Seok Seo. "Classification of Radar Signals with Convolutional Neural Networks". In: *2018 Tenth International Conference on Ubiquitous and Future Networks (ICUFN)*. 2018, pp. 894–896. DOI: 10.1109/ICUFN.2018.8436647.

[80] *Sequence Modelling: Recurrent and Recursive Nets*. URL: https://www.deeplearningbook.org/contents/rnn.html.

[81] Diederik P. Kingma and Jimmy Ba. *Adam: A Method for Stochastic Optimization*. 2017. arXiv: 1412.6980 [cs.LG].

[82] David E. Rumelhart, Geoffrey E. Hinton, and Ronald J. Williams. "Learning representations by back-propagating errors". In: *Nature* 323 (Oct. 1986), pp. 533–536. ISSN: 1476-4687. URL: https://doi.org/10.1038/323533a0.

[83] Ronald J. Williams and David Zipser. "Gradient-based learning algorithms for recurrent networks and their computational complexity". In: *Backpropagation: Theory, Architectures, and Applications*. USA: L. Erlbaum Associates Inc., 1995, pp. 433–486. ISBN: 0805812598.

[84] Sepp Hochreiter and Jürgen Schmidhuber. "Long Short-Term Memory". In: *Neural Computation* 9.8 (Nov. 1997), pp. 1735–1780. ISSN: 0899-7667. DOI: 10.1162/neco.1997.9.8.1735. eprint: https://direct.mit.edu/neco/article-pdf/9/8/1735/813796/neco.1997.9.8.1735.pdf. URL: https://doi.org/10.1162/neco.1997.9.8.1735.

[85] Ralf C. Staudemeyer and Eric Rothstein Morris. "Understanding LSTM - a tutorial into Long Short-Term Memory Recurrent Neural Networks". In: *CoRR* abs/1909.09586 (2019). arXiv: 1909.09586. URL: http://arxiv.org/abs/1909.09586.

[86] L.G.M. Baas Becking. "On the analysis of sigmoid curves". In: *Acta Biotheor* 8 (June 1946), pp. 42–59. URL: https://doi.org/10.1007/BF01555951.

[87] Sridhar Narayan. "The generalized sigmoid activation function: Competitive supervised learning". In: *Information Sciences* 99.1 (1997), pp. 69–82. ISSN: 0020-0255. DOI: https://doi.org/10.1016/S0020-0255(96)00200-9. URL: https://www.sciencedirect.com/science/article/pii/S0020025596002009.

[88] *Long short-term memory (LSTM) layer for recurrent neural network (RNN).* URL: https://uk.mathworks.com/help/deeplearning/ref/nnet.cnn.layer.lstmlayer.html.

[89] *Sentinel missions overview.* URL: https://sentinels.copernicus.eu/web/sentinel/missions.

[90] *Sentinel missions overview.* URL: https://earth.esa.int/eogateway/missions/earthcare.

[91] *HY-2 (Haiyang-2).* URL: https://www.eoportal.org/satellite-missions/hy-2a.

[92] Ilias Theodorou, Carmine Clemente, and Massimiliano Vasile. "Space object detection and characterisation with a passive space-borne bistatic radar". In: *68th International Astronautical Congress, IAC 2017*. Proceedings of the International Astronautical Congress, IAC. AUS: International Astronautical Fed-

eration (IAF), Sept. 2017, pp. 341–345. ISBN: 9781510855373. URL: https://strathprints.strath.ac.uk/76391/.

[93] Ogutu B. Osoro and Edward J. Oughton. "A Techno-Economic Framework for Satellite Networks Applied to Low Earth Orbit Constellations: Assessing Starlink, OneWeb and Kuiper". In: *IEEE Access* 9 (2021), pp. 141611–141625. DOI: 10.1109/ACCESS.2021.3119634.

[94] Federal Communications Commission. *Application for modification of authorization for the SpaceX NGSO satellite system*.

[95] Federal Communications Commission. *Petition for Declaratory Ruling to Modify the U.S. Market Access Grant for the OneWeb Ku-band and Ka-Band NGSO FSS System*. 2023.

[96] Vincent J. Riot, Lance M. Simms, and Darrell Carter. "Lessons Learned Using Iridium to Communicate with a CubeSat in Low Earth Orbit". In: *Journal of Small Satellites* 10.1 (Feb. 2021). ISSN: 2327-4123. URL: https://www.osti.gov/biblio/1770026.

[97] Warren L. Stutzman and Gary A. Thiele. *Antenna Theory and Design*. 3rd. Hoboken, NJ: John Wiley & Sons, 2012. ISBN: 978-0-470-57664-9.

[98] Constantine A Balanis. *Antenna theory: analysis and design*. Wiley-Interscience, 2005.

[99] George Casu, Cătălin Moraru, and Andrei Kovacs. "Design and implementation of microstrip patch antenna array". In: *2014 10th International Conference on Communications (COMM)*. 2014, pp. 1–4. DOI: 10.1109/ICComm.2014.6866738.

[100] Peng Lv, Hu Liu, Yan Li, and Buning Tian. "An X-band space-borne low-profile lightweight patch antenna array using integrated design". In: *2019 IEEE MTT-S International Wireless Symposium (IWS)*. 2019, pp. 1–3. DOI: 10.1109/IEEE-IWS.2019.8804059.

[101] A. Fenn. "Theoretical and experimental study of monopole phased array antennas". In: *IEEE Transactions on Antennas and Propagation* 33.10 (1985), pp. 1118–1126. DOI: 10.1109/TAP.1985.1143499.

[102] Alberto Hernández-Escobar, Takashi Tomura, Ryosuke Hasaba, Hiroshi Taneda, and Issei Watanabe. "An Inverted-L Monopole Array With High Beam Coverage for Antenna-in-Package Modules at the 151.5–164 GHz Band". In: *IEEE Access* 12 (2024), pp. 107144–107152. DOI: 10.1109/ACCESS.2024.3436856.

[103] Roger F. Harrington. *Time-Harmonic Electromagnetic Fields*. Piscataway, NJ: John Wiley & Sons, 2001. ISBN: 978-0-7803-6035-8.

[104] L. B. Cebik. *Straightening Out the Inverted-L*. http://www.cebik.com/content/a10/il/il.html. Accessed: [Insert Date of Access]. 2000.

[105] A.D. Wunsch and Sheng-Pin Hu. "A closed-form expression for the driving-point impedance of the small inverted L antenna". In: *IEEE Transactions on Antennas and Propagation* 44.2 (1996), pp. 236–242. DOI: 10.1109/8.481653.

[106] Roel X. F. Budé, Amr Elsakka, Ulf Johannsen, and A. Bart Smolders. "Wide-Scan Focal Plane Arrays for mmWave Point-to-Multipoint Communications". In: *IEEE Open Journal of Antennas and Propagation* 3 (2022), pp. 112–123. DOI: 10.1109/OJAP.2021.3136721.

[107] S. Ooe, S. Nakata, M. Iwashita, and N. Kaya. "New Receiving Ground Antenna Using Active Phased Array Antenna for Nano for Nano-Satellites". In: *The 5th Nano-Satellite Symposium* (2013).

[108] Shiela Prasad and R. W. P. King. "Experimental study of inverted L-, T-, and related transmission-line antennas". In: *Journal of Research of the National Bureau of Standards* 65.5 (Sept. 1961). September–October, pp. 449–454.

[109] Andrew T. Gobien. "Chapter 3: The Inverted-L Antenna and Variations". In: *Investigation of Low Profile Antenna Designs for Use in Hand-Held Radios*. Ed. by Andrew T. Gobien. Accessed: 2025-08-31. Blacksburg, Virginia: Virginia Polytechnic Institute and State University, 1997. Chap. 3. URL: https://vtechworks.lib.vt.edu/handle/10919/36959.

[110] L. Huitema and T. Monediere. "Compact Antennas — An overview". In: *Progress in Compact Antennas*. Ed. by Laure Huitema. Rijeka: IntechOpen, 2014. Chap. 1. DOI: 10.5772/58837. URL: https://doi.org/10.5772/58837.

[111] B&Z Technologies. *LNA, 10 MHz to 12GHz. Model: BZ-P0101200-251040-131616*. URL: https://bnztech.com/datasheets/BZ-P0101200-251040-131616.pdf.

[112] VBE Technology. *10-12GHz, Ku-Band, Low Noise Amplifier (LNA)*. URL: https://www.vbejammer.com/sale-10497310-10-12ghz-ku-band-low-noise-amplifier-lna.html.

[113] Reyhan Baktur. "CubeSat Link Budget: Elements, calculations, and examples". In: *IEEE Antennas and Propagation Magazine* 64.6 (2022), pp. 16–28. DOI: 10.1109/MAP.2022.3201250.

[114] Fulin Xue, Yiming Zhang, Junlong Li, and Hui Liu. "Circularly Polarized Cross-Dipole Antenna for UHF RFID Readers Applicated in the Warehouse Environment". In: *IEEE Access* 11 (2023), pp. 38657–38664. DOI: 10.1109/ACCESS.2023.3253542.

[115] David M. Pozar. *Microwave Engineering*. 4th ed. John Wiley & Sons, 2011.

[116] Simão da Graça Marto, Sebastián Díaz Riofrío, Christos Ilioudis, Carmine Clemente, and Massimiliano Vasile. "Satellite manoeuvre detection with multistatic radar". English. In: *Journal of the Astronautical Sciences* 70.5 (Sept. 2023). ISSN: 0021-9142. DOI: 10.1007/s40295-023-00399-3.

[117] Bobak Shahriari, Kevin Swersky, Ziyu Wang, Ryan P. Adams, and Nando de Freitas. "Taking the Human Out of the Loop: A Review of Bayesian Optimization". In: *Proceedings of the IEEE* 104.1 (2016), pp. 148–175. DOI: 10.1109/JPROC.2015.2494218.

[118] "Chi-square Goodness of Fit Test". In: *The Concise Encyclopedia of Statistics*. New York, NY: Springer New York, 2008, pp. 72–76. ISBN: 978-0-387-32833-1. DOI: 10.1007/978-0-387-32833-1_55. URL: https://doi.org/10.1007/978-0-387-32833-1_55.

[119] Ahmed Tealab. "Time series forecasting using artificial neural networks methodologies: A systematic review". In: *Future Computing and Informatics Journal* 3.2 (2018), pp. 334–340. ISSN: 2314-7288. DOI: https://doi.org/10.1016/j.fcij.2018.10.003. URL: https://www.sciencedirect.com/science/article/pii/S2314728817300715.

[120] H. M. Ozaktas, Z. Zalevsky, and M. A. Kutay. *The Fractional Fourier Transform with Applications in Optics and Signal Processing*. Wiley, Chichester, 2001.

[121] Luis B. Almeida. "The Fractional FourierTransform and Time-Frequency Representations". In: *IEEE Transactions on Signal Processing* 42.11 (Nov. 1994).

[122] Alex Graves, Santiago Fernández, and Jürgen Schmidhuber. "Bidirectional LSTM Networks for Improved Phoneme Classification and Recognition". In: *Artificial Neural Networks: Formal Models and Their Applications – ICANN 2005*. Ed. by Włodzisław Duch, Janusz Kacprzyk, Erkki Oja, and Sławomir Zadrożny. Berlin, Heidelberg: Springer Berlin Heidelberg, 2005, pp. 799–804. ISBN: 978-3-540-28756-8.

[123] Christos Ilioudis, Carmine Clemente, and John Soraghan. "GNSS-based passive UAV monitoring: a feasibility study". In: *IET Radar, Sonar & Navigation* 14.4 (2020), pp. 516–524. DOI: https://doi.org/10.1049/iet-rsn.2019.0308. eprint: https://ietresearch.onlinelibrary.wiley.com/doi/pdf/10.1049/iet-rsn.2019.0308. URL: https://ietresearch.onlinelibrary.wiley.com/doi/abs/10.1049/iet-rsn.2019.0308.

[124] I. Papoutsis, C.J. Baker, and H.D. Griffiths. "Netted radar and the ambiguity function". In: *IEEE International Radar Conference, 2005.* 2005, pp. 883–888. DOI: 10.1109/RADAR.2005.1435952.

[125] T. Derham, S. Doughty, C. Baker, and K. Woodbridge. "Ambiguity Functions for Spatially Coherent and Incoherent Multistatic Radar". In: *IEEE Transactions on Aerospace and Electronic Systems* 46.1 (2010), pp. 230–245. DOI: 10.1109/TAES.2010.5417159.

[126] *Basic Description of the Two Line Element (TLE) Format*. URL: https://www.space-track.org/documentation#/tle.

[127] A. De Maio and M.S. Greco. *Modern Radar Detection Theory*. Electromagnetics and Radar. Institution of Engineering and Technology, 2015. ISBN: 9781613531990. URL: https://books.google.co.uk/books?id=ZKGiCwAAQBAJ.

[128] Pedro A. Capó-Lugo and Peter M. Bainum. "2 - Two body orbital motion". In: *Orbital Mechanics and Formation Flying*. Ed. by Pedro A. Capó-Lugo and Peter M. Bainum. Woodhead Publishing, 2011, pp. 7–35. ISBN: 978-0-85709-054-6. DOI: https://doi.org/10.1533/9780857093875.7. URL: https://www.sciencedirect.com/science/article/pii/B9780857090546500027.

[129] Qianghui Zhang, Junjie Wu, Wenchao Li, Yulin Huang, Jianyu Yang, and Haiguang Yang. "Near-Space TOPSAR Large-Scene Full-Aperture Imaging Scheme Based on Two-Step Processing". In: *Sensors* 16.8 (2016). ISSN: 1424-8220. DOI: 10.3390/s16081177. URL: https://www.mdpi.com/1424-8220/16/8/1177.

[130] Ousmane O. Sy, Simone Tanelli, Nobuhiro Takahashi, Yuichi Ohno, Hiroaki Horie, and Pavlos Kollias. "Simulation of EarthCARE Spaceborne Doppler Radar Products Using Ground-Based and Airborne Data: Effects of Aliasing and Nonuniform Beam-Filling". In: *IEEE Transactions on Geoscience and Remote Sensing* 52.2 (2014), pp. 1463–1479. DOI: 10.1109/TGRS.2013.2251639.

[131] M. Zhan, P. Huang, X. Liu, J. Sheng, J. Chen, and Y. Sun. "Coherent accumulation detection for a maneuvering target with doppler ambiguity and doppler aliasing". In: *IET International Radar Conference (IET IRC 2020)*. Vol. 2020. 2020, pp. 1421–1424. DOI: 10.1049/icp.2021.0575.

[132] Kenneth M. Peterson. "Satellite Communications". In: *Encyclopedia of Physical Science and Technology (Third Edition)*. Ed. by Robert A. Meyers. Third Edition. New York: Academic Press, 2003, pp. 413–438. ISBN: 978-0-12-227410-7. DOI: https://doi.org/10.1016/B0-12-227410-5/00673-6. URL: https://www.sciencedirect.com/science/article/pii/B0122274105006736.

[133] MINOLI and NO. *SATELLITE SYSTEMS ENGINEERING IN AN IPV6 ENVIRONMENT*. 1st ed. CRC PRESS, 2009.

[134] *Space Surveillance Sensors: The Millstone Hill Radar (May 5, 2012)*. URL: https://mostlymissiledefense.com/2012/05/05/space-surveillance-sensors-millstone-hill-radar/.

[135] Michael Buonsanto. *Millstone Hill*. Tech. rep. MIT Haystack Observatory, 1992.

[136] Takashi Iida and Hiromitsu Wakana. "Communications Satellite Systems". In: *Encyclopedia of Physical Science and Technology (Third Edition)*. Ed. by Robert A. Meyers. Third Edition. New York: Academic Press, 2003, pp. 375–408. ISBN: 978-0-12-227410-7. DOI: https://doi.org/10.1016/B0-12-227410-5/00882-6. URL: https://www.sciencedirect.com/science/article/pii/B0122274105008826.

[137] Partha Sarathi Nandy and Deepak Putrevu. "Impact of ionosphere on high-bandwidth chirp in L-band SAR and its mitigation". In: *Earth Observing Missions and Sensors: Development, Implementation, and Characterization IV*. Ed. by Xiaoxiong J. Xiong, Saji Abraham Kuriakose, and Toshiyoshi Kimura. Vol. 9881. International Society for Optics and Photonics. SPIE, 2016, 98811Q. DOI: 10.1117/12.2223826. URL: https://doi.org/10.1117/12.2223826.

[138] E. Chapin, S.F. Chan, B.D. Chapman, C.W. Chen, J.M. Martin, T.R. Michel, R.J. Muellerschoen, X. Pi, and P.A. Rosen. "Impact of the ionosphere on an L-band space based radar". In: *2006 IEEE Conference on Radar*. 2006, 8 pp.-. DOI: 10.1109/RADAR.2006.1631775.

[139] U. Jakobus and F.M. Landstorfer. "Improved PO-MM hybrid formulation for scattering from three-dimensional perfectly conducting bodies of arbitrary shape". In: *IEEE Transactions on Antennas and Propagation* 43.2 (1995), pp. 162–169. DOI: 10.1109/8.366378.

[140] *Technical Characteristics of the Effelsberg 100-m Radio Telescope*. URL: https://web.archive.org/web/20120222064356/http://www.mpifr-bonn.mpg.de/div/effelsberg/antenna/antenna_spec.html.

[141] Lincoln Laboratory. *The Millstone Hill Propagation Study: Progress in FY 1970*. 1970. URL: https://apps.dtic.mil/sti/pdfs/AD0717156.pdf.

[142] Debora Pastina, Micaela Contu, Pierfrancesco Lombardo, Marina Gashinova, Alessandro De Luca, Liam Daniel, and Mikhail Cherniakov. "Target motion estimation via multi-node forward scatter radar system". In: *IET Radar, Sonar & Navigation* 10.1 (2016), pp. 3–14. DOI: https://doi.org/10.1049/iet-rsn.2015.0130. eprint: https://ietresearch.onlinelibrary.wiley.com/doi/pdf/10.1049/iet-rsn.2015.0130. URL: https://ietresearch.onlinelibrary.wiley.com/doi/abs/10.1049/iet-rsn.2015.0130.

[143] M. Gashinova, L. Daniel, M. Cherniakov, P. Lombardo, D. Pastina, and A. De Luca. "Multistatic Forward Scatter Radar for accurate motion parameters estimation of low-observable targets". In: *2014 International Radar Conference*. 2014, pp. 1–4. DOI: 10.1109/RADAR.2014.7060336.

[144] D.M. Gould, R.S. Orton, and R.J.E. Pollard. "Forward scatter radar detection". In: *RADAR 2002*. 2002, pp. 36–40. DOI: 10.1109/RADAR.2002.1174649.

[145] Krzysztof Kulpa, Mateusz Malanowski, Marcin Baczyk, and Piotr Krysik. "Passive radar detection range enhancement using forward scatter geometry". In: *2015 16th International Radar Symposium (IRS)*. 2015, pp. 54–59. DOI: 10.1109/IRS.2015.7226393.

[146] Daniel Rowland et al. "The Worldwide Network of Radars: LeoLabs' Global SSA Services". In: *Proceedings of the Advanced Maui Optical and Space Surveillance Technologies Conference (AMOS)*. 2021. URL: https://amostech.com/TechnicalPapers/2021/Poster/Rowland.pdf.

[147] J. Haimerl et al. "Space Fence System Overview". In: *Proceedings of the Advanced Maui Optical and Space Surveillance Technologies Conference (AMOS)*. 2015. URL: https://amostech.com/TechnicalPapers/2015/SSA/Haimerl.pdf.